M. E.

MECHANICAL ENGINEERING
OCT 9 1959
LIBRARY

JOURNAL OF THE

AERO/SPACE SCIENCES

VOLUME 26 OCTOBER, 1959 NUMBER 10

CONTENTS

Rocket Propulsion Systems for Interplanetary Flight ..... GEORGE PAUL SUTTON 609

Shroud Tests of Pressure and Heat Transfer Over Short Afterbodies With Separated Wakes ..... MARTIN H. BLOOM AND ADRIAN PALLONE 626

Optimum Path of an Airplane—Minimum Time to Climb ... THEODORE THEODORSEN 637

Spherical Cap Snapping ..... HERBERT B. KELLER AND EDWARD L. REISS 643

Unsteady Laminar Compressible Boundary Layers on an Infinite Plate With Suction or Injection ..... KWANG-TZU YANG 653

A Study of Creep Collapse of a Long Circular Cylindrical Shell Under Uniform External Pressure ..... N. J. HOFF, W. E. JAHSMAN, AND W. NACHBAR 663

Readers' Forum 670

LIBRARY
PURDUE UNIVERSITY

Published by
INSTITUTE OF THE AERONAUTICAL SCIENCES, INC.

JOURNAL OF THE AERO/SPACE SCIENCES

Editor: W. R. SEARS

Director, Graduate School of Aeronautical Engineering, Cornell University

Associate Editor: ROBERT R. DEXTER *Managing Editor:* RITA J. TURINO

Editorial Assistant: CAROLINE TAYLOR

Editorial Committee

Aerodynamics and Fluid Mechanics

H. Julian Allen
Holt Ashley
Dean R. Chapman
Francis H. Clauser
Hugh L. Dryden
John C. Evvard
Antonio Ferri
Alexander Flax
Wallace D. Hayes
R. T. Jones
Carl Kaplan
H. W. Liepmann
C. C. Lin
H. F. Ludloff
Harold Luskin
Clark B. Millikan
Henry T. Nagamatsu
H. J. E. Reid
George S. Schairer
G. B. Schubauer
John Stack
Theodore Theodorsen
Arthur N. Tifford
Th. von Kármán

Flight Testing

R. R. Gilruth
Melvin N. Gough
W. L. Howland
W. F. Milliken, Jr.

Rotating Wing Aircraft

F. B. Gustafson
K. H. Hohenemser
Bartram Kelley
R. B. Maloy
Ralph McClarren
R. H. Miller
R. H. Prewitt
Igor I. Sikorsky

Structures

John E. Duberg
R. R. Heldenfels
N. J. Hoff
Samuel Levy
J. F. McBrearty
W. Ramberg
E. E. Sechler
F. R. Shanley
C. R. Strang
S. Timoshenko

Meteorology

C. F. Brooks
D. M. Little
F. W. Reichelderfer
K. C. Spengler

Vibration and Flutter

Lee Arnold
M. A. Biot
R. L. Bisplinghoff
Harold A. Cheilek
I. E. Garrick
Martin Goland

Aircraft Design

W. E. Beall
E. H. Heinemann
Hall L. Hibbard
Richard Hutton
C. L. Johnson
A. A. Kartveli
F. K. Teichmann

Electronics

K. C. Black
M. V. Kiebert, Jr.
David S. Little
Paul Rosenberg
Giles J. Strickroth

Physiologic Problems

H. G. Armstrong
Louis H. Bauer
Robert J. Benford
W. Randolph Lovelace, II
Ross A. MacFarland

Flight Propulsion

William Bollay
George W. Brady
R. P. Kroon
Frank E. Marble
Abe Silverstein
E. S. Taylor

Instruments

Alan G. Binnie
Charles H. Colvin
Frank R. Cook
C. S. Draper
S. G. Eskin
C. F. Savage
R. C. Sylvander

SUBSCRIPTION RATES

JOURNAL OF THE AERO/SPACE SCIENCES (formerly Journal of the Aeronautical Sciences), Published Monthly. United States and Possessions: 1 Year, $15.00; Single Copies, $1.50. Foreign Countries Including Canada (American Currency Rates): 1 Year, $16.00; Single Copies, $1.50.

AERO/SPACE ENGINEERING, Published Monthly. United States and Possessions: 1 Year, $5.00; Single Copies, $0.50. Foreign Countries Including Canada (American Currency Rates): 1 Year, $6.00; Single Copies, $0.50.

Notices of change of address should be sent to the Institute at least 30 days prior to actual change of address.

Manuscripts for publication, proofs, and all correspondence should be addressed to the Editorial Office of the JOURNAL.

Publication Office, 20th and Northampton Sts., Easton, Pa. Correspondence regarding subscriptions may be addressed to the Editorial Office of the JOURNAL OF THE AERO/SPACE SCIENCES, 2 East 64th Street, New York 21, N. Y.

© *Copyright, 1959, by the Institute of the Aeronautical Sciences, Inc.*

Second-Class Mail Privileges Authorized at Easton, Penna. Acceptance for mailing at a special rate of postage provided for in Section 1103, Act of October 3, 1917, authorized April 29, 1937.

JOURNAL OF THE AERO/SPACE SCIENCES

VOLUME 26 OCTOBER, 1959 NUMBER 10

Rocket Propulsion Systems for Interplanetary Flight

GEORGE PAUL SUTTON*

Massachusetts Institute of Technology

Summary

A comparison is made of several different propulsion systems for interplanetary flight. Liquid and solid propellant rockets, propulsion systems which use nuclear energy sources, arc heating rockets, magneto-plasma devices, ion rocket propulsion, solar heating rockets, and solar sails are briefly described and their current status reviewed. Engine performance requirements for different interplanetary missions are established. These several propulsion systems are then compared on the basis of several performance criteria, environmental characteristics, vehicle requirements, reliability, current status, growth potential, and efficiency. Predictions on various propulsion system capabilities and an analysis of multiple rocket engine reliability is included. It is concluded that electrical rockets are superior for long-time interplanetary flight applications, and that chemical rockets are satisfactory for most of the immediate applications in "near" space. None of the several propulsion schemes discussed can be rejected until further technical work has been accomplished.

Introduction

MANY DIFFERENT TYPES of rocket propulsion systems have been proposed for interplanetary flight. In this paper an attempt is made to give some of the principal characteristics of several of these propulsion systems, to list some of the requirements imposed by interplanetary flight and to compare the merits and potential areas of engine application.

The discussion concerns the mid-course propulsion for interplanetary transfer trajectories, and therefore will not include propulsion systems for take-off, landing, or operation in the strong gravitational fields of the planets. By eliminating the boosters from this paper, the discussion will be concentrated on the relatively low thrust, long duration propulsion systems for interplanetary travel, and the maneuvers for taking off or returning to a satellite orbit.

Presented as the IAS 1959 Minta Martin Aeronautical Lecture, M.I.T., March 18, 1959.

Received March 4, 1959. Revised and received May 18, 1959.

* Formerly, Hunsaker Professor of Aeronautical Engineering, Department of Aeronautics and Astronautics, M.I.T. Now, Chief Scientist, Advanced Research Projects Agency, Department of Defense, and Director, Advanced Research Projects Division, Institute for Defense Analyses.

Propulsion Systems

Four categories of propulsion systems are discussed in this paper. They are (1) the liquid propellant and solid propellant rockets which generate energy from chemical combustion, (2) those that use nuclear energy as their source of power, (3) those that use electrical or electromagnetic devices for the acceleration of mass, and, finally, (4) those that use electromagnetic radiation (light waves) to obtain a propulsive force. Simple schematic diagrams for the basic types of propulsion engines are shown in Figs. 1, 2, 3, and 6 and simple engine performance parameters are listed in Table 1. There are many different types and forms of each of the engines which are enumerated in this discussion and, therefore, it is virtually impossible to cover all the possible versions. Thus, the descriptions given in this section are cursory and are primarily intended to identify the various systems. A comparison of their performance and operating characteristics is given in the following sections.

(a) *Chemical Rockets*

There are two principal types, those using *liquid propellants* and those using *solid propellants*. (See Fig. 1.) Both today are well developed and understood.[1] In the chemical reaction, energy is released which is converted into the heating of a working fluid (in this case, the reaction products themselves), and this gaseous working fluid in turn is expanded and accelerated in a nozzle to very high velocities, thus converting some of the enthalpy into the kinetic energy of the jet. There appear to be no fundamental limitations as to the size of these chemical propulsive devices, and many

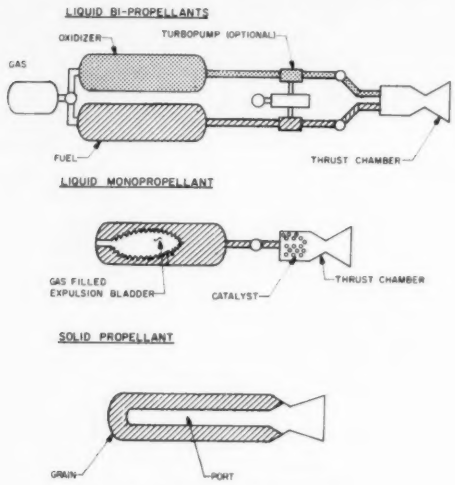

Fig. 1. Chemical rockets.

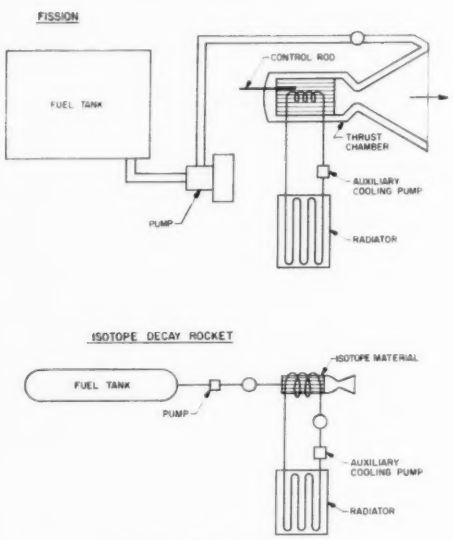

Fig. 2. Nuclear rockets.

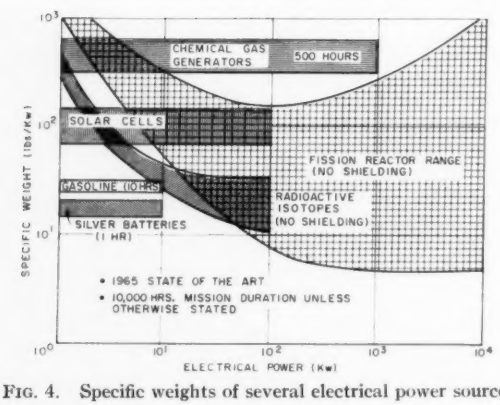

Fig. 4. Specific weights of several electrical power sources.

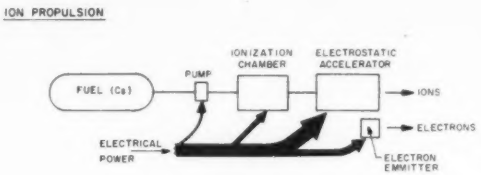

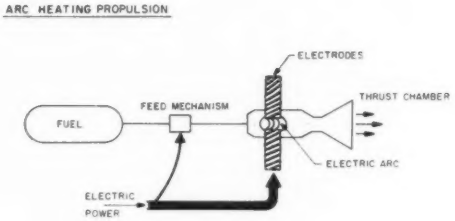

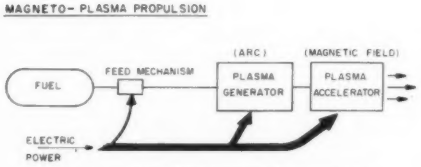

Fig. 3. Electrical propulsion systems.

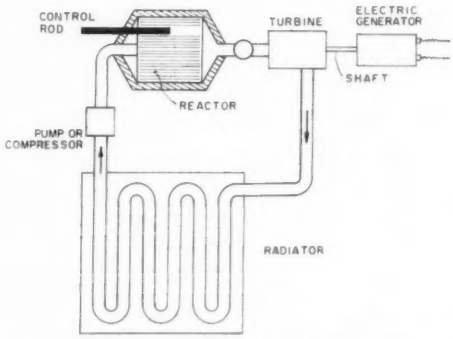

Fig. 5. Electrical power generation with a reactor.

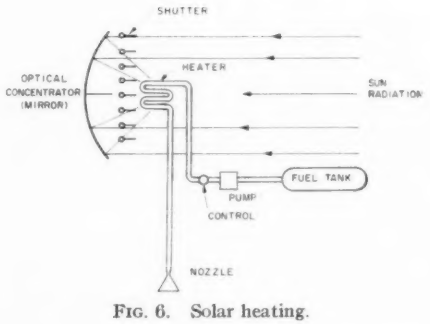

Fig. 6. Solar heating.

TABLE 1
Ranges of Specific Impulse, Thrust-to-Weight Ratio, and Duration

System	Specific Impulse (sec.)*	Thrust-to-Weight Ratio	Typical Duration
Chemical	200–420	10^{-2}–10^{2}	minutes (high thrust) hours (low thrust)
Fission	500–1,100	10^{-2}–10	same
Isotope Decay	400–700	10^{-5}–10^{-3}	days
Arc Heating	400–2,000	10^{-4}–10^{-2}	days
Magneto-plasma	5,000–25,000	10^{-5}–10^{-3}	weeks
Ion	5,000–60,000	10^{-5}–10^{-3}	months
Solar Heating	400–700	10^{-3}–10^{-2}	days

* Vacuum expansion.

different forms and types have been explored and built. The duration of operation and the acceleration that can be imparted to interplanetary vehicles by chemical rockets can be very high. The restarting of a liquid propellant rocket requires the purging and cleaning of the liquids and reaction products from the injection manifolds. It is fundamentally very difficult to stop a solid propellant rocket engine without destroying it; consequently, restarting a solid propellant rocket appears impractical.

The use of high energy chemicals such as fluorine, hydrogen, boron compounds, and others has led to the evolution of propellants which provide perhaps fifteen to thirty per cent higher specific impulse than those in common use today. They will soon be in use. While they give improved performance, their active chemical nature causes design problems and operational hazards.

The maximum energy that can be derived from chemical combustion is limited, by the fundamental nature of the propellant and reaction product chemicals and to their bonds, to about 420 sec. of specific impulse, as shown in Table 1.[2] There does not appear to be a promising approach for further increasing this energy release. Although such devices as the use of free radicals have been studied, they do not appear to be promising at this time.[3, 4]

Although liquid *monopropellants* generally do not have as much specific impulse (about 200–225 sec.) as liquid bipropellants or solid propellants, they have the marked advantage of permitting a very simple, restartable low chamber pressure rocket engine with a gas pressurized feed system.[5]

(*b*) *Nuclear Propulsion*

Today there are three types of nuclear energy release—namely, fission, fusion, and decay of radioactive isotopes. In the first type (see Fig. 2) the heat is usually generated by the *fission* of uranium in a solid reactor framework.[6, 7, 8] This heat then is conducted to the surface of this solid body where it is transferred to a working fluid, usually hydrogen. This working fluid is gasified and heated to very high temperatures. Subsequently it is expanded through a supersonic nozzle and accelerated to very high velocities and therefore to high kinetic energies. The principle of operation is basically identical to that of a liquid propellant rocket except that the energy for heating the gases does not come from chemical combustion but from fission. The temperature that can be so attained is theoretically almost unlimited. Because it is possible to choose a working fluid of very low molecular weight it is possible to obtain higher specific impulses with this particular type of propulsion than with the chemical fuels. However, the degradation of physical strength of materials which occurs at high temperatures limits the maximum working fluid temperature to perhaps 4,000 to 6,000°F., and therefore limits the performance that can be attained with this device.

There are also other basic problems that are not present in liquid propellant rockets. For example, the high intensity neutron and gamma radiation emanating from the nuclear reactor heats all hardware adjacent to the reactor. These parts must be artificially cooled in order to keep their physical strength. Simple flanges and bolts in the immediate vicinity of the reactor have to be cooled.

In interplanetary space there is no air and therefore there is no scattering of nuclear radiation. The shielding of sensitive equipment or a human crew can thus be achieved by relatively simple shadow shields and by designing the space ship in such a manner as to interpose a large distance between the reactor and the sensitive payload. While this is a much lighter weight system than the conventional full radiation shield, it causes some severe design problems.

The reactor's control and the coordination of this control with the flow control is difficult. The nuclear activity determines the amount of heat released and the flow going through the reactor determines the heat that can be absorbed from the reactor. These have to be matched in each flow passage, particularly during transient operations, and care has to be exercised to see that there will be no undue cooling or heating of the solid parts. The residual energy that is present in all nuclear fission reactors is a source of considerable concern. Provisions have to be made either to throw the reactor away after use (and let it vaporize itself) or to keep it cooled by some auxiliary cooling mechanism which rejects excess heat to space. Such a cooling circuit is shown in Fig. 2.

It would be desirable to release the heat directly in the propulsive working fluid by using a liquid or gaseous reactor. In this case the solid outer walls containing the reactor vessel would be cooler than the gas and the fission reaction would take place inside the working fluid at substantially higher gas temperatures.[9] Calculations indicate that this would be tremendously difficult to achieve economically in small, lightweight machines without losing large amounts of uranium.

The use of *fusion*, which is the second way of using nuclear energy in propulsion, could become very attractive but is not as yet sufficiently understood to be

practical.[10–12] The advantages here would be a lack of fission products (which can poison the surrounding environment and the operating crew) and the ability to release the energy directly to the working fluid (which could be hydrogen) and therefore the attainment of substantially higher performance. To date, a controlled, prolonged fusion reaction has not been achieved. It appears that such machines will be large and heavy and will not be feasible for a long time. Therefore no further discussion of fusion rocket will be given in the remainder of this paper.

The third type of nuclear propulsion uses energy from *radioactive isotope decay*.[13] This type lends itself to a relatively simple propulsive device. The decay of radioactive isotopes gives off energy in the form of either alpha, beta, or gamma radiation, or all three. Some isotopes produce only alpha and beta particles and their energy is readily converted to heat. Others have a major portion of their energy in gamma rays, which are harmful to electronic equipment and human beings and require shielding. By choosing the proper isotope almost all the decay energy can be transferred to a working fluid. Such materials as cerium, polonium, thulium, and thallium can be considered as isotopes for heating of hydrogen. Some of these are fission products of uranium—e.g., cerium—and are obtained by the chemical refinement of spent reactor fuel elements; others can be obtained by irradiation of a pure substance in a special reactor—e.g., thallium and polonium. All are very expensive to produce.

Because it is difficult today to fabricate and concentrate large amounts of such radioactive material in a single part without some special provisions and because the weight per unit power output is relatively high, this type of propulsion device will use small amounts of isotopes only. It will have a high fixed weight. In order to obtain reasonably high fluid temperatures (1,000 to 3,000°F.), the flow rate per unit area through the isotope energy source will be low and has to be properly matched. If developed, the isotope decay rocket, therefore, will be suitable for low thrust-to-weight ratios and very low thrusts (less than one pound). At a later date it may be possible to conceive of practical units for medium large thrusts.

Heat is rejected from the isotope at all times and it will be necessary to provide an artificial cooling system to prevent the melting or vaporizing of the isotope material when the propulsive system itself is not operating. Depending on the design and the isotope material, it will be possible to convert between 50 and 100 per cent of the decay energy into heat. Unfortunately, the energy level diminishes with time in accordance with the law of radioactive decay. Because hydrogen can be used as a working fluid, the performance of this particular device is relatively good and can exceed 600 or 700 sec. if sufficiently high temperatures can be attained. This is 50 to 100 per cent better than chemical rockets, as shown in Table 1. One of the outstanding virtues of this particular device is its simplicity. This should make it particularly attractive for relatively reliable operation in space. However, the device can be highly radioactive and will require shielding in the vehicle as well as on the launching test stands.

In general, all three nuclear rocket systems are still in the exploratory or research stage. Because the technical problems are difficult, these devices will not fly soon.

(*c*) *Electrical Propulsion*

Today there are basically three types of electrical propulsion that are of interest to space flight (see Fig. 3). The first, *arc heating propulsion*, is basically electrical heating of a working fluid, the second, *ion propulsion*, uses the electrostatic acceleration of positively charged ions, and the third method will be referred to as *magneto-plasma* propulsion. The energy is supplied from a vehicle-borne energy source which is separate from the propulsive device. The required power per unit thrust is generally very large, for it increases linearly with the specific impulse. For reasonable thrust levels (larger than 0.1 lb.) a nuclear reactor power plant is assumed here for all electrical propulsion devices, because (as will be discussed later) it gives the lowest weight for high-powered energy sources.

In an *arc heating rocket propulsion* device the electrical energy is added to the working fluid completely within an arc, which is struck between two electrodes.[14, 15] This arc creates a plasma of the working fluid and as the working fluid is blown through the arc, it is heated. A plasma is an electrically neutral fluid containing electrically activated particles such as positive ions and negative electrons. Only a relatively small portion of the electrical energy is actually put into the kinetic energy of the working fluid, perhaps as much as 15 to 20 per cent. A good part of the electrical energy is unfortunately lost in the resistance of the electrode as heat rejection to the chamber walls, and as radiation. If it is possible to use the propellant as regenerative coolant, then perhaps 85 per cent of all the electrical energy is transferred as heat to the working fluid and some 50 to 60 per cent as kinetic energy of the jet. With a low flow of hydrogen the chamber material temperatures (with regenerative cooling) could become too high and an auxiliary cooling system with a separate heat sink may be required.

To date, some good work has been done on the problem of the thrust chamber, the arc, and its confinement, but further work is needed on eliminating electrode erosion (needed for long life), a power supply and conversion system, and the development of light weight hardware.

A schematic diagram as shown in Fig. 3 shows the basic principle of an *ion rocket*.[16–20] Contact ionization (the contact of two dissimilar materials of different work function will strip electrons) seems to be preferred over other methods because of its relatively good efficiency, simplicity of actual operation, and its good prospect for prolonged operation. The resulting ions are accelerated by an electrostatic field of high

voltage (in excess of 10,000 volts), and the ions ejected attain very high speeds. Depending on the voltage and the atomic weight of the ions, speeds will vary up to and exceed 1 million ft. per sec.; this corresponds to specific impulses of over 60,000 sec. The ions must be neutralized by reabsorbing the electrons that were originally stripped, so that no further electrostatic retarding forces are exerted upon the ions once they flow past the last electrode. This would generally be done by emitting electrons near the ion discharge port. The energy required to ionize the working fluid is small compared to the energy required for electrostatic acceleration. There are some thermal radiation losses.

The fundamental relation for the specific impulse, specific thrust (thrust per unit weight), and the thrust of an ion propulsion unit are given in references 17 and 20 and indicate that the accelerating voltage, the particle weight of the ion (usually the atomic weight), the number of electrons that are stripped off the ion, and the magnitude of the total flow are important critical parameters. Materials of high atomic weight such as uranium or cesium are significantly better because they require less power for the same thrust than one of a higher specific impulse.

In a magneto-plasma rocket acceleration of a plasma can be accomplished in at least two ways, by changing or collapsing magnetic fields and by the interaction of electric current and a steady magnetic field. In the first method it is possible to impart additional kinetic energy to a plasma but this must be done in a cyclic process.[21, 22] Plasma is created at high temperature, usually in an arc, and accelerated by means of changing magnetic fields. Because of the rotation induced in the plasma it has been necessary to resort to annular plasmas (smoke-rings) and a concentric barrel type accelerator. One of the problems is to keep the walls free of the plasma so as to minimize the heat transfer to the walls. This can be done by magnetic fields which constrain the plasma from reaching the walls. By choosing a working fluid of low molecular weight, such as hydrogen, it is possible to obtain high specific impulses in excess of 15,000 sec. The driving force is expressed as a magnetic pressure which is a function of the maximum magnetic field strength and the permeability of the working fluid. With proper techniques and proper geometries it may be possible to transfer over 90 per cent of the magnetic energy into kinetic energy of the moving fluid. This device and the ion rocket can give specific impulses 100 to 200 times those of chemical rockets. Unfortunately, in its present form this device requires a bank of relatively heavy capacitors, heavy conductors, fancy switches, and a high energy power source.

It is also possible to accelerate a plasma in a steady flow process by passing an electric current (at right angles to the flow) through it, while at the same time imposing a magnetic field (which is also at right angles to both the flow and current).[23] The force that is so exerted on the plasma is proportional to the current and the flux density of the magnetic field. This is fundamentally the basic principle of the electrical plasma generator, except current is put into the working fluid instead of being drawn out.[24] The specific impulse valve here is perhaps 1,000 to 1,500 sec.

Any of these electrical propulsion systems require a lot of electrical energy. A comparison of several different types of electrical energy sources is shown in Fig. 4. This information is reproduced in part from reference 25. Nuclear fission reactors (with a relatively fixed critical mass) and, to a lesser extent, isotopes with heavy shields do not increase proportionately in size with additional power output. Therefore their specific weight tends to decrease as the power is increased. The uncertainty in the weight and the wide variation that is possible with all of these methods indicate that design parameters are not well established. Since the thrust that can be obtained from, say, 10 Megawatt of thermal power in a nuclear reactor gives only a few pounds, nuclear reactors seem to be essential today for arc heating, ion, and magneto-plasma systems of reasonable thrust. While a solar energy source would be simpler in many ways, the thrust output for present mirrors would be in the micropound range and this has only limited practical application.

Unfortunately, the nuclear power reactor for electrical rockets (and in this case also the isotope decay rocket) require radiators to reject waste heat into space. A closed thermodynamic cycle is generally used, as shown in Fig. 5. High heat sink temperatures will reduce the size of required radiator area, but diminish the efficiency of the cycle. For a given power there is therefore an optimum radiator temperature. The penetration of radiators by meteoritic particles will be treated in more detail in a subsequent section.

These radiators and the energy sources are very heavy, and any inefficiency in the system simply requires them to be heavier yet. Although methods for direct conversion of heat to electricity have been developed recently, their efficiencies appear to be inferior to that of a thermodynamic turbogenerator. Until the weight and efficiency of thermoelectric converters is improved, they do not appear attractive, particularly for high power requirements.

In general, all three of the electric propulsion systems are relatively unexplored. Although considerable work is going on in all these and related fields, the effort is still largely exploratory. The principal technical problems are not only associated with the propulsive device, but also with the power source and efficient conversion and control mechanism. A good invention here would be welcome. The development of a lightweight vehicle-bound nuclear reactor would probably pace the development schedule of any of these electrical schemes.

(*d*) *Solar Heating Rocket*

This proposed propulsion system is shown in a very simple schematic diagram in Fig. 6. It uses solar radiation energy to heat a working fluid, say hydrogen,

to temperatures between perhaps 1,000 and 2,000°F. The optical system of this device has to be pointed at all times exactly toward the sun (the half angle of the sun as seen from the earth is only 16 minutes) and this may be difficult in a vehicle which rotates and maneuvers. The propulsion system will not function when in the shadow of a planet. At the distances of Mars and Venus the sun energy density is 43 per cent and 192 per cent, respectively, of that on the Earth. At Pluto the sun's radiation is less than 1 per cent as strong as that on earth. The versatility of this solar rocket system is therefore somewhat restricted.

Most of the radiation energy from the sun is in the near infrared and visible spectrum. At the radius of the earth from the sun there is an incident radiation of approximately 0.122 B.t.u./ft.^{2}-sec. This translates itself into a necessary area of 8 sq. ft. per kilowatt of captured power if a 100 per cent power conversion efficiency is assumed. An optical system is necessary to provide a high-temperature heat source for a thermodynamic fluid. However a good, lightweight solar concentration system in space will probably be able to use only about 20 to 65 per cent of the incident sun's radiation at the actual heater for conversion into useful energy.[26–28] There are optical losses due to absorption, structural shadows, surface roughness, scattering, vectoring errors in pointing the optical systems exactly at the sun, and imperfection in the parabolic, spherical, or cylindrical shape of the optical surfaces. In addition, there is the problem of efficiently converting the heat into suitable propulsive power. With all these losses the required actual area per kilowatt of useful propulsive power will be close to 80 sq. ft. If the same output is expected near Mars then 200 sq. ft. will be needed.

With very good optical systems it should be possible to concentrate the sun's incident energy to somewhere between 4 and 14 B.t.u./ft.^{2}-sec. at a target area. Not all of this heat will be absorbed by the target area. Some of it will be radiated off into empty space. One proposed method of construction is to use an inflated plastic mylar sphere, half of which is coated with reflecting metal on the inside, the other half acting as a transparent window.[29, 30] If the plastics withstand the environmental space conditions, then this method gives a lightweight system design. Once the sphere is inflated, then the gas could be lost by diffusion or meteorite penetration, but it still may be possible to hold the metal reflector by electrical means.

If it is estimated that approximately one third of a pound per square foot of area is needed and if direct heating of hydrogen is used, then the acceleration that can be obtained with such a vehicle could be in the order of one one hundredth the acceleration of gravity. If solar energy were used in conjunction with ion propulsion of one pound thrust, then the optical mirrors can have dimensions of several hundred feet in diameter. It is of course impossible to transport such a big optical system inside a ferry vehicle, unless some clever folding or inflating mechanism or an actual assembly in space is contemplated. This folding or furling of an optical surface presents some real problems in minimizing the weight and in arriving at a clever design for assuring the necessary optical curvature and surface. Small solar heating rockets of less than, say, two kilowatts may become practical soon, since their mirrors could be transported without folding or inflation.

(e) *Light Wave Propulsion*

Photons have the properties of particles as well as waves. The reflection of light can be considered the bouncing of photons off a surface. The radiation pressure of sunlight at the earth's distance from the sun is about 10^{-7} lb./ft.^{2}, but this again diminishes as the square of the distance from the sun. The pressure sensed on a perfectly reflecting surface is twice as large.

This reflection permits the use of solar pressure forces for spaceship *attitude control* and the concept of *solar sailing*.[31] By extending light weight reflectors from a spaceship on long moment arms, it is possible to turn spaceships completely around in a few hours. Solar sailing gives small forces only in the general direction away from the sun, and this limits some of the maneuvers that can be undertaken. A typical acceleration would be only 5×10^{-7} ft./sec.^{2} in the vicinity of the earth and this is equivalent to a velocity gain of only a few feet per second in one year. A really light weight design of a solar reflector could be achieved by stretching a very thin plastic sail (less than 0.001 in. thick) between inflated "baloney" cells; this presents many interesting design problems.

Because there is no working fluid or energy source carried in the vehicle, this type of propulsion is very economical in weight. The photon velocity is that of the speed of light, and relativistic effects must be considered.

The photon rocket has often been mentioned in the literature[32, 33] as basically a strong light source with a reflector. The emission of a unidirectional beam of photons would cause a thrust reaction. Calculations indicate, however, that the required energy is far beyond the capacity of present concepts and the efficiency and the cooling problem of the mirrors would not permit the design of a practical device of this type based on present technology. The photon rocket is therefore eliminated from further discussion.

In addition to the four basic types of systems described here, many others have been considered, but are not discussed here. For example, the possibility of direct emission of particles from a nuclear reactor, or electrons from a thermoionic source has been considered but rejected as impractical at this time.[34, 35] Furthermore, there are combination systems, such as those combining features of chemical and electrical rockets.

Performance Evaluation

In this section the flight performance of these various types of propulsion systems for interplanetary

missions is examined. It is difficult to generalize and select the best of these propulsion systems. Instead it is proper to examine the application of various propulsion systems to various specific space flights and to select one good engine system (or more) for each specific case.[36, 37]

First, some fairly well-established engine parameters for various propulsion systems will be examined. Then the requirements of several different space flight maneuvers will be presented and these in turn will be related to several engine parameters.

(*a*) *Simple Engine Performance Parameters*

These include the following principal parameters: *specific impulse*, *engine weight* (or *engine specific weight*), *thrust*, and *duration of power application*.

The engine performance parameters are intimately related to the vehicle parameters and the mission requirements, such as the energy that has to be added, the trajectory, the number of stages and their relative weights, the mass ratios (ratio of initial stage weight to final weight, i.e., without propellant), the duration of thrust application, and the number of operations. These will be discussed further in a subsequent section.

An appreciation of the relative values of specific impulse and thrust to weight ratio can be found in Table 1. It can be seen that the chemical and fission rocket engines, while relatively poor in specific impulse, have a high thrust capability, while the electrical systems have a high engine weight and only a very low thrust, but this thrust is delivered at high specific impulse. The isotope decay and solar heating rockets are in between in value. Since the jet power required per unit thrust increases as the specific impulse is increased, the electrical devices must carry a heavy power supply with them to furnish this increased energy.

Fig. 7 shows the relation between *acceleration* (which is also the thrust-to-weight ratio of the vehicle), *specific impulse* (or exhaust velocity) and the *specific power*, which is defined here as the ratio of kinetic energy in the jet per unit of time and the overall weight of the vehicle system including its energy source mechanism. The shaded areas indicate the approximate regions of the several engines.

Chemical and nuclear engines, which operate only for a relatively short time, have the best values of specific power. The other devices operate for long durations, and pack much less power output per unit weight.

TABLE 2
Velocity Requirements For Various Typical Spaceflight Maneuvers

Planet	Escape (or Landing) From Ground	Escape (or Landing) From a Satellite Orbit	Interorbit Transfer From Earth
Moon	7,700	2,260	
Earth	36,700		
Mars	16,800	4,940	11,500
Venus	33,370	9,900	11,300
Jupiter	197,700	57,800	20,600
Saturn	119,200		24,000
Sun	2,023,000		

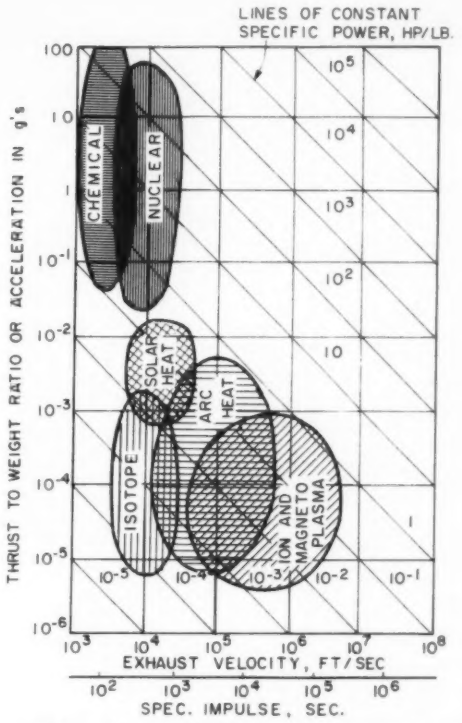

FIG. 7. Regions of accelerations and specific powers for various rockets.

This is partly due to some of their poor efficiencies, as will be discussed later. A good means for reducing the weight of power source and machinery would be very helpful here.

The very low flight acceleration of the electrical and isotope decay systems means longer periods of time for accelerating to a given vehicle speed. Thus, these units basically require more flight time for acceleration than those that can accelerate fast. The specific impulse of the electrical units is higher than that of the others, and this means they need to carry less propellant; if the engine weights are reasonable, then this implies that they can carry a heavier payload than, say, a chemical rocket (even though it may take longer) for many interplanetary missions. These devices show promise for becoming the freight vehicles for the interplanetary shuttle traffic. We will examine this in more detail later.

(*b*) *Trajectory Velocity Requirements*

There are seven different basic maneuver requirements. The suitability of the various propulsion systems for these interplanetary maneuvers is shown in Table 3. The required vehicle velocity increments can be computed approximately for each of these seven separately and then added. They are as follows:

(1) *Escape From Earth Gravity Field*—As was previously explained, it is assumed that the interplanetary flight starts in an orbit above the earth's surface; in this case, the interplanetary propulsion system has to supply only the energy necessary for increasing the

TABLE 3
Suitability of Various Propulsion Systems to Different Interplanetary Maneuvers

MANEUVER	CHEMICAL	FISSION	ISOTOPE DECAY	ARC HEATING	MAGNETO-PLASMA	ION	SOLAR HEATING	SOLAR SAIL
ESCAPE FROM ORBIT	○	○	▨	▨	▨	▨	▨	▨
INTERPLANETARY TRANSFER	▨	▨	○	○	○	○	○	▨*
CHANGE OF PLANE	▨	▨	○	○	○	○	○	▨*
ORIENTATION	○	▨	○	○	○	○	○	○
TRAJECTORY CORRECTIONS	○	▨	○	○	○	○	○	●*
TARGET APPROACH	▨	▨	○	○	○	○	○	●*
CAPTURE	○	○	▨	▨	▨	▨	▨	●

○ SUITABLE
▨ ACCEPTABLE
● UNDESIRABLE

* Forces in general direction of radiation.

velocity from that of the orbit about the earth to that required for escape. See Table 2. Basically this is equivalent to overcoming the gravitational attraction of the earth above a circular orbit altitude and escape from the earth. Because the gravitational field is fairly strong, it is desirable to apply this energy increment in a short period of time—i.e., at high acceleration—so that the amount of energy necessary to fight the gravitational field is minimized.

It can be shown that a thrust-to-weight ratio higher than 0.5 will give only negligibly small gravitational losses. This means that chemical and nuclear rockets are the only ones suitable for this maneuver. Electrical, solar heating, and isotope rockets require a characteristic spiral escape trajectory, which not only consumes additional energy, but also requires much more time in space. For a fast interplanetary getaway, a rocket with a low thrust-to-weight ratio is not desirable for the escape maneuver.

(2) *Interplanetary Orbit Transfer*—The second energy increment that has to be applied to the interplanetary vehicle by the propulsion system is required to go into the selected transfer orbit from one planet to another. It is basically the energy necessary to overcome the gravitational field of the sun and to correct for the differences in tangential velocities of the launching planets and the vehicle in its prescribed orbit. The idealized minimum energy is given by what is known as a Hohmann ellipse, which is tangent at the aphelion to the orbit of the outer planet and at the perihelion to that of the inner planet. The sun is at the prime focus of the ellipse. In this case maximum use is made of the tangential velocity of the two planets—namely, the launching planet and the target planet. Unfortunately, the Hohmann ellipse which is the path of minimum energy requires the planets to be in favorable relative position with respect to each other, and this event occurs at infrequent intervals. It is often desirable to fly along a "faster" transfer orbit that requires more energy yet saves transit time. This will permit more frequent interplanetary trips and minimize exposure to interplanetary environment; however, it will require considerable additional energy. It will also permit more flexibility in the date of launching. It is not always necessary or desirable to apply thrust for this particular maneuver separately; often this energy is applied at the same time as the escape maneuver.

(3) *Change of Plane*—An additional increment of velocity or energy is needed to change the flight vector from the plane of the elliptic of one planet to that of another planet.[38] For example, Mars rotates in a plane which is inclined at 1.85° to that of the earth. This amount of energy is often small, can be zero, but it also can be large. The exact amount depends on the specific locations of the launching and target planets at the time of the flight, and the exact position and time of the vehicle when this correction is applied.

(4) *Trajectory Corrections*—The next increment of propulsive energy that has to be applied to the interplanetary vehicle is concerned with corrections to the flight path or the vehicle's orbit. It is intended to correct for errors in navigation devices, guidance system, computer, booster system, or pilot. They are intimately connected with the magnitudes of the errors inherent in automatic guidance, and these corrections can be small when accurate guidance and navigation systems are used. It is also intended to correct for errors in the "solar map," for the exact orbit and position of the planets is not known accurately at this time.

Changes of the planes of the trajectory and flight path corrections do not need to be applied suddenly, but can be allowed to take place over fairly long periods of time, perhaps weeks or even months. Therefore, a low thrust-to-weight ratios and a high specific impulse are ideally suited for these maneuvers. See Table 3.

(5) *Vehicle Orientation*—The next energy requirement imposed upon the propulsion system concerns the rotary maneuvering of the spaceship. This basically means an adjustment in pitch, yaw, and roll to orient the spaceship in a specified direction. First of all any residual moment that is imparted to the spaceship by the last rocket engine and any disturbing torques have to be counteracted. When making navigational observations it may be necessary in some designs to orient and point the whole spaceship in the direction of various stars in the sky. Also when transmitting or receiving communications data through directionally oriented communication equipment, or when solar energy is caught by a directional optical system, it will be necessary to rotate and point very accurately certain types of spaceships. One way to achieve this is by means of a low-thrust propulsion system. This maneuver requires accurately adjustable devices capable of giving small torques in any direction. A simple, mul-

tiple nozzle monopropellant system or a series of solar radiation pressure reflectors appear ideally suited for this application.

(6) *Target Planet Approach*—When approaching a target planet it will become necessary to change the tangential velocity of the vehicle to match that of the target planet. This can be either an acceleration or a deceleration depending on the specific trajectory. With low thrust-to-weight ratio engines this maneuver has to be started while quite some distance away from the target planet, while high-acceleration engines (chemical or nuclear) can do this rapidly in the immediate vicinity of the planet.

(7) *Capture Maneuver*—The last propulsion requirement from an interplanetary propulsion system is very similar to the first only it is applied in the reverse direction. It is the application of energy to permit the proper entering into an approach orbit about the target planet. It is concerned with orienting the spaceship from its interplanetary transfer path to a planetary or satellite path around the target planet. Again, this particular maneuver requires the application of relatively large forces and the overcoming of a relatively high gravitational field. This maneuver into an orbit about the target planet does not provide for actual landing on the planet. This in turn requires the overcoming of much larger gravitational forces and the interplanetary propulsion system is generally not suitable for this purpose. Usually a separate high thrust stage will be required to achieve the landing maneuver from the orbit about the planet to its surface.

For high thrust-to-weight ratio engines (larger than 0.5) the approach path to the target planet is very sensitive to the exact time of starting the thrust for the capture orbit maneuver. Because of navigational inaccuracies it is very likely that the original orbit that will be attained will be very different from the one that eventually is desired because of the close tolerances that have to be observed between the relative positions of the vehicle and the target planet and their relative velocities. It will therefore very likely be necessary to modify the initial elliptical capture orbit into the desired orbit which may be circular or which may have to be rotated to give a polar orbit with respect to the target planet. This will require an additional increment of velocity in order to achieve the desired flight path. Such a satellite orbit transfer maneuver may be very necessary if a landing is later attempted from the satellite about the target planet. For low thrust-to-weight ratio engines this maneuver will be executed in a spiral of successively smaller radius of curvature. Again this requires much time.

Typical values for various mission requirements are given in Table 2. Listed here are the idealized velocities that would be attained in a gravity-free space for any specific maneuver if the ship moves in a straight line. From values like these it is possible to obtain approximate numbers for the total velocity requirement for a spaceship, as shown in Fig. 8, simply by adding the respective individual velocity requirements.

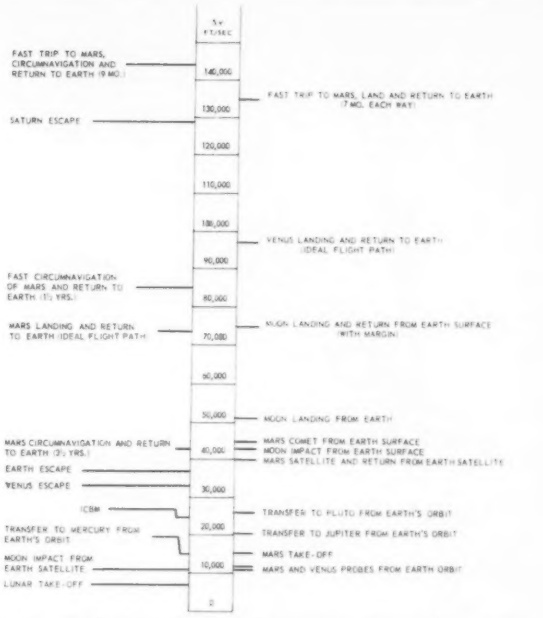

FIG. 8. Equivalent velocity increments for various space missions.

This addition gives a hypothetical mission velocity increment, which is equivalent to the velocity that the vehicle could attain in a gravity-free vacuum.

It can be seen that a propulsion system that can be throttled may have merit, as long as this change in thrust is not accompanied by serious losses in performance. Then it would be possible to have a relatively high thrust for planet escape and capture maneuvers (this will minimize the time spent in fighting gravity) and a lower thrust and hopefully an improved specific impulse for the other interplanetary maneuvers. The isotope decay rocket, the nuclear rocket, and electrical devices have this capability. If specific impulse does not change unfavorably it can be shown that this throttling leads to a saving in vehicle weight and size.[39]

(c) *Relation of Specific Impulse and Mass Ratio*

The space vehicle mission will dictate the velocity increment that is to be delivered by the interplanetary transfer propulsion system. From this velocity increment ΔV it is possible to derive the specific impulse, the mass ratio of the propulsion system, and the staging of the propulsion vehicle.

$$\Delta V = \sum_{k=1}^{k=n} c_k \ln [(M_0)_k/(M_p)_k]$$

$$\Delta V = c_1 \ln [(M_0)_1/(M_p)_1] + c_2 \ln [(M_0)_2/(M_p)_2] + c_3 \ln [(M_0)_3/(M_p)_3] \ldots$$

ΔV = Required velocity increment

c = Rocket exhaust velocity = Specific impulse (sec.) $\times$ 32.2

$$\frac{M_0}{M_p} = \text{Mass ratio} = \frac{\text{Initial mass}}{\text{Final mass}}$$

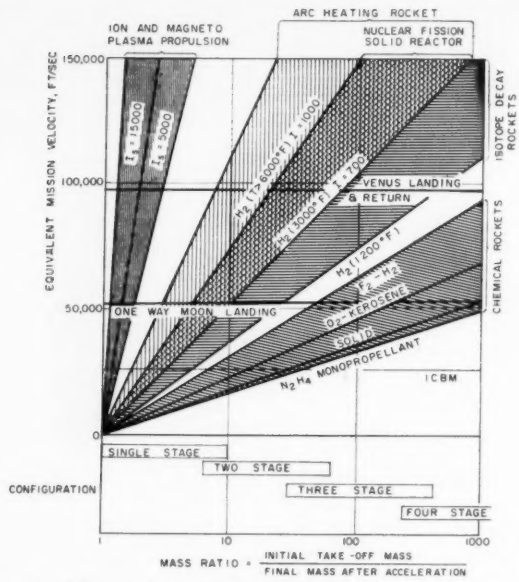

FIG. 9. Mass ratio, equivalent mission velocity, and specific impulse.

Subscripts n, 1, 2, 3, etc., refer to the number of stages.

Fig. 9 gives a plot of the required velocity versus the required mass ratio for different specific impulses. The same specific impulse is assumed for all stages of a multi-stage vehicle. It can be seen from this figure that different propulsion systems require different mass ratios to achieve the same nominal mission. Or, in other words, different payloads can be carried by different propulsion systems of the same initial mass for the same velocity requirement. It can be seen that for very ambitious velocity requirements, such as a Venus round trip, some of the low energy types of propulsion systems are no longer suitable because they would require too many high-performance stages in order to accomplish the mission. At the bottom of Fig. 9 is indicated the number of stages that are likely to be realized with reasonable structural allowance. It can be seen that the high energy propulsion systems permit a considerable improvement by having a lower number of stages and also (this is not shown on this chart) in the payload that can be carried.

The actual mass ratios of space vehicles can be found only by detail work (studies, designs, and development); the values in Fig. 9 are only a guide of what is required.

The velocity increments that are required for fast trips along non-minimum energy trajectories increase rapidly (and the payload decreases) as the flight time is diminished. This is shown in Figs. 10 and 11 where a hypothetical Mars round trip is indicated. The information was taken from reference 39 but was slightly modified to allow for trajectory corrections, and delays at the target. The assumptions made for this calculation are listed in the reference. It can be seen that a decrease of travel time can more than double the velocity requirements. A specific mission therefore must also be defined in terms of the exact orbit and the time it takes to traverse it. This particular Mars mission and any other mission can have an infinite variety of actual flight paths and, therefore, energy requirements. It can be seen in Fig. 10 that a shortening of the trip time requires also considerable sacrifice in payload. A 50 per cent increase in specific impulse would be needed to permit a 25 per cent reduction in transit time. A faster trip does not merely mean a greater expenditure of energy for the transfer orbit, but also additional energy for changing the velocity vector of the vehicle once it gets near the target planet. It can be seen from this Figure that with present day power supply systems (specific weights of 20 to 30 lb./hp.) and present propellants (300 to 400 sec. of specific impulse) allow a reasonably fast but not a very fast round trip to Mars.

It must be borne in mind that the same interplanetary rocket engines can be used for more than one of the seven different maneuver requirements listed in a previous section, and in some cases even for four or five. This means that such an engine is used intermittently and therefore must be capable of restarting. The propellant and the energy that is not expanded in earlier maneuvers can be available for the remaining maneuvers. For example, if very little navigational correction is required on a specific trip, and if the position of the planets at the time of launching was favorable so that little energy had to be expended to change the inclination of the orbital plane, then this extra energy could be applied to decrease the time of the return trip. The problem is similar to the determination of the amount of spare fuel that must be carried by an airplane to account for headwinds, different flight plans, delays, etc. Even if two or more separate stages were used, it would still be possible to shift the flight path to accommodate unusual energy expenditures during any one specific maneuver. It is not known at this time, however, if a guidance system will be capable of coping with a variety of different flight plans that are fostered by trying to achieve a good utilization of all available propulsive energy and/or working fluid.

As was described previously, the low thrust-to-weight ratio engines are particularly suited for interplanetary transfers and the higher thrust engines for operation in a fairly strong gravitational field. This means that different engines will be used for different maneuvers.

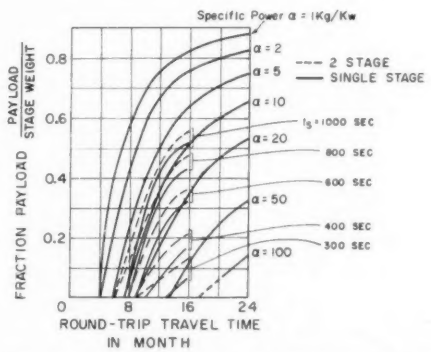

FIG. 10. Payload fraction for different specific impulses (chemicals) and different specific powers (electrical systems), as a function of the round trip travel time to Mars.

A multiple-stage vehicle will be favored where each stage uses an engine best suited for its specific set of maneuvers. If, for example, it is desired to send an exploratory probe to become a satellite of Jupiter ($\Delta V \cong 155{,}000$ ft./sec.) it would be reasonable to have one or two chemical or nuclear rockets for Earth escape, an electrical system for the transfer orbit and its corrections, the same electrical rocket stage for an approach to Jupiter and the vehicle's capture into a satellite orbit, (perhaps even a separate chemical rocket to augment this maneuver) the same electrical rocket for the escape from the Jupiter satellite orbit and the return interplanetary transfer, and even some of the slowing down maneuver, and finally perhaps another chemical rocket for the capture maneuver into a decreasing orbit about the Earth. This would involve an overall mass ratio of about 200. With a big chemical booster of 1,500,000-lb. thrust it would be possible to bring perhaps 5,000 lbs. back to earth after a Jupiter exploration trip of perhaps three and a half years.

A feeling for the payload that can actually be sent to Mars can be obtained from Table 4. This is based on calculations done by V. Larsen. Here it was assumed that a given weight is in orbit about the Earth at 300 mile altitude and that different types of engines are used to get into a satellite orbit about Mars. The payloads are those that can actually be transported into the satellite orbit. The electrical systems have the highest payload capacity and therefore look very attractive for the future, even though it is a complex device with nuclear radiation hazards.

From Fig. 8 and Table 2 it can be seen that the velocity requirements increase appreciably for the further planets and the escape velocity requirements for the heavier planets are many times larger than those of the planets in the inner solar system. This means that for missions to the outer solar system, the energy requirements are much larger. Wherever large energy requirements are involved it is expedient to apply the rocket engines with the highest specific impulse—namely, the electrical systems. It would therefore be appropriate to divide interplanetary missions into three separate categories as follows: (1) missions in the immediate vicinity of Earth and the moon, (2) interplanetary missions within the inner solar system (between Mars and the sun), and (3) interplanetary missions to the outer solar system (beyond Mars).

For the first category of missions, chemical systems are more than adequate and accelerations below approximately 0.01g are too small to be useful in satellite or moon missions. These missions therefore are largely restricted to using chemical or possibly nuclear or solar heating engines.

TABLE 4

Payload Fraction for a Mars Satellite Mission Using the Same Initial Weight in an Earth Orbit

Chemical (solid and liquid)	9–13%
High Energy Chemical	16%
Nuclear Fission	25%
Ion	32%

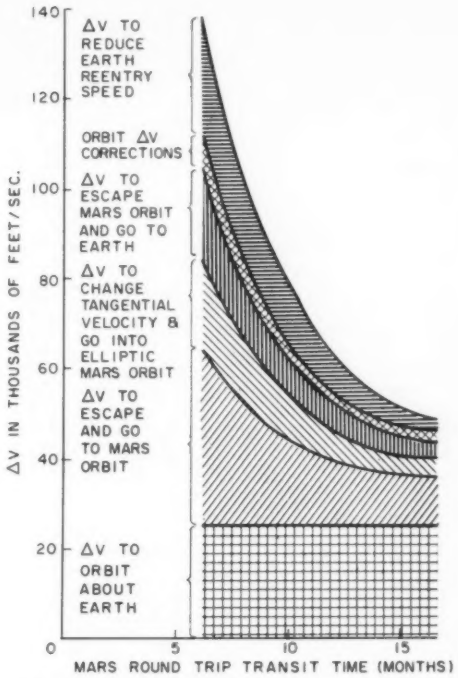

FIG. 11. Equivalent velocity requirements for a Mars satellite and return mission for different round-trip travel times.

For the missions in the inner solar system, accelerations of about 0.0001g are satisfactory to give good acceleration because sufficient time and distance is available in interplanetary flight to achieve high flight velocities with these small accelerations and therefore short transit times. This allows then the use of all power plants except a few types of electrical systems which have very heavy energy sources and power conversion systems and have thrust-to-weight ratios less than this value.

For missions to the outer solar system, however, almost any kind of a system that has an acceleration greater than $10^{-5}g$ would be satisfactory to achieve fast transit times. Here again, sufficient travel time is available that these low accelerations can give very respectable velocities when applied over the period of several months or even years. The electrical propulsion systems, therefore, are uniquely qualified, and, in fact, at this time they have no serious competition for the more complex missions to the outer solar system.

Environmental Conditions

The engine, as well as the rest of the vehicle, is exposed to some very unusual environmental conditions, as follows.

(*a*) *High Vacuum*

Prolonged exposure to a high vacuum will require materials which will not evaporate or change their characteristics. For example, certain soldered joints have soldering materials with vapor pressures which

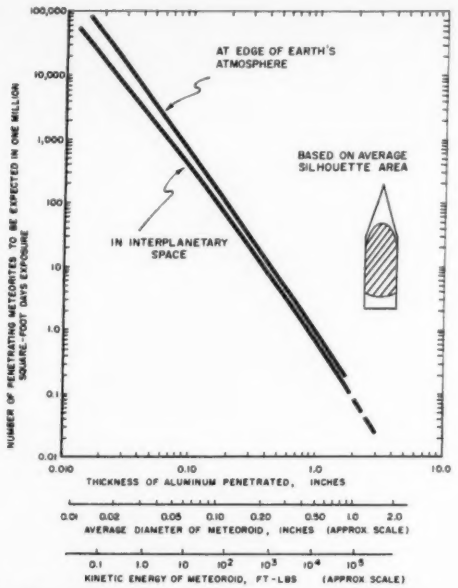

FIG. 12. Meteor hazard for interplanetary vehicles.

can be higher than those prevalent in empty space. Therefore, these materials will disappear very slowly. Certain other materials reportedly lose some of their strength properties in a high vacuum, and this needs further investigation. The selection of materials will thus be influenced by the vacuum.

(*b*) *Zero Gravity*

Over most of the interplanetary trajectory the gravitational acceleration in any one direction will be either zero or very close to zero. This can cause certain engine component problems. For example in closed cycle power generating systems where liquids are evaporated by heat and again condensed, there is the problem of separating the vapor from the liquid. Without gravity this separation becomes more difficult. There is also the problem of taking liquid from a partially empty tank. Many present-day components such as switches or valves rely on gravity to perform some of their functions. This will no longer be possible in space flight and new design techniques will have to be applied.

(*c*) *Thermal Equilibrium*

The ambient temperature of the vehicle is controlled by the emmittance (or absorptance) of the surface materials which receive thermal radiation from the sun and reject radiation to outer space and by the ability of the parts inside the vehicle to distribute heat between the surface and the bulky hardware. The thermal equilibrium of the engine therefore depends very much on the basic overall thermal design of the interplanetary vehicle, and provisions have to be made for seeing that no one part is heated excessively by solar radiation and no other part in the shadow of the vehicle becomes too cold. Because certain parts of any power producing machine are generally very hot, there exists the problem of taking the internally generated heat and dissipating it properly.

(*d*) *Radiation*

The engine will be subjected to various kinds of electromagnetic radiation and corpuscular impacts, such as ultra-violet light, cosmic rays, gamma rays, protons, etc. Exposed organic material, for example, may undergo change if subjected to strong ultra-violet rays. This is a problem that is not peculiar to the engine alone, but affects the whole space vehicle and a solution must be found for resisting this incident radiation and the harmful secondary induced radiation.

(*e*) *Meteorites and Meteoroids*

The impact of small but relatively fast moving particles presents a hazard to all space vehicles and their components. Statistical evaluations based on presently known data on meteorites and meteoroids show that every interplanetary vehicle will suffer impact damage. A penetration by a small particle could cause loss of gas pressure or liquid propellants or stress concentrations in highly loaded skins and structures. It could cause ignition of solid propellants and it can render most pieces of machinery inoperative. Until a satisfactory precautionary or remedial solution can be found for coping with this impact problem, it will be necessary to provide for duplicate systems, to minimize the size and the exposed surface area and also rely on heavy walls to prevent penetration of smaller particles. All three of these courses of action may be actually used. By putting several propulsion systems in series or parallel within the same vehicle stage, it will be possible to fulfill the mission, even though one or more of the individual propulsion systems will be inoperative. The reliability of a multiple engine system is examined in the next section.

Fig. 12 shows the results of calculations made by P. Sandorff with the existing knowledge of meteoritic particle distribution using the methods proposed by Whipple.[40] Shown is the required thickness on the outside wall of a space vehicle to prevent penetration. The data on which these calculations are based are admittedly incomplete.

It may be fortuituous that heavy structures are needed with certain types of propulsion systems—for example, chemical propulsion systems that require heavy tanks or heavy cylindrical thrust chamber cases (as in solid propellants) or nuclear reactors, which may require much shielding. In these cases it would be possible to combine structure or a shield against radiation with meteorite resistance.

In general, it is fair to say that most of the environmental problems are not too well understood today, even though a lot of work is now going on in many laboratories. Until a few actual interplanetary probes bring back data, this will continue to be a somewhat mysterious area.

Design and Operation Evaluation

This covers some of the practical factors, such as various specific engine requirements, development and operational requirements, reliability and growth potential. A general comparison can be found in Table 5. Here an examination of each specific point is not warranted, because the designations are somewhat arbitrary. But it is intended to convey the impression that none of the systems are ideal and all have some uncertainties and limitations. Of course these design and operational requirements will vary from mission to mission and have to be tailored to the specific application.

(*a*) *Restart Capability*

As mentioned previously, many missions require application of thrust at different time intervals. Therefore, a typical interplanetary rocket has to be capable of restarting several times during a space flight journey of several years. In liquid propellant this brings about the problem of ignition in a vacuum or the expulsion of liquids in tanks at zero gravity. In those propulsion systems that involve nuclear power, it requires the starting up and the shutting down or partial shutting down of a nuclear reactor. There is little need for a fast rocket startup of a few seconds or a fast shutdown in space because there is lots of time.

(*b*) *Thrust Vector Control*

As previously mentioned in the mission velocity requirements, the propulsion system has to have provisions for applying torque and thrust in directions other than that of the original direction. Therefore, interplanetary propulsion systems may have to permit a vector change of thrust direction and also a means of applying torques or moments to the vehicle in order to turn it around for either navigational observations or for the application of thrust in an entirely different direction. For certain types of trajectory, it will be necessary to vary the amount of total impulse (change magnitude of thrust or duration) that can be delivered by the interplanetary propulsion system at any one firing so that large or small corrections can be made to the trajectory, or so that the pilot in a manned interplanetary vehicle has the option of changing the course.

TABLE 5
Comparison of Technical Features

	EXPERIENCE TO DATE	VARIABLE THRUST FEATURE	VARIABLE VECTOR DIRECTION	AUXILIARY POWER TAKE-OFF	GROWTH CAPABILITY	RELATIVE SIMPLICITY	RESTART CAPABILITY	COMPACTNESS OF DESIGN	PRESENT DAY RELIABILITY
LIQUID PROPELLANT CHEMICAL	○	○	○	◍	◍	○	○	○	○
SOLID PROPELLANT CHEMICAL	○	●	○	◍	◍	○	●	○	○
FISSION	◍	◍	●	◍	○	●	●	◍	●
ISOTOPE	●	◍	○	◍	○	◍	◍	○	◍
ARC HEAT	●	◍	◍	○	○	●	○	◍	●
MAGNETO-PLASMA	●	●	◍	○	○	●	○	◍	●
ION	●	●	◍	○	○	●	◍	◍	●
SOLAR HEAT	◍	◍	◍	◍	○	◍	○	●	◍
SOLAR SAIL	●	◍	◍	●	○	◍	○	◍	◍

○ WELL KNOWN, FEASIBLE
◍ UNCERTAIN OR LIMITED
● LARGELY UNEXPLORED OR DIFFICULT

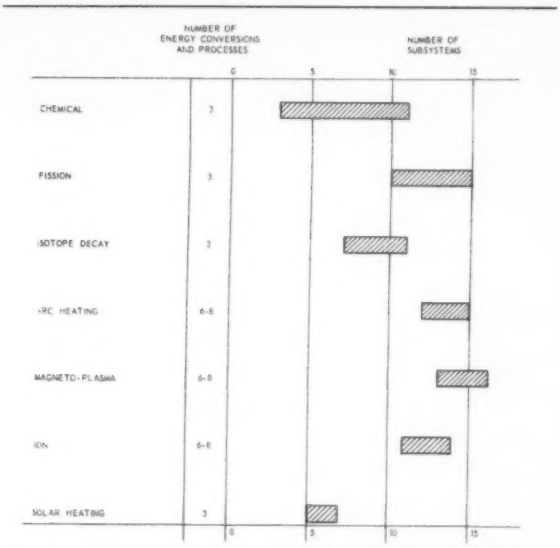

FIG 13. Relative complexity of various propulsion systems.

(*c*) *Acceleration During Boost*

The interplanetary propulsion system must be capable of withstanding the accelerations that are imposed upon it while being accelerated as an upper stage of a booster or sustainer during the take-off from a planet. For example, this requires special design provisions for carrying thin tanks.

(*d*) *Volume*

Because these vehicles have to be transported by a booster or a sustainer through the atmosphere, it is desirable to have the propulsion system occupy a small volume so that it can be easily stored in the booster vehicle and so that it presents a minimum of target area for meteoritic matter. It is interesting to note that those propulsion systems which are small in occupied volume are not necessarily those that are the lightest.

(*e*) *Reliability*

One good indicator of reliability problems is the *relative complexity* of the various propulsion systems. Fig. 13 compares a number of the major subsystems in several of these propulsion systems and also the number of energy conversion processes that have to be

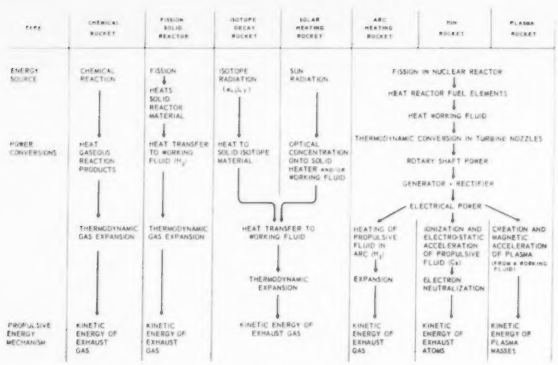

FIG. 14. Energy conversions in various rockets.

achieved for each particular rocket type. The energy conversion processes are illustrated in Fig. 14 to show the types of conversion that were considered. These subsystem numbers are somewhat arbitrary, and the range shown in this chart allows for variation in concept and system design.

It can be seen that the electrical systems are considerably more complicated than the other propulsion systems. This is primarily due to the fact that they require fairly complicated and separate electrical power sources. From an inspection of a number of subsystems it is obvious that the chemical rocket and the solar heating rocket and perhaps also the isotope decay device are considerably simpler than the other devices. The liquid monopropellant rocket system looks particularly attractive because of its simplicity, ability to restart, and design flexibility.

On the basis of these relatively crude comparisons of the complexity of the subsystems and the number of energy conversion processes, it can be concluded that the chemical rocket will be attractive for a long time, because of its inherent simplicity, and that other propulsion systems will be an order of magnitude less reliable for a long time to come.

The amount of reliability needed for accomplishing a long and complicated space journey is extremely high and exceeds in some cases the reliability of some of the best equipment now being used on the earth, such as telephone switching equipment. The time necessary and the number of tests necessary to convince ourselves (on earth) that the equipment will have the required reliability is indeed very large. It is therefore a question as to what reliability will eventually be obtained from the space vehicles and whether it is desirable to do extensive long duration testing on the ground in order to be assured of success in an eventual flight. It is more desirable (and it may be cheaper) to test devices in an actual flight vehicle, without having too many tests on the ground under simulated conditions, and to design duplicate systems to improve the reliability. Therefore, many components and systems will be tested in a satellite station prior to an interplanetary trip. A rocket engine satellite test station will probably become a necessary development tool of the future.

If multiple engines are used in sequence, the overall reliability suffers because of the increased complexity, unless spare engines are also used. While this means that extra weight has to be carried along, it enhances the chances of the success of the mission.

The probability of failure P is plotted in Fig. 15; it is computed from the relation

$$P = \sum_{k=m+1}^{k=n} \binom{n}{k} (1 - r)_k (r)^{n-k}$$

where

n = number of engines in a given stage
m = number of spare engines in a given stage
$n - m$ = number of engines required to fulfill the mission
r = reliability of a single engine (probability that it will work)—assumed independent of n
k = random engine designation
$\binom{n}{k}$ = binomial coefficient $= \dfrac{n!}{k!\,(n-k)!}$

It can be seen that multiple rocket engines with one or two spares have improved reliability compared to single engines. If a single engine has a reliability of 0.990 (1 failure in 100 tries) then 6 engines with 1 spare or a total of 7 engines will fail only once in 500 tries or 5 engines with 2 spares will fail only once in 2,930 operations. If the initial single engine reliability is poor, then clustering of multiple engines does not help too much.

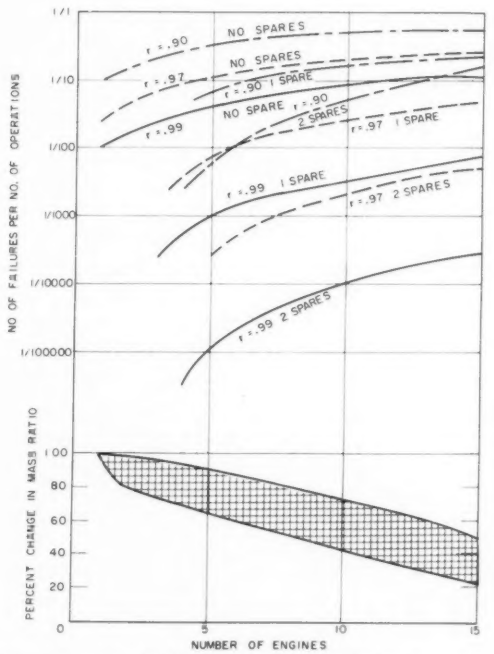

FIG. 15. Failure probability and per cent variation in mass ratio for single and multiple rocket engines.

Also shown in Fig. 15 is the penalty in the mass ratio that has to be incurred by duplicating many of the components. This curve shows the percentage decrease in mass ratio as a function of the number of engines. The upper curve refers to simple, relatively highly stressed hardware, such as a monopropellant pressurized gas system, and the lower regions refer to engines which contain heavy nuclear reactors, whose critical mass is fairly independent of the flow or thrust. The other engine types probably fall in between.

When choosing the number of multiple engines one has to balance between reliability and increased weight. It is reasonable to prefer a number of engines over a single engine when long trips are involved, and particularly when meteoritic damage can put a single engine out of operation.

An alternate scheme of improving reliability is to use the concept of the multiple vehicle expedition as proposed by von Braun[41] and originally performed by Columbus. This scheme is only applicable to manned vehicles, where it is presumably possible to transfer people from one vehicle to another.

(*f*) *Growth and Design Flexibility*

In selecting a propulsion system, obviously those will be favored that show the technical capability of improved performance and improved application versatility at future times. It has been the experience that it is easier with certain propulsion systems to improve the fuel economy or the specific impulse, the relative weight of the propulsion system per unit thrust, the power output, or, in this case, the thrust, and to add such features as variable thrust and variable thrust direction at a later time.

It is often desirable to use the propulsion system for purposes other than providing a push to the vehicle. Into this type of function fall such items as providing auxiliary power to the vehicle, providing the ability for directional control and stability, providing high pressure fluids to the vehicle and serving as a heat source to other subsystems of the vehicle. A number of the propulsion systems are fundamentally limited in their growth capabilities and design versatility as indicated by Table 5.

TABLE 6
Development Status of Various Rocket Engines

	ANALYSIS	BASIC RESEARCH	ENGINE DEVELOPMENT FACILITIES	DEVELOPMENT OF TERRESTIAL VERSION	PILOT PRODUCTION OF TERRESTIAL VERSION	DEVELOPMENT OF SPACE VERSION
LIQUID PROPELLANT	○	○	○	○	○	○
SOLID PROPELLANT	○	○	○	○	○	○
MONOPROPELLANT	○	○	○	○	●	●
FISSION	○	◍	◍	◍	●	●
FUSION	◍	◍	●	●	●	●
RADIOACTIVE ISOTOPE DECAY	◍	◍	◍	●	●	●
ARC HEATING	◍	◍	◍	●	●	●
MAGNETO-PLASMA	○	◍	●	●	●	●
ION	○	◍	◍	●	●	●
SOLAR HEATING	○	◍	◍	◍	●	●
SOLAR SAIL	◍	●	●	●	●	●

○ COMPLETED, AVAILABLE
◍ UNDER WAY
● NOT ACCOMPLISHED OR AVAILABLE

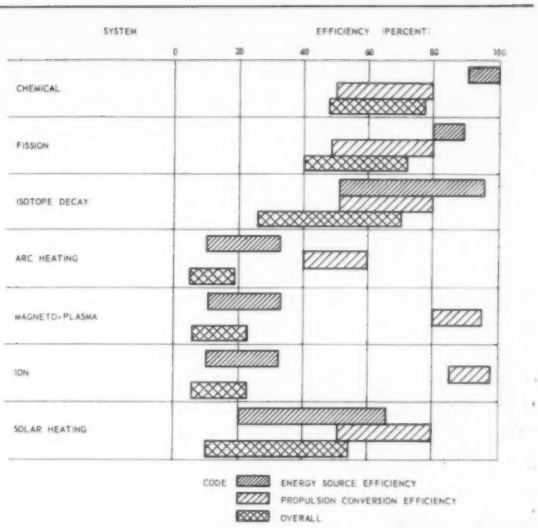

FIG. 16. Relative efficiencies of power conversion for different propulsion systems.

(*g*) *Status and Development Effort*

The development effort that is expended is closely tied in with the desired reliability. As shown in Table 6 some of the interplanetary engine concepts are still very much in their infancy and will need research and invention as well as development effort before they can be considered practical. Only the chemical rocket engines are fairly thoroughly explored and can be designed with a reasonable degree of confidence today.

(*h*) *Energy Conversion Efficiency*

There are many losses in the process of energy conversion from the source to the propulsive form. As was previously mentioned, any inefficiency unfortunately contributes to increased weight, poorer mass ratio, or inferior specific impulse. Of all the various propulsion systems the chemical propulsion systems can be relatively very efficient, as shown in Fig. 16. The most inefficient process appears to be in the generation of electrical power necessary for the ion, arc heating and magneto-plasma propulsion systems. If a way could be found to improve the weight per unit output of this process of generating electricity, then all

electrical propulsion systems would become considerably more attractive since the power source weights could be decreased by a large factor and the acceleration and versatility of electrical rockets for space flight application would be considerably improved.

Conclusions

The various propulsion systems that have been discussed—namely, the liquid and solid propellant rockets, the nuclear fission rocket, the radioactive isotope decay rocket, the arc heating rocket, the ion rocket, the magneto-plasma rocket and the solar heating rocket—all operate on essentially different basic principles and therefore their characteristics as engines are different. Those that give high exhaust velocity (the electrical devices) require heavy power machinery, are complex, convert only a small percentage of their available energy into a propulsively useful form, and can give only low accelerations. They therefore require a longer time to maneuver in a strong gravitational field. The chemical and fission rockets on the other hand give high accelerations and very light machines, but relatively low specific impulse. The solar and isotope decay heating devices have intermediate capabilities. The monopropellant liquid rocket offers simplicity but also low performance, and will find use as a navigation error correction device and an attitude control mechanism. The solar sail is simple but its versatility is limited because of the low and essentially unidirectional forces that can be obtained, and the variation of these forces within the solar system.

Because of the unusual environmental conditions, the design concepts of the interplanetary engine will be different than those that are in common practice today for ballistic missiles. The environmental conditions will force us to find new discoveries, different materials, novel fabrication techniques, new failure detection methods, or new lightweight tanks, and these engines will look very different compared with present-day devices.

Different stages of the same vehicle will use different engines, each designed to fulfill one or more specific interplanetary maneuvers in the best possible way. Standard interplanetary stages will be designed and modified slightly for different missions. For the same basic weight in an earth orbit, the electrical systems will be capable of carrying the most payload (the chemical systems will carry the least) to a given interplanetary target. For the long range outlook, they are the most attractive in performance.

Only the chemical rockets are developed to the state where they are considered ready for interplanetary service. The solar heating and isotope can probably be developed soon, but only in the low thrust regime. The nuclear fission rocket and the electrical devices with their nuclear power source will not be ready for interplanetary flight for some time to come. Small low thrust electrical systems using solar energy may become practical sooner. Larger solar energy optical systems also need considerable further effort. None of the experimental propulsion systems can be rejected at this time until technological progress proves them unsound. Even the concepts of photon rockets and fusion devices, which are considered impractical today, may become practical with further discoveries.

All the various systems seem to offer some growth potential in improved performance, efficiency, lower engine weights, or thrust. But the real need seems to be for a simple lightweight high energy source to replace an airborne nuclear reactor. Because of the complexity and development difficulty of some of these devices, it may be a long time before they become sufficiently reliable to fly. Because of the strong neutron and gamma radiation hazard, nuclear rockets will probably not be used with manned vehicles.

There appear to be three regimes of interplanetary travel for which the engine requirements will be different. The interplanetary transfer orbit maneuver will be performed differently for missions in the immediate vicinity of the earth, such as moon flights; it will be different for missions in the inner solar system and different again for missions in the outer solar system. High specific impulse units with very low accelerations in the order of $10^{-5}g$ will be desirable for fast missions to Jupiter and beyond. For missions in the immediate vicinity of the earth, acceleration in excess of $10^{-2}g$ will be required. The missions, therefore, in terrestrial and lunar space can and will be performed largely with chemical rocket units. Those in the inner solar system will again be performed largely with chemical propulsion units for the immediate future with some of the other propulsion engines becoming superior at a later time. However, for missions to the outer solar system it is essential that some high-performance rocket engine such as the electrical units be developed.

It can be anticipated that there will be two basically different types of missions to any one of the planets. One will convey people and will require fast transit time and therefore a large amount of excess energy. These will be multiple stage units and they will initially contain no nuclear rockets in order to avoid radiation problems. The second category one might call "freight vehicles" and they will be used to carry various types of equipment and supplies to the planets, and they should use electrical and nuclear propulsion.

Because of the reliability problem of running a power plant for several years and because of the meteoritic penetration problem, it will become desirable to use several propulsion systems on the same vehicle stage in such a manner that a failure of any one system will not cause a failure to achieve a mission. Mission requirement cannot be determined completely accurately and some spare energy capacity will have to be carried along. If this reserve is not needed during a specific flight then it can be applied on the return trip to achieve a faster home journey.

It will become necessary to establish space laboratories for the development and testing of interplanetary rocket engines. These probably will be specially con-

trolled satellites that permit operation of engines in the proper environment. In fact, it is likely that a major portion of the satellites about the earth soon will become test devices for the development of hardware for interplanetary missions.

References

[1] Sutton, George P., *Rocket Propulsion Elements*, John Wiley & Sons, New York, 1956.

[2] Tormey, J. T., *Liquid Rocket Propellants—Is There an Energy Limit*, Industrial and Engineering Chemistry, Vol. 49, pp. 1339–1343, September, 1957.

[3] Jackson, Julius L., *Stabilized Free Radicals*, paper presented at Advanced Propulsion Systems Symposium, Rocketdyne, AFOSR, Los Angeles, California, 1957.

[4] Moe, George, and Armstrong, Don L., *Research on Free Radicals as Rocket Propellants*, paper presented at Advanced Propulsion Systems Symposium, Rocketdyne, AFOSR, Los Angeles, California, 1957.

[5] Alperin, Morton, et al., (Eds.), "Vistas in Astronautics," Truax, R. A., *Rocket Engines for Outer Space*, p. 202, Pergamon Press, New York, 1958.

[6] Bussard, R. W., and De Lauer, R. D., *Nuclear Rocket Propulsion*, McGraw-Hill Book Company, Inc., New York, 1958.

[7] Rosenblum, M. H., Rinehart, W. T., and Thompson, T. L., *Rocket Propulsion with Nuclear Energy*, ARS paper No. 559-57, December, 1957.

[8] Shephard, L. R., and Cleaver, A. V., *The Atomic Rocket*, J. Brit. Interplanetary Soc., Vol. 7, pp. 184, 234, 1948, Vol. 8, pp. 23, 59, 1949.

[9] Bussard, Robert W., *Concepts for Future Nuclear Rocket Propulsion*, Jet Propulsion, Vol. 28, No. 4, p. 223, April, 1958.

[10] Post, R. F., *Controlled Fusion Research—An Application of the Physics of High Temperature Plasmas*, Rev. Modern Physics, Vol. 28, p. 338, 1956.

[11] Kaeppeler, H. J., *Zur Frage der Verwendbarkeit thermonuklearer Reaktionen in Raketen*, Raketentechnik und Raumfahrtforschung, Heft 3, p. 60, October, 1957, Stuttgart; Band 11, Heft 1, p. 13, 1958.

[12] Tsien, H. S., *Thermonuclear Power Plants*, Jet Propulsion, Vol. 26, 1956.

[13] Hittman, F., *The Feasibility of Producing Power from Radioisotopes*, presented at American Nuclear Society Meeting, June, 1957.

[14] Cann, Gordon, Adriano Ducati, and Vernon Blackman, *Experimental Studies on the Thrust from a Continuous Plasma Jet*, paper presented at Advanced Propulsion Systems Symposium, Rocketdyne, AFOSR, Los Angeles, California, 1957.

[15] Gregory, H. F., and Alperin, M., (Eds.), "Vistas in Astronautics," Vol. II, Howard, D. F., *Experimental Studies on Plasma Jet Propulsion*, Pergamon Press, 1959.

[16] Willinski, M. I., and Orr, E. C., *Project Snooper, A Program for Unmanned Interplanetary Reconnaissance*, Jet Propulsion, Vol. 28, No. 11, November, 1958.

[17] Stuhlinger, E., *Electrical Propulsion System for Space Ships with Nuclear Power Source*, Journal of Astronautics, Winter, 1955, Spring, 1956, and Summer, 1956.

[18] Shepherd, L. R., *Electric Propulsion Systems in Space Flight*, paper presented at the Ninth International Astronautical Congress, Amsterdam, 1958.

[19] Gregory, H. F., and Alperin, M., (Eds.) "Vistas in Astronautics," Vol., II, Langmuir, D. B., *Problems of Thrust Production by Electrostatic Fields*, Pergamon Press, 1959.

[20] Boden, R. G., *The Ion Rocket Engine*, Rocketdyne Report R-645, Canoga Park, California, August 26, 1957.

[21] Gregory, H. F., and Alperin, M., (Eds.), "Vistas in Astronautics," Vol., II, Patrick, R. M., Sr., *A Description of a Propulsive Device which Employs a Magnetic Field as the Driving Force*, Pergamon Press, 1959.

[22] Bostick, Winston H., *Thrust from Plasma*, paper presented at Advanced Propulsion Systems Symposium, Rocketdyne, AFOSR, Los Angeles, California, 1957.

[23] Malin, M. E., et al., *Application of Electric-Arc Plasma Generators to Propulsion*, paper presented at Ninth International Astronautical Federation, Amsterdam, 1958.

[24] Rosa, Richard J., *Magnetohydrodynamic Generators and Propulsive Devices*, paper presented at Advanced Propulsion Systems Symposium, Rocketdyne, AFOSR, Los Angeles, California, 1957.

[25] Schnetzer, E., and Corliss, W., *A One Megawatt Nuclear Power Package for Applications in Outer Space*, General Electric Flight Propulsion Laboratory Dept., paper presented at the Detroit Meeting of the American Nuclear Society, December, 1958.

[26] Hiester, Nevin K., Tietz, Thomas E., and De La Rue, R., Jr., *Economic Factors in Furnace Design*, The Journal of Solar Energy Science and Engineering, Vol., I, Nos. 2, 3, p. 28, April–July, 1957.

[27] Hisada, Taro, et al., *Concentration of the Solar Radiation in a Solar Furnace*, The Journal of Solar Energy Science and Engineering, Vol., 1, No. 4, p. 14, October, 1957.

[28] Hukuo, Nobuhei, and Mii, Hisao, *Design Problems of a Solar Furnace*, The Journal of Solar Energy Science and Engineering, Vol. 1, Nos. 2, 3, p. 108, April–July, 1957.

[29] Ehricke, Krafft A., *Comparison of Propulsion Systems: Solar Heating, Arc-Thermodynamics, and Arc-Magnetohydrodynamics*, paper presented at Advanced Propulsion Systems Symposium, Rocketdyne, AFOSR, Los Angeles, California, 1957.

[30] Ehricke, Krafft A., *The Solar Powered Space Ship*, ARS paper No. 310–56, June, 1956.

[31] Ehricke, Krafft A., *Instrumented Comets—Astronautics of Solar and Planetary Probes*, American Rocket Society, paper 493–57.

[32] Shepherd, L. R., *A Survey of Possible Propulsion Systems*, paper presented at The Second International Symposium on the Physics and Medicine of the Atmosphere and Space, San Antonio, Texas, 1958.

[33] Alperin, M., et al., (Eds.), "Vistas in Astronautics," Stuhlinger, E., *Propulsion Systems for Space Ships*, Pergamon Press, 1958.

[34] Safonov, George, *Direct Power Conversion—Part 2, The Fission-Electric Reactor*, paper presented at Advanced Propulsion Systems Symposium, Rocketdyne, AFOSR, Los Angeles, California, 1957.

[35] Colgate, S. A., and Aamodt, R. L., *Plasma Reactor Promises Direct Electric Power*, Nucleonics, Vol. 15, No. 8, August, 1957.

[36] Alperin, Morton, et al., (Eds.), "Vistas in Astronautics," Sutton, G. P., *A Preliminary Comparison of Potential Propulsion Systems for Space Flight*, Pergamon Press, New York, 1958.

[37] Dillaway, R. B., *Typical Propulsion Systems for Space Flight*, Space Propulsion Session, IAS 26th Annual Meeting, New York, January 27–30, 1958.

[38] Laning, J. H., Jr., Frey, E. J., and Trageser, M. B., *Preliminary Considerations on the Instrumentation of a Photographic Reconnaissance of Mars*, Instrumentation Laboratory, M.I.T., April, 1958.

[39] Gregory, H. F., and Alperin, M., (Eds.), "Vistas in Astronautics," Vol. II, Irving, J. H., and Blum, E. K., *Comparative Performance of Ballistic and Low-Thrust Vehicles for Flight to Mars*, Pergamon Press, 1959.

[40] Alperin, M., et al., (Eds.), "Vistas in Astronautics," p. 115, Whipple, Fred L., *The Meteoritic Risk to Space Vehicles*, Pergamon Press, 1958.

[41] von Braun, W., *The Mars Project*, University of Illinois Press, 1953.

Shroud Tests of Pressure and Heat Transfer Over Short Afterbodies With Separated Wakes†

MARTIN H. BLOOM* AND ADRIAN PALLONE**

Polytechnic Institute of Brooklyn

Summary

Experimental measurements of pressures and heat-transfer rates over three blunt afterbodies of small fineness ratio in fully separated wakes are presented. The afterbodies are generally similar in shape but have different stepdown heights from the end of the forebody.

Tests were made by means of a new shroud technique over a range of Reynolds Numbers closely corresponding to typical flight conditions at Mach Numbers on the order of 20, considering models on the order of 5 ft. in diameter at about 120,000 ft. altitude. Stagnation temperatures on the order of 1,300°R. to 1,600°R. were employed. Surface temperatures varied between 560°R. and 800°R.

Strictly speaking, the test flows correspond to prototype flows which would be created by a forebody consisting of a sharp or slightly blunted 54° half angle cone which turns cylindrical for a short distance and then connects with the afterbody. Judiciously interpreted, the results may be considered to have a somewhat wider applicability for approximation purposes. The results are presented and compared with each other in terms of nondimensional variables based on flow conditions at the end of the forebody.

The pressure distribution along an afterbody is seen to be roughly uniform in each run. For a given point on an afterbody, the ratio of pressure to the stagnation pressure at the forebody end (or exit) decreases with increasing stagnation pressure or Reynolds Number. The present pressures and pressure-Reynolds Number variations (Fig. 8) are compared with values obtained from Chapman's Mach 2 or 3 base-pressure data; qualitative and some quantitative agreement is noted. In the Reynolds Number range comparable to those of the present tests, Chapman's exit boundary layers were considered to be laminar. An approximate check of the heat-transfer rate at the forebody end in the present tests also indicates a laminar rate. No information was obtained concerning the possible transition of the free-mixing separated boundary layer covering the wake. An adverse pressure gradient on the cylindrical end of the forebody [Figs. 7(a) and 7(c)] was observed.

Heat-transfer rates are seen to be roughly uniform over an afterbody in each run, although some increase in the streamwise direction is noted. The afterbody Nusselt Number (N) varies with the Reynolds Number (R_s evaluated at the forebody end) roughly in the manner $N \sim R_s^{\omega}$ where generally $\omega > 1$ (Fig. 13).

Heat rates on the rear faces of the afterbodies are almost twice the values on the sides. The heat rates on the large-step body are higher than those on the body of zero stepdown height.

In an addendum, it is shown that the Prandtl-Meyer expansion angle of the flow leaving the afterbody increases with increasing test Reynolds Number, and that the corresponding local Mach Number square increases linearly with Reynolds Number. The effect is to keep the local wake Reynolds Numbers virtually constant with increasing test Reynolds Number while the afterbody heat rates increase sharply. The expansion angle on the afterbody of zero stepdown height is significantly smaller than on the stepped down bodies; this may affect the decreased heat rates on this body.

Received October 2, 1958. Revised and received January 26, 1959.

† This work is part of a research project at Polytechnic Institute of Brooklyn, Aerodynamics Laboratory, sponsored by the Aeronautical Research Laboratory of the Air Research and Development Command, Contract No. AF 33(616)-3265, Project No. 1366, Task No. 70169.

* Professor of Aeronautical Engineering.

** Research Associate.

Symbols

A	=	factor in Eq. (1)
C_p	=	pressure coefficient $(p - p_a)/[(1/2)\rho_a u_a^2]$
c_p	=	constant pressure specific heat
D_0	=	maximum forebody diameter (in the present configuration this value occurs at the exit shoulder)
h	=	enthalpy
k	=	conductivity
L	=	distance along the surface from the noise stagnation point to exit
M	=	Mach Number
N	=	Nusselt Number $qD_0(c_p)_s/(h_s - h_w)k_s$
Nu^*	=	Nusselt Number based on local conditions (notation of reference 10)
p	=	pressure (psia)
q	=	surface heat flux, B.t.u /ft.^{2} sec.
R_a	=	Reynolds Number based on exit conditions, $\rho_a u_a D_0/\mu_a$
R_B	=	Reynolds Number based on local wake conditions $\rho_B u_B D_0/\mu_B$
R_{ex}	=	Reynolds Number based on local conditions and length from nose stagnation point to local position (notation of reference 10)
R_L	=	Reynolds Number based on L; $\rho_f u_f L/\mu_f$
R_s	=	stagnation Reynolds Number $D_0(\rho_s\sqrt{h_s}/\mu_s)$
R_s/D_0	=	Reynolds Number per ft. $\rho_s\sqrt{h_s}/\mu_s$
s	=	distance along surface of base measured from rear stagnation point
T	=	temperature (°R.)
u	=	velocity
x	=	distance along axis of shroud
μ	=	viscosity coefficient
ρ	=	density
$\Delta\nu$	=	Prandtl-Meyer expansion angle at exit

Subscripts

a	=	exit
B	=	base (local conditions at wake boundary or within wake)
f	=	of flight
s	=	stagnation
sc	=	stagnation in chamber prior to shroud
w	=	wall

Introduction

EXPERIMENTAL STUDIES concerning the flow field properties in the blunt-base region of a body in supersonic flow are usually made by subjecting a complete model to a test flow which is as close as possible to the flight Mach Number and Reynolds Number of interest.[1, 2] In this way, an attempt is made to duplicate the essential features of both the inviscid flow and the viscous-inviscid interactions in the base region.

It has been reasoned that the dominant parameters for the afterbody flow field behavior are those at the end of the forebody—that is, in the vicinity of the rear shoulder from which the lateral boundary layer of the body is shed downstream.[2, 3] Conditions at the rear shoulder are often termed the "exit conditions." This point of view implies that the explicit influence of the undisturbed flow properties and of the flow around the forebody are not of primary significance. Rather, they are of importance only in so far as they establish the exit flow conditions. Moreover, any upstream flows which lead to the establishment of the same or "similar" (from the standpoint of model scaling) exit flows should serve to produce similar base-region flows over geometrically similar bases.

A point which warrants attention in this approach is the nature of the *characteristic length* which is most suitable for the correlation of the base phenomena with respect to Reynolds Number effects. Several proposed linear quantities have been: the base diameter (D_0) at the shoulder, the stepdown height, Δ, from the shoulder to the afterbody if such geometry is present, the exit boundary-layer thickness, δ_a, and the linear distance L along the surface from nose-stagnation-point to exit. The distance L is not related to δ_a in a simple way, since the relation depends on the boundary-layer history over the forebody.

Chapman, Kuehn, and Larson[4] have presented data on the ratio of base pressure to exit pressure (p/p_a) for two-dimensional bodies with various short wedge-shaped afterbodies having different stepdown heights. The tests were made over a range of Reynolds Numbers at Mach 2 for each afterbody. However, only one measurement position for the base pressure was used in each case. Presumably, there was no flow reattachment on the afterbodies. The data for p/p_a falls into a reasonably systematic band when plotted against the following parameter $[(L/D_0)/(\rho_a u_a D_0/\mu_a)]^{1/2}$, where, in this case, D_0 denotes the body thickness at the exit position. These results indicate that the pressure ratios are, to a considerable extent, independent of the stepdown height and are not very sensitive to changes in afterbody shape in this two-dimensional case. Furthermore, since L/D_0 was constant over a range of Reynolds Numbers for the tests of reference 5, the explicit effects of L/D_0 or δ_a/D_0 on the results cannot be estimated. However, for small values of δ_a/D_0, this effect is not expected to be large. A decrease in p/p_a with increasing R_a is shown, indicating a closing-in of the wake. In the rather low R_a range of these tests, laminar flows would be expected.

A further point of interest is the influence on the wake characteristics of the *shape of the inviscid streamlines* located at some radial distance out from the exit shoulder of the body and extending downstream as a streamtube enclosing the wake region. The form of this streamtube and the flow properties along it in the region immediately downstream of the exit shoulder are determined by the upstream flow field. The streamtube properties downstream of this initial region are influenced by both the forebody flow and the viscous-inviscid interaction in the wake. The extent of the streamtube portion which is determined by the forebody flow alone depends upon the exit Mach Number which delineates a Mach line extending downstream from the exit shoulder and intersecting the streamline in question.

On the basis of the assumption that the contours of the inviscid streamtubes enveloping the wake are insensitive to the wake flow details—at least over the initial streamtube section previously cited—an experimental procedure has been devised for the purpose of duplicating an inviscid streamtube in the wake region and examining the wake properties associated with this streamtube shape. The procedure consists of enclosing the afterbody region of the model in a contoured channel which has the effective shape of one of the base-region streamtubes, a correction being made in general for the boundary-layer displacement effects on the channel wall. The shroud contour may be determined on the basis of an inviscid analysis or, conceivably, with the aid of full-model experiments.

In practice, the initial portion of the shroud may be computed as a continuation of the inviscid forebody supersonic flow field since the viscous wake flow does not affect this region. The downstream portion of the shroud, which is affected by the wake, reflects its disturbances obliquely downstream. Therefore, the influence of those disturbances can be felt in the initial part of the wake only by virtue of a feedback through a subsonic portion of the wake. For afterbodies of small fineness-ratio for which the detached exit boundary layer of the wake does not re-impinge on the body, and for which the wake regains its supersonic velocity within a few body diameters downstream of exit, the effects of the downstream section of the shroud do not influence the flow over the afterbody. Thus, for small fineness-ratio afterbodies, the downstream segment of the shroud need not be established with great accuracy. The sensitivity of the wake properties to the exact upstream contour of the shroud requires investigation; it is not dealt with further in this report.

The possibility of shrouding the base region was mentioned initially by Ferri and Libby[5, 6] in a general discussion of the shroud method of testing forebodies and other aerodynamic surfaces. In connection with flows other than wakes, the shroud method consists of impressing on a body a prescribed pressure and

velocity distribution in order to simulate the required boundary-layer characteristics. This is accomplished by channeling the flow around the body by means of a contoured shroud which establishes the appropriate area-ratio distribution of the channel over the body. In this manner, a desired heat flux or shear stress distribution can be applied to the body together with the associated pressure distribution. The shroud method has the advantage that large models can be utilized with relatively small amounts of test fluid. Furthermore, test Reynolds Numbers equivalent to those encountered in flight can be achieved since the channeled flows are usually in the subsonic or low supersonic range. With this technique, Reynolds Numbers can be varied according to a desired program. However, nonuniform entropy distributions in a flow field cannot be duplicated with the technique now being utilized.

The objective of the present investigation is to determine experimental pressure distributions and heat-transfer rates on blunt afterbodies (three) with a fineness-ratio of about 1 under zero angle-of-attack conditions. It is desired to simulate Mach Number and Reynolds Number conditions equivalent to those in flight but using stagnation temperatures on the order of 1,400°R. to 1,600°R. Primary consideration is given to the pressure and heat-transfer distributions over the afterbodies and to the effects of changes in Reynolds Number. For the pressure, comparisons are made with other base pressure results obtained in full-model tests.

In the present tests, an inviscid streamtube is duplicated from a position near the forebody sonic region to a position two exit shoulder diameters downstream of the exit shoulder. Following the previous reasoning, the detailed contour is significant here only for points up to about 1 diameter beyond the exit station. The shroud is continued downstream of the two-diameter position with a cylindrical contour for an additional five diameters.

The particular shroud-shape utilized here was established by Robert Byrne of General Applied Science Laboratories, Inc. A 54° half-angle sharp cone was considered as a forebody shape. The design flow was at Mach 20 yielding an attached bow shock. The resulting conical flow field was obtained by neglecting real gas effects and assuming a constant specific heat ratio of 1.4.

The flow field was continued beyond the sonic line and around the break in the cone surface by the method of characteristics including rotation. The particular streamline for the shroud shape was selected by establishing the magnitude of the mass flow which was to be supplied by the test facility (PIBAL), and thereby setting the flow area between the body and the chosen stream surface. The basic shroud shape was the same for the three afterbodies studied.

A boundary-layer displacement correction was not applied to the shroud for the following reasons: (1) a comparable error is incurred in neglecting real gas effects in the determination of the basic contour if an interpretation of the results in terms of flight conditions is desired; (2) the same shroud contour is utilized for the study of flows over a range of Reynolds Numbers. Therefore, the required boundary-layer correction would vary from test to test.

In the design flow-field calculation, constant $\gamma = 1.4$ and a sharp conical forebody were assumed mainly for reasons of simplicity. However, it was judged that real gas effects would not alter the shroud shape enough to have a significant influence on the afterbody data trends. Additionally, it was considered that for practical purposes the flow field in the skirt region of a sharp cone is the same as that of a "slightly blunted" cone. A criterion for "slight" blunting can be established by regarding the flow through the central streamtube which passes through the nonconical region of the detached bow shock, and, thus, has a lower stagnation pressure than that behind the conical part of the shock. If this streamtube is sufficiently small, it will be swallowed by the boundary layer before it reaches the end of the cone and the blunting can be considered "slight." In this case, it is sufficiently accurate to consider that the inviscid flow is the same as that of a sharp cone. This flow which is isentropic in the forebody region can be duplicated by the base-shroud.

As previously mentioned, the shroud technique as now constituted cannot be used to duplicate the explicit presence of vorticity which may exist in the actual prototype flow field. However, it can be used to simulate streamline shapes which may have been influenced by the vorticity. Thus, it is of use, in applying the shroud method, to distinguish between the explicit and implicit effects of vorticity.

Despite the restrictions previously cited concerning the class of forebody flows covered by the present shroud setup, a reader may wish to draw an inference from the present afterbody results to assess analogous effects for flows created by more blunt nose-cones. Several effects of the blunting may be considered in this regard:

(1) It is recalled that the present forebody consists of a 54° half-angle cone over which the flow is subsonic up to the end of the conical part whether the cone is sharp or blunted. Thus, the *sonic region* is located at the end of the conical surface in both the sharp and blunt configurations.

(2) The changed *stagnation-pressure* distribution in the flow field leaving the forebody is a parameter of importance. For large amounts of blunting, the inviscid flow in the region near the body will have a relatively uniform stagnation pressure whose value is that behind the most normal portion of the bow shock. The changed stagnation-pressure level in the absence of vorticity is taken into account in the subject tests since the present shroud represents the flow field near the body. For intermediate degrees of bluntness, stagnation-pressure gradients will be present in the flow field; these cannot be duplicated with the present

setup, although the average change in stagnation-pressure level can still be taken into account.

In the subject 54° half-angle-cone configuration, stagnation pressure gradients caused by blunting would be relatively mild compared to those on more slender cones. A change in shock angle from 90° to 60° (corresponding to a 54° cone half-angle with $\gamma = 1.4$ at Mach 20) would cause an increase in stagnation pressure by a factor of about two behind the shock. A decrease in shock angle from 90° to 45° would raise the stagnation pressure by a factor of six. This may be compared to a stagnation-pressure decrease by a factor of 10,000 across the normal shock at Mach 20.

(3) The effect of the blunting on the *streamline shape* duplicated by the shroud is of interest. In this regard, primary consideration can be given to the part of the streamline directly following the forebody and not influenced by the wake or base pressure. It is believed that for the present forebody cone-angle, this part of the streamline will not be severely influenced by blunting when vortical effects are not strong near the body. However, this is strictly a matter of the author's judgment for the purpose of this discussion and must be subject to future confirmation or revision. In making this assessment, it is assumed that the body geometry in the sonic region remains unchanged, and that the sonic position and shock geometry in the sonic region will not be strongly altered by the blunting. Thus, the flow field immediately following the sonic region would not be altered greatly by blunting the present cone.

(4) Finally, the effects of vorticity on the *mixing characteristics* of the free boundary layer over the wake may be considered. This vorticity does not appear near the boundary layer when the forebody is a sharp cone, or when it is very blunt, as previously stated. It may arise for intermediate degrees of bluntness but is not expected to have a first-order effect on the free mixing.

The laminar, transitional, or turbulent nature of the boundary layer which comes off the forebody and forms the free-mixing region bounding the wake is an important factor in determining the wake properties. This factor will be discussed further in the body of the paper. However, it may be mentioned here that no boundary-layer trips were used in the present tests.

In the present test series, maximum model diameters (those at the exit shoulder) are 5 in. Forebody stagnation pressures, corresponding to those which would exist on the body surface in flight, were varied in a range between 40 and 105 psia.

The authors wish to acknowledge the suggestion of this investigation by Dr. Antonio Ferri. Also acknowledged with thanks is the cooperation of Messrs. Robert Byrne and Ira Nathan of General Applied Science Laboratories, Inc., in planning and designing the test setup. Dr. Paul A. Libby provided helpful discussions. The main hardware for the test rig was initially designed, built, and used in a series of tests sponsored by the General Applied Science Laboratories, Inc., and the General Electric Company M.O.S.D.

Experimental Procedure

Experiments for this investigation were conducted in the hypersonic facility of the Polytechnic Institute of Brooklyn Aerodynamics Laboratory. Use was made of a high-temperature-pressure air source[7] producing stagnation temperatures up to 3,000°R., stagnation pressures up to 600 psia, flow rates on the order of 10 lb./sec., and runs up to 2 min. in duration. Attached to this air supply is an axially symmetric Mach 6 nozzle with a 1.5 in. diameter throat and 12 in. diameter test section. The shroud rig for the present test series was inserted into the existing nozzle (see Fig. 1). The throat of the existing nozzle may be closed by a plug. As a result, it serves as a valve for starting the tests and as a safety orifice to limit the mass flow through the heater. A vacuum exhaust system is employed.

In practice, the shroud and model form a second throat downstream of the Mach 6 nozzle throat. Therefore, a shock forms in the low supersonic portion of the Mach 6 nozzle so that the expanded portion of the nozzle serves as a stagnation chamber for the shroud rig. The shroud stagnation pressure is thus four to eight times lower than the actual heater supply pressure in this setup. The magnitude of this ratio depends on the throat area formed by the shroud and model.

Photographs of several components of the test rig are shown in Figs. 2(a), 2(b), and 2(c).

Shroud Coordinates

As previously outlined, the shroud coordinates were established using a forebody configuration consisting of a sharp 54° half-angle cone with a flat base. The inviscid flow field was calculated for Mach 20 with a constant value of the specific heat ratio equal to 1.4. The initial part of the flow was obtained as a conical flow. Beyond the sonic region near the edge of the skirt, the calculation was continued by the method of characteristics including rotation. The flow was expanded around the corner of the skirt and the determination of streamline shapes carried on up to positions two body diameters downstream of the end of the cone. Beyond that position, a cylindrical contour was used.

By considering a change in flow deflection from the cone half-angle of 54° to the horizontal, it is seen that the local Mach Number changes from 1.13, its value on the cone, to 3.34, with a corresponding Mach angle of 17.4°. Wake disturbances will not influence the streamlines upstream of the Mach line making an angle of 17.4° with the horizontal. For streamlines near the body, this limits the wake influence to point further downstream than 1.5 diameters from the cone end. Even beyond this position, disturbances generated by the wake will probably be

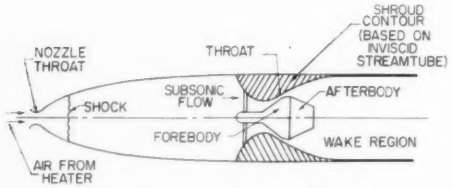

FIG. 1. Schematic drawing of test rig.

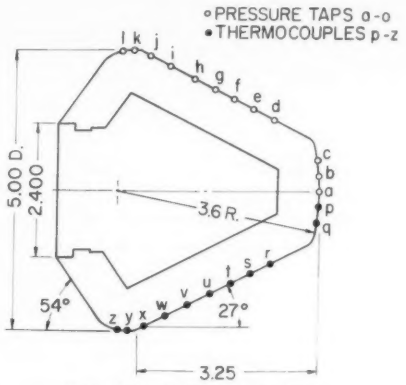

FIG. 4(a). Model 1 (no step).

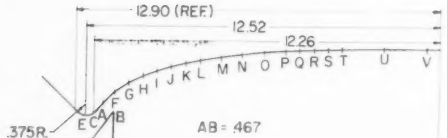

PT.	THEOR. PRED. MACH	X	PT.	THEOR. PRED. MACH	X
A	1.0	11.91	N	3.38	7.00
F	1.465	11.50	O	3.61	6.25
G	1.934	11.00	P	3.64	5.50
H	2.24	10.50	Q	3.70	5.00
I	2.55	10.00	R	3.78	4.50
J	2.70	9.50	S	3.85	4.00
K	2.85	9.00	T	3.91	3.50
L	3.03	8.50	U		2.00
M	3.21	7.75	V		0.50

FIG. 3. Shroud coordinates (in.).

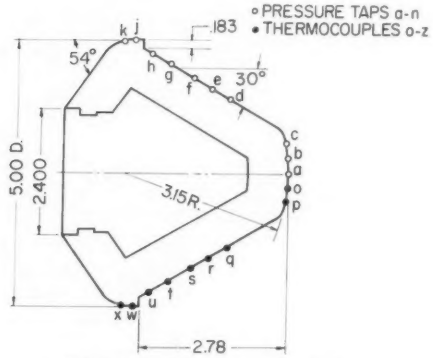

FIG. 4(b). Model 2 (medium step).

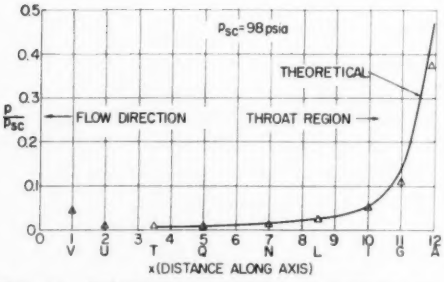

FIG. 5. Estimated and measured pressure distributions on shroud: model 2 (medium step).

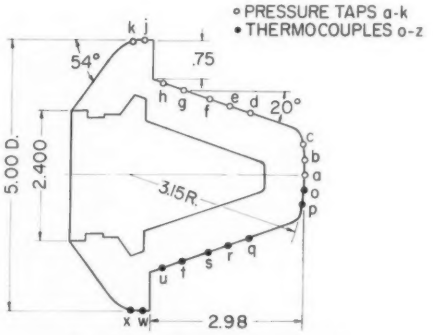

FIG. 4(c). Model 3 (large step).

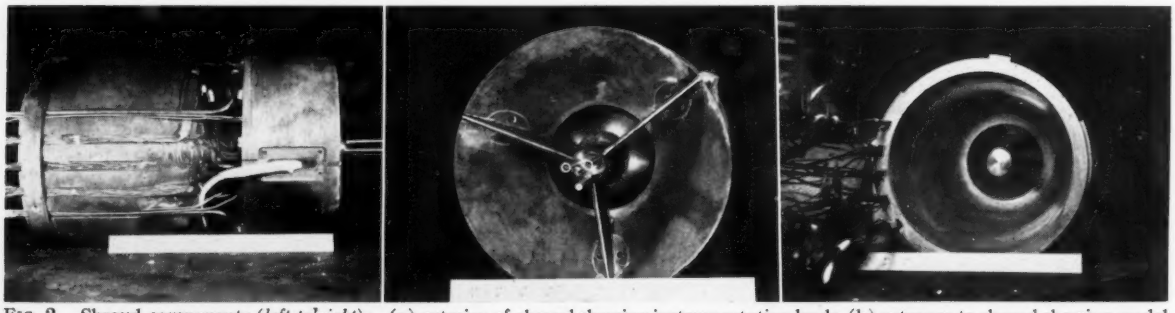

FIG. 2. Shroud components (*left to right*): (a) exterior of shroud showing instrumentation leads, (b) entrance to shroud showing model mount and stagnation pressure and temperature probes, and (c) rear view of shroud with model inserted.

reflected downstream a sufficient distance that they will contact the wake after it has become supersonic again, and, thus, not likely to affect the wake flow near the body by feedback.

The shroud coordinates and theoretical Mach Number distribution on the shroud are shown in Fig. 3.

With a model base diameter of 5 in. selected on the basis of wind-tunnel dimensions, a gap of 0.50 in. was selected at the sonic line to permit mass flows on the order of 10 lb./sec. during the tests. Boundary-layer corrections were not made on the shroud in view of the fact that a comparable error is incurred in neglecting real gas effects in a Mach 20 calculation, and that test Reynolds Numbers are varied during a test series requiring a varying correction.

Estimated and measured pressure and Mach Number distributions along the shroud are shown in Figs. 5 and 6. It is also noted that the model shapes used here have a short cylindrical section prior to the afterbody [see Figs. 4(a), 4(b), and 4(c)].

Models and Instrumentation Points

The three models tested are shown in Figs. 4(a), 4(b), and 4(c). Also shown are the locations of surface pressure taps and surface heat-flux meters. Pressure taps were located along the shroud, as shown in Fig. 3. The models are constructed of stainless steel type 304.

Measurements

Pressures on both the shroud and models were measured by means of mercury manometers and are accurate within ± 0.05 psi. The stagnation pressure p_{sc} in the region just prior to the shroud was continually recorded by means of an electrical transducer.

Heat-transfer measurements were made by means of the transient, insulated plug technique described, for example, in reference 8. In this method, the temperature history of the exposed surface of a plug (heat meter) within the model is recorded during a test. The plug is cylindrical and is insulated from the thick model wall by means of a small air gap, except for a thin region near the exposed surface which is in contact with the remainder of the model surface. The plug material is the same as that of the model. Iron-constant thermocouples are used here. Care is taken that the initial temperature throughout the plug and model is uniform. The heat-transfer rates at the exposed surface are determined by the solution of a classical one-dimensional heat conduction problem. The interior surface of the plug is assumed to be perfectly insulated.

Two types of data reduction procedures were employed. The first consisted of solving the heat conduction problem by using an analog computer with the conduction problem setup in finite difference form. This procedure was used largely for long runs in which the surface temperature rose appreciably. A check on these values was made by means of a hand computer for which an integral form of the heat conduction solution, for example, as described in reference 10, was used.

A second data reduction procedure was used for short tests during which the heat-transfer rates were small and surface temperature rises were small. Under these conditions, it can be assumed that the surface heat flux (not necessarily the heat-transfer coefficient) is constant with time. In this case, the surface temperature varies proportionally to the square root of the time, and the slope of the plot of T_w vs. $\sqrt{t}$ is proportional to the heat-transfer rate.

The results of the two methods of heat-transfer data reduction were in good agreement with each other. The individual values of the heat flux obtained by these procedures are believed to be accurate within ± 15 per cent of the true value. The stagnation temperature T_{sc} in the region just prior to the shroud was recorded continuously on a strip chart recorder. The stagnation pressure and temperature probes are shown mounted on the model support in Figs 2(a), 2(b), and 2(c).

Types of Runs

Two types of test runs were made for heat transfer: (1) Runs at constant p_{sc} were made. These were relatively short, on the order of 30 sec. overall if only heat rates were measured, or on the order of 60 sec. if pressures were measured as well. (2) Runs were made during which the pressure p_{sc} was varied from 40 to 105 psia in approximately 100 sec. overall. During these runs, the pressures were permitted to remain constant for a time at two or three levels to allow the pressures to become stabilized at these values. However, the heat rates obtained from the continuous temperature traces of the heat meters yielded a continuous variation of heat-transfer rate with p_{sc} or Reynolds Number.

The surface temperatures on the afterbodies during the constant p_{sc} tests were low, on the order of 550°R., and remained low and uniform during the first 10 sec. of the test; the initial part of the test was used for heat-transfer data reduction. This maintenance of low afterbody temperatures was due to the magnitude of the absolute heat fluxes being applied and to the heat sink effect of the thick model wall. Temperature rises between one and 5°R./sec. were observed.

During the long variable p_{sc} runs, cumulative temperature rises of as much as 200°R. were experienced.

Presentation and Discussion of Results

The list of runs and run conditions are given in Table 1. The pressures p_{sc} shown are those existing in the chamber immediately prior to the shroud. These are comparable to the stagnation pressure behind the bow shock and existing along the forebody surface in the sonic region of the body. The Reynolds Number per ft. is defined as $R_s/D_0 = \rho_s\sqrt{\bar{h}_s}/\mu_s$.

TABLE 1
List of Runs

Run	p_{sc}(psia)	T_s(°R.)	$(R_a/D_b) \times 10^{-6}$	Remarks
		Model 1 (no step)		
1	40–100	1,500	9.4–22.0	for temperature only
2	79	1,570	16.32	for temperature and pressure
3	105	1,520	32.04	for temperature and pressure
		Model 2 (medium step)		
1	98	1,300	25	for pressure only
2	47–68–89	1,310	12–17.3–22.7	for pressure only
3	45–67–88	1,290	11.8–17.5–23	for pressure only
		Model 3 (large step)		
1	48–97	1,430	10.3–3.23	for temperature only
2	45–67	1,430	10.1–15.1	for pressure only

Pressure

A typical measured pressure distribution on the shroud is shown in Fig. 5. It is compared to that estimated by R. Byrne in the shroud design and is seen to be in reasonable agreement with the theoretical values, at least up to station N, which is about one diameter downstream of the model exit. The corresponding Mach Number distribution is shown in Fig. 6.

The measured pressure distributions on the models are shown in Figs. 7(a), 7(b), and 7(c). Only one point was measured on the cylindrical shoulder of Model 2. As a result, the variation in pressure along this shoulder cannot be seen there. However, two points were measured on Models 1 and 3 and these show a marked adverse pressure gradient. The pressures increase by factors of 1.3 to 2. This appears to be due to an overexpansion followed by a recompression to the theoretical Prandtl-Meyer value which yields a shoulder Mach Number of 3.3, as previously noted. A weak shock or series of compression waves would be expected to be present in this region. These would propagate downstream at an angle comparable to the exit Mach angle.

The pressure distribution on the afterbody is fairly uniform. No marked differences in pressure are noted on the flattened rear faces of the afterbodies. The afterbody pressure levels are on the order of 1/4 to 1/2 of the exit pressure. The ratio of afterbody pressure to p_{sc} decreases with increasing values of p_{sc}. This trend can be seen more clearly from the plot of p/p_{sc} vs. p_{sc} for various pressure tap locations, as shown in Figs. 8(a), 8(b), and 8(c).

The pressure ratio p/p_{sc} is seen to decrease in a rather systematic way with increasing values of p_{sc}. The value of p_{sc} characterizes the test Reynolds Number. Curves of the stagnation Reynolds Number per ft. R_s vs. p_{sc} for various values of T_s in the test range are shown in Fig. 9. The relation between the exit Reynolds Number R_a and the stagnation value R_s for various exit Mach Numbers M_a is shown in Fig. 10. For $M_a = 3.3$, $R_a/R_s = 0.15$. Furthermore, the interpretation of R_s in terms of flight conditions, based on conditions behind a conical shock and, alternatively, behind a normal shock which would occur at the nose of a blunt body, are shown in Fig. 11; real gas effects assuming thermodynamic equilibrium were used in constructing Fig. 11.

Shown for comparison in Figs. 8(a), 8(b), and 8(c) are estimated values of the pressure ratio p/p_{sc} obtained by the use of data given by Chapman in reference 1. The procedure employed in using Chapman's results to obtain estimates under the present test condition involves the use of Reynolds Number and Mach Number interpolations. It may be noted that the forebodies used by Chapman were generally slender. As a result, *the free-stream test values were the same as the exit values* (subscripts a and f are equivalent). The result of Chapman's base pressure tests at various M_f for a body with a fineness ratio of 3.1 and $R_L = 5 \times 10^6$ are shown in Fig. 23.[1] With the Mach Number M_a obtained experimentally here a base pressure coefficient can be determined from the above-mentioned figure. The Reynolds Number effect on the base pressure coefficient can then be estimated from Fig. 19[1] which presents base pressure data for $M_f = M_a = 2.0$ for various R_L. With this figure, it is assumed that the Reynolds Number effect at a given Mach Number can be expressed as follows:

$$[(p_B - p_a)/(1/2)\rho_a u_a^2]_{(\text{test } RL)} = A[(p_B - p_a)/(1/2)\rho_a u_a^2]_{RL = 5 \times 10^6} \quad (1)$$

where A depends on the test R_L and denotes the ratio of the pressure coefficient at two different R_L and at a constant Mach Number. The results of this estimate are shown plotted in Figs. 8(a), 8(b), and 8(c), and are seen to be in qualitative agreement with the present results.

The variation of base pressure coefficient with Reynolds Number (R_L) measured by Chapman (Fig. 19)[1] shows a strong increase in this coefficient with increasing R_L in the lower R_L range of the region designated as laminar. The comparable Reynolds Numbers (R_a) of the present tests fall in this lower range. Since the average base pressure trend with R_a obtained in the present tests are in qualitative agreement with estimates based on Chapman's values in this range, it can be surmised that the boundary layer at exit in the present tests is laminar.

In comparing the pressure levels on the afterbodies having three different step-heights, it is seen from Figs. 7(a), 7(b), and 7(c) that the pressure ratios p/p_{sc} are close to each other for the three models at the higher values of p_{sc} (or R_s). However, at the lower values of p_{sc} the no-step pressures are higher by a factor of two than those of the stepped afterbodies. The difference increases with decreasing values of p_{sc}.

Heat Transfer

The heat-transfer results are plotted in terms of a Nusselt Number based on stagnation conditions with the exit diameter as a reference length—that is, $N =$

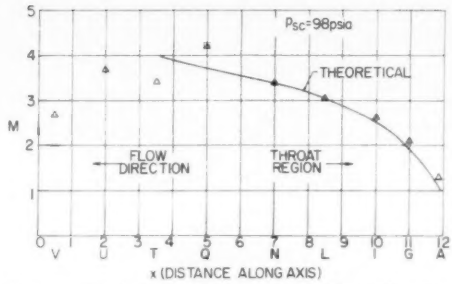

FIG. 6. Estimated and measured Mach Number distributions on shroud: model 2.

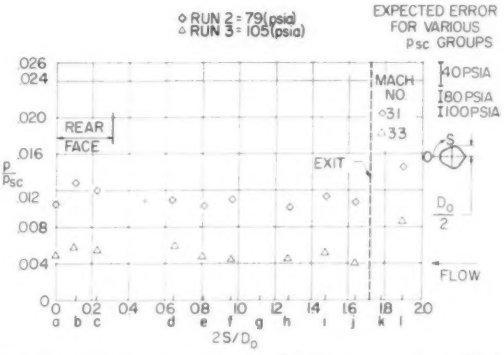

FIG. 7(a). Measured pressure distributions over model 1 (no step).

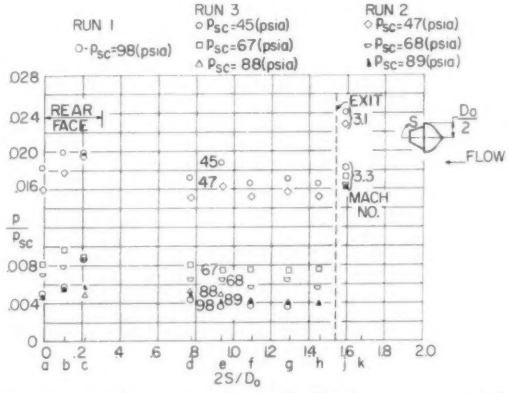

FIG. 7(b). Measured pressure distributions over model 2 (medium step).

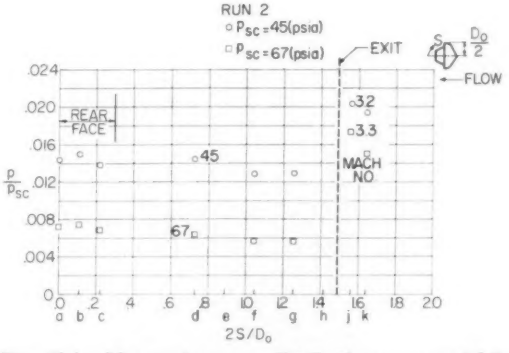

FIG. 7(c). Measured pressure distributions over model 3 (large step).

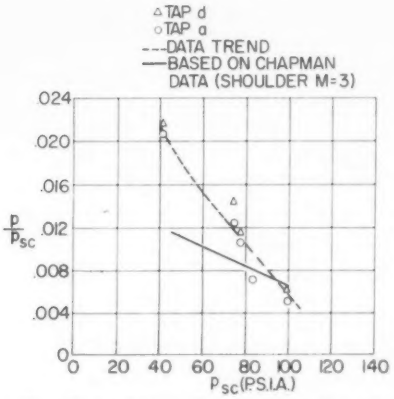

FIG. 8(a). Measured pressure ratio p/p_{sc} on model for representative stations vs. stagnation pressure p_{sc} and rough comparison with low-speed data: model 1 (no step).

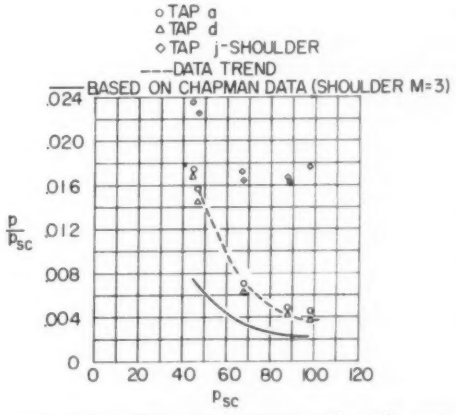

FIG. 8(b). Measured pressure ratio p/p_{sc} on model for representative stations vs. stagnation pressure p_{sc} and rough comparison with low-speed data: model 2 (medium step).

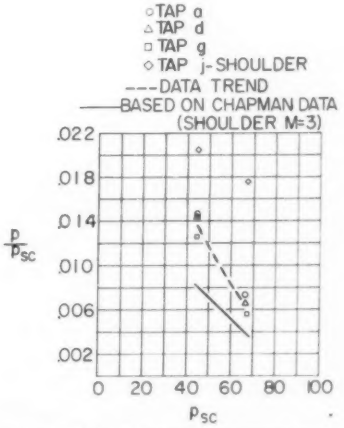

FIG. 8(c). Measured pressure ratio p/p_{sc} on model for representative stations vs. stagnation pressure p_{sc} and rough comparison with low-speed data: model 3 (large step).

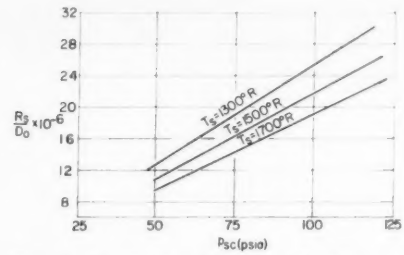

FIG. 9. Stagnation Reynolds Number per ft.: $\rho_s\sqrt{h_s}/\mu_s$ vs. p_{sc} for various values of T_s.

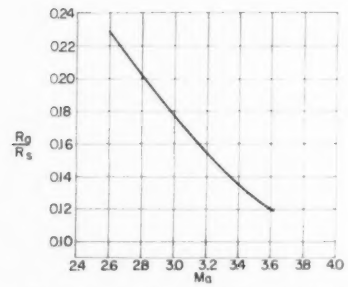

FIG. 10. Ratio of exit Reynolds Number per ft.: $\rho_a u_a/\mu_a$ to stagnation Reynolds Number per ft. for various values of exit Mach Number M_a.

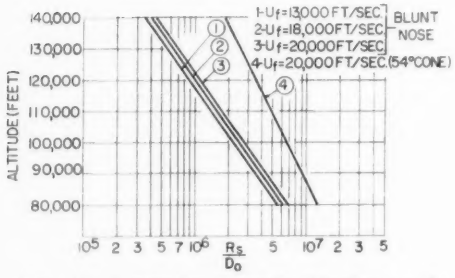

FIG. 11. Stagnation Reynolds Number per ft. vs. altitude for various flight velocities for conditions behind a normal shock (including real gas effects for thermodynamic equilibrium).

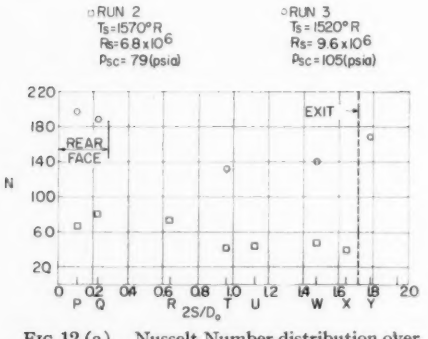

FIG 12 (a). Nusselt Number distribution over afterbody for two stagnation pressures: model 1 (no step).

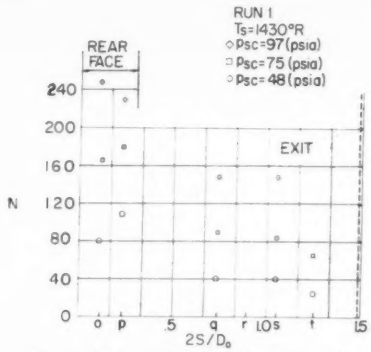

FIG. 12(b). Nusselt Number distribution over afterbody for three stagnation pressures: model 3 (large step).

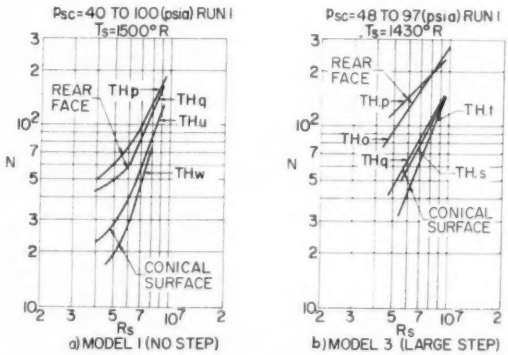

FIG. 13. Nusselt Number vs. Reynolds Number for various locations.

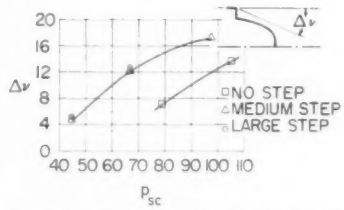

FIG. 14. Flow expansion angle at exit position.

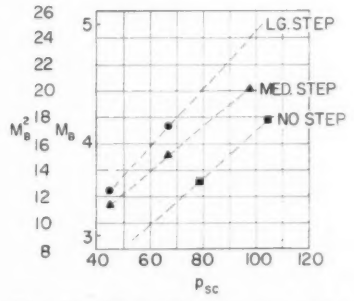

FIG. 15. Mach Number over wake near exit position.

$D_0\, qc_{ps}/(h_s - h_w)k_s$. This quantity is uniquely related to the analogous parameter based on exit conditions—that is, $D_0\, qc_{pa}/(h_s - h_w)k_a$ if a fixed exit Mach Number is specified.

The Nusselt Number distributions over the afterbodies are shown in Figs. 12(a) and 12(b). As previously stated, stagnation temperatures during the tests ranged from 1,300°R. to 1,600°R. while surface temperatures ranged from 560°R. to 800°R., yielding ratios of T_s/T_w between 1.8 and 3.0. Although heat-transfer measurements were not made on Model 2, it is believed that the Reynolds Number effects on heat transfer will be qualitatively similar for the three models tested.

As shown in Figs. 12(a) and 12(b), the Nusselt Number over Models 1 and 3 increase somewhat in the streamwise direction. The values on the flattened rears of the afterbodies are almost twice the values on the conical sides.

To indicate more clearly the effect of variations in N and p_{sc} for a given heat meter location, the effects on N of varying p_{sc} are plotted in Fig. 13. In these figures, the Reynolds Number R_s is used for the abscissa rather than the pressure p_{sc}. The variations of Nusselt Number with Reynolds Number are roughly expressible in the manner $N \sim R^{\omega}$ where $\omega > 1$. The Nusselt Numbers for comparable values of R_s are higher on the large-step afterbody (Model 3) than on the no-step afterbody (Model 1).

Only a single value of N was obtained on the cylindrical shoulder during the present tests. This was obtained during a constant pressure run on Model 1 and is shown in Fig. 12(a). Because of errors incurred by conduction through the Model from the forebody, the results of variable p_{sc} runs could not be used to obtain additional values on the shoulder.

This value of N on the shoulder agrees closely with a theoretical value obtained using a well-known equation for laminar flat-plate heat-transfer based on exit flow conditions and a length equal to the surface distance from the nose of the model mount to the exit station. This is an additional indication (see previous comment concerning pressure variation) that the boundary layer at exit is laminar.

No information has been obtained concerning the behavior of the free-mixing layer beyond the exit station. It may have been laminar, transitional, or turbulent. Moreover, no examination of the detailed features of the flow within the separated wake was made.

Addendum

After the present paper had been completed, related papers by Rabinowicz[9] and Powers, Stetson, and Adams[10] became available to the authors. Both describe shock tube investigations.

Reference 9 describes several preliminary measurements of heat-transfer rates on the flat base of a side-supported hemisphere-cylinder over which the flow was turbulent. These indicated that the rates near the periphery were on the order of one-half or one-third the rates on the cylindrical surface, while at the base-center the rates were on the order of those on the cylindrical surface.

The study of reference 10 was of a more detailed nature. It consisted of an extensive series of heat-transfer measurements on stepped-down cylindrical afterbodies (two different step-heights) extending from a hemisphere-cylinder forebody (length equal to diameter) and connecting to the model support. The afterbodies were sufficiently long so that the separated flows became reattached. Schlieren and shadow observations were made, while pressures were estimated or taken from other tests. Several aspects of this study are of interest in connection with the present work.

(1) In reference 10, the observed flow deflections of the free-mixing reattached boundary line were invariant with test Reynolds Number for either laminar (20°) or turbulent (15.5°) boundary-layer flow over the forebody. In the present detached flows, the changing pressure ratios measured and shown in Fig. 8 indicate Prandtl-Meyer expansion angles at exit increasing almost linearly from about 5° to 17° with increasing stagnation pressure or exit Reynolds Number (Fig. 14). This trend is in agreement with that indicated by Chapman in the laminar low Reynolds Number range of his tests (Fig. 19).[1] In fact, this trend is considered here as one evidence that the exit boundary layer is laminar, the other item of evidence being a laminar heat rate at the end of the forebody. (See also reference 11.)

(2) In reference 10, local Reynolds Numbers beyond the end of the forebody, based on contour length over the forebody, are associated with natural transition or turbulent flow over the forebody for values above 4×10^5. This corresponds to values of 6 to 8×10^5 at the forebody end. The comparable Reynolds Numbers of Chapman (Fig. 19)[1] for transition and turbulence are above 4×10^6, at Mach 2—that is, about five times higher. Differences of this kind in various wind-tunnel tests are not uncommon.

(3) The afterbody heat-transfer results of reference 10 are presented in terms of local inviscid flow variables over a solid surface replacing the separated wake boundary. The results of the present paper are given in terms of stagnation conditions which are related to conditions at the end of the forebody by Fig. 10 when the exit Mach Number is known. It is of interest to express the present results in terms of local wake conditions as determined by the measured wake pressures, and to compare them with the results in Fig. 10 of reference 10. For this purpose, the pressures and heat rates of the first two or three test points beyond the forebody are considered. A significant result is observed—namely, that for each afterbody the local Reynolds Number over the wake is virtually invariant with respect to p_{sc} or stagnation Reynolds Number (approximately here for a given T_s and $\mu \sim T^{3/4}$,

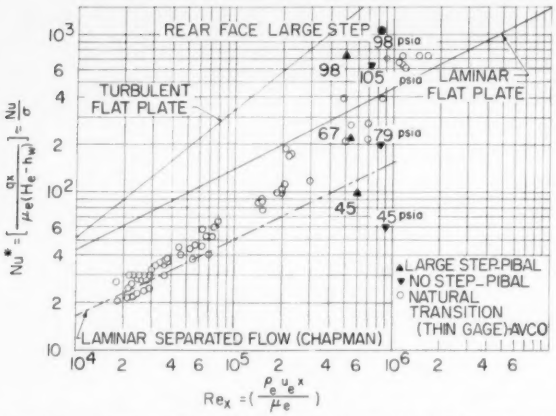

FIG. 16. Comparison of AVCO result (Fig. 10 of reference 10) and present data.

$R_B \sim \sqrt{p_s p_B}$), while the local Mach Number and flow deflection increase almost linearly with p_{sc} (Fig. 14). Thus, the afterbody heat rates vary over a wide range, for example, in the notation of reference 10 from $Nu^* = 90$ to 750 for a given $R_{ex} = 5.5 \times 10^5$. Therefore, for completely detached wakes, the local wake Reynolds Number alone does not seem to be a suitable correlation parameter. Rather increased heat rates are associated with increased local Mach Numbers over the wake and with a closing in of the wake. These factors probably affect the circulation mechanism in the wake region between the free mixing boundary and the body at a given local Reynolds Number R_B. The heat rates range from well below to well above the laminar predictions but stay below the local turbulent estimate (see Fig. 16).

Thus, it seems that the Nusselt Number—Reynolds Number trend shown in Fig. 10^{10} (see also Fig. 16 here) depends strongly on the Reynolds Number independence of the wake Mach Number as established by the wake reattachment for either laminar or turbulent flow. In the present detached wakes, there exists an additional factor engendered by the wake convergence, which is Reynolds Number dependent.

(4) It remains to be pointed out that the data of the present paper fall into the Reynolds Number range classified as transitional or turbulent in reference 10. It is somewhat difficult to reconcile this fact with the aforementioned evidences of laminar flow in the present tests.

(5) The previous discussion concerning wake convergence was applicable to the part of the wake immediately following the forebody. The pressures generally are somewhat higher on the rear face of each afterbody, and the heat rates are also higher. However, even the highest measured heat rate (on the rear face of the large-step model at high p_{sc}) is less than the estimated local turbulent flat plate value (Fig. 16).

Conclusions

(1) The feasibility of simulating hypersonic wake flows by the shroud technique is demonstrated in connection with a study of pressures and heat-transfer rates over three short afterbodies with different step-down heights.

(2) Pressures along an afterbody are roughly uniform in a single test but are somewhat higher on the rear face.

(3) For a given point on an afterbody, the ratio p/p_{sc} decreases with increasing p_{sc} or R_s. This effect is associated with a Prandtl-Meyer expansion angle at exit which increases with p_{sc} indicating a closing-in of the wake boundary. In the present tests, this angle increases from 7° to 17°. The local Mach Number squared just beyond the forebody-end varies linearly with p_{sc} or R_s in the range of the tests. However, the local Reynolds Number over this wake region is almost invariant with p_{sc}. The expansion angle is smaller on the zero-step-height body than on the others.

(4) The pressure-Reynolds Number trend is similar to that observed by Chapman[1] in the laminar range.

(5) An adverse pressure gradient on the cylindrical end of the forebody was observed.

(6) Heat rates (obtained on two afterbodies) are roughly uniform over an afterbody in a single run. Some increase in the streamwise direction is noted. Heat rates on the rear face of an afterbody are almost twice the values on the sides. Rates on the large-step body are higher than those on the zero-step-height body; this effect is possibly associated with the increased closing in of the wake boundary on the large-step body.

(7) Afterbody Nusselt Numbers (N) vary with test Reynolds Number (R_s) roughly in the manner $N \sim R_s^{\omega}$ where, generally, $\omega > 1$.

References

[1] Chapman, D. R., *An Analysis of Base Pressure at Supersonic Velocities and Comparison with Experiment*, NACA Rep. 1051, 1951.

[2] Love, E. S., *Base Pressure at Supersonic Speeds on Two-Dimensional Airfoils and on Bodies of Revolution with and without Fins Having Turbulent Boundary Layers*, NACA TN 3819, January, 1957.

[3] Ferri, A., and Pallone, A., *Note on the Flow Fields on the Rear Part of Blunt Bodies in Hypersonic Flow*, WADC TN 56-294, July, 1956.

[4] Chapman, D. R., Kuehn, D. M., and Larson, H. K., *Investigation of Separated Flows in Supersonic and Subsonic Streams with Emphasis on the Effect of Transition*, NACA TN 3869, March, 1957.

[5] Ferri, A., and Libby, P.A., *The Hypersonic Facility of the Polytechnic Institute of Brooklyn and Its Application to Problems of Hypersonic Flight*, AGARD Rep. No. 136, August, 1957.

[6] Ferri, A., and Libby, P. A., *A New Technique for Investigating Heat Transfer and Surface Phenomena Under Hypersonic Flow Conditions*, Readers' Forum, Journal of the Aeronautical Sciences, pp. 464–465, Vol. 24, No. 6, June, 1957.

[7] Bloom, M. H., *A High Temperature-Pressure Air Heater*, WADC TN 55-694, November, 1956.

[8] Cresci, R. J., and Libby, P. A., *Some Heat Conduction Solutions Involved in Transient Heat Transfer Measurements*, WADC TN 57-236, August, 1957.

(*Continued on page 662*)

Optimum Path of an Airplane—Minimum Time to Climb

THEODORE THEODORSEN*

Republic Aviation Corporation

Summary

In this paper, the theory of variation is applied to the determination of the minimum time to climb for an airplane of constant weight. It is evident that when sufficient boundary conditions are given—that is, for the beginning and the end point of the path—there is one and only one curve corresponding to the minimum time to climb. Because of the relative complexity of the resulting differential equation, it is convenient to generate such paths by a step-by-step procedure. The end point is then bracketed by proper choice of the higher derivatives at the origin.

It is evident that any decrease in weight during the time of the flight may also be properly bracketed by solving for the two limiting cases of initial and final weights of the airplane. It will be observed, however, that the decrease in weight is actually too small to be of significance on the shape of the path. The solution is in a form which readily lends itself to routine machine calculation. Numerical calculations have been completed for a large number of cases pertaining to the Republic F-105 fighter-bomber. Experimental flight tests are in the planning stage.

(1) Introduction

THE PROBLEM IS to determine the path of an airplane of given performance which corresponds to the shortest time between the end points of the path. This condition corresponds to finding the minimum of the Euler-Lagrange integral

$$t = \int_0^H [dh/(v \sin \gamma)]$$

where h is the height, v is the velocity, and γ the angle of the path with the horizon. In this integral, there exists a relation between v and γ. In this case, the relation is complex, and one has to resort to the use of Lagrange multipliers.

It is also evident that the minimum time of flight between two points depends upon the boundary conditions prescribed at each point. If the solution were obtained in explicit form, it will contain a sufficient number of arbitrary constants to fit the condition at the two extreme points. If the differential equation is to be solved by a step-by-step procedure, it is necessary to bound the constants pertaining to the boundary condition at the second point by an appropriate selection of the values of the higher derivatives at the origin.

(2) Performance Parameters

To establish the relation between v and γ, one must write down the equations governing the motion of the airplane. These are:

$$T - D = W \sin \gamma + (W/g)\,(dv/dt) \tag{1}$$

and

$$L = W \cos \gamma + (W/g)v(d\gamma/dt) \tag{2}$$

Here T, D, and L are the thrust, drag, and lift, respectively. W is the weight of the airplane. There is also another relation indicating the decrease in the weight of the airplane as the fuel is consumed:

$$dW/dt = -\mu T \tag{3}$$

where μ is the specific fuel consumption in lbs. of fuel per sec. per lb. of thrust.

Next, we shall introduce conventional coefficients C_T, C_D, and C_L.

$$C_T = T/[(1/2)\rho v^2 S], \text{ etc., with } \beta = 2W/\rho S$$
$$C_T = (T/W)\,(\beta/v^2)$$

We shall further use derivatives with respect to h instead of time derivatives.

$$d/dt = (d/dh)\cdot(dh/dt) = v \sin \gamma \cdot (d/dh)$$

The three equations then read:

$$C_T - C_D = (\beta/v^2)[\sin \gamma + (v\dot{v}/g) \sin \gamma]$$

$$C_L = (\beta/v^2)[\cos \gamma + (v^2/g)\dot{\gamma} \sin \gamma]$$

$$\mu C_T = -(\dot{W}/W)\,(\beta/v) \sin \gamma$$

The dependent variables v and γ will now be changed to

$$v = \sqrt{\epsilon} \quad \text{or} \quad \epsilon = v^2$$

and

$$p = \cos \gamma \quad \dot{p} = -\dot{\gamma} \sin \gamma$$

One then has

$$C_T - C_D = (\beta/\epsilon)\sqrt{1 - p^2}\,[1 + (\dot{\epsilon}/2g)] \tag{4}$$

$$C_L = (\beta/\epsilon)[p - (\epsilon\dot{p}/g)] \tag{5}$$

$$C_T = -(\dot{W}/W)\beta(\sqrt{1 - p^2}/\sqrt{\epsilon})\,(1/\mu) \tag{6}$$

In regard to the third equation, extreme numerical complications occur if this is included in the solution of the problem. For an airplane, the relative decrease in weight during the climb is a small fraction of the total weight. Note further that the W only occurs in the factor $\beta = 2W/\rho S$. If W were known in advance as a function of h, there would be no error. In a second approximation, it would be possible to give W and, therefore, β very accurately as a function of h. (Dots are used in the following to denote derivatives with respect to h.)

In fact, from Eq. (6):

Received September 9, 1958. Revised and received December 3, 1958.

* Director of Scientific Research.

$$\dot{W} = -(1/2)C_{T\mu}\rho S\sqrt{\epsilon}/\sqrt{1-p^2}$$

Therefore,

$$\dot{\beta} = (d/dh)\ (2W/\rho S) = -(2W/\rho^2 S)\ (d\rho/dh) + (2/\rho S)\ (dW/dh)$$

or

$$\dot{\beta} = -C_{T\mu}(\sqrt{\epsilon}/\sqrt{1-p^2}) - (2W/\rho^2 S)\dot{\rho} = -C_{T\mu}(\sqrt{\epsilon}/\sqrt{1-p^2}) - \beta(\dot{\rho}/\rho)$$

In a step-by-step integration, it is, therefore, feasible to adjust β and $\dot{\beta}$ to the proper value which includes the decreasing value of W in $\dot{\beta}$. Likewise, for $\ddot{\beta}$

$$\ddot{\beta} = -\beta[(\ddot{\rho}/\rho) - (\dot{\rho}/\rho)^2] - \dot{\beta}(\dot{\rho}/\rho) - (1/2)C_{T\mu} \times \{[\dot{\epsilon}/\sqrt{\epsilon}\ \sqrt{(1-p^2)}] + [2\sqrt{\epsilon}\ \dot{p}p/\sqrt{(1-p^2)^3}]\}$$

In a first-order approximation (W = constant), the terms containing μ may be left out.

Thus, $\ddot{\beta}$ involves the quantities β, $\dot{\beta}$, and functions of ϵ and p which are all given at each step. Strictly speaking, the Euler-Lagrange relation should also be minimized with respect to W and $\dot{W}$.

The use of another Lagrangian multiplier to take the term (6) into account may actually be handled in an entirely similar manner. The λ's may be eliminated, and a single equation results. However, the complexity of this relation is not justified as the numerical results can be obtained with much greater simplicity by the method of correction for W. We shall, therefore, not directly include the term $\dot{W}$ in the following treatment.

(3) Solution of the Euler-Lagrange Equations

We shall now proceed to solve the minimum problem relating to the climb of an airplane. For reference, we shall restate the important conditional relations used in conjunction with the direct solution of the Euler-Lagrange equation. These are from Eqs. (4) and (5):

$$C_T - C_D = (\beta/\epsilon)\ \sqrt{1-p^2}\ [1 + (\dot{\epsilon}/2g)] \quad (7)$$

$$C_L = \beta[(p/\epsilon) - (\dot{p}/g)] \quad (8)$$

The equation for the time reads with one Lagrange multiplier

$$t = \int_0^H \Big(1/[\sqrt{\epsilon}\ \sqrt{1-p^2}] + \lambda\{C_T - C_D - (\beta/\epsilon)\ \sqrt{1-p^2}[1 + (\dot{\epsilon}/2g)]\}\Big)dh \quad (9)$$

where C_D is a function of M and C_L

and $$C_L = \beta\{(p/\epsilon) - (\dot{p}/g)\}$$

Calling the integrand G, one has then the following conditions for minimum value of the integral between zero and H,

$$\partial G/\partial\epsilon = (d/dh)\ (\partial G/\partial\dot{\epsilon}) \quad \text{and} \quad \partial G/\partial p = (d/dh)\ (\partial G/\partial\dot{p}) \quad (10)$$

Carrying out the partial differentiation, one has (c_s = speed of sound)

$$\partial G/\partial\epsilon = -(1/2)\ (1/\sqrt{\epsilon^3})\ (1/\sqrt{1-p^2}) + \lambda\{[(\partial C_T/\partial M) - (\partial C_D/\partial M)]\ [1/(2\sqrt{\epsilon}\ c_s)] + (\partial C_D/\partial C_L)\ (\beta p/\epsilon^2) + (\beta/\epsilon^2)\ \sqrt{1-p^2} \times [1 + (\dot{\epsilon}/2g)]\} = A + \lambda B \quad (11)$$

$$\partial G/\partial\dot{\epsilon} = -\lambda(\beta/\epsilon)\sqrt{1-p^2}\ (1/2g) = -\lambda C \quad (12)$$

where $$C = +(\beta/\epsilon)\ \sqrt{1-p^2}\ (1/2g)$$

$$\partial G/\partial p = p/[\sqrt{\epsilon}\ \sqrt{(1-p^2)^3}] - \lambda(\beta/\epsilon)\ \{(\partial C_D/\partial C_L) - (p/\sqrt{1-p^2}) \times [1 + (\dot{\epsilon}/2g)]\} = a + \lambda b \quad (13)$$

$$\partial G/\partial\dot{p} = \lambda(\partial C_D/\partial C_L)\ (\beta/g) = -\lambda c \quad (14)$$

where $$c = -(\partial C_D/\partial C_L)\ (\beta/g)$$

The Euler-Lagrange equations then read:

$$\left.\begin{aligned} A + \lambda B + (d/dh)\ (\lambda C) &= 0 \\ \text{and} \quad a + \lambda b + (d/dh)\ (\lambda c) &= 0 \end{aligned}\right\} \quad (15)$$

or developed:

$$\left.\begin{aligned} A + \lambda B_0 + \dot{\lambda} C &= 0 \\ a + \lambda b_0 + \dot{\lambda} c &= 0 \end{aligned}\right\} \quad (16)$$

where $B_0 = B + \dot{C}$, and $b_0 = b + \dot{c}$. Elimination of λ and $\dot{\lambda}$ brings the following relation:

$$\{(Ab_0 - aB_0)/(Cb_0 - cB_0)\} + (d/dh)\ \{(Ac - aC)/(Cb_0 - cB_0)\} = 0 \quad (17)$$

with $X = (Ab_0 - aB_0)$, $Y = (Cb_0 - cB_0)$, $Z = (Ac - aC)$ the Eq. (17) may be written:

$$(X/Y) + (d/dh)\ (Z/Y) = 0$$

or $$(X/Y) + (\dot{Z}/Y) - (Z/Y^2)\dot{Y} = 0$$

and $$(X/Z) + (\dot{Z}/Z) - (\dot{Y}/Y) = 0$$

where $$\dot{Y} = \dot{C}b_0 + C\dot{b}_0 - \dot{c}B_0 - c\dot{B}_0$$

With $B_0 = B + \dot{C}$ and $b_0 = b + \dot{c}$, $\dot{Y}$ simplifies to

$$\dot{Y} = \dot{C}(b + \dot{c}) + C(\dot{b} + \ddot{c}) - \dot{c}(B + \dot{C}) - c(\dot{B} + \ddot{C})$$

or $$\dot{Y} = C(\dot{b} + \ddot{c}) - c(\dot{B} + \ddot{C}) + \dot{C}b - \dot{c}B$$

Also,

$$\dot{Z} = \dot{A}c + A\dot{c} - \dot{a}C - a\dot{C}$$
$$X = A(b + \dot{c}) - a(B + \dot{C})$$
$$Y = C(b + \dot{c}) - c(B + \dot{C})$$
$$Z = Ac - aC$$

One thus has the relation:

$$(X + \dot{Z})Y = Z\dot{Y} \quad \text{or} \quad WY = Z\dot{Y}$$

where $W = (X + \dot{Z}) = A(b + \dot{c}) - a(B + \dot{C}) + \dot{A}c + A\dot{c} - \dot{a}C - a\dot{C}$

or $$W = A(b + 2\dot{c}) - a(B + 2\dot{C}) + \dot{A}c - \dot{a}C$$

We shall use the equation in the final form:

$$\dot{Y} = WY/Z$$

or written out

$$C(\ddot{b} + \dddot{c}) - c(\ddot{B} + \dddot{C}) + \dot{C}\ddot{b} - \dot{c}\ddot{B} = \frac{\{A(\ddot{b} + 2\dot{c}) - a(\ddot{B} + 2\dot{C}) + \dot{A}c - \dot{a}C\}\{C(\dot{b} + \dot{c}) - c(\dot{B} + \dot{C})\}}{\{Ac - Ca\}}$$

or with $\dddot{c}$ containing the highest derivative

$$C\dddot{c} = -C\ddot{b} + c(\ddot{B} + \dddot{C}) - \dot{C}\ddot{b} + \dot{c}\ddot{B} + \frac{\{A(\ddot{b} + 2\dot{c}) - a(\ddot{B} + 2\dot{C}) + \dot{A}c - \dot{a}C\}\{C(\dot{b} + \dot{c}) - c(\dot{B} + \dot{C})\}}{\{Ac - Ca\}}$$

Rearranged with certain cancellations:

$$C\dddot{c} = -C\ddot{b} + c(\ddot{B} + \dddot{C}) + \frac{\{C(\dot{b} + 2\dot{c}) - c(\dot{B} + 2\dot{C})\}\{A(\dot{b} + \dot{c}) - a(\dot{B} + \dot{C})\} + (\dot{A}c - \dot{a}C)[C(\dot{b} + \dot{c}) - c(\dot{B} + \dot{C})]}{\{Ac - Ca\}} \tag{18}$$

The highest derivative $\dddot{p}$ is contained in the quantity $\dddot{c}$ on the left side and nowhere else. Thus, $\dddot{c}$ or $\dddot{p}$ can always be calculated when the lower derivatives of c and p are given. This separation is important in a stepwise integration procedure.

The expression for c is

$$c = -(\partial C_D/\partial C_L)(\beta/g)$$

or, also,

$$c = -(2\beta/g)KC_L$$

where K is a function of Mach Number only. (See later.)

Then

$$c = -(2\beta^2/g)K\{(p/\epsilon) - (\dot{p}/g)\}$$

With all other quantities constant, one has, therefore,

$$\ddot{c} = (2\beta^2/g^2)K\ddot{p} + \text{lower order terms}$$

The quantity

$$Ac - aC = (1/2)(1/\sqrt{\epsilon^3})(1/\sqrt{1 - p^2})(2\beta/g)KC_L - (p/\sqrt{\epsilon})[1/\sqrt{(1 - p^2)^3}] \times (\beta/\epsilon)\sqrt{1 - p^2}(1/2g) = (1/\sqrt{\epsilon^3}) \times (1/\sqrt{1 - p^2})(\beta/g)[KC_L - (1/2)p/\sqrt{1 - p^2}]$$

with $p = \cos\gamma$ and $\sqrt{1 - p^2} = \sin\gamma$ one has

$$Ac - aC = (1/\sqrt{\epsilon^3})\,(1/\sin\gamma)\,(\beta/g) \times [KC_L - (1/2)\cot\gamma] = L_0$$

which may be introduced in Eq. (18) that now reads

$$L_0C\dddot{c} = -L_0[C\ddot{b} - c(\ddot{B} + \dddot{C})] + \{C(\dot{b} + 2\dot{c}) - c(\dot{B} + 2\dot{C})\}\{A(\dot{b} + \dot{c}) - a(\dot{B} + \dot{C})\} + (\dot{A}c - \dot{a}C)\{C(\dot{b} + \dot{c}) - c(\dot{B} + \dot{C})\} \tag{19}$$

Eq. (19) together with the conditional relations (4) and (5) constitute the solution of the problem. The independent p with three derivatives and the independent ϵ with two derivatives occur in the two equations. Three boundary conditions are therefore required for p and two for the ϵ curve. Because of the conditional relation (4), only four constants are needed for a given case. Both p and ϵ are evidently smooth and well-behaved functions of simple nature. The cosine of the angle γ evidently lies a little below unity, and the velocity parameter ϵ lies between certain fixed values. The fact that the functions are smooth and well behaved makes a step-by-step integration convenient and permits the use of large intervals or steps.

(4) Physical Significance of Parameters

Improper choice of initial conditions will lead to minimum curves of only mathematical interest. If, for instance, at any point h the values of p, $\dot{p}$, and ϵ lead to a value of C_L [Eq. (5)] which is greater than the maximum value of C_L of the particular airplane, the solution must be discarded as having no physical meaning. Similarly, if the quantity $\epsilon\dot{p}$ or the product of the quantities ϵ and $\dot{p}$ exceeds a certain value, then also the solution ceases to have a physical meaning. It is seen that, with $\epsilon = v^2$ and $\dot{p} = 1/R$ negative (with center of curvature above).

$$\epsilon\dot{p} = v^2/R \tag{20}$$

corresponds to an upward acceleration normal to the airplane

$$a_n = v^2/R$$

and to a corresponding downward mass force. If a_n exceeds the permissible structural limit, the answer must be discarded. Note the *negative* $\dot{p}$ corresponds to an upward acceleration, and that, therefore, a *negative* $\ddot{p}$ gives an increase in this acceleration along the path (equivalent to the pilot moving the stick rearward.)

Thus, in summary, it is noted that the variables at any point must not violate prescribed physical conditions in regard to aerodynamics, structures, and power plant limitations. These limitations do not appear in the mathematical formulation of the problems.

In regard to numerical values of the physical parameters, it is necessary that the drag polar be given at each Mach Number:

$$C_D = f(C_L)_{M = \text{constant}}$$

or, in general, $C_D = f(C_L, M)$

We need the quantities

$$\{\partial C_D/\partial C_L\}_{M = \text{constant}} \quad \text{and} \quad \{\partial C_D/\partial M\}_{C_L = \text{constant}}$$

Note that C_D is a function of C_L and M. Further, C_L, according to Eq. (5), depends on h and the variables p, $\dot{p}$ and ϵ, and M is a simple function of ϵ:

$$M = \sqrt{\epsilon}/c_s \tag{21}$$

The quantities $\partial C_D/\partial C_L$ and $\partial C_D/\partial M$ are obtainable from graphs of experimental results or from direct calculations. In either case, it is physically correct to use C_D in the following form:

$$C_D = C_{D_0} + KC_L^2 \tag{22}$$

It is important to note that C_{D_0} and K are functions of Mach Number only and do *not* depend on C_L. Plot both of these functions versus Mach Number to get the best possible agreement with the given data. For subsonic Mach Number, both C_{D_0} and K are reasonably constant with the latter value equal to

$$K = 1/(\pi A_R)$$

where A_R is the adjusted aspect ratio.

With the above relation, one has

$$\partial C_D/\partial C_L = 2KC_L \tag{23}$$

where K is function of M only, and

$$\partial C_D/\partial M = (dC_{D_0}/dM) + (dK/dM)C_L^2 \tag{24}$$

Note that the experimental coefficients are really represented by a combined quantity occurring in the term B, Eq. (11)—namely,

$$(\partial/\partial M)\ (C_T - C_D)_{C_L=\text{constant}}$$

and the other coefficient $\partial C_D/\partial C_L$, which occurs in the terms B, b, and c, is simply $2KC_L$ where K once and for all may be plotted as a function of M.

(5) Initial or Boundary Conditions

With this discussion of the physical parameters and their limitations, we shall proceed to consider the boundary conditions. It is immediately evident that the smoothest path will be obtained when the airplane is pointed generally in the "right" direction at the origin. For a very small value of H, the given height, the best answer is an almost straight line between the end points. For a large height, much thrust is used up on the acceleration, and the slope may point somewhere below the intended end point, depending on the mission.

As stated above, four initial conditions are required. The entire curve and the described mission will depend on this choice. Fortunately, it is quite a straightforward procedure to produce a coverage of all desired missions by systematically varying the initial conditions. It is further noted that it is quite possible to give the correct order of magnitude of the desired initial quantities. These are evidently tied up with the final altitude H and the maximum climb angle γ_m of the particular aircraft.

The initial climb angle must obviously be chosen far below the maximum value so as to permit considerable acceleration from the beginning. In fact, a value less than half of the maximum will yield normal missions. We shall, therefore, put

$$p_0 \cong \cos\ (\gamma_m/2)$$

where γ_m is the maximum climb angle. Note that this and the following treatments are only intended to give the order of magnitude of the initial quantities involved.

To obtain the initial value of $\dot{p}$, note that

$$\dot{p}_0 = -(1/R)$$

with $\dot{p}_0$ negative for inereasing climb angle (center of curvature above aircraft at origin). The radius of curvature evidently should be of such a value as to slowly increase the climb angle from, say, $(1/2)\gamma_m$ to γ_m in, say, half the total distance which is in the order of $(2H/\gamma_m)$. One, therefore, has the relation

$$R_0(\gamma_m/2) = (2H/\gamma_m) \quad \text{or} \quad R_0 = 4H/\gamma_m^2$$

We shall, therefore, choose

$$\dot{p}_0 = -(\gamma_m^2/4H)$$

as the appropriate order of magnitude. With p and $\dot{p}$ chosen, one may use the relation (5)

$$C_L = (\beta/\epsilon)\ [p - (\epsilon\dot{p}/g)]$$

to choose the value of ϵ which gives an acceptable value of C_L, or vice versa.

The fourth and final required value at the initial point is the $\ddot{p}_0$. Evidently, there is in most long distance nonacrobatic missions an inflexion point at some distance in the order of approximately half the final height. At this point, the value of $\dot{p} = 0$. This gives $\ddot{p}_0$ approximately

$$\ddot{p}_0 = -(2\dot{p}/H) = +(\gamma_m^2/2H^2) \tag{25}$$

(6) Calculation Procedure

With p_0, $\dot{p}_0$, and ϵ known, the value of $\dot{\epsilon}$ follows from Eq. (4), using for C_D the value of Eq. (22):

$$C_D = C_{D_0} + K\ C_L^2$$

The conditional relations (4) and (5) may be written in the summarized form:

$$\dot{\epsilon} = f(\epsilon, p, \dot{p}) \tag{26}$$

Hence, $\dot{\epsilon}$ is always fixed and known if ϵ, p, and $\dot{p}$ are given. Further, with $\ddot{p}$ given, $\ddot{\epsilon}$ is also obtainable from Eqs. (4) and (5). From these equations, it follows again

$$\ddot{\epsilon} = f(\epsilon, p, \dot{p}, \ddot{p}) \tag{27}$$

Hence, $\ddot{\epsilon}$ can be calculated when $\ddot{p}$ and the lower derivatives of p and ϵ are known. Derivation of Eq. (4) gives in fact:

$$\begin{aligned}(\partial C_T/\partial h) + (\partial C_T/\partial M)\ (dM/dh) - (\partial C_D/\partial C_L)\ \times \\ (dC_L/dh) - (\partial C_D/\partial M)\ (dM/dh) = [(\dot{\beta}/\epsilon) - (\beta\dot{\epsilon}/\epsilon^2)]\ \times \\ \sqrt{1-p^2}\ [1 + (\dot{\epsilon}/2g)] - (\beta/\epsilon)\ (1/\sqrt{1-p^2})\ \times \\ p\dot{p}[1 + (\dot{\epsilon}/2g)] + (\beta/\epsilon)\ \sqrt{1-p^2}(\ddot{\epsilon}/2g)\end{aligned} \tag{28}$$

with $dM/dh = (1/2\sqrt{\epsilon})\ (\dot{\epsilon}/c_s) - (\sqrt{\epsilon}\dot{c}_s/c_s^2)$

$\partial C_D/\partial M = (dC_{D_0}/dM) + (dK/dM)C_L^2$

and $$C_L = (\beta/\epsilon)[p - (\epsilon\dot{p}/g)]$$

the value of $\ddot{\epsilon}$ is determined.

Finally, the remaining quantity $\dddot{p}$ is calculated to comply with the Euler-Lagrange equation. With p, ϵ, and the derivatives of p given at a certain point h, we may then proceed to the next point $h + dh$ and obtain p, $\dot{p}$, $\ddot{p}$, and ϵ. The conditional equations then supply $\dot{\epsilon}$ and $\ddot{\epsilon}$. We may again calculate $\dddot{p}$ as for the origin. Thus, the entire curve is obtained step by step.* Because of the smoothness of the p curve, rather large steps are permissible. To repeat, with

$$\begin{aligned} p &= p_0 + \dot{p}_0 h \\ \dot{p} &= \dot{p}_0 + \ddot{p}_0 h \\ \ddot{p} &= \ddot{p}_0 + \dddot{p}_0 h \\ \epsilon &= \epsilon_0 + \dot{\epsilon}_0 h + [(1/2)\ddot{\epsilon}_0 h^2 + \dots] \end{aligned}$$

the Taylor expansion is used to determine ϵ, p, and the derivatives of p at each step. Then, by conditional relations (26) and (27),

$$\dot{\epsilon} = f_1(p, \dot{p}, \epsilon) \text{ and } \ddot{\epsilon} = f_2(p, \dot{p}, \ddot{p}, \epsilon)$$

With all six quantities thus determined, we may solve for $\dddot{p}$. Let us next survey the required performance coefficients. The drag polars are presumably available for several Mach Numbers within the range. For each Mach Number, determine the best value of K in the equation:

$$C_D = C_{D_0} + K\,C_L^2$$

where C_{D_0} is the drag coefficient at zero lift. The value of K is, theoretically,

$$K = S/(4\,Q)$$

where S is, as before, the surface of the lifting area, and Q is the cross section of the air mass deflected downward by the wing. For subsonic flow, the latter is a circle of diameter equal to the span of the wing L. Therefore, for subsonic flow

$$K = (1/4)\,[L\bar{c}/(\pi/4)L^2] = 1/(\pi A_R)$$

where A_R is the effective aspect ratio $L/\bar{c}$ and $\bar{c}$ is the mean chord. For supersonic flow $K \simeq (\sqrt{M^2 - 1})/4$, for Mach Numbers $\gg 1$ or approximately $= M/4$.

If the curves are available experimentally, it is desirable to obtain the best value of K from such data. Both C_{D_0} and K are, theoretically, functions of Mach Number only. Plot $C_{D_0}(M)$ and $K(M)$. Next, plot the experimental values of the thrust coefficient.

$$C_T = C_T\,(M, h)$$

The value of C_T is adjusted by the automatic controls as a function of the ambient temperature to maintain the turbine maximum temperature at a permissible level. Plot C_T (M) for several values of h (or standard temperature). Note, in considering the derivatives of C_T and C_D, that these are given as functions of M and the latter also as function of C_L while C_L, in turn, is a function of M and p, and M is a function of ϵ (and h), Eq. (21).

The six coefficients of the Euler-Lagrange equations may be written with the experimental derivatives as:

$$A = -(1/2)\,(1/\sqrt{\epsilon^3})\,(1/\sqrt{1 - p^2})$$

$$B = \{(\partial C_T/\partial M) - (\partial C_{D_0}/\partial M) - (\partial K/\partial M)C_L^2\} \times (1/2\sqrt{\epsilon}c_s) + (\beta/\epsilon^2)\{2KC_Lp + \sqrt{1 - p^2}\,[1 + (\dot{\epsilon}/2g)]\}$$

$$C = (\beta/\epsilon)\sqrt{1 - p^2}\,(1/2g)$$

$$a = p/\sqrt{\epsilon}\sqrt{(1 - p^2)^3}$$

$$b = -(\beta/\epsilon)\,\{2KC_L - [p/\sqrt{1 - p^2}]\,[1 + (\dot{\epsilon}/2g)]\}$$

$$c = -(2\beta KC_L/g)$$

We may also give:

$$\dot{C} = [(\dot{\beta}/\epsilon) - (\beta\dot{\epsilon}/\epsilon^2)]\sqrt{1 - p^2}\,(1/2g) - (\beta/\epsilon)\,(1/\sqrt{1 - p^2})\,(p\dot{p}/2g)$$

$$\dot{c} = -(2\dot{\beta}/g)KC_L - (2\beta/g)\,(dK/dM)C_L\dot{M} - (2\beta K\dot{C}_L/g)$$

where $C_L = \beta[(p/\epsilon) - (\dot{p}/g)]$ and $M = \sqrt{\epsilon}/c_s$

(7) Discussion of Numerical Procedure

With the number of derivatives involved, it is of some interest to clarify the necessary numerical procedure. First, it is noted that four quantities uniquely determine the situation at each point. These may be chosen to be p, $\dot{p}$, $\ddot{p}$, and ϵ.

When and if desired, the higher derivatives of ϵ are then obtained by the conditional relation (4) with Eqs. (5) and (22).

$$\dot{\epsilon} = f(p, \dot{p}, \epsilon) = (2g\epsilon/\beta\sqrt{1 - p^2}) \times \{C_T - C_{D_0} - K\beta^2[(p/\epsilon) - (\dot{p}/g)]^2\} - 2g$$

$$\ddot{\epsilon} = f(p, \dot{p}, \ddot{p}, \epsilon)$$

We may now solve for the quantity $\dddot{p}$ resulting from the restriction to an optimum path.

In order to proceed to the next step, we must again obtain the four quantities p, $\dot{p}$, $\ddot{p}$, and ϵ. No relation exists among these quantities, and they must, therefore, be obtained directly by Taylor expansions. Since $\dddot{p}$ at the previous point must necessarily be known, we obtain readily the new values of p and its first and second derivative. To get the new value of ϵ, it is seen that we must know $\dot{\epsilon}$ at the preceding point. This is necessary and in all cases sufficient. This is because any derivative of ϵ can be obtained directly from the four basic parameters p, $\dot{p}$, $\ddot{p}$, and ϵ. Hence, four—and only four—Taylor expansions are required.

We may now make a few remarks about the numerical procedure. Eq. (17) may be written in the form

* The calculation procedure is actually an individual matter. Once Eq. (17) or (18), with the conditions (4), (5), and (22), have been programed on the electronic computer, experience is gained as to the choice of the initial parameters and their effect in bracketing the end condition.

$$F + (d/dh)f = 0$$

$$2F\Delta h = -f(\epsilon + \dot{\epsilon}\Delta h)\dot{\epsilon}_{\Delta h}(p + \dot{p}\Delta h) \times (\dot{p} + \ddot{p}\Delta h)\,(\ddot{p} + \dddot{p}\Delta h) + f(\epsilon - \dot{\epsilon}\Delta h)\dot{\epsilon}_{-\Delta h}(p - \dot{p}\Delta h) \times (\dot{p} - \ddot{p}\Delta h)\,(\ddot{p} - \dddot{p}\Delta h)$$

or, in a simpler form,

$$F\Delta h = -f(\epsilon + \dot{\epsilon}\Delta h)\dot{\epsilon}_{\Delta h}(p + \dot{p}\Delta h) \times (\dot{p} + \ddot{p}\Delta h)\ddot{p}_{\Delta h} + f(\epsilon, \dot{\epsilon}, p, \dot{p}, \ddot{p})$$

Briefly, with ϵ, p and $\dot{p}$ in Taylor expansion $\dot{\epsilon}$ is obtained from these, and $\ddot{p}$ at Δh is then calculated directly by the last formula. The next step is again to obtain ϵ, p, and $\dot{p}$ which is simple since $\dot{\epsilon}$ and $\ddot{p}$ are known at the first point. Thus, everything repeats as before: $\dot{\epsilon}$ is obtained by the conditional relation and $\ddot{p}$ is again calculated. Note that this amounts to determining the change in the curvature of the path.

Eq. (18) or (19) is mathematically in a cleaner form. However, $\ddot{p}$ and $\ddot{\epsilon}$ appear as a result of performing the differentiation. The quantities p, $\dot{p}$, $\ddot{p}$, and ϵ again fix the condition and must be obtained by Taylor expansions, $\dot{\epsilon}$ and $\ddot{\epsilon}$ are obtained directly from the conditional relation, and $\ddot{p}$ is then calculated from the main formulas (18) or (19). It is, therefore, noted that the first procedure given above involves lower derivatives and employs a simpler formulation.

Acknowledgment and Comment

The author wishes to acknowledge the excellent cooperation of Dr. Mary Payne, S. Pines, and Dr. G. Nomicos in programing the equations on the Republic Aviation Corporation 704 Electronic Computer and in acquiring the considerable experience required in selecting and bracketing the initial variables so as to obtain specific cases of interest.

Large potential gains are indicated. In one example: A climb to 50,000 ft. shows a saving of about 30 per cent in the time required for the ideal path as compared with the time for a constant Mach climb to the same height. The technique is particularly useful to show the proper maneuvers to obtain the maximum altitude for a given airplane. It is significant that the optimum path is characterized by a much smaller climb angle through the first segment of the path and by a corresponding steeper climb near the end. Note that the results are exact, the accuracy being only dependent on the accuracy of the characteristic parameters of the airplane.

A New Reprint

Journal of the Aeronautical Sciences

Now entitled Journal of the Aero/Space Sciences

Available September 1959

Volumes 1–5, 1934–1937/1938, paper bound set	$140.00
Volumes 1–2, 1934–1935, single volumes, paper bound	20.00
Volumes 3–5, 1935/1936–1937/1938, single volumes, paper bound	35.00

In Preparation

Volumes 6–8, 1938/1939–1940/1941

(Reproduced with the permission of the original publisher, Institute of the Aeronautical Sciences, Inc.)

Please address orders and inquiries to:

Johnson Reprint Corporation
111 Fifth Avenue, New York 3, N.Y.

Change of Address

Since the Post Office Department does not as a rule forward magazines to forwarding addresses, it is important that the Institute be notified of changes in address 30 days in advance of publishing date to ensure receipt of every issue of the JOURNAL and AERO/SPACE ENGINEERING.

Notices should be printed legibly and sent directly to:

Subscription Department
Institute of the Aeronautical Sciences, Inc.
2 East 64th Street, New York 21, N.Y.

Spherical Cap Snapping†

HERBERT B. KELLER* AND EDWARD L. REISS*
New York University

Summary

A nonlinear boundary value problem for the determination of the rotationally symmetric deformations of a clamped spherical cap under external pressure is solved by finite differences. The numerical solutions are obtained by employing a previously developed iteration procedure. A special case of the difference equations is solved explicitly and yields a justification of the iteration method as well as insight into the properties of the more accurate numerical solutions.

Buckled and unbuckled equilibrium states are obtained and the shape of the pressure-deflection curve which is usually assumed for these states is verified for a large class of caps. Close estimates are given for the upper and lower buckling loads and an intermediate buckling load—i.e., the "dead-weight" load. The stresses and deflections in the buckled and unbuckled states are examined and compared with an asymptotic solution valid in the interior of very thin shells. Boundary layers are found to develop in the buckled states both as the loading increases and as the thickness of the shell decreases.

(1) Introduction

IT IS CUSTOMARY to assume, as proposed by von Kármán and Tsien,[1] that the curve of pressure versus maximum deflection for the rotationally symmetric deformations of a spherical cap subject to external pressure is similar‡ to that of Fig. 1. The implications of such a non-monotone pressure-deflection curve are that there exist *three possible states of equilibrium* for each pressure in the range $p_L < p < p_U$ and *only one equilibrium state* for each pressure outside this interval. The points on the branch UO of the curve correspond to unbuckled states, those on the branch LN to buckled states, and those on the segment UL to "unstable" states. If the characteristic of Fig. 1 is correct the cap must buckle at some pressure in the interval $p_L \leq p \leq p_U$ and hence we call p_L and p_U, respectively, the lower and upper buckling loads.

It may be conjectured, following Friedrichs,[2] that there is an intermediate buckling load, p_M, in the range $p_L < p_M < p_U$, for which the corresponding buckled and unbuckled states have equal potential energies. For all loads in the interval $p_L \leq p < p_M$ the unbuckled states have *less* energy than the corresponding buckled states and conversely for $p_M < p \leq p_U$. Then it may be concluded that, as a result of some random disturbance, it is possible for the cap to "snap" from unbuckled equilibrium states with $p_M < p \leq p_U$ to buckled states which have less energy.†† If this is the true mechanism of buckling the buckling load must lie in the interval $p_M < p \leq p_U$ and is probably close to p_M.

The rotationally symmetric equilibrium states of the cap may be defined in terms of two functions which render stationary an energy integral. Equivalently, they may be defined in terms of the solutions of a boundary value problem for two coupled nonlinear ordinary differential equations containing two parameters. A theoretical verification of the assumed pressure-deflection curve of Fig. 1 should follow from a knowledge of the uniqueness (or, more properly, nonuniqueness‡‡) properties of the solutions of such problems. To our knowledge, a direct theoretical study of these properties has not been made.

The first investigation[1] into the nonlinear buckling of shallow spherical caps applied the Rayleigh-Ritz procedure to an inaccurate energy formulation of the problem. Estimates of p_L were obtained and curves similar to that of Fig. 1 resulted from the particular choice of trial functions used. Modifying an improved energy formulation due to Friedrichs,[2] Tsien[3] again used a Rayleigh-Ritz procedure but the resulting pressure-deflection curves were only double-valued. However, it is not clear that Friedrichs' formulation, as modified by Tsien, is applicable to clamped caps.**

Other investigations have been concerned with determining p_U and the stresses and deflections in the unbuckled states. In such studies approximate solutions of the boundary value problem have been sought by applying perturbation methods,[4, 5] power series calculations,[6, 7, 8] and linearizations.[9] Of these the power series method seems to have been most successful and indeed with it some buckled states have been obtained[6] for loads near p_U. In similar but less consistent calculations[8] other results are reported for extremely shallow caps—i.e., close to circular plates which do not buckle.

In this paper we present a new method for solving the equilibrium problem for a clamped shallow spherical cap. The method consists in solving, by iterations, a finite difference approximation of the boundary value

Received December 19, 1958.

† This research was supported in whole or in part by the United States Air Force under Contract No. AF 49(638)-161 monitored by the Air Force Office of Scientific Research of the Air Research and Development Command. Reproduction in whole or in part is permitted for any purpose of the United States Government.

* Scientist, Institute of Mathematical Sciences.

‡ Provided the cap is sufficiently curved to permit buckling.

†† A physical interpretation of Friedrichs' conjecture, as applied to a variety of buckling problems, is essentially given by Tsien.[3] His "dead-weight" load is analogous to p_M.

‡‡ The previous discussion suggests that for some ranges of the parameters the solutions are unique while for other ranges there are at least three solutions.

** References 1–3 are mainly concerned with the related problem of buckling of complete spherical shells. The comments above apply only to the sections of these papers which consider, or seem directly applicable to, the spherical cap or segment.

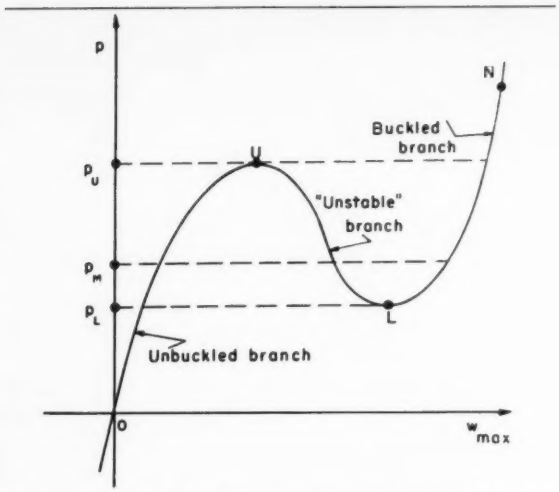

FIG. 1. Assumed form of pressure-deflection characteristic for a shallow spherical cap which can buckle.

problem. This procedure has previously been applied with considerable success to the related nonlinear problems of bending and buckling of thin circular plates.[10, 11] The iterates are most conveniently evaluated by high-speed digital computers. The present study is confined to caps which deform in the "first mode" (see references 6 and 9 and Section 7).

For caps subjected to external pressure loads the finite difference method does, in fact, yield solutions which correspond to the buckled and unbuckled branches of Fig. 1. Thus nonunique solutions are obtained for all loads in $p_L < p < p_U$ and unique solutions are obtained for essentially all loads outside of this interval. In contrast, the power-series solutions correspond only to unbuckled states and, for a small range of shell geometries, to buckled states for loads near p_U. The upper buckling load is more accurately determined by the present method than by the power-series method. In addition, equally precise values of p_L and p_M, which were unobtainable by power series, are calculated.

A special case of the difference method can be solved explicitly. This furnishes a simple model which has all of the known qualitative features of the buckling phenomena. The model suggests procedures for the proper application of the iteration scheme and yields a heuristic justification of it. Solutions corresponding to the "unstable" branch of Fig. 1 can also be obtained for this model.

For caps subjected to internal pressure (i.e., $p < 0$) there is no buckling and the application of the present method is found to be simpler than when $p > 0$. However, these results will not be discussed in this paper.

(2) Formulation of the Boundary Value Problem

Let the cap be that portion of a spherical shell of radius R and thickness $2h$ which subtends an angle 2Λ at the center of the sphere. The equilibrium equations for rotationally symmetric deformations of such a shell which is thin (i.e., $h/\Lambda R \ll 1$) and shallow (i.e., $\Lambda \ll 1$) have been derived from a nonlinear elasticity theory with small strains and finite but small deflections.[6] In dimensionless variables these equations become

$$L\,\gamma(x) = \rho[x^2 - \alpha^2(x)] \tag{1a}$$

$$L\,\alpha(x) = \rho[\alpha(x)\,\gamma(x) + Px^2] \tag{1b}$$

where the differential operator L is defined by

$$L\,f(x) \equiv x(d/dx)\{(1/x)(d/dx)[xf(x)]\} \tag{2}$$

and the dimensionless quantities are

$$\left.\begin{aligned} x \equiv \theta/\Lambda, \quad \alpha(x) &\equiv (1/\Lambda)[\theta + (1/R)(dw/d\theta)], \\ W(x) \equiv w(\theta)/\rho hC, \quad P &\equiv (R/h)^2(p/2EC), \\ \rho \equiv (\Lambda^2/C)(R/h), \quad C^2 &\equiv 2/3(1-\nu^2) \end{aligned}\right\} \tag{3}$$

Here θ is the polar angle of the cap, $\Lambda\alpha$ is the slope with respect to the horizontal of the tangent plane to the deformed surface, w is the normal displacement of the middle surface of the cap from its unstrained position (positive inward), p is the uniform external pressure (positive inward), E is Young's modulus, and ν is Poisson's ratio. $\gamma(x)$ is a stress function defined such that the longitudinal and circumferential membrane stresses, σ_θ and σ_ϕ, respectively, and the corresponding dimensionless stresses, Σ_θ and Σ_ϕ, are given by

$$\Sigma_\theta(x) \equiv (R/h)[2\sigma_\theta(\theta)/EC] = \gamma(x)/x \tag{4a}$$

$$\Sigma_\phi(x) \equiv (R/h)[2\sigma_\phi(\theta)/EC] = d\gamma(x)/dx \tag{4b}$$

The longitudinal and circumferential bending stresses on the inner surface, σ_θ^B and σ_ϕ^B, and the corresponding dimensionless stresses Σ_θ^B and Σ_ϕ^B, are given in terms of the reduced slope α by

$$\Sigma_\theta^B(x) \equiv (R/h)[2\sigma_\theta^B(\theta)/3EC^2] = 1 + \nu - \{[d\alpha(x)/dx] + \nu[\alpha(x)/x]\}, \tag{5a}$$

$$\Sigma_\phi^B(x) \equiv (R/h)[2\sigma_\phi^B(\theta)/3EC^2] = 1 + \nu - \{\nu[d\alpha(x)/dx] + [\alpha(x)/x]\} \tag{5b}$$

If e is the potential energy of the shell and $\mathcal{E}$ a dimensionless potential energy, it can be shown that

$$\mathcal{E} \equiv e/[(\pi/2)EC^2\Lambda^2h^3] = \int_0^1 [\Sigma_\theta^2 + \Sigma_\phi^2 - 2\nu\Sigma_\theta\Sigma_\phi + 2(d\alpha/dx)^2 + 2(\alpha/x)^2 + 4P\rho x\alpha]\,x\,dx - P\rho - 2 \tag{6}$$

At the center of the cap, $x = 0$, the assumption of rotationally symmetric deformations implies that

$$\alpha(0) = \gamma(0) = 0 \tag{7a}$$

The edge is held fixed and clamped and thus, at $x = 1$,

$$\alpha(1) = 1, \quad [d\gamma(1)/dx] - \nu\gamma(1) = 0 \tag{7b}$$

Eqs. (1) subject to the boundary conditions (7) complete the formulation of the equilibrium problem for the shallow spherical shell. In the absence of any theoretical knowledge of the existence, uniqueness, or properties of the solutions of this problem we seek numerical solutions. Of interest are the upper and lower

buckling loads P_U and P_L, the conjectured "intermediate buckling load," P_M, and a description of the stresses and deflections throughout the shell.

(3) Formulation of Difference Equations and Iteration Procedure

To obtain numerical solutions we replace Eqs. (1) and (7) by approximating difference equations and solve the resulting nonlinear algebraic system by iterations. For this purpose the range of the dimensionless polar angle, $0 \leq x \leq 1$, is divided into J equal intervals by the net points

$$x_j = j\Delta x, \quad j = 0, 1, \ldots, J; \quad \Delta x \equiv 1/J \tag{8}$$

At each point of this net the functions $\alpha(x_j)$ and $\gamma(x_j)$ are assumed to be approximated by corresponding quantities $\bar{\alpha}(x_j)$ and $\bar{\gamma}(x_j)$ which satisfy the finite difference equations

$$L_\Delta \bar{\gamma}(x_j) = \rho[x_j^2 - \bar{\alpha}^2(x_j)] \tag{9a}$$

$$L_\Delta \bar{\alpha}(x_j) = \rho[\bar{\alpha}(x_j)\bar{\gamma}(x_j) + Px_j^2], \quad 1 \leq j \leq J-1 \tag{9b}$$

Here the difference operator, L_Δ, obtained by replacing derivatives in the differential operator (2) by centered difference quotients, is defined by

$$L_\Delta f(x_j) \equiv [x_j/(\Delta x)^2]\{\{1/[x_j + (1/2)\Delta x]\} \times [x_{j+1}f(x_{j+1}) - x_j f(x_j)] - \{1/[x_j - (1/2)\Delta x]\} \times [x_j f(x_j) - x_{j-1}f(x_{j-1})]\} \tag{10}$$

Thus, the difference equations (9) are approximations to the differential equations (1). At the end points, $j = 0$ and $j = J$, the approximating quantities are to satisfy the difference equivalents of the boundary conditions (7):

$$\bar{\alpha}(x_0) = \bar{\gamma}(x_0) = 0 \tag{11a}$$

$$\bar{\alpha}(x_J) = 1, \quad \bar{\gamma}(x_J) = [(1 + \nu\Delta x/2)/(1 - \nu\Delta x/2)]\bar{\gamma}(x_{J-1}) \tag{11b}$$

Eqs. (9) and (11) form a system of $2(J + 1)$ nonlinear algebraic equations in the $2(J + 1)$ unknowns $[\bar{\alpha}(x_j), \bar{\gamma}(x_j)]$. For a sufficiently small net spacing, Δx, we expect some solution of this algebraic problem to yield a "close" approximation to a solution $[\alpha(x), \gamma(x)]$ of Eqs. (1) and (7). In general the algebraic system has many solutions, the number depending upon the "degree" of the system. However, most of these solutions, no doubt, involve complex roots and hence are spurious. It is the real solutions which we seek and, as shown in Section (4), there may be more than one of them. The question of the number of real roots of Eqs. (9) and (11) is important and is discussed further in Sections (4) and (7).

Since the nonlinear algebraic system cannot, in general, be solved explicitly we seek approximate solutions by means of an iteration procedure. Starting from some initial estimate, $[\bar{\alpha}_0(x_j), \bar{\gamma}_0(x_j)]$, of the solution for fixed values of P and ρ, we define a sequence of iterates, $[\bar{\alpha}_n(x_j), \bar{\gamma}_n(x_j)]$, by the recursions

$$L_\Delta \bar{\gamma}_{n+1}(x_j) = \rho[x_j^2 - \bar{\alpha}_n^2(x_j)] \tag{12a}$$

$$L_\Delta \bar{\alpha}^*_{n+1}(x_j) = \rho[\bar{\alpha}_n(x_j)\bar{\gamma}_{n+1}(x_j) + Px_j^2] \tag{12b}$$

$$\bar{\alpha}_{n+1}(x_j) = \lambda\bar{\alpha}^*_{n+1}(x_j) + (1 - \lambda)\bar{\alpha}_n(x_j) \tag{12c}$$

Each of the iterates must also satisfy the boundary conditions (11). The above system then reduces to $3(J - 1)$ equations in the $3(J - 1)$ unknowns $[\bar{\gamma}_{n+1}(x_j), \bar{\alpha}^*_{n+1}(x_j), \bar{\alpha}_{n+1}(x_j)]$, $1 \leq j \leq J - 1$. However, for each n, Eqs. (12a) form a *linear* system which can be solved explicitly† for the $\bar{\gamma}_{n+1}(x_j)$. Using these quantities, the same is then true of the system (12b) which can be solved for the $\bar{\alpha}^*_{n+1}(x_j)$. Finally Eq. (12c) can be evaluated to yield the quantities $\bar{\alpha}_{n+1}(x_j)$.

The number λ, which is called the "relaxation parameter" in analogy with iterative solutions of linear systems, must be determined such that the iterations (12) converge to a solution. We assume that this can be done for all loads P applied to some wide range, $0 < \rho < 20$, of shells. An indication of the plausibility of this conjecture is given in Section (4) and in the successful computations reported in Section (6). A more thorough investigation of the convergence of the iteration scheme (12) when applied to the related problem of the bending of thin circular plates is presented in references 10 and 11 (where the relaxation parameter, λ, is denoted by θ).

(4) The Three Point Model

The difference equations for a net with $J = 2$ can be solved explicitly. This special case furnishes a model from which a qualitative description of the buckling phenomena and a heuristic justification of the convergence of the iterations can be obtained. It must be emphasized that this simple model may yield correct orders of magnitude but not quantitatively accurate results.

On this net with only three points the difference equations (9) and (11) involve six unknowns: $[\bar{\alpha}(x_j), \bar{\gamma}(x_j)]$, $j = 0, 1, 2$. Three of these unknowns are prescribed by the boundary conditions (11). Then eliminating $\bar{\gamma}(x_1)$, and $\bar{\gamma}(x_2)$ we obtain, for the single unknown $\bar{\alpha}(x_1) = \alpha$, the equation

$$f(\alpha, \rho) \equiv \alpha^3 - B(\rho)\,\alpha = K(P, \rho) \tag{13}$$

Here we have introduced the coefficients

$$B(\rho) \equiv (1/4) - (a^2/\rho^2), \quad K(P, \rho) \equiv [1 - (3/32)P\rho](a^2/2\rho^2) \tag{14}$$

where

$$a^2 \equiv (128/9)[(1 - \nu/2)/(1 - \nu/4)] > 0$$

Since Eq. (13) is a cubic equation it can be solved explicitly by standard algebraic procedures.

However, it is convenient to view the solutions of

† The coefficient matrix of this system is nonsingular and of tridiagonal or Jacobi form. Hence, it can be factored into the product of two upper and lower triangular matrices, each having nonzero elements only on the diagonal and adjacent to it. The system is then solved by evaluating two two-term recursions.

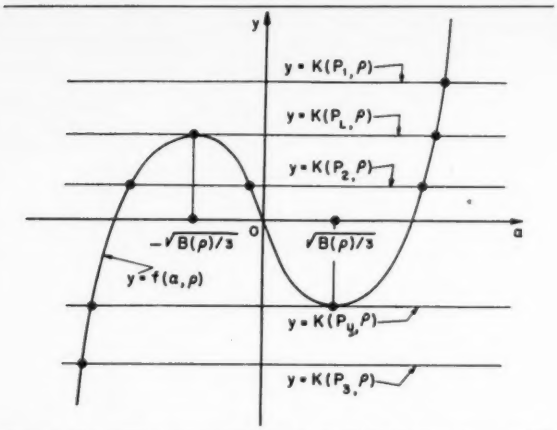

FIG. 2. Schematic representation of solutions in the three point model when $\rho > \rho_0$.

Eq. (13) for fixed P and ρ, as the abscissas of the intersections in the (α, y) plane of the curve $y = f(\alpha, \rho)$ with the horizontal line $y = K(P, \rho)$ (see Fig. 2). It then follows, from Eq. (14), that for each ρ in $0 < \rho < \rho_0 \equiv 2a$, $B(\rho) < 0$ and hence Eq. (13) has one and only one real solution for every P. Since a necessary condition for buckling is that there exist at least two real solutions—i.e., equilibrium states—for some load it can be concluded that no spherical cap with $0 \leq \rho < \rho_0$ can buckle (for the three point model). Similarly, it can be shown that for each $\rho > \rho_0$ there is an interval of P values for which Eq. (13) has three real solutions. For loads outside this interval there is only one real solution. The least (greatest) value of P for which three real solutions exist is the lower (upper) buckling load; these values are, for $\rho > \rho_0$,

$$\left.\begin{matrix} P_L(\rho) \\ P_U(\rho) \end{matrix}\right\} = (32/3\rho) \mp (16\rho/3^{5/2}a^2)[1 - (\rho_0^2/\rho^2)]^{3/2} \quad (15)$$

Graphs of these buckling loads and the accurate values determined from a 50 point net [see Sections (5) and (6)] are shown in Fig. 3.

It can be shown that the iteration scheme (12) applied to the present case, $J = 2$, is equivalent to solving Eq. (13) by

$$\alpha_{n+1} = \alpha_n - \lambda(\rho^2/a^2)[f(\alpha_n, \rho) - K(P, \rho)] \quad (16)$$

If α is a root of Eq. (13) it satisfies Eq. (16) and thus the error in each iterate,

$$\epsilon_n \equiv \alpha - \alpha_n$$

must satisfy

$$\epsilon_{n+1} = \epsilon_n - \lambda(\rho^2/a^2)[f(\alpha, \rho) - f(\alpha_n, \rho)] \quad (17)$$

By standard procedures[12] a necessary condition for convergence of the iterates is found to be

$$\left|1 - \lambda(\rho^2/a^2)[\partial f(\alpha, \rho)/\partial\alpha]\right| < 1 \quad (18)$$

Thus λ must be confined to the intervals

$$0 < \lambda < 2a^2/\rho^2(\partial f/\partial\alpha), \quad \text{if} \quad \partial f/\partial\alpha > 0$$

$$2a^2/\rho^2(\partial f/\partial\alpha) < \lambda < 0, \quad \text{if} \quad \partial f/\partial\alpha < 0$$

If, in addition, the initial error, ϵ_0, is sufficiently small it follows from Eq. (17) that

$$\epsilon_n \approx \{1 - \lambda(\rho^2/a^2)[\partial f(\alpha, \rho)/\partial\alpha]\}^n \epsilon_0 \quad (19)$$

and hence by Eq. (18) the error decays geometrically. In the absence of precise knowledge of the error for any iterate the best value of λ is that value, λ_{op}, for which the left side of Eq. (18) vanishes:

$$\lambda_{op} = a^2/\{\rho^2[\partial f(\alpha, \rho)/\partial\alpha]\} \quad (20)$$

Schematic graphs of λ_{op} versus P for $\rho > \rho_0$ and $\rho < \rho_0$ are shown in Fig. 4. Note that when "buckling" may occur (i.e., $\rho > \rho_0$) λ_{op} is triple-valued for all P in $P_L < P < P_U$.

The previous convergence analysis is valid only if the initial iterate, α_0, and, consequently, all subsequent iterates are close to the desired root. This is, in fact, a general requirement of all iterative root finding techniques.[12] Thus, if a particular root is known, a neighboring root may be obtained by the iteration method. In this manner, starting from the known unbuckled solution $\bar{\alpha}(x_1) = x_1(=1/2)$ for $P = 0$, a sequence of roots on the unbuckled branch can be obtained for an increasing sequence of loads; say (see Fig. 2)

$$P_1 < P_L < P_2 < P_U$$

It is clear that there is no difficulty near $P = P_L$ on the unbuckled branch. However, at $P = P_U$ there is a double root and the iteration scheme fails [since $\partial f/\partial\alpha = 0$ and Eq. (18) cannot be satisfied]. Thus, the unbuckled solution *at* the upper buckling load cannot be obtained, but roots very close to it can.

For a pressure $P = P_3 > P_U$ there is only one root (a buckled state) and it is not close to any unbuckled solution. However, if the initial iterate, α_0, is an unbuckled solution then $\epsilon_0 < 0$ and $f(\alpha, \rho) - f(\alpha_0, \rho) < 0$ (see Fig. 2). From Eq. (17), with $\lambda > 0$ as shown in

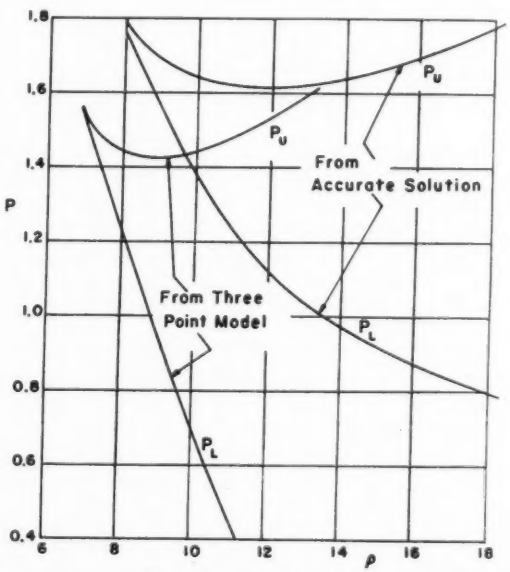

FIG. 3. Upper and lower buckling loads determined from the three point model and from the accurate solutions.

Fig. 4, this implies $\epsilon_1 > \epsilon_0$ and, if the error has not changed sign, it has decreased in magnitude. Thus, in any event, the first iterate changes in the direction of the root and all that is required for convergence is that one of the first "few" iterates fall close to the root (in which case the previous analysis becomes valid). Thus it is possible for the iterations to converge, or "jump," to a buckled solution even though the initial iterate is an unbuckled solution.

After one root on the buckled branch is obtained all other roots on this branch (not too close to the double root at $P = P_L$) can be determined. In an analogous manner solutions on the unstable branch can be obtained; here, however, negative values of λ_{op} must be used (see Fig. 4).

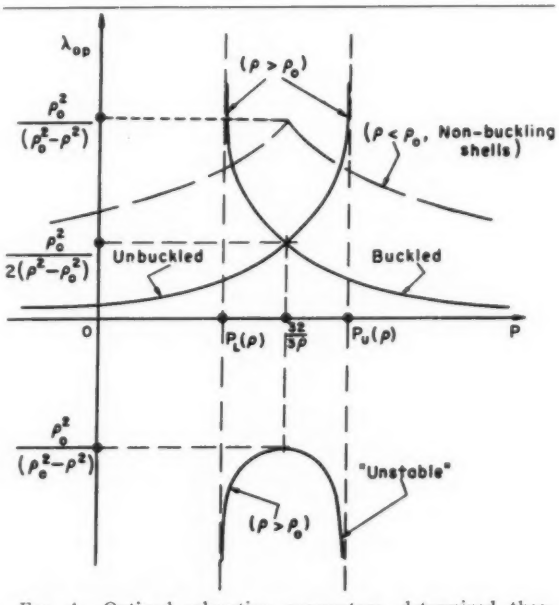

FIG. 4. Optimal relaxation parameters, determined theoretically, for the three point model (representative values of ρ).

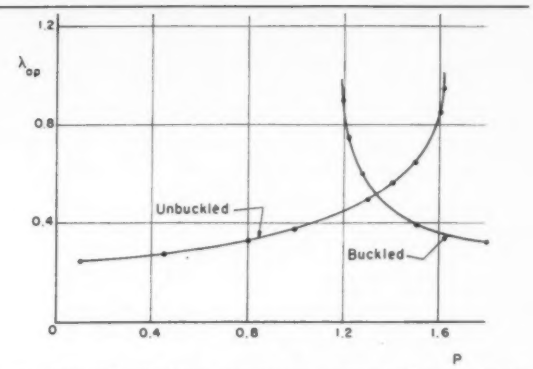

FIG. 5. Optimal relaxation parameters, determined numerically, for a 50 point net ($\rho = 11.31$).

(5) Computational Techniques

A solution of the difference equations (9) and (11) can be an accurate approximation to a solution of Eqs. (1) and (7) only if the net spacing, Δx, is "sufficiently small." An acceptable value of $\Delta x = 1/J$ is determined by comparing the solutions of a series of test calculations in which P and ρ are fixed and the net is then successively refined, say $J = 10, 25, 50, 200$. The solutions obtained with the 50 and 200 point nets are in good agreement for all P except those in the immediate neighborhood of the buckling loads. There they are found to differ by, at most, 5 per cent. As this is not considered too significant an error the 50 point net was used throughout the computations. Moreover, most of the unbuckled solutions for the 25 point net agree with those for the finer nets.

In applying the iteration scheme (12) to solve the difference equations, procedures are required to determine when the iterations have converged, to determine an initial iterate, and to select an optimal value of λ. As a numerical criterion for convergence we require

$$\delta_n \equiv \max_{0 \le j \le J} \left\{ \left| \bar{\alpha}_n(x_j) - \bar{\alpha}_{n-1}(x_j) \right|, \left| \bar{\gamma}_n(x_j) - \bar{\gamma}_{n-1}(x_j) \right| \right\} < 10^{-6} \quad (21)$$

It should be noted that $\lim_{n \to \infty} \delta_n = 0$ is only a necessary condition for convergence. Test calculations were made with 10^{-6} replaced by 10^{-5} and 10^{-8} in this condition. No significant change in the solutions was observed.

As implied by Eq. (19), and verified by calculations, the number of iterations required to satisfy Eq. (21) varies sharply as λ is changed. The optimal value, λ_{op}, for fixed P and ρ is that value which minimizes the number of iterations. For the model discussed in Section (4) it was possible to obtain this quantity explicitly [see Eq. (20)]. However, to determine λ_{op} for the finer nets we resort to a series of test calculations. Graphs of $\lambda_{op}(P)$ for various values of ρ are obtained from these tests and they are found to be qualitatively similar to those branches of Fig. 4 on which $\lambda > 0$. In Fig. 5 a graph of the computed values of $\lambda_{op}(P)$ is given for a shell with $\rho = 11.31$. It is found, similar to the behavior implied by Fig. 4, that $\lambda_{op}(P)$ generally decreases as ρ increases.

The initial iterate should be as close an approximation to the solution as possible. In analogy with the three point model, we use, for any P and a fixed value of ρ, the "solution" for a neighboring value of P. In detail we proceed as follows for any fixed value of ρ: For P near zero (the shell is then only slightly deformed from the spherical shell) we take

$$\bar{\alpha}_0(x_j;\, \rho,\, P) = \bar{\alpha}(x_j;\, \rho,\, 0) \equiv x_j$$

and iterate until Eq. (21) is satisfied. Having the solution for any load P, the initial iterate for a load $P + \delta P$ is taken as

$$\bar{\alpha}_0(x_j;\, \rho,\, P + \delta P) = \bar{\alpha}(x_j;\, \rho,\, P)$$

and the iterations, employing a previously determined value of $\lambda_{op}(P + \delta P)$, are performed. It is observed that the number of iterations required for convergence

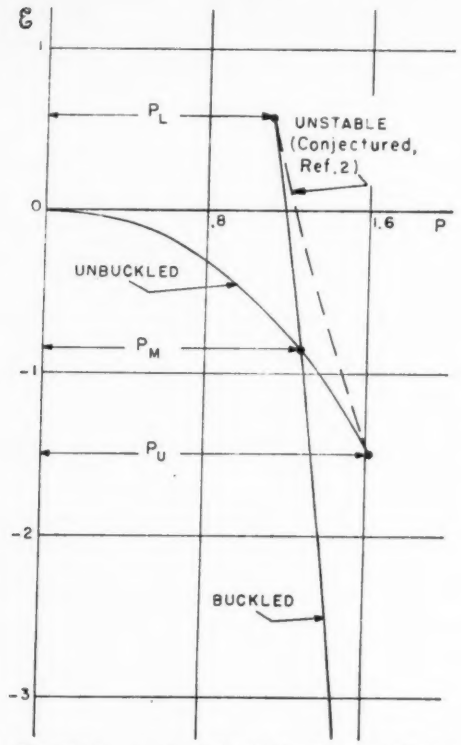

FIG. 6. Potential energy, in the buckled and unbuckled states, as a function of P ($\rho = 12$).

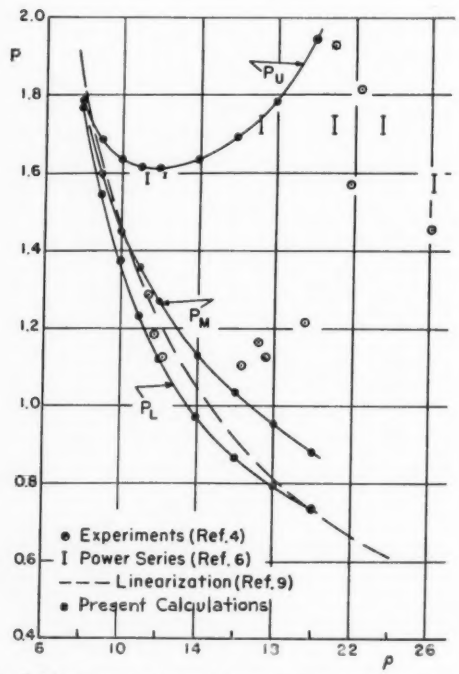

FIG. 7. Critical loads obtained from experiments and theories.

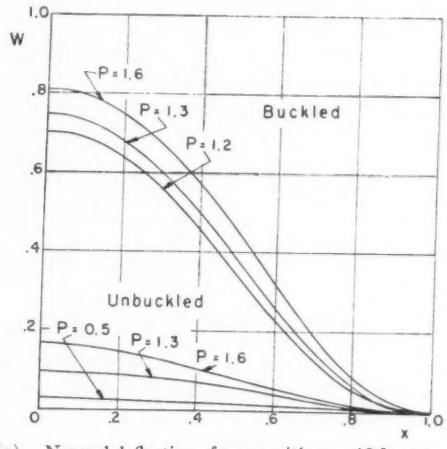

FIG. 8(a). Normal deflection of a cap with $\rho = 12$ for a sequence of P values.

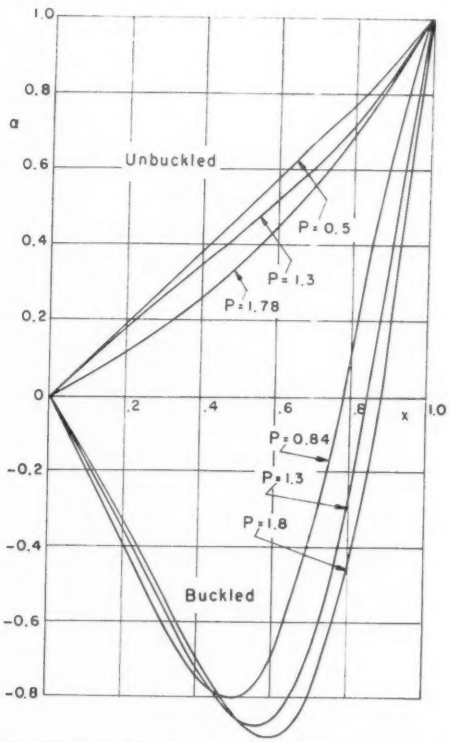

FIG. 8(b). Slope of deformed surface of a cap with $\rho = 18$ for a sequence of P values.

increases as $P \to P_U$ from below—i.e., on the unbuckled branch.

Following this procedure we use as an initial iterate an unbuckled solution and have no difficulty in obtaining a buckled solution for $P = P_U + \delta P$, provided δP is not too small. (This would correspond to the difficulty, discussed in Section (4), of using the iteration scheme to find a double root.) The solution thus "jumps" from the unbuckled to the buckled state when P_U is exceeded. It is found that even though $\lambda_{op}(P)$ from the unbuckled branch is used the iterations converge to the buckled solution. However, if it is anticipated that "buckling" is about to occur and $\lambda_{op}(P)$ from the buckled branch is used, the convergence is much faster. Once buckling has been observed, which is obvious from the large changes in the solution—i.e., a "jump" in the deflection—we employ λ_{op}'s from the buckled branch and proceed as before, now obtaining buckled solutions for increasing and decreasing values of the load about P_U. As $P \to P_L$ from above, the buckled solutions require more iterations for convergence. When the load is finally reduced to $P = P_L - \delta P$, below the lower buckling load, the solution "jumps" back to a previously obtained solution in the unbuckled state. Thus, for the interval $P_L < P < P_U$ we obtain two distinct sets of solutions of the difference equations which, no doubt, correspond to pairs of non-unique solutions of the boundary value problem.

When the iterations have converged for a value of P and ρ the stresses, deflections, and potential energy are computed. For this purpose we employ obvious finite difference equivalents of the definitions (3)–(6). A summary and discussion of the results obtained in this manner are presented below.

(6) Presentation of Results and Asymptotic Solution

For each of eleven values of ρ in the interval $6 \leq \rho \leq 20$ solutions have been obtained† for P ranging from zero to above P_U. The resulting curves of pressure versus maximum deflection have the form of the buckled and unbuckled branches shown in Fig. 1.

The numerically determined upper buckling load, P_U, is defined to lie in the interval

$$\bar{P} \leq P_U \leq \bar{P} + \delta P$$

if an unbuckled solution has been obtained for $P = \bar{P}$ and, using this solution as the initial iterate, a buckled solution is obtained for $P = \bar{P} + \delta P$. The lower buckling load is located in a similar manner. For these determinations we use $\delta P = 0.01$. In this way we have located P_L and P_U to an accuracy of at least 1.3 per cent (see Fig. 7). The intermediate buckling load, P_M, is determined from the point of intersection of the curves of the potential energy, $\mathcal{E}$, versus P for the buckled and unbuckled states (see Fig. 6). These curves substantiate Friedrichs' conjecture[2] as applied to the buckling of spherical caps.

The critical pressures thus determined are presented in Fig. 7 along with experimentally measured buckling pressures and some corresponding quantities from previous studies. The resolution of this Figure is too coarse to clearly indicate the distinct critical values obtained for $\rho = 8$. No buckling was observed for $\rho \leq 6$ and thus the value ρ_0, which separates caps that can buckle from those that cannot buckle, must lie in the interval $6 < \rho_0 < 8$. No attempt has been made to sharpen this estimate. The critical pressures determined by power series for $\rho \leq 20$ are in fair agreement with the present values of P_U. Also, in this range, the critical pressure, P_{cr}, defined by a linearization pro-

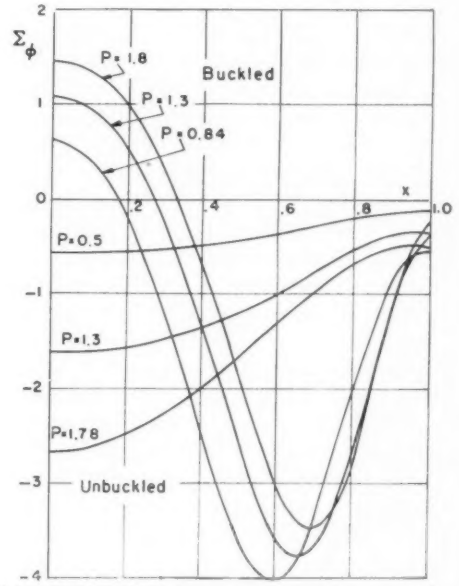

FIG. 8(c). Circumferential membrane stress in a cap with $\rho = 18$ for a sequence of P values.

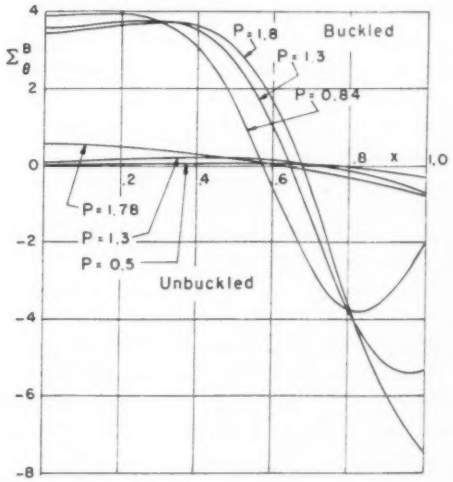

FIG. 8(d). Longitudinal bending stress on the inner surface of a cap with $\rho = 18$ for a sequence of P values.

† All computations employed $\nu = 0.32$ and were performed on the Atomic Energy Commission's IBM-704 computer at New York University. We wish to acknowledge the aid of S. Weinberg and H. Mullish in coding the problem for the machine.

cedure[9] is seen to fall between P_L and P_M and hence may be an approximation to either. The experimentally determined buckling loads for caps with $16 < \rho < 20$ are above the P_M curve as would be expected if caps actually snap according to the energy buckling mechanism. However, for $11 < \rho < 13$ the experimental critical loads† are between P_L and P_M. For $\rho > 20$ the power series critical pressures[6] are in fair agreement with the experiments but it is not yet clear which of the critical loads, P_L, P_M, or P_U, if any, the power series results represent.

Graphs of reduced stresses, deflections, and slopes in both buckled and unbuckled states are each presented in Figs. 8(a) through 8(d) for one of two representative caps—i.e., ρ values. Although the deflection, $W(x)$ in Fig. 8(a), retains the same form in the buckled and unbuckled states, its amplitude is increased by a large factor in the buckled state. This is one of the features employed to determine the occurrence of buckling. As the load increases the slope, $\alpha(x)$ in Fig. 8(b), decreases steadily, throughout the cap, from its undeformed value $\alpha(x) = x$. Upon buckling, $\alpha(x)$ becomes negative throughout most of the shell, with a minimum near the edge, and rapidly increases to satisfy the clamping condition $\alpha(1) = 1$. As P increases from P_L this negative minimum decreases and approaches the edge while the slope of $\alpha(x)$ near the center decreases in magnitude. This behavior of the buckled states is characteristic of the formation of a boundary layer as $P \to \infty$.

The circumferential membrane stress, Σ_ϕ in Fig. 8(c), is negative, and hence compressive, throughout the shell in all unbuckled states. There is a compressive maximum at the center which increases with P. However, in the buckled states Σ_ϕ may vary from tensile to compressive. If the maximum stress is at the center it is tensile. There are again indications of a boundary layer developing in the buckled states as P increases. The longitudinal membrane stress, Σ_θ (not shown), is similar to Σ_ϕ, but with less pronounced maxima and minima.

The longitudinal bending stress, $\Sigma_\theta{}^B$ in Fig. 8(d), changes sign in both buckled and unbuckled states but has much larger maxima when the cap is buckled. The circumferential bending stress (not shown) is similar and the boundary-layer formation is again obvious in the buckled states.

The corresponding power-series solutions,[6] which were obtained for the unbuckled states, are in good agreement with the present results. The maximum deviations occur for P near P_U.

In Figs. 9(a) through 9(d), stresses, deflections, and slopes in buckled and unbuckled states are plotted for a fixed value of P and an increasing sequence of ρ values. Now a boundary layer is seen to develop in the buckled state as $\rho \to \infty$. A simple "asymptotic solution" of the boundary value problem, Eqs. (1) and (7), which is found below is compared with the results shown in Figs. 9.

To obtain this asymptotic solution we divide Eqs. (1) by ρ and let $\rho \to \infty$. The differential equations then degenerate into the algebraic equations

$$\alpha(x)\,\gamma(x) + Px^2 = 0, \quad x^2 - \alpha^2(x) = 0 \tag{22}$$

There are two solutions of this system, corresponding to the buckled and unbuckled states, which we designate as follows.

Unbuckled asymptotic solution:

$$\alpha_u(x) = x, \quad \gamma_u(x) = -Px \tag{23a}$$

Buckled asymptotic solution:

$$\alpha_b(x) = -x, \quad \gamma_b(x) = Px \tag{23b}$$

Using these solutions in Eq. (3)–(5), the corresponding stresses and deflections are found to be

$$W_u(x) = 0, \quad \Sigma_{\theta,\,u}(x) = \Sigma_{\phi,\,u}(x) = -P, \quad \Sigma_{\theta,\,u}{}^B(x) = \Sigma_{\phi,\,u}{}^B(x) = 0 \tag{24a}$$

$$W_b(x) = 1 - x^2, \quad \Sigma_{\theta,\,b}(x) = \Sigma_{\phi,\,b}(x) = P, \quad \Sigma_{\theta,\,b}{}^B(x) = \Sigma_{\phi,\,b}{}^B(x) = 2(1 + \nu) \tag{24b}$$

Both of the solutions (23) satisfy the boundary conditions (7a) at the origin and the unbuckled solution satisfies only one of the conditions (7b) at the edge. Since neither solution satisfies all the conditions at the edge they can be good approximations to the exact solutions for large ρ only in the interior of the shell. More accurate approximations can be sought by applying boundary-layer methods.[13]

The asymptotic quantities (23)–(24) for $P = 1.5$ are shown as dotted lines in Figs. 9. It is clear that the numerical solutions approach the asymptotic solution in the interior as ρ increases. This can be seen more clearly from some unbuckled solutions obtained in reference 6 for values as high as $\rho = 64$. (For example, in Fig. 9b of reference 6 the asymptotic solution is the horizontal line of ordinate 10, and for $\rho = 64$ the error is less than 5 per cent.)

(7) Discussion and Conclusions

The finite difference solutions are satisfactory for all caps in the range $0 \leq \rho \leq 20$ as they give a complete description of the buckled and unbuckled equilibrium states and the critical loads. For caps with $\rho > 20$, buckled and unbuckled states have been obtained but the numerical jumping to a buckled state as P increases has not been observed. Thus, the critical loads have not been determined. In addition, as a result of the weak convergence criterion (21), the validity of the solutions for these caps is questionable when P is "large."

It is of interest to note that both experiments[4] and calculations[6] show that in the unbuckled state there exist different "modes" of deformation for different ρ intervals. The modes may be characterized by the number of maxima and minima of $W(x)$. Since a

† It should be noted that accurate experiments are more difficult to perform for shallower shells.

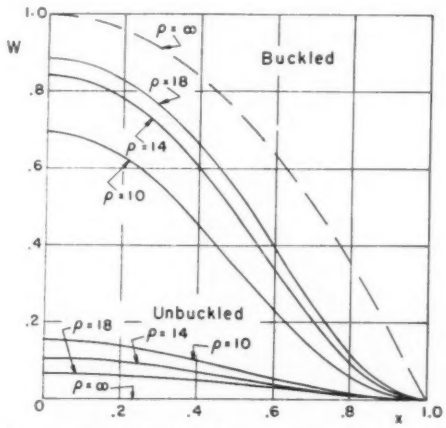

FIG. 9(a). Normal deflection of a sequence of caps for a load of $P = 1.5$.

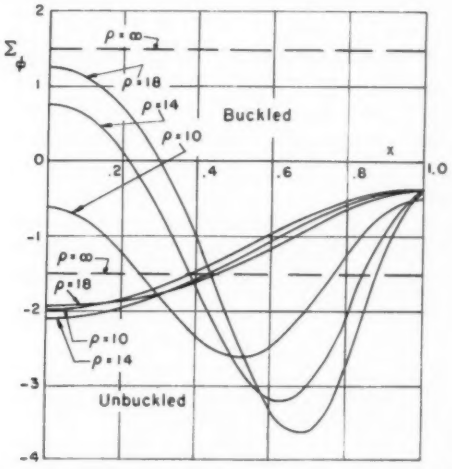

FIG. 9(c). Circumferential membrane stress in a sequence of caps for a load of $P = 1.5$.

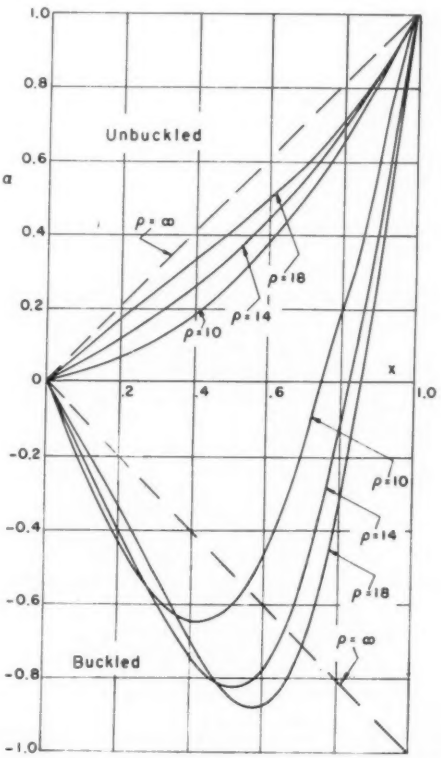

FIG. 9(b). Slope of deformed surface of a sequence of caps for a load of $P = 1.5$.

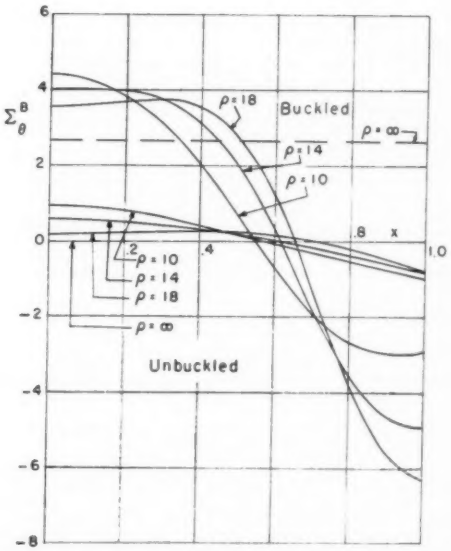

FIG. 9(d). Longitudinal bending stress on the inner surfaces of a sequence of caps for a load of $P = 1.5$.

change in mode occurs near $\rho = 20$ we are led to the following conjecture: the iteration procedure, in its present form, may be inadequate for calculating the more oscillatory solutions and/or there may be a more fundamental change in the nature of the solutions—i.e., the number of equilibrium states may increase with the ρ intervals.

Some insight into these possibilities may be gained by a study of the algebraic system obtained from the difference Eqs. (9) and (11) for a fine mesh. A preliminary investigation indicates that indeed the number of real solutions of this system may increase with ρ. In addition, a study of the corresponding iteration procedure (12) suggests that the relaxation parameter λ should be replaced by a function, $\lambda(x_j)$, and that the convergence criterion, Eq. (21), should be improved.

References

[1] von Kármán, T., and Tsien, H. S., *The Buckling of Spherical Shells by External Pressure*, Journal of the Aeronautical Sciences, Vol. 7, No. 2, pp. 43–50, December, 1939.

[2] Friedrichs, K. O., *On the Minimum Buckling Load for Spherical Shells*, Von Kármán Anniversary Volume, pp. 258–272, California Institute of Technology, Pasadena, 1941.

[3] Tsien, H. S., *A Theory for the Buckling of Thin Shells*, Journal of the Aeronautical Sciences, Vol. 9, No. 10, pp. 373–384, August, 1942.

[4] Kaplan, A., and Fung, Y. C., *A Nonlinear Theory of Bending and Buckling of Thin Elastic Shallow Spherical Shells*, NACA TN 3212, 1954.

[5] Archer, R. R., *Stability Limits for a Clamped Spherical Shell Segment Under Uniform Pressure*, Quarterly of Applied Mathematics, Vol. 15, No. 4, pp. 355–366, 1958.

[6] Reiss, E. L., Greenberg, H. J., and Keller, H. B., *Nonlinear Deflections of Shallow Spherical Shells*, Journal of the Aeronautical Sciences, Vol. 24, No. 7, pp. 533–543, July, 1957.

[7] Simons, R. M., *A Power Series Solution of the Nonlinear Equations for Axi-Symmetrical Bending of Shallow Spherical Shells*, Journal of Mathematics and Physics, Vol. 35, No. 2, pp. 164–176, 1956.

[8] Wienitschke, H. S., *On the Nonlinear Theory of Shallow Spherical Shells*, Journal of the Society for Industrial and Applied Mathematics, Vol. 6, No. 3, pp. 209–232, 1958.

[9] Reiss, E. L., *Axially Symmetric Buckling of Shallow Spherical Shells Under External Pressure*, Journal of Applied Mechanics, Vol. 25, No. 4, pp. 556–560, 1958.

[10] Keller, H. B., and Reiss, E. L., *Iterative Solutions for the Nonlinear Bending of Circular Plates*, Communications on Pure and Applied Mathematics, Vol. 11, No. 3, pp. 273–292, 1958.

[11] Keller, H. B., and Reiss, E. L., *Nonlinear Bending and Buckling of Circular Plates*, Proceedings of the Third National Congress of Applied Mechanics, pp. 375–385, Providence, R.I., 1958.

[12] Hildebrand, F. B., *Introduction to Numerical Analysis*, pp. 443–458; McGraw-Hill Book Company, Inc., New York, 1956.

[13] Reissner, E., *Symmetric Bending of Shallow Shells of Revolution*, Journal of Mathematics and Mechanics, Vol. 7, No. 2, pp. 121–140, 1958.

Notice to Contributors

To expedite review, an additional copy of both the manuscript and figures should be submitted. The manuscript submitted for publication *must* be a double- or triple-spaced original. There should be wide margins on all sides of the sheets and triple spacing around formulas to allow for the marking of directions to the printer.

Original drawings (jet black India ink on white paper or tracing cloth) should accompany the manuscript. *(Blueprints are not acceptable.)* Photographs *must* be on glossy white paper. The smallest lettering on 8- by 10-in. figures should be no less than $^1/_4$ in. high.

Formulas should be typewritten or carefully written in pen and ink. The difference between capital and lower-case letters and Greek symbols should be clearly distinguished.

See Inside Back Cover of this issue for further details

Advances in Aeronautical Science

Proceedings of the First International Congress of the Aeronautical Sciences, Madrid, 1958 (2 Vols.)

In these two volumes are published the 46 papers presented by the world's outstanding specialists in the field of aeronautics and astronautics at the First International Congress of the Aeronautical Sciences held in Madrid in September, 1958, under the leadership of Prof. Theodore von Kármán. Some 600 delegates from 25 countries, including an official delegation from the U.S.S.R., attended, and the meeting was so successful that it was decided to hold similar congresses at 2-year intervals in future.

The volumes have a full author and subject index and number 1,200 pages. The *Proceedings*, edited by Th. von Kármán, A. M. Ballantyne, H. Blenk, R. R. Dexter, M. Roy, and H. L. Dryden, are of special interest to aerodynamicists, aeronautical engineers, rocketry research workers, and propulsion engineers.

The *Proceedings* (price, $30.00) may be obtained by writing to: *Sales Director, Pergamon Press, Inc., 122 East 55 St., New York 22, N.Y.*

Unsteady Laminar Compressible Boundary Layers on an Infinite Plate With Suction or Injection†

KWANG-TZU YANG**
University of Notre Dame

Summary

This study deals with unsteady compressible laminar boundary layers on an infinitely extended porous plate. An integral solution based on two types of assumed velocity and temperature profiles is presented for the general case where the unsteady free-stream velocity and rate of surface suction or injection are both arbitrary. Also indicated is an exact solution, applicable, however, only to certain specific unsteady free-stream and surface suction or injection variations. The reliability and range of validity of the integral solutions is then established on the basis of numerical results from the exact solution. Finally, several general qualitative conclusions of the unsteady effects of free-stream velocity and surface suction or injection on laminar boundary-layer behavior are made.

Symbols

a_1, a_2, a_3, a_4 = coefficients in velocity polynomial
b_1, b_2, b_3, b_4 = coefficients in temperature polynomial
$b_{2\infty}$ = constant relating to b_2 as $E \rightarrow \infty$
c_f = skin-friction coefficient $\tau_w/[(1/2)\rho_\infty u_\infty^2]$
c_p = specific heat
C = matching constant in Chapman-Rubesin's viscosity-temperature law
E = $u_\infty^2/c_p(T_w - T_\infty)$
f_1, f_2 = universal functions of a_2
F = function of η introduced in Eq. (33)
g_1, g_2 = functions of b_2
G = function of η
h = coefficient of heat transfer
H = function introduced in Eq. (33)
I = function of t^*
J = function defined in Eq. (16)
J_∞ = constant relating to J as $E \rightarrow \infty$
k = thermal conductivity
K = function defined in Eq. (12)
L = characteristic length of plate
N = Nusselt Number hL/k_w
R = Reynolds Number $u_\infty L/\nu_\infty$
R_0 = Reynolds Number $u_0 L/\nu_\infty$
S = physical constant in Sutherland's viscosity-temperature law
t = time variable in (y, t) system
$\bar{t}$ = time variable in $(Y, \bar{t})$ system
t^* = dimensionless time variable $u_0\bar{t}/L$
T = temperature variable
u, v = velocity components in the x and y directions, respectively
u_0 = a constant reference velocity
u^* = u/u_∞
W = $\Delta_1^2/C\nu_\infty$
x, y = coordinates along and normal to the plate surface, respectively
Y = Dorodnitsyn variable
Z = $\delta_1^2/C\nu_\infty$
α = constant unsteadiness parameter
β = constant parameter for unsteady free-stream flow
γ = constant parameter for unsteady suction and injection
Γ = $(\Delta_1/C\nu_\infty)(\rho_w v_w/\rho_\infty)$
Γ_∞ = constant relating to Γ as $E \rightarrow \infty$
δ = a certain momentum boundary-layer thickness
δ_1 = displacement thickness defined in Eq. (11)
δ_2 = a momentum boundary-layer thickness defined in Eq. (12)
δ_p = a momentum boundary-layer thickness defined in Eq. (19)
δ^* = $\int_0^\infty (1 - u^*)d\eta$
Δ = a certain thermal boundary-layer thickness
Δ_1 = a thermal boundary-layer thickness defined in Eq. (11)
Δ_2 = a thermal boundary-layer thickness defined in Eq. (16)
Δ_p = a thermal boundary-layer thickness introduced in the temperature polynomial
ζ = $c_p(T - T_\infty)/u_\infty^2$
η = $(Y/L)\sqrt{R_0/C(1 - \alpha t^*)}$
θ = $(T - T_\infty)/(T_w - T_\infty)$
λ = $(\delta_1/C\nu_\infty)(\rho_w v_w/\rho_\infty)$
μ = dynamic viscosity
ν = kinematic viscosity
ρ = density
σ = Prandtl Number
τ = shear stress

Subscripts and Superscripts

w = plate surface conditions
∞ = conditions in the free stream or at the outer edge of the boundary layer
$(')$ = derivative with respect to the independent variable

Received October 13, 1958.

† This work represents part of research sponsored by the National Science Foundation under Contract NSF G-2772 with the University of Notre Dame.

** Associate Professor, Department of Mechanical Engineering.

(1) Introduction

USEFUL INFORMATION on laminar boundary-layer behavior under different surface and free-stream conditions has in the past been obtained from studying boundary-layer development on infinitely extended flat plates. These results also represent asymptotic solutions to the corresponding semi-infinite plate problems at large distances away from the leading edge. For steady conditions, Schlichting[1] indicated a simple solution to the incompressible flow case with constant rate of suction at the plate surface. The corresponding

compressible flow problem was treated by Illingworth,[2] who considered the two-dimensional Navier-Stokes' equations of motion and the corresponding energy equation. Solutions are also available in the literature to certain specific unsteady problems. Illingworth[3] investigated and obtained a solution to the case of laminar compressible flow on an infinite plate set in motion impulsively from rest based on boundary-layer assumptions. This evidently corresponds to Rayleigh's well-known classical solution for the incompressible flow case.[4] More recently, Stuart,[5] in an attempt to verify certain results of Lighthill's approximate analysis[6] for the problem of an arbitrary and heated cylinder oscillating in the direction of an oncoming incompressible flow, succeeded in obtaining exact solutions to the Navier-Stokes' equations of motion and the corresponding energy equation for a special case of an infinite plate with an insulated and porous surface. In a recent paper, Hasimoto[7] provided two new exact solutions to the incompressible Navier-Stokes' equations of motion for the unsteady infinite plate problem, one being that the free-stream velocity is arbitrarily unsteady and the velocity normal to the plate surface is constant, and the other a similarity solution, for which the free-stream velocity varies as a power of time and the normal velocity is inversely proportional to the square root of time.

In the steady flow theory, it is now well established that suction at the surface of a cylinder provides an effective means of stabilizing the laminar boundary layer; while, on the other hand, adequate surface cooling can be accomplished by surface injection (transpiration cooling). However, the corresponding effects on boundary-layer characteristics under unsteady conditions, especially when the flow is compressible, are relatively unknown. This problem is complicated in that the free-stream velocity, as well as the suction or injection velocity at the surface, could all be arbitrary functions of time. Hasimoto's similarity solution[7] for the incompressible case is pertinent to this problem, but unfortunately the numerical results shown are not sufficient for others to draw any specific conclusion.

The present study also deals with the infinitely extended porous flat plate problem. However, the more general case of a compressible flow is considered. The purpose of this paper is (1) to provide an approximate integral procedure by which the laminar boundary-layer characteristics such as skin-friction and heat-transfer rates at the plate surface may be evaluated for any combination of arbitrarily unsteady free-stream and suction or injection velocities, (2) to present an exact solution to the same problem, but for certain specific unsteady conditions, (3) to demonstrate the reliability and limitation of the integral procedure on the basis of numerical results from the exact solution, and, finally, (4) to draw certain specific conclusions on the effects of surface suction or injection and unsteadiness in the free-stream flow on different laminar boundary-layer characteristics.

(2) Laminar Boundary-Layer Equations

In the present analysis, the following assumptions are used: (1) normal velocity of surface suction or injection is small such that the usual boundary-layer assumptions are still valid, (2) all derivatives with respect to the x coordinate are negligible, (3) the pressure is constant throughout the flow field, (4) the plate surface temperature remains constant, (5) c_p and σ are arbitrary constants, and (6) Chapman and Rubesin's viscosity-temperature law is valid. Unsteady compressible laminar boundary-layer equations based on assumptions (3) and (5) for a flat plate with space coordinate system fixed on the plate has already been given by Moore.[8] By introducing additional assumptions (2) and (4), these same equations are readily simplified to

$$\rho(\partial u/\partial t) + \rho v(\partial u/\partial y) = \rho(du_\infty/dt) + (\partial/\partial y)[\mu(\partial u/\partial y)] \quad (1)$$

$$(\partial \rho/\partial t) + [\partial(\rho v)/\partial y] = 0 \quad (2)$$

$$\rho c_p[(\partial T/\partial t) + v(\partial T/\partial y)] = (\partial/\partial y)[k(\partial T/\partial y)] + \mu(\partial u/\partial y)^2 \quad (3)$$

Now the continuity equation (2) may be integrated, resulting in

$$\rho v = \rho_w v_w - \rho_\infty(\partial Y/\partial t) \quad (4)$$

where the time-dependent function v_w is the normal velocity at the surface, negative for suction and positive for injection, and Y is the Dorodnitsyn variable defined by

$$Y = \int_0^y (\rho/\rho_\infty)dy$$

After ρv is eliminated according to Eq. (4), Eqs. (1) and (3) may further be simplified in following a change of coordinates from a (y, t) system to a $(Y, \bar{t})$ system, where $\bar{t} = t$, by utilizing assumption (6). The resulting equations now read

$$(\partial u/\partial \bar{t}) + [(\rho_w/\rho_\infty)v_w](\partial u/\partial Y) = (du_\infty/d\bar{t}) + C\nu_\infty(\partial^2 u/\partial Y^2) \quad (5)$$

$$(\partial T/\partial \bar{t}) + [(\rho_w/\rho_\infty)v_w](\partial T/\partial Y) = (C\nu_\infty/\sigma)(\partial^2 T/\partial Y^2) + (C\nu_\infty/c_p)(\partial u/\partial Y)^2 \quad (6)$$

where C is the matching constant in Chapman and Rubesin's viscosity-temperature law and may be evaluated from

$$C = (T_w/T_\infty)^{1/2}[(T_\infty + S)/(T_w + S)]$$

where S has a value of 216°R. for air. The initial condition generally depends on a particular problem, while the boundary conditions are simply

$$Y = 0, \quad u = 0, \quad T = T_w \quad \text{(constant)}$$

$$Y \to \infty, \quad u \to u_\infty, \quad T \to T_\infty \quad \text{(constant)}$$

Note that Eq. (5) is entirely independent of the transformed energy Eq. (6), and hence may be treated separately.

(3) An Integral Solution

In this Section, an approximate integral solution to Eqs. (5) and (6) is presented for the general problem in which u_∞ and v_w are both prescribed, but arbitrary functions of time. It represents the asymptotic solution under these unsteady conditions. In view of its high degree of accuracy and simplicity in application, as will be demonstrated later, this solution should prove useful in dealing with the physically important problem of a finite porous plate with a given set of free-stream and surface suction or injection unsteadiness.

By introducing the following dimensionless dependent variables:

$$u^* = u/u_\infty, \quad \theta = (T - T_\infty)/(T_w - T_\infty)$$

Eqs. (5) and (6) reduce, respectively, to

$$(1/u_\infty)[\partial(u_\infty u^*)/\partial \bar{t}] + [(\rho_w/\rho_\infty)v_w](\partial u^*/\partial Y) = (1/u_\infty)(du_\infty/d\bar{t}) + C\nu_\infty(\partial^2 u^*/\partial Y^2) \quad (7)$$

$$(\partial\theta/\partial\bar{t}) + [(\rho_w/\rho_\infty)v_w](\partial\theta/\partial Y) = (C\nu_\infty/\sigma)(\partial^2\theta/\partial Y^2) + [C\nu_\infty u_\infty{}^2/c_p(T_w - T_\infty)](\partial u^*/\partial Y)^2 \quad (8)$$

which, when integrated with respect to Y, yield readily the following integral momentum and energy equations, respectively:

$$(1/u_\infty)[d(u_\infty\delta_1)/d\bar{t}] = (\rho_w/\rho_\infty)v_w + C\nu_\infty(\partial u^*/\partial Y)_w \quad (9)$$

$$d\Delta_1/d\bar{t} = (\rho_w/\rho_\infty)v_w - (C\nu_\infty/\sigma)(\partial\theta/\partial Y)_w + [C\nu_\infty u_\infty{}^2/c_p(T_w - T_\infty)]\int_0^\delta (\partial u^*/\partial Y)^2 dY \quad (10)$$

where

$$\delta_1 = \int_0^\delta (1 - u^*)dY, \quad \Delta_1 = \int_0^\delta \theta dY \quad (11)$$

and δ and Δ are functions of time to be defined later.

Before these integral equations are solved, it is first necessary to introduce certain velocity and temperature profiles. Two types of profiles are considered in the present study. One is an exponential function, which has previously been used by Schlichting[9] and Lew[10] in steady flow problems, and the other, the well-known fourth-degree polynomial. The integral solution is now described in terms of these two types of profiles with the case of exponential function to be treated first.

Since it is independent of Eq. (10), Eq. (9) is first considered. The velocity profile $u^*(Y, \bar{t})$ is assumed to have the following form:

$$u^*(Y, \bar{t}) = 1 - e^{-[Y/\delta_e(\bar{t})]}\{1 - [Y/\delta_e(\bar{t})]K(\bar{t})\} \quad (12)$$

where $\delta_e(\bar{t})$ and $K(\bar{t})$ are to be determined from Eq. (9) together with a surface condition and K is to assume negative values only. One advantage of using this exponential form is that the usual conditions in the free stream such as $u^*(\infty, \bar{t}) = 1$, $\partial u^*(\infty, \bar{t})/\partial Y = 0$, and $\partial^2 u^*(\infty, \bar{t})/\partial Y^2 = 0$ are automatically satisfied with Y approaching infinity. Thus, with $\delta = \infty$ and Eq. (12) introduced, Eq. (9) reduces to

$$dZ/d\bar{t} = 2(1 - K^2) + 2\lambda - 2Z[(1/u_\infty)(du_\infty/d\bar{t})] \quad (13)$$

where

$$Z = \delta_1{}^2/C\nu_\infty, \quad \lambda = (\delta_1/C\nu_\infty)[(\rho_w/\rho_\infty)v_w]$$

with the help of the following identity:

$$\delta_1/\delta_e = 1 - K$$

according to Eq. (11). In addition, Eq. (7), when evaluated at the plate surface, becomes

$$[(\rho_w/\rho_\infty)v_w](\partial u^*/\partial Y)_w = (1/u_\infty)(du_\infty/d\bar{t}) + C\nu_\infty(\partial^2 u^*/\partial Y^2)_w \quad (14)$$

which in turn may be written as

$$\lambda(1 - K^2) + (2K + 1)(1 - K)^2 = [(1/u_\infty)(du_\infty/d\bar{t})]Z \quad (15)$$

With a given initial value of Z, Eq. (13), with the aid of Eq. (15), may be solved by any standard numerical procedure, yielding $Z(\bar{t})$, $K(\bar{t})$, and $\lambda(\bar{t})$.

An almost identical treatment may now be applied to Eqs. (8) and (10). By introducing a similar exponential function for the transformed temperature profile as indicated below

$$\theta(Y, \bar{t}) = e^{-[Y/\Delta_e(\bar{t})]}\{1 - [Y/\Delta_e(\bar{t})]J(\bar{t})\} \quad (16)$$

where J also is to assume negative value only, the following pair of dimensionless equations corresponding to Eqs. (13) and (15) for the momentum field may be obtained:

$$dW/d\bar{t} = 2\Gamma + (2/\sigma)(1 - J^2) + (E/2)(K^2 + 2K + 2)(1 - K)(\Gamma/\lambda) \quad (17)$$

$$\sigma\Gamma(1 - J^2) + (2J + 1)(1 - J^2) + E\sigma(\Gamma/\lambda)^2(1 - K^2)^2 = 0 \quad (18)$$

where

$$W = \Delta_1{}^2/C\nu_\infty, \quad \Gamma = (\Delta_1/C\nu_\infty)[(\rho_w/\rho_\infty)v_w], \quad E = u_\infty{}^2/c_p(T_w - T_\infty)$$

In a specific problem, any standard numerical procedure may again be used to solve Eqs. (17) and (18), resulting in $W(\bar{t})$, $J(\bar{t})$, and $\Gamma(\bar{t})$.

Now the integral solution based on fourth-degree polynomials for the profiles is described. In Eqs. (9) and (11), δ may now be replaced by a momentum boundary-layer thickness δ_p, and δ_1 then is obviously a displacement thickness. The fourth-degree velocity polynomial is written in its usual form:

$$u^*(Y, \bar{t}) = a_1(Y/\delta_p) + a_2(Y/\delta_p)^2 + a_3(Y/\delta_p)^3 + a_4(Y/\delta_p)^4 \quad (19)$$

where the coefficients a_1, a_3, and a_4 may all be expressed in terms of a_2 in view of the free-stream conditions

$$u^*(\delta_p, \bar{t}) = 1, \quad \partial u^*(\delta_p, \bar{t})/\partial Y = 0, \quad \partial^2 u^*(\delta_p, \bar{t})/\partial Y^2 = 0$$

resulting in

$$a_1 = f_1(a_2), \quad a_3 = -2 - a_2, \quad a_4 = (a_2/3) + 1$$

where $$f_1(a_2) = 2 - (a_2/3)$$

When Eq. (19) is introduced in Eq. (9), we have

$$dZ/d\bar{t} = 2\lambda(1 - f_1 f_2) + 2f_1 f_2 + 4a_2 f_2^2 \qquad (20)$$

where $$f_2(a_2) = \delta_1/\delta_p = (18 + a_2)/60$$

Furthermore, Eq. (14) in this case reduces to

$$\lambda f_1 f_2 - 2a_2 f_2^2 = [(1/u_\infty)(du_\infty/d\bar{t})]Z \qquad (21)$$

It is obvious that Eqs. (20) and (21) correspond directly to Eqs. (13) and (15) for the case of exponential profiles.

Based on another fourth-degree polynomial for the transformed temperature profile,

$$\theta(Y, \bar{t}) = 1 + b_1(Y/\Delta_p) + b_2(Y/\Delta_p)^2 + b_3(Y/\Delta_p)^3 + b_4(Y/\Delta_p)^4$$

where Δ_p replaces Δ in Eq. (10), and b_1, b_3, and b_4 are expressible in terms of b_2 from the usual free-stream conditions, a similar treatment yields the following equations:

$$dW/d\bar{t} = 2\Gamma + (2/\sigma)g_1 g_2 + (2E/105)f_2(\Gamma/\lambda)(a_2^2 - 8a_2 + 156) \qquad (22)$$

$$2b_2 g_2^2 + \sigma\Gamma g_1 g_2 + \sigma E f_1^2 f_2^2 (\Gamma/\lambda)^2 = 0 \qquad (23)$$

where $g_1 = 2 + (b_2/3)$ and $g_2 = (18 - b_2)/60$.

Finally, these solutions in the $(Y, \bar{t})$-system may readily be changed back to those in the original physical system by means of the following inverse transformation.

$$y = Y + [(T_w/T_\infty) - 1]\int_0^y \theta dY, \quad t = \bar{t} \qquad (24)$$

In addition, such laminar boundary-layer characteristics as skin friction and surface heat transfer may also be simply calculated according to the following relations:

For exponential profiles

$$\left.\begin{aligned} c_f R^{1/2} &= [\tau_w/(1/2)\rho_\infty u_\infty^2](u_\infty L/\nu_\infty)^{1/2} = 2(1 - K^2)(CL/Zu_\infty)^{1/2} \\ NR^{-1/2} &= (hL/k_w)(u_\infty L/\nu_\infty)^{-1/2} = (1 - J^2)(T_\infty/T_w)(L/CWu_\infty)^{1/2} \end{aligned}\right\} \qquad (25)$$

For fourth-degree polynomials

$$\left.\begin{aligned} c_f R^{1/2} &= 2f_1 f_2 (CL/Zu_\infty)^{1/2} \\ NR^{-1/2} &= g_1 g_2 (T_\infty/T_w)(L/CWu_\infty)^{1/2} \end{aligned}\right\} \qquad (26)$$

where L is a characteristic length of the plate. The relative accuracy and range of validity of using these two different types of profiles will be indicated in a later section.

(4) An Exact Solution

The primary purpose of this section is to present an exact solution to Eqs. (5) and (6) for a set of specific free-stream flow and surface conditions. This exact solution has a dual function in providing not only a basis for establishing the accuracy and range of reliability of the integral procedure but also results from which certain specific conclusions may be drawn on the effects of unsteady free-stream and surface unsteadiness on different laminar boundary-layer characteristics. As mentioned previously, Hasimoto[7] has recently obtained a similarity solution to the incompressible Navier-Stokes' equations of motion for the case of an infinite plate moving unsteadily in a fluid with surface suction or injection. In the present solution, Eq. (5), which is independent of Eq. (6), is solved in a manner similar to that used by Hasimoto. A similarity solution, however, is not possible for Eq. (6), which fortunately may be solved, after a suitable transformation, by the usual method of separation of variables.

According to the following change of independent variables:

$$\eta = (Y/L)[R_0/C(1 - \alpha t^*)]^{1/2}, \quad t^* = u_0\bar{t}/L$$

where α is a constant parameter, Eq. (5) may be written as

$$\{[\alpha\eta/2(1 - \alpha t^*)] + [(\rho_w/\rho_\infty)v_w] \times (L/u_0)[R_0/C(1 - \alpha t^*)]^{1/2}\}(\partial u^*/\partial\eta) + (\partial u^*/\partial t^*) = [(1 - u^*)/u_\infty](du_\infty/dt^*) + [1/(1 - \alpha t^*)](\partial^2 u^*/\partial\eta^2) \qquad (27)$$

Now it is possible to obtain a similarity solution for Eq. (27) if

$$\left.\begin{aligned} u^* &= u^*(\eta), \quad u_\infty = u_0(1 - \alpha t^*)^{-\beta}, \\ [(\rho_w/\rho_\infty)v_w](R_0^{1/2}/u_0) &= \gamma[C/(1 - \alpha t^*)]^{1/2} \end{aligned}\right\} \qquad (28)$$

where β and γ are both arbitrary constants. The associated ordinary differential equation may be derived readily, and is shown as

$$u^{*\prime\prime} - [(\alpha/2)\eta + \gamma]u^{*\prime} - \alpha\beta u^* + \alpha\beta = 0 \qquad (29)$$

which must be solved with the following boundary conditions:

$$u^*(0) = 0, \quad u^*(\infty) = 1 \qquad (30)$$

The three constant parameters α, β, and γ, in Eq. (29) all have certain physical meanings. The quantity α is an indication of unsteadiness in the problem. When α is zero, the present problem reduces to a steady flow case. In the unsteady problem, it is assigned a numerical value of -1 without loss of generality, because of the arbitrary scale factor in the definition of t^*. The negative sign is essential, since from Eq. (29) it is seen that the coefficient $[(\alpha/2)\eta + \gamma]$ of the $u^{*\prime}$ term must assume negative values as η approaches infinity in order that the boundary condition $u^*(\infty) = 1$ can be satisfied. The quantity β is a parameter relating to the unsteadiness in the free-stream flow with negative values indicating acceleration and positive values indicating deceleration. The significance of γ is self-evident and it may be considered as a suction (negative values) or injection

(positive values) parameter. It is also interesting to note that, for $\alpha = -1$, $\beta = 0$, and any γ, the problem reduces to one with steady free-stream flow and unsteady surface suction or injection.

Now the transformed energy equation (6) is considered. Even though a similarity solution is still obtainable for a particular case $\beta = 0$, it is, however, not desirable because of the restriction on β. Fortunately, an exact solution to Eq. (6) for the general case may be obtained by the usual method of separation of variables. In using the same transformation of coordinates from the $(Y, \bar{t})$ system to the (η, t^*) system and introducing a new dimensionless dependent variable ζ defined by

$$\zeta = c_p(T - T_\infty)/u_\infty^2$$

Eq. (6) is readily reduced to

$$(1 - \alpha t^*)(\partial\zeta/\partial t^*) + [(\alpha/2)\eta + \gamma](\partial\zeta/\partial\eta) + 2\alpha\beta\zeta = (1/\sigma)(\partial^2\zeta/\partial\eta^2) + (du^*/d\eta)^2 \quad (31)$$

The corresponding boundary conditions are

$$\zeta(0, t^*) = c_p(T_w - T_\infty)/u_\infty^2 = 1/E, \qquad \zeta(\infty, t^*) = 0 \quad (32)$$

Eq. (31) is a linear nonhomogeneous partial differential equation which may be solved as follows: The complete solution may be written as

$$\zeta(\eta, t^*) = F(\eta, t^*) + H(\eta, t^*) \quad (33)$$

where $F(\eta, t^*)$ is a particular solution to the nonhomogeneous equation and $H(\eta, t^*)$ the complementary solution to the homogeneous part of Eq. (31). By inspection, F may be assumed to be independent of t^* and is governed by the differential equation

$$(1/\sigma)(d^2F/d\eta^2) - [(\alpha/2)\eta + \gamma](dF/d\eta) - 2\alpha\beta F = -(du^*/d\eta)^2 \quad (34)$$

with the boundary conditions $F(0) = 0$ and $F(\infty) = 0$. The complementary solution $H(\eta, t^*)$ is obtainable by the method of separation of variables—i.e.,

$$H(\eta, t^*) = G(\eta)I(t^*)$$

which, when substituted in the homogeneous part of Eq. (31), yields the following identities:

$$I(t^*) = 1/E \quad (35)$$

$$G''(\eta) - \sigma[(\alpha/2)\eta + \gamma]G'(\eta) = 0 \quad (36)$$

In view of Eqs. (32), Eq. (36) must be solved with boundary conditions $G(0) = 1$ and $G(\infty) = 0$. Finally, the complete solution to the transformed energy equation (6) may be written as

$$\zeta(\eta, t^*) = F(\eta) + (1/E)G(\eta) \quad (37)$$

Physically, $G(\eta)$ is related to the temperature profile in the boundary layer when the free-stream velocity is low or the flow is incompressible, while $F(\eta)$ represents the effect of friction heat on the same temperature profile when the free-stream velocity becomes high.

Numerical results of the exact solution have been calculated for only a few combinations of the three parameters α, β, and γ. However, the number of cases calculated is still sufficiently large to permit drawing certain conclusions on the effects of unsteady surface suction or injection and free-stream flow on laminar boundary-layer characteristics such as skin friction and heat transfer. As already pointed out, without loss of generality, it is only necessary to assign two values to α, zero for the steady case and -1 for the unsteady case. The free-stream velocity parameter β is assigned the following values: -1, -0.5, 0, $+0.5$, $+1$; and the surface suction or injection parameter γ: -4, -3, -2, 0, $+1$, $+2$.

Now the solutions to ordinary differential equations (29), (34), and (36) with their respective boundary conditions are considered. All these equations are linear, and of the second order, and consequently may be solved by any one of the standard numerical procedures.[11] However, solutions in closed form may also be arrived for certain specific values of the parameters. In the case of steady conditions (i.e., $\alpha = 0$), the following results are readily obtainable:

$$u^*(\eta) = 1 - e^{\gamma\eta} \quad (38)$$

$$F(\eta) = [\sigma/(4 - 2\sigma)](e^{\sigma\gamma\eta} - e^{2\gamma\eta}) \quad (39)$$

$$G(\eta) = e^{\sigma\gamma\eta} \quad (40)$$

It is noted that Eq. (38), under the condition of constant property values, reduces identically to that of the corresponding incompressible flow case, and only suction is allowable (i.e., $\gamma < 0$), in order to realize sensible velocity profiles. When the problem is unsteady (i.e., $\alpha = -1$), the function $G(\eta)$ is independent of β and is given for any γ by

$$G(\eta) = 1 - \left(\int_0^\eta e^{\sigma[-(\eta^2/4)+\gamma\eta]}\,d\eta \Big/ \int_0^\infty e^{\sigma[-(\eta^2/4)+\gamma\eta]}\,d\eta\right) \quad (41)$$

In addition, we have for $\alpha = -1$, $\beta = 0$, and any γ,

$$u^*(\eta) = \int_0^\eta e^{-(\eta^2/4)+\gamma\eta}\,d\eta \Big/ \int_0^\infty e^{-(\eta^2/4)+\gamma\eta}\,d\eta \quad (42)$$

$$F(\eta) = \int_0^\eta e^{\sigma[-(\eta^2/4)+\gamma\eta]} \left(\left\{\int_0^\infty \left[e^{\sigma[-(\eta^2/4)+\gamma\eta]} \int_0^\eta \sigma(u^{*\prime})^2 e^{-\sigma[-(\eta^2/4)+\gamma\eta]}\,d\eta\right] d\eta \Big/ \int_0^\infty e^{\sigma[-(\eta^2/4)+\gamma\eta]}\,d\eta\right\} - \int_0^\eta \sigma(u^{*\prime})^2 e^{-\sigma[-(\eta^2/4)+\gamma\eta]}\,d\eta\right) d\eta \quad (43)$$

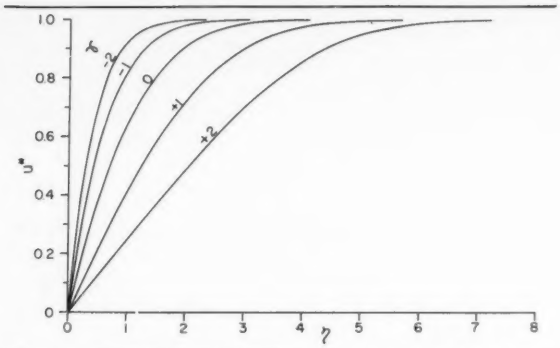

FIG. 1. Unsteady velocity profiles for $\alpha = -1$ and $\beta = -1$.

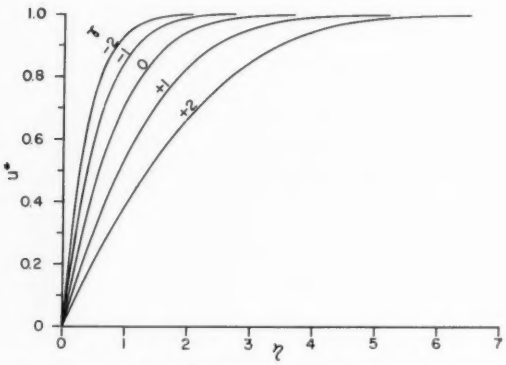

FIG. 2. Unsteady velocity profiles for $\alpha = -1$ and $\beta = -1/2$.

and for $\alpha = -1, \beta = +0.5$, and any $\gamma < 0$,

$$u^*(\eta) = 1 - e^{-(\eta^2/4)+\gamma\eta} \tag{44}$$

For all the other cases for which solutions in closed form are not obtainable, the step-by-step numerical calculation procedure for general second-order linear equations[11] has been used, and all the starting values have been obtained from power-series expansion. The calculations for $F(\eta)$ have been carried out with $\sigma = 0.7$.

Figs. 1–5 inclusive indicate the resulting solution to Eq. (29) at different β and γ values for the unsteady problem, and illustrate, in particular, the effects of both free-stream unsteadiness and surface suction and injection on the velocity profiles. Their effects on the temperature distribution in the boundary layer are indirectly shown in Figs. 6–11 in terms of the two functions $F(\eta)$ and $G(\eta)$ in view of the fact that according to the definition of ζ and Eq. (37), the temperature profile is given by

$$\theta = (T - T_\infty)/(T_w - T_\infty) = G(\eta) + E(t^*)F(\eta) \tag{45}$$

Physical interpretation of these Figures should be referred back to the physical coordinates (y, t) through the following inverse transformations:

$$y = L[C(1 - \alpha t^*)/R_0]^{1/2} \left\{ \eta + (u_\infty^2/c_p T_\infty) \times \int_0^\eta F(\eta)d\eta + [(T_w/T_\infty) - 1] \int_0^\eta G(\eta)d\eta \right\}, \quad t = t^* L/u_0$$

From these solutions, boundary-layer characteristics such as skin friction and surface heat transfer may then be readily calculated according to the following respective relations:

$$c_f R^{1/2} = [2u_0 u^{*\prime}(0)/u_\infty][C/(1 + t^*)]^{1/2} \tag{46}$$

$$NR^{-1/2} = -(T_\infty/T_w)[u_0/Cu_\infty(1 + t^*)]^{1/2} \times [G'(0) + E(t^*)F'(0)] \tag{47}$$

Characteristic quantities such as $u^{*\prime}(0)$, $G'(0)$, and $F'(0)$ will be shown in Section (5) when the approximate integral solution is compared with the exact solution.

(5) Reliability and Range of Validity of the Integral Solution

In view of the fact that adequate ranges of variation of unsteady free-stream velocity and surface suction and injection are covered by the constant parameters used in the exact solution, the exact results provide an excellent basis for establishing the reliability and range of validity of the approximate integral solution. To do this, it is only necessary to calculate from the integral solution those characteristic quantities $u^{*\prime}(0)$, $G'(0)$, and $F'(0)$ for different combinations of parameters and then to compare their values with those from the exact solution.

From the exact solution, we may write

$$dZ/d\bar{t} = -\alpha\delta^{*2}, \quad \lambda = \gamma\delta^*, \quad (Z/u_\infty)(du_\infty/d\bar{t}) = \alpha\beta\delta^{*2} \tag{48}$$

where δ^* is defined as

$$\delta^* = \int_0^\infty (1 - u^*)d\eta$$

and is related to the quantity δ_1 in the integral solution through

$$\delta^* = (\delta_1/L)\,[R_0/C(1 - \alpha t^*)]^{1/2}$$

When these identities are substituted into Eqs. (13) and (15), the following pair of algebraic equations results:

$$\left.\begin{aligned} &\alpha(2\beta - 1)\delta^{*2} - 2\gamma\delta^* - 2(1 - K^2) = 0 \\ &\alpha\beta\delta^{*2} - \gamma(1 - K^2)\delta^* - (2K + 1)(1 - K)^2 = 0 \end{aligned}\right\} \tag{49}$$

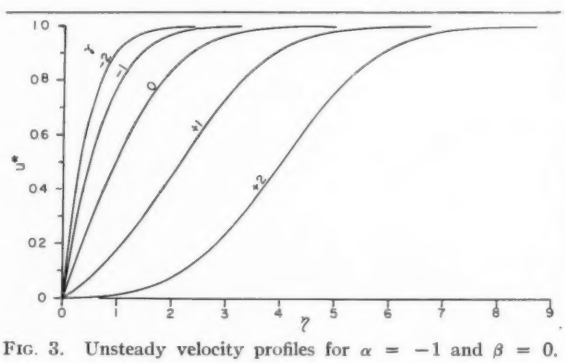

FIG. 3. Unsteady velocity profiles for $\alpha = -1$ and $\beta = 0$.

from which the two unknowns K and δ^* may be readily calculated for any combination of α, β, and γ. The characteristic quantity $u^{*\prime}(0)$ may then be determined simply from $u^{*\prime}(0) = (1 - K^2)/\delta^*$.

A similar substitution of Eq. (48) into Eqs. (20) and (21) yields the corresponding equations based on polynomials:

$$\left.\begin{aligned} &\alpha\delta^{*2} + 2\gamma(1 - f_1f_2)\delta^* + 2f_1f_2 + 4a_2f_2^2 = 0 \\ &\alpha\beta\delta^{*2} - \gamma f_1f_2\delta^* + 2a_2f_2^2 = 0 \end{aligned}\right\} \quad (50)$$

where a_2 and δ^* are the unknowns. $u^{*\prime}(0)$ is then evaluated as

$$u^{*\prime}(0) = f_1f_2/\delta^*$$

For the steady case (i.e., $\alpha = 0$), both Eqs. (49) and (50) give $u^{*\prime}(0) = -\gamma$, which agrees perfectly with the exact solution, Eq. (38). In the unsteady case (i.e., $\alpha = -1$), comparisons can only be made for individual cases, as shown in Table 1. Note that $u^{*\prime}(0)$ values based on polynomials are not indicated for negative values of γ, since in most of these cases no physically sensible results are obtainable. The general agreement between the exact results and that from the integral solutions is excellent, except in cases where laminar separation given by the condition $u^{*\prime}(0) = 0$ is approached. This, however, is not surprising, since in steady laminar boundary-layer theory it is known that most integral solutions do not predict separation point satisfactorily. Under suction conditions, it is seen that the integral solution based on exponential profiles yields very accurate results, especially when acceleration and suction rate are large. However, the same solution based on polynomials does enjoy some advantage in accuracy for cases with surface injection over that based on exponential profiles. This advantage becomes more pronounced when the laminar separation is approached.

TABLE 1

$u^{*\prime}(0)$ Values for Different Unsteady Parameters β and γ With $\alpha = -1$

γ	β	-1	$-(1/2)$	0	$+(1/2)$	$+1$
-4	Exact					3.874
	Exponential					3.874
	Polynomial					—
-3	Exact				3.0	2.833
	Exponential				3.0	2.831
	Polynomial				—	—
-2	Exact	2.555	2.391	2.208	2.0	1.752
	Exponential	2.561	2.397	2.213	2.0	1.740
	Polynomial	—	—	—	—	—
-1	Exact	1.770	1.565	1.320	1.0	
	Exponential	1.784	1.580	1.333	1.0	
	Polynomial	—	—	—	—	
0	Exact	1.128	0.886	0.564		
	Exponential	1.155	0.921	0.612		
	Polynomial	1.333	0.843	0.548		
$+1$	Exact	0.690	0.449	0.113		
	Exponential	0.725	0.500	0.207		
	Polynomial	0.671	0.445	0.147		
$+2$	Exact	0.445	0.249	0.005		
	Exponential	0.474	0.288	0.071		
	Polynomial	0.443	0.256	0.040		

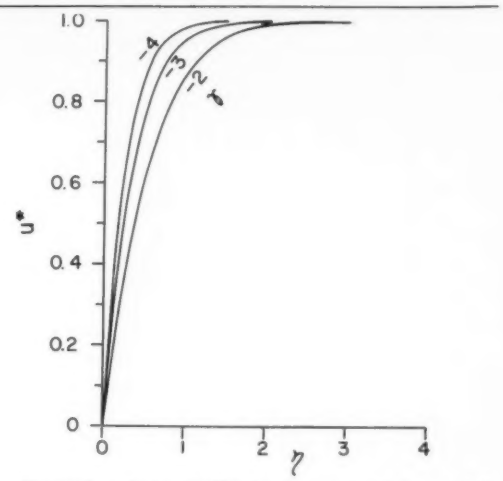

FIG. 4. Unsteady velocity profiles for $\alpha = -1$ and $\beta = +1/2$.

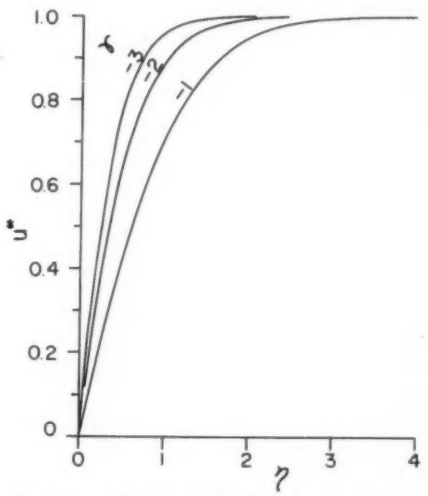

FIG. 5. Unsteady velocity profiles for $\alpha = -1$ and $\beta = +1$

The comparison of thermal-layer calculations may be made in two parts. One is to compare $G'(0)$ values, which, according to Eq. (47), are directly related to the coefficients of heat transfer in low-speed flow, and the other is to compare values of $F'(0)$, which represent contributions of friction heat to the rate of heat transfer at the plate surface. From Eq. (37), we have

$$(\partial\zeta/\partial\eta)_{\eta=0} = F'(0) + (1/E)G'(0) \quad (51)$$

in which the partial derivative may also be expressed in terms of the temperature gradient at the plate, as follows:

$$(\partial\zeta/\partial\eta)_{\eta=0} = -(1/E)[C(1 + t^*)/R_t]^{1/2}(\partial\theta/\partial Y)_w \quad (52)$$

A combination of Eqs. (51) and (52) then yields

$$G'(0) = -\{[C(1 + t^*)/R_0]^{1/2}(\partial\theta/\partial Y)_w\}_{E\to 0} \quad (53)$$

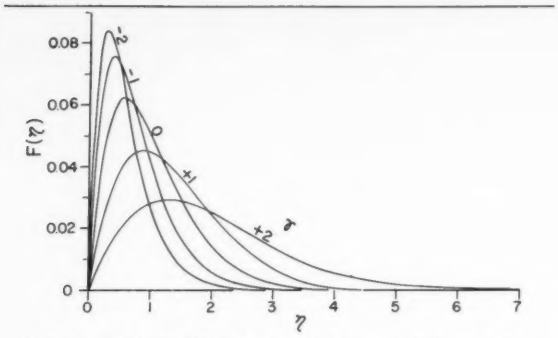

FIG. 6. $F(\eta)$ profiles for $\alpha = -1$, $\beta = -1$, and $\sigma = 0.7$.

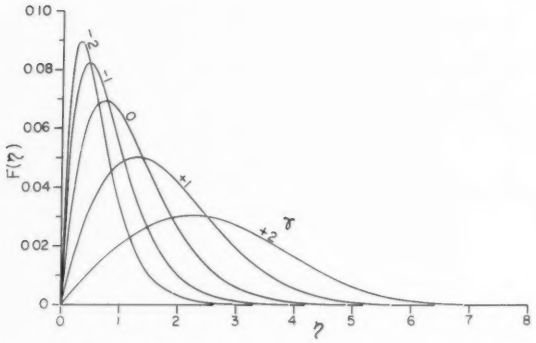

FIG. 7. $F(\eta)$ profiles for $\alpha = -1$, $\beta = -1/2$, and $\sigma = 0.7$.

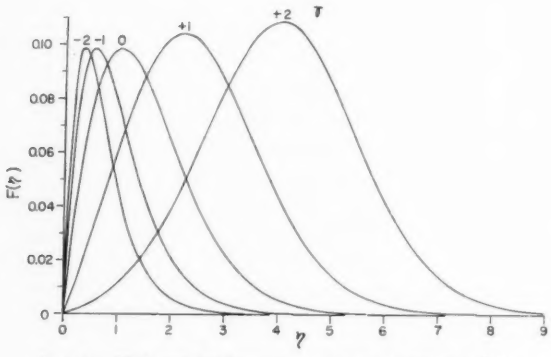

FIG. 8. $F(\eta)$ profiles for $\alpha = -1$, $\beta = 0$, and $\sigma = 0.7$.

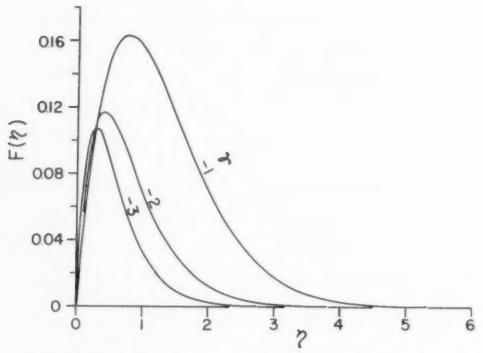

FIG. 9. $F(\eta)$ profiles for $\alpha = -1$, $\beta = +1/2$, and $\sigma = 0.7$.

$$F'(0) = -\{(1/E)[C(1 + t^*)/R_0]^{1/2}(\partial\theta/\partial Y)_w\}_{E\to\infty} \tag{54}$$

Note, by introducing the two types of transformed temperature profiles indicated in Section (3), the following respective equations are obtained:

For the exponential profile

$$\left.\begin{aligned} G'(0) &= -[(1 - J^2)\gamma/\Gamma]_{E\to 0} \\ F'(0) &= -[(1 - J^2)\gamma/E\Gamma]_{E\to\infty} \end{aligned}\right\} \tag{55}$$

For the polynomial

$$\left.\begin{aligned} G'(0) &= -(g_1g_2\gamma/\Gamma)_{E\to 0} \\ F'(0) &= -(g_1g_2\gamma/E\Gamma)_{E\to\infty} \end{aligned}\right\} \tag{56}$$

In the case of exponential profiles, Eqs. (17) and (18) reduce, respectively, to

$$\left.\begin{aligned} (\Gamma/\gamma)^2 &= 2\Gamma + (2/\sigma)(1 - J^2) \\ \delta\Gamma(1 - J^2) &+ (2J + 1)(1 - J)^2 = 0 \end{aligned}\right\} \tag{57}$$

in which Γ and γ are unknowns for a set of specified values of γ and σ. It is interesting to note that $G'(0)$, according to Eqs. (55) and (57), is independent of the flow parameter β, a feature which agrees with the exact solution, Eq. (41). A similar consideration may also be made of Eqs. (22) and (23), which, when again evaluated at $E = 0$, become

$$\left.\begin{aligned} (\Gamma/\gamma)^2 &= 2\Gamma + (2/\sigma)g_1g_2 \\ 2b_2g_2^2 &+ \sigma\Gamma g_1g_2 = 0 \end{aligned}\right\} \tag{58}$$

respectively. With $\sigma = 0.7$, $G'(0)$ values have been calculated for different values of γ from Eqs. (55), (57), (58), and (56). The results, together with those calculated from the exact solution, are shown in Table 2. It is seen that the approximate values based on exponential profiles again agree very well with the exact values under suction conditions, while those from the polynomials tend to be more accurate when injection prevails. The polynomial solution again does not yield sensible results when suction is large.

Now the approximate calculations of $F'(0)$ are considered. As E approaches infinity, it is expected that J and Γ associated with the exponential profiles behave,

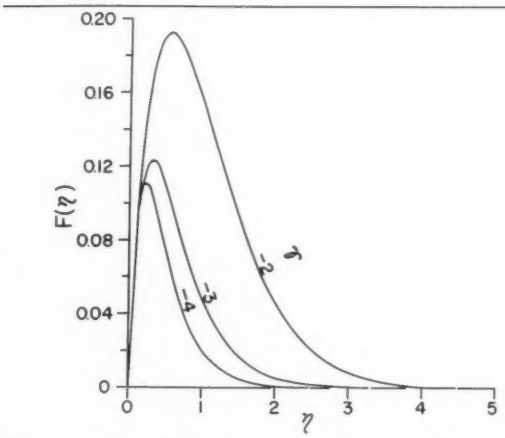

FIG. 10. $F(\eta)$ profiles for $\alpha = -1$, $\beta = +1$, and $\sigma = 0.7$.

respectively, as

$$J = -J_\infty E, \quad \Gamma = \Gamma_\infty E$$

where J_∞ is a positive constant, and Γ_∞ is also a constant, but has the same sign as that of γ considered. Accordingly, Eqs. (17) and (18), as $E \to \infty$, reduce, respectively, to

$$\left.\begin{aligned} &[\sigma u^{*\prime}(0)/4][(K^2 + 2K + 2)/(1 + K)] + \\ &\qquad [\sigma(4\beta - 1)/2\gamma]\Gamma_\infty = \gamma J_\infty{}^2/\Gamma_\infty \\ &2J_\infty{}^3 + \sigma J_\infty{}^2\Gamma_\infty = \{\sigma[u^{*\prime}(0)]^2/\gamma^2\}\Gamma_\infty{}^2 \end{aligned}\right\} \quad (59)$$

The two unknowns J_∞ and Γ_∞ may then be solved uniquely. Finally, $F'(0)$ is determined from

$$F'(0) = -[(1 - J^2)\gamma/E\Gamma]_{E\to\infty} = \gamma J_\infty{}^2/\Gamma_\infty \quad (60)$$

The corresponding equations based on polynomials may be similarly derived, and they are shown as follows:

$$\left.\begin{aligned} &[\sigma u^{*\prime}(0)/105][(a_2{}^2 - 8a_2 + 156)/f_1] + \\ &\qquad [\sigma(4\beta - 1)/2\gamma]\Gamma_\infty = \gamma b_{2\infty}{}^2/180\Gamma_\infty, \\ &b_{2\infty}{}^3 + 10\sigma b_{2\infty}{}^2\Gamma_\infty = \{1800\sigma[u^{*\prime}(0)]^2/\gamma^2\}\Gamma_\infty{}^2 \end{aligned}\right\} \quad (61)$$

$$F'(0) = \gamma b_{2\infty}{}^2/180\Gamma_\infty \quad (62)$$

where the constant $b_{2\infty}$ is introduced through $b_2 = -b_{2\infty}E$. Table 3 shows the calculated $F'(0)$ values from Eqs. (59), (60), (61), and (62) as compared to those according to the exact solution. It is evident that the overall agreement is very satisfactory, except in those cases close to laminar separation. The relative merits of the two types of profiles used in the integral solution with respect to $F'(0)$ values are seen to be the same as those already indicated.

Since these comparisons have covered adequate ranges of variation of the two unsteady parameters β and γ, it may be concluded, for the general unsteady problem on the basis of the results of these comparisons, (1) that the integral solution presented previously is capable of yielding accurate results on unsteady laminar boundary-layer behavior except in the immediate neighborhood of laminar separation, (2) that under unsteady suction conditions, the integral procedure based on exponential profiles may be used, and the result is expected to be accurate, especially when the suction rate and acceleration are large, and (3) that the integral solution with polynomial profiles tends to yield more accurate results when injection occurs at the plate surface, especially when laminar separation is approached.

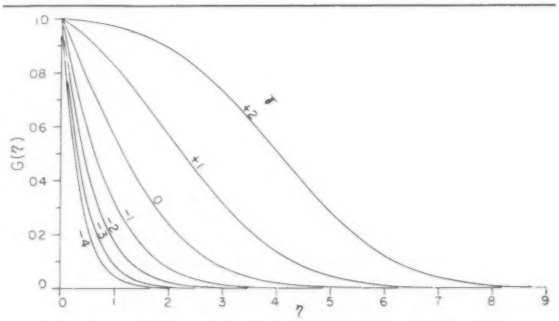

FIG. 11. $G(\eta)$ profiles for $\alpha = -1$, any β, and $\sigma = 0.7$.

TABLE 2

$G'(0)$ Values for Different Unsteady Parameter γ With $\alpha = -1$, $\sigma = 0.7$, and any β

γ		$G'(0)$
−4	Exact	−2.913
	Exponential	−2.917
	Polynomial	—
−3	Exact	−2.246
	Exponential	−2.248
	Polynomial	—
−2	Exact	−1.598
	Exponential	−1.603
	Polynomial	—
−1	Exact	−0.990
	Exponential	−1.004
	Polynomial	—
0	Exact	−0.472
	Exponential	−0.512
	Polynomial	−0.458
+1	Exact	−0.133
	Exponential	−0.209
	Polynomial	−0.155
+2	Exact	−0.015
	Exponential	−0.061
	Polynomial	−0.050

(6) Some General Conclusions

In a practical application with a set of specific unsteady free-stream flow and surface suction or injection conditions, conclusions can only be drawn after the integral procedure is applied and result obtained. However, in view of the fact that the results of the exact solution do cover cases with acceleration, deceleration, unsteady suction, and injection, it is possible to draw

TABLE 3

$F'(0)$ Values for Different Unsteady Parameters β and γ With $\alpha = -1$ and $\sigma = 0.7$

γ	β	−1	−(1/2)	0	+(1/2)	+1
−4	Exact					1.456
	Exponential					1.437
	Polynomial					—
−3	Exact				1.108	1.139
	Exponential				1.099	1.107
	Polynomial				—	—
−2	Exact	0.804	0.785	0.774	0.788	0.957
	Exponential	0.807	0.785	0.777	0.776	0.963
	Polynomial	—	—	—	—	—
−1	Exact	0.515	0.486	0.466	0.525	
	Exponential	0.512	0.479	0.452	0.401	
	Polynomial	—	—	—	—	
0	Exact	0.282	0.240	0.207		
	Exponential	0.274	0.226	0.169		
	Polynomial	0.475	0.244	0.189		
+1	Exact	0.129	0.086	0.052		
	Exponential	0.123	0.078	0.024		
	Polynomial	0.132	0.080	0.034		
+2	Exact	0.054	0.025	0.005		
	Exponential	0.053	0.025	0.002		
	Polynomial	0.055	0.023	0.006		

certain qualitative conclusions about these unsteady effects on laminar boundary-layer behavior over infinite plates.

(1) The skin friction at the plate increases with increasing acceleration, independent of whether there is suction or injection at the surface. It also increases with increasing rate of suction for any given unsteadiness in the free-stream flow. These effects are generally known, since they may be readily arrived from quasi-steady solutions.

(2) As long as acceleration prevails in the free-stream flow, including the case of zero acceleration, no laminar separation is possible, unless the rate of injection becomes infinite. This is well substantiated by results shown in Table 1. In fact, this conclusion may also be shown from the integral solution. At laminar separation (i.e., $K = -1$), Eq. (15) reduces to

$$du_\infty/d\bar{t} = -(4u_\infty/Z)$$

indicating that this condition is only satisfied when the free-stream flow is decelerating, since both u_∞ and Z must always be positive.

(3) In steady flow theory, it is known that laminar separation to a certain extent is related to the instability of the laminar boundary layer. If this is also true in the unsteady case, then it will be relatively difficult to maintain a stable laminar boundary layer under deceleration conditions, unless an adequate rate of suction is provided.

(4) When the flow is incompressible, the rate of heat transfer at the plate surface, according to the exact solution, is independent of the unsteadiness in the free-stream flow. In the general unsteady problem, it is very likely that this heat-transfer rate is only a weak function of the flow unsteadiness. This conclusion, at least, agrees with one of the findings of the present writer in dealing with another unsteady laminar boundary-layer problem involving a pressure gradient.[12] Furthermore, this rate of heat transfer increases with increasing suction, but decreases with increasing injection. This is evident in view of Table 2.

(5) The contribution of friction heat on the rate of heat transfer at the plate surface in the compressible flow case may be considered on the basis of Eq. (47) and values indicated in Table 3. For large $E(t^*)$ values, which correspond physically to high velocities in the free-stream flow, the contribution of friction heat decreases with decreasing suction and increasing injection. It also decreases with decreasing acceleration. Furthermore, when deceleration becomes large under suction conditions, the trend is reversed and the friction-heat contribution becomes increasingly larger in magnitude.

References

[1] Schlichting, H., *Die Grenzschicht mit Absaugung und Ausblasen*, Luftfahrtforschung, Vol. 19, p. 179, 1942.

[2] Illingworth, C. R., *Some Solutions of the Equations of Flow of a Viscous Compressible Fluid*, Proceedings, Cambridge Philosophical Society, Vol. 46, pp. 469–478, 1950.

[3] Illingworth, C. R., *Unsteady Laminar Flow of Gas Near an Infinite Flat Plate*, Proceedings, Cambridge Philosophical Society, Vol. 46, Pt. 4, pp. 603–613, 1950.

[4] Howarth, L., *Rayleigh's Problem for a Semi-Infinite Plate*, Proceedings, Cambridge Philosophical Society, Vol. 46, pp. 127–140, 1950.

[5] Stuart, J. T., *A Solution of the Navier-Stokes and Energy Equations Illustrating the Response of Skin Friction and Temperature of an Infinite Plate Thermometer to Fluctuations in Stream Velocity*, Proceedings, Royal Society of London, Series A, Vol. 231, pp. 116–130, 1955.

[6] Lighthill, M. J., *The Response of Laminar Skin Friction and Heat Transfer to Fluctuations in the Stream Velocity*, Proceedings, Royal Society of London, Series A, Vol. 224, pp. 1–23, 1954.

[7] Hasimoto, H., *Boundary Layer Growth on a Flat Plate With Suction or Injection*, J. Phys. Soc. Japan, Vol. 12, pp. 68–72, 1957.

[8] Moore, F. K., *Unsteady Laminar Boundary-Layer Flow*, NACA TN 2471, 1951.

[9] Schlichting, H., *Boundary Layer on Flat Plate Under Condition of Suction and Air Injection*, Luftfahrtforschung, Vol. 19, No. 9, pp. 293–301, 1942.

[10] Lew, H. G., *On the Compressible Boundary Layer Over a Flat Plate With Uniform Suction*, Reissner Anniversary Volume, pp. 42–60, J. W. Edwards, Ann Arbor, Michigan, 1949.

[11] Hildebrand, F. B., *Introduction to Numerical Analysis*, McGraw-Hill Book Company, Inc., 1956.

[12] Yang, K. T., *Unsteady Laminar Boundary Layers in an Incompressible Stagnation Flow*, J. Appl. Mech., Vol. 25, No. 4, pp. 421–427, 1958.

Shroud Tests of Pressure and Heat Transfer Over Short Afterbodies With Separated Wakes

(Continued from page 636)

[9] Rabinowicz, J., *Measurement of Turbulent Heat Transfer Rates on the Aft Portion and Blunt Base of a Hemisphere Cylinder in the Shock Tube*, Jet Propulsion, Vol. 28, No. 9, pp. 615–620, September, 1958.

[10] Powers, William E., Stetson, Kenneth F., and Adams, Mac C., *A Shock Tube Investigation of Heat Transfer in the Wake of a Hemisphere-Cylinder, With Application to Hypersonic Flight*, AVCO Research Laboratory, Research Rep. No. 30, August, 1958.

[11] Lehnert, R., and Schermerhorn, V. L., *Correlation of Base Pressure and Wake Structure of Sharp- and Blunt-Nose Cones With Reynolds Number Based on Boundary-Layer Momentum Thickness*, Readers' Forum, Journal of the Aero/Space Sciences, Vol. 26, No. 3, p. 185, March, 1959

A Study of Creep Collapse of a Long Circular Cylindrical Shell Under Uniform External Pressure

N. J. HOFF,* W. E. JAHSMAN,** AND W. NACHBAR***

Lockheed Aircraft Corporation

Summary

A long, thin-walled cylindrical shell is loaded by a uniform external pressure. Equations are developed for the time behavior of the shape of the cross section under the following conditions: (a) the shell material exhibits only secondary (steady) creep deformations expressible by a power creep law; (b) the initial and subsequent mode shape of the deviations from circularity of any cross section is two-lobed; and (c) the shell construction is of the sandwich type, with concentric cylindrical membranes taking normal stresses and an annular core supporting shear without deformation. Explicit solutions are obtained for the particular case of the cubic creep law. It is shown that the nondimensional amplitude of the cross-sectional mode shape (briefly, shape factor) will become infinite in a finite time. Curves of shape factor versus time and of collapse time versus initial value of the shape factor are presented. Also given are an explicit expression for and a curve of the expected variation in collapse time owing to uncontrollable deviations from a nominal initial value of the shape factor. It is shown that the expected variation is small if the nominal initial shape factor value is sufficiently large.

Symbols

A = cross-sectional area per unit length of shell wall
B = point on shell circumference defined by R, ϕ
H = horizontal force in shell wall
J_2 = second stress invariant
K = creep law constant
L = length of column
M = bending moment in shell wall (per unit length)
N = bending moment in shell wall at $\phi = 0$ (per unit length)
P = compressive force in shell wall (per unit length)
R = radial distance from point on circumference of shell to center of shell
$\bar{R}$ = average radius of shell
S = shear force in shell wall (per unit length)
V = vertical force in shell wall (per unit length)
X = $\alpha\bar{R}/\rho$; weighted shape factor of cross section
Y = $N/\alpha p\bar{R}^2$
Z = $(1 - Y)/\alpha$
d_0 = initial deviation from straightness of column
h = sandwich shell wall thickness
h_e = wall thickness of equivalent homogeneous shell
k = creep law constant
n = creep law exponent
p = uniform external pressure acting on shell
s = circumferential arc length
t = time
t_{cr} = critical time
x, y, z = rectangular coordinates
α = shape factor of cross section
β = angle between tangent to circumference and normal to R
$\dot{\epsilon}$ = creep strain rate
$\dot{\kappa}_a$ = time rate of change of the geometric curvature of shell in plane of the cross section
$\dot{\kappa}_c$ = time rate of change of the curvature obtained through creep law and equilibrium considerations
λ = creep law constant
ρ = shell wall radius of gyration
σ = stress
τ = $[(nk/3)(p\bar{R}/A\lambda)^n(\bar{R}/\rho)^2]^{-1}$, time constant
ϕ = polar angle
ξ = variable of integration
Δt = time increment
Δt_{cr} = deviation in critical time
ΔX_0 = uncertainty in initial shape-factor amplitude

Subscripts and Superscripts

B = point corresponding to R, ϕ
i = concave side of the tube
o = convex side of the tube or initial value
z = axial direction
ϕ = circumferential direction
$'$ = referring to column; derivative with respect to ϕ; or referring to deviatoric stress

Introduction

A LONG, thin-walled cylindrical shell, whose material is subject to creep, is under the action of a uniform external pressure, p. The cross section is assumed to have some slight initial deviation from circularity. This initial deviation is increased by the creep deformations at an increasing rate with time until the cylinder collapses. In the subsequent analysis of creep collapse, the following simplifying assumptions are made: (a) the shell wall construction is of the ideal sandwich type; i.e., bending moments and normal forces are supported by membrane stresses in two concentric cylindrical sheets, and shear is supported without deformation by the core annulus between the sheets; (b) the sheet material exhibits only secondary creep deformation; primary creep as well as elastic and plastic deformations are absent; and (c) the initial as well as all later shapes of the cross section are quasi-elliptically cylindrical,

Received June 23, 1958. Presented at the Thermal Stress Session, Twenty-Seventh Annual Meeting, IAS, New York, January 26–29, 1959.

* Head, Department of Aeronautical Engineering, Stanford University, and Consultant, Lockheed Missiles and Space Division.

** Research Scientist, Lockheed Missiles and Space Division.

*** Staff Scientist, Lockheed Missiles and Space Division.

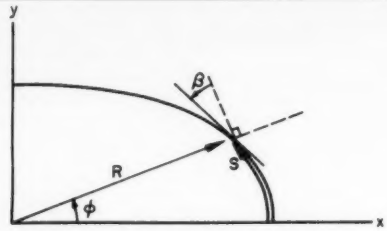

FIG. 1. Shape of the median line of cross section.

corresponding to the two-lobe mode of collapse in the elastic case.

The analysis proceeds by developing two separate expressions for the time rate of change of the curvature at every point along the median line of the deformed cross section. In the first expression, the curvature rate is calculated by employing differential geometry alone; this curvature rate is designated as $\dot{\kappa}_g$. In the second expression, the curvature rate is related to the external pressure and the shape of the deformed cross section. This relationship is accomplished in three steps: first, by relating the curvature rate to the strain rate of the cylindrical sheet elements; second, by relating the strain rate to stress and stress resultants through the creep law; and, finally, by relating the stress resultants to the imposed loading through the equations of equilibrium. The time rate of change of curvature found in this manner is called $\dot{\kappa}_c$. If the exact shape of the deformed cross section were known, $\dot{\kappa}_g$ and $\dot{\kappa}_c$, as computed from this shape, would be identically equal at every point along the median line. But, since the deformation is constrained according to condition (c) above, $\dot{\kappa}_g$ and $\dot{\kappa}_c$ are not identically equal, even though their maximum, minimum, and nodal points coincide. However, the assumed shape of the deformed cross section has one free parameter, which is a function of time and is called the shape factor. At any time, this factor can be so chosen that $\dot{\kappa}_g$ and $\dot{\kappa}_c$ are made approximately equal according to some criterion. The criterion chosen here involves a continuous collocation technique such that the average value of the difference $(\dot{\kappa}_g - \dot{\kappa}_c)$ over any quadrant of the cross section between nodes will vanish. Imposition of this condition establishes a differential equation, the solution of which gives the growth of the shape factor in time as a function of the shell dimensions, pressure, material properties, and initial deviation. The differential equation can be solved by quadratures.

For the case of the cubic creep law, the integration is carried out explicitly and a simple, closed formula is obtained for time as a function of a weighted shape factor which is proportional to the maximum amplitude of the deformation. This formula shows that the amplitude will grow from a small positive initial value beyond bounds in a finite time interval. This time interval is designated as the critical time. The time behavior of the amplitude is such that it will become large and grow rapidly only for times close to the critical time. For this reason, the critical time is considered likely to be a close approximation to the actual observed creep collapse time of the shell.

Only one paper on the general subject of the creep collapse of shells subjected to external pressure is known to the authors. This is the work of Sundström,[1] which deals with the problem of a cylindrical shell of finite length under axial compression and external pressure. Although the problem which Sundström considers is more general than that presented here, the assumptions on the moment distribution, which are necessary in Sundström's work in order to obtain a solution, appear to be somewhat restrictive. Sundström does not present explicit solutions, so that a comparison of the results of the two analyses is not possible.

Analysis of Collapse Phenomenon

At any time, t, the median line in the cross section is defined by a functional relationship of the type, $R = R(\phi, t)$. A typical $R - \phi$ curve is plotted in Fig. 1.

In Fig. 1, R is the radial distance from the origin to a point on the median line of the cross section, ϕ is the angle subtended by the radius and the x axis, s is the circumferential arc length from the x axis to the radius, and β is the angle between the tangent to the circumference at $R(\phi)$ and a normal to the radius. Expressions for β, the differential arc length ds, and the curvature κ_g in terms of R and its derivatives[2] are

$$\beta = -\tan^{-1}(R'/R) \tag{1a}$$

$$\kappa_g = (R^2 + 2R'^2 - RR'')/(R^2 + R'^2)^{3/2} \tag{1b}$$

$$ds = (R^2 + R'^2)^{1/2} d\phi \tag{1c}$$

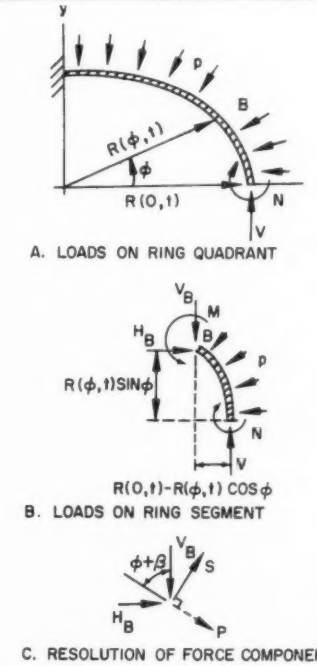

FIG. 2. Forces and moments acting on a ring.

The prime denotes differentiation with respect to ϕ.

At any time, equations of equilibrium relating forces and bending moments in the ring to the external uniform pressure, p, and the deformed shape of the cross section may be written if the motion of the ring is so slow that inertia terms can be neglected. A two-lobe collapse mode is assumed, so that it is sufficient to consider equilibrium conditions in one quadrant of the ring (see Fig. 2). The quadrant is taken to be bounded by axes of symmetry.

Force equilibrium equations in the x and y directions may be written by inspection of Fig. 2(b)

$$H_B - pR(\phi, t) \sin \phi = 0 \tag{2a}$$

$$V - V_B - p[R(0, t) - R(\phi, t) \cos \phi] = 0 \tag{2b}$$

As a consequence of symmetry, shear forces at $\phi = 0$ and $\phi = \pi/2$ must vanish. This fact has already been used in arriving at Eq. (2a), and, if V_B is set equal to zero at $\phi = \pi/2$ in Eq. (2b), the following equation is obtained for V:

$$V - pR(0, t) = 0 \tag{2c}$$

Eqs. (2a) and (2c) can be transformed to a more useful form by substituting into the relations for the normal and shear forces P and S as obtained by inspection of Fig. 2(c),

$$P = H_B \sin (\phi + \beta) + V_B \cos (\phi + \beta) \tag{3a}$$

$$S = H_B \cos (\phi + \beta) - V_B \sin (\phi + \beta) \tag{3b}$$

the expressions for H_B and V_B as given by Eqs. (2a) and (2b). The result is

$$P = pR(\phi, t) \cos \beta \tag{4a}$$

$$S = -pR(\phi, t) \sin \beta \tag{4b}$$

Moment equilibrium about point B may be written, by inspection of Fig. 2(b), as

$$N + (p/2)[R(0, t) - R(\phi, t) \cos \phi]^2 + (p/2)[R(\phi, t) \times \sin \phi]^2 - M - V[R(0, t) - R(\phi, t) \cos\phi] = 0 \tag{5a}$$

Substitution for V from Eq. (2c) and simplification give

$$M = N + (p/2)[R^2(\phi, t) - R^2(0, t)] \tag{5b}$$

The statically indeterminate bending moment, N, is still to be determined.

To avoid complications in the superposition of compressive and bending stresses in consequence of the nonlinearity of the creep law, the wall of the cylinder is assumed to be constructed in accordance with the sandwich principle. As shown in Fig. 3, it consists of two sheets of area $A/2$, separated by a distance $h = 2\rho$. The ratio of the thickness of each sheet to the thickness of the shell is so small that powers of this ratio higher than the first can be neglected against the ratio itself. The sheets carry the normal stresses only, while the core, not resistant to normal stress, is capable of transmitting shearing stresses without deformation. Work carried out by Patel, et al.[3] has shown that these

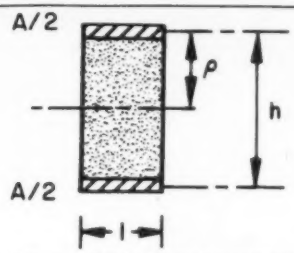

FIG. 3. Sandwich wall construction.

assumptions represent the actual conditions with acceptable accuracy.

Under these assumptions, the normal circumferential stresses in the sheet on the convex side, subscript o, and on the concave side, subscript i, can be given as

$$\sigma_o = (1/A)[P - (M/\rho)] \tag{6a}$$

$$\sigma_i = (1/A)[P + (M/\rho)] \tag{6b}$$

The force P and the stresses σ are positive when they are compressive. The moment M is positive if it has the same sense as N in Fig. 2.

The ring, to represent the cylinder from which it was cut, must be in a state of plane strain. This means that normal stresses arise in the direction of the axis of the cylinder. The biaxial strain rate law to be used here was proposed earlier by Odqvist[4]

$$\dot{\epsilon}_\phi = (3K/2\lambda^n)(3J_2')^{(n-1)/2}\sigma_\phi' \tag{7a}$$

$$\dot{\epsilon}_z = (3K/2\lambda^n)(3J_2')^{(n-1)/2}\ \sigma_z' \tag{7b}$$

where K and λ are constants having the dimensions of time^{-1} and stress, and n is a number greater than one. The dot denotes differentiation with respect to time. J_2', the second scalar invariant of the deviatoric stress tensor, is always positive, and the sign of the strain rate, $\dot{\epsilon}$, is determined by the sign of the stress deviator, σ'. J_2', σ_ϕ', and σ_z' are given by the relations

$$J_2' = (1/3)(\sigma_\phi^2 + \sigma_z^2 - \sigma_\phi\sigma_z) \tag{8a}$$

$$\sigma_\phi' = (2/3)\sigma_\phi - (1/3)\sigma_z \tag{8b}$$

$$\sigma_z' = (2/3)\sigma_z - (1/3)\sigma_\phi \tag{8c}$$

where σ_ϕ and σ_z are the principal normal stresses in the circumferential and axial directions.

The condition of plane strain is represented by setting $\dot{\epsilon}_z$ equal to zero. Inspection of Eq. (7b) shows that this condition is equivalent to the requirement that σ_z' vanish, since J_2' is always positive. Then, by Eq. (8c),

$$\sigma_z = (1/2)\sigma_\phi \tag{8d}$$

and Eq. (7a) may be rewritten as

$$\dot{\epsilon} = k(\sigma/\lambda)^n \tag{9}$$

where $k = (3/4)^{[(1/2)(n+1)]}\ K$. The subscript ϕ has been omitted for convenience in later calculations.

Substitution for σ in Eq. (9) by means of Eqs. (6a) and (6b) leads to the following relations between strain

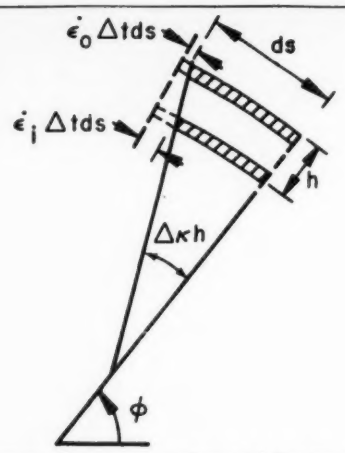

FIG. 4. Geometry for curvature change of element of length ds.

rates in the inner and outer sheets, and bending moments and forces in the ring:

$$\dot{\epsilon}_o = (k/A^n\lambda^n)P^n[1 - (M/P\rho)]^n \tag{10a}$$

$$\dot{\epsilon}_i = (k/A^n\lambda^n)P^n[1 + (M/P\rho)]^n \tag{10b}$$

In a time increment, Δt, strains at the inner and outer sheets of an element of length ds change by an amount $\dot{\epsilon}_i\Delta t$ and $\dot{\epsilon}_0\Delta t$. As shown in Fig. 4, the change in curvature of the element is given by

$$\Delta\kappa_c = (1/h)(\dot{\epsilon}_i\Delta t - \dot{\epsilon}_0\Delta t)$$

or

$$\dot{\kappa}_c = (1/h)(\dot{\epsilon}_i - \dot{\epsilon}_0) \tag{11}$$

The rotation rate at one point on the median line located by the angle ϕ with reference to the point $\phi = 0$ can be obtained from the relation defining the relative rotation rate $\Delta\dot{\theta}$; viz.,

$$\Delta\dot{\theta} = \int_0^{s(\phi)} \dot{\kappa}_c\, ds \tag{12}$$

The magnitude of the moment N can be calculated from the condition of compatibility of rotation rates. Because of the symmetry imposed on the quadrant shown in Fig. 2, the relative rotation rate between $\phi = 0$ and $\phi = \pi/2$ must vanish. Hence, by Eq. (12),

$$\Delta\dot{\theta} = \int_0^{s(\pi/2)} \dot{\kappa}_c\, ds = 0 \tag{13}$$

By substituting first for $\dot{\epsilon}_0$ and $\dot{\epsilon}_1$ in Eq. (11) by means of Eqs. (10a) and (10b), then for P and $(M/P\rho)$ by means of Eqs. (4a) and (5b), an expression for the unknown moment N is obtained.

Shape of the Median Line

It has been tacitly assumed that the dependence of R and ϕ is known explicitly. This is now taken in the form

$$R(\phi, t) = \bar{R}[1 + \alpha(t)\cos 2\phi] \tag{14}$$

where α is referred to hereafter as the shape factor and is dimensionless, positive, and time-dependent. The two-lobe mode shape is selected because it corresponds to the fundamental buckling mode shape of long elastic cylinders under uniform external pressure. The shape factor, α, indicates the degree of distortion of the cross section at any time.

Substitution for $R(\phi, t)$ in Eqs. (1a), (1b), (1c), (4a), and (5b) gives

$$\beta = \tan^{-1}[2\alpha \sin 2\phi/(1 + \alpha\cos 2\phi)] \tag{15a}$$

$$\dot{\kappa}_g = \frac{1}{\bar{R}}\left\{\frac{1 + 6\alpha\cos 2\phi + \alpha^2(5 + 3\sin^2 2\phi)}{[1 + 2\alpha\cos 2\phi + \alpha^2(1 + 3\sin^2 2\phi)]^{3/2}}\right\} \tag{15b}$$

$$ds = \bar{R}[1 + 2\alpha\cos 2\phi + \alpha^2(1 + 3\sin^2 2\phi)]^{1/2}d\phi \tag{15c}$$

$$P = p\bar{R}\left\{\frac{1 + 2\alpha\cos 2\phi + \alpha^2\cos^2 2\phi}{[1 + 2\alpha\cos 2\phi + \alpha^2(1 + 3\sin^2 2\phi)]^{1/2}}\right\} \tag{16a}$$

$$M = N - (\alpha p\bar{R}^2/2)[2(1 - \cos 2\phi) + \alpha\sin^2 2\phi] \tag{16b}$$

If the above expressions are used, determination of N and of the mode amplitude factor, α, is lengthy but not particularly difficult. The expressions simplify considerably when the shape of the cross section differs only slightly from the circle. Under these conditions, $\alpha \ll 1$ and Eqs. (15) and (16) can be simplified to

$$\beta \simeq \tan^{-1}(2\alpha\sin 2\phi) \tag{17a}$$

$$\kappa_g \simeq \bar{R}^{-1}(1 + 3\alpha\cos 3\phi) \tag{17b}$$

$$ds \simeq \bar{R}(1 + \alpha\cos 2\phi)d\phi \tag{17c}$$

$$P \simeq p\bar{R}(1 + \alpha\cos 2\phi) \tag{18a}$$

$$M = N - (\alpha p\bar{R}^2)[(1 - \cos 2\phi) + (1/2)\alpha\sin^2 2\phi] \tag{18b}$$

The α^2 term in Eq. (18b) for M is retained because both M and N are of order $(\alpha p\bar{R}^2)$ when α is small. This conclusion may be reached by observing that the curvature rate [time derivative of Eq. (17b)] has equal and opposite values at $\phi = 0$ and $\phi = \pi/2$. Since one expects similar behavior by the bending moment in the ring, by Eq. (18b)

$$M(0) \simeq -M(\pi/2)$$

or

$$N \simeq \alpha p\bar{R}^2$$

An improved approximation to N (and hence to M) will therefore require terms of order α^2.

The relation between curvature rate and moments and forces in the ring is obtained by combining Eqs. (4a), (5b), (10a), and (10b) with Eq. (11)

$$\dot{\kappa}_c = \left(\frac{k}{A^n\lambda^n h}\right)P^n\left\{\left[1 + \left(\frac{M}{P\rho}\right)\right]^n - \left[1 - \left(\frac{M}{P\rho}\right)\right]^n\right\} = \left(\frac{2nk}{A^n\lambda^n h}\right)P^n\left(\frac{M}{P\rho}\right)\times\left[1 + \frac{(n-1)(n-2)}{1\cdot 2\cdot 3}\left(\frac{M}{P\rho}\right)^2 + \frac{(n-1)(n-2)(n-3)(n-4)}{1\cdot 2\cdot 3\cdot 4\cdot 5}\left(\frac{M}{P\rho}\right)^4 + \cdots\right] \tag{19}$$

When n is an integer (which can usually be assumed with sufficient engineering accuracy), the expression in braces in Eq. (19) is a polynomial of degree $(n-1)$ in $M/P\rho$; otherwise, the series converges if $M/P\rho < 1$.

Eqs. (18a) and (18b) are combined to obtain an expression for $M/P\rho$,

$$\frac{M}{P\rho} = X\,\frac{(Y - 1 + \cos 2\phi) - (1/2)\alpha \sin^2 2\phi}{1 + \alpha \cos 2\phi} \tag{20a}$$

where

$$X \equiv \alpha\bar{R}/\rho \tag{20b}$$

$$Y \equiv N/\alpha p\bar{R}^2 \tag{20c}$$

X is defined as a weighted shape factor and equals the ratio of the radial displacement amplitude, $\alpha\bar{R}$, to the radius of gyration, ρ. Although α may be small compared to one, X need not be because α is multiplied by $\bar{R}/\rho$, a number much greater than one. Hence, all powers of X will be retained in subsequent expansions, although powers of α^2 and higher will be neglected as compared to one. Observations on N made earlier indicate that Y will be of order one. Consequently, Y will be expressed as*

$$Y = 1 - \alpha Z \tag{20d}$$

where Z is of order one.

Substituting for Y in Eq. (20a), expanding, and neglecting higher order terms in α, we obtain

$$M/P\rho = X\{\cos 2\phi - \alpha[Z + (1/2) + (1/2)\cos^2 2\phi]\} \tag{21a}$$

When raised to the mth power, Eq. (21a) gives (after linearization)

$$(M/P\rho)^m = X^m\{\cos^m 2\phi - m\alpha \cos^{m-1} 2\phi[Z + (1/2) + (1/2)\cos^2 2\phi]\} \tag{21b}$$

By Eq. (18a) the expression for P^n (after linearization) is

$$P^n = p^n\bar{R}^n(1 + n\alpha \cos 2\phi) \tag{21c}$$

The complete expression for the curvature rate is then found by substituting Eqs. (21b) and (21c) into Eq. (19) and linearizing:

$$\dot{\kappa}_c = \left(\frac{2nk}{h}\right)\left(\frac{p\bar{R}}{A\lambda}\right)^n X\left(\left\{\cos 2\phi + \frac{(n-1)(n-2)}{1\cdot 2\cdot 3}X^2\cos^3 2\phi + \frac{(n-1)(n-2)(n-3)(n-4)}{1\cdot 2\cdot 3\cdot 4\cdot 5}\times\right.\right.$$
$$\left.X^4\cos^5 2\phi + \ldots\right\} - \alpha\left[\left(Z + \frac{1}{2}\right) + \left[-\left(n - \frac{1}{2}\right) + 3\left(Z + \frac{1}{2}\right)\frac{(n-1)(n-2)}{1\cdot 2\cdot 3}X^2\right]\cos^2 2\phi +$$
$$\left.\frac{(n-1)(n-2)}{1\cdot 2\cdot 3}X^2\left[-\left(n - \frac{3}{2}\right) + 5\left(Z + \frac{1}{2}\right)\frac{(n-3)(n-4)}{4\cdot 5\cdot}X^2\right]\cos^4 2\phi + \ldots\right\}\right) \tag{22}$$

To solve for Z, the compatibility condition for the ends of the quadrant, Eq. (13), is used:

$$Z = \left\{\frac{1}{2}\left(n - \frac{1}{2}\right) + \frac{(n-1)(n-2)}{2^2\cdot 4}\left(n - \frac{5}{2}\right)X^2 + \frac{(n-1)(n-2)(n-3)(n-4)}{2^2\cdot 4^2\cdot 6}\left(n - \frac{9}{2}\right)X^4 + \ldots\right\} \div$$
$$\left\{1 + \frac{(n-1)(n-2)}{2^2}X^2 + \frac{(n-1)(n-2)(n-3)(n-4)}{2^2\cdot 4^2}X^4 + \ldots\right\} \tag{23a}$$

As can be shown by differentiation, Z has its maximum value at $X = 0$, where

$$Z_{max} = (1/2)[n - (1/2)] \tag{23b}$$

Since Eqs. (23a) and (23b) indicate that the assumption of Z of the order of one is justified, Eq. (22) for $\dot{\kappa}_c$ may be further simplified by neglecting terms of order α as compared to one. What remains is a series involving products of X and $\cos 2\phi$

$$\dot{\kappa}_c = \left(\frac{2nk}{h}\right)\left(\frac{p\bar{R}}{A\lambda}\right)^n X\left[\cos 2\phi + \frac{(n-1)(n-2)}{1\cdot 2\cdot 3}X^2\cos^3 2\phi + \frac{(n-1)(n-2)(n-3)(n-4)}{1\cdot 2\cdot 3\cdot 4\cdot 5}X^4\cos^5 2\phi + \ldots\right] \tag{24a}$$

An expression for the geometrical curvature rate, $\dot{\kappa}_g$, may be obtained by differentiating Eq. (17b) with respect to time:

$$\dot{\kappa}_g = 3(\rho/\bar{R}^2)\dot{X}\cos 2\phi \tag{25a}$$

Normally, $\dot{\kappa}_c = \dot{\kappa}_g$. Eq. (25a), however, involves only the single product of $\dot{X}$ and $\cos 2\phi$. The discrepancy in ϕ-dependence between Eqs. (24a) and (25a) results from the assumption made on the shape of the cross section. The exact shape could be obtained as the solution to Eq. (19) if the variables $\kappa_c = \kappa_g$, P, and $M/P\rho$ were replaced by R and its ϕ and t derivatives as given in Eqs. (1a), (1b), (4a), and (5b). The result would be a nonlinear partial differential equation which could probably be integrated only numerically. Constraining the cross section to deform in a two-lobe mode circumvents this problem, although it does give rise to the discrepancy between

* That $Y = 1$ when $\alpha = 0$ can be shown by solving Eqs. (13) and (19) at $\alpha = 0$.

Eqs. (24a) and (25a). Actually, the discrepancy is probably rather small—maximum, minimum, and zero points agree. An acceptable relation for X may be obtained by applying a continuous collocation technique to the two equations. The two expressions are integrated over an octant of the ring (curvature rate changes sign every $\pi/4$ radians) with the following results:

$$\dot{\kappa}_c = \frac{4}{\pi}\int_0^{\pi/4} \dot{\kappa}_c d\phi = \frac{2}{\pi}\left(\frac{2nk}{h}\right)\left(\frac{p\bar{R}}{A\lambda}\right)^n X\left[1 + \frac{(n-1)(n-2)}{1^2\cdot 3^2}X^2 + \frac{(n-1)(n-2)(n-3)(n-4)}{1^2\cdot 3^2\cdot 5^2}X^4 + \ldots\right] \tag{24b}$$

$$\bar{\dot{\kappa}}_g = (4/\pi)\int_0^{\pi/4} \dot{\kappa}_g\, d\phi = (2/\pi)3(\rho/\bar{R}^2)\dot{X} \tag{25b}$$

The averaged curvatures are equated to give

$$\dot{X} = \frac{X}{\tau}\left[1 + \frac{(n-1)(n-2)}{1^2\cdot 3^2}X^2 + \frac{(n-1)(n-2)(n-3)(n-4)}{1^2\cdot 3^2\cdot 5^2}X^4 + \ldots\right] \tag{26}$$

where $\tau^{-1} \equiv (nk/3)(p\bar{R}/A\lambda)^n(\bar{R}/\rho)^2$. The time dependence of X may be found by integration of Eq. (26)

$$t = \int_{X_0}^{X} [d\xi/\dot{X}(\xi)] \tag{27}$$

where X_0 is the value of X at $t = 0$, including initial elastic displacement.

Example of Cubic Creep Law

When the creep law is a cubic ($n = 3$), Eqs. (23a) and (26) reduce to

$$Z = (5/4)\{[1 + (1/20)X^2]/[1 + (1/2)X^2]\} \tag{28}$$

$$\dot{X} = (X/\tau)[1 + (2/9)X^2] \tag{29}$$

where $\tau^{-1} = k(p\bar{R}/A\lambda)^3(\bar{R}/\rho)^2$. Z is seen to vary between 5/4 and 5/40 for variations in λ between zero and infinity; hence, it is certainly of order one. Eq. (29) can be integrated directly to

$$t/\tau = (1/2)\log\{[X_c^2 + (9/2)]/[X_0^2 + (9/2)(X_0/X)^2]\} \tag{30}$$

A plot of X/X_c versus t/τ for $X_0 = 1.73$ is given in Fig. 5. This value of X_c was chosen as representative for the following reason: in a 1-in.-radius shell, an initial deviation of 5 mils is reasonable; this corresponds to an initial value α_0 of shape factor equal to 0.005. In the sandwich shell, the value of $\bar{R}/2\rho \equiv R/h$ for these values of X_0 and α_0 is 173. If we conceive of an equivalent homogeneous wall shell and assume that the normal stress distribution in creep is linear over the cross section, then for this shell $h_s = h/\sqrt{3}$ and $R/h_s = 100$, which is about the order of magnitude found for practical shells. It should be pointed out, however, that since the actual stress distribution in creep is nonlinear, the equivalence between homogeneous and sandwich shells can at best be considered a first approximation.

Inspection of Fig. 5 shows that the amplitude of the shape factor increases rather slowly during the major portion of the tube lifetime. Only after 90 per cent or more of the total lifetime has elapsed does the amplitude begin to rise abruptly. Lifetime, or "critical time," is that value of t/τ at which X/X_c becomes indefinitely large. It is found from Eq. (30) by letting $X_0/X \to 0$:

$$t_{cr}/\tau = (1/2)\log[1 + (9/2X_0^2)] \tag{31a}$$

When $X_0 = 1.73$, $t_{cr}/\tau = 0.458$. It is represented by the dashed vertical line in Fig. 5.

The form of Eq. (31a) is identical to the form found by Hoff[5] for the axially loaded column—viz.,

$$t'_{cr}/\tau' = (1/2)\log[1 + (4/X_0'^2)] \tag{31b}$$

where

$$(\tau')^{-1} \equiv k(P'/A'\lambda)^3[(\sqrt{3}L/\pi)/\rho']^2, \quad X_0' \equiv d_0/\rho'$$

d_0 is the initial deviation from straightness of the midlength of the column, and L is the length of the column. All other primed quantities are similar to what has been defined previously for the shell, the primes referring to the column. It is interesting to note the correspondence between the time constants τ and τ', and the shape factors X_0 and X_0': $p\bar{R}/A\lambda$ and $P'/A'\lambda$ are merely ratios of the nominal normal stress in the cross section to the creep parameter λ, so that the time constants τ and τ' are completely equivalent if the modified length $\sqrt{3}L/\pi$ of the column can be associated with the average radius $\bar{R}$ of the shell. This association is equivalent to replacing the shell with an axially loaded column whose length is $(1/2\sqrt{3})$ times the circumference of the shell. The equivalence between the shape factors X_0 and X_0' is seen when it is recalled that the

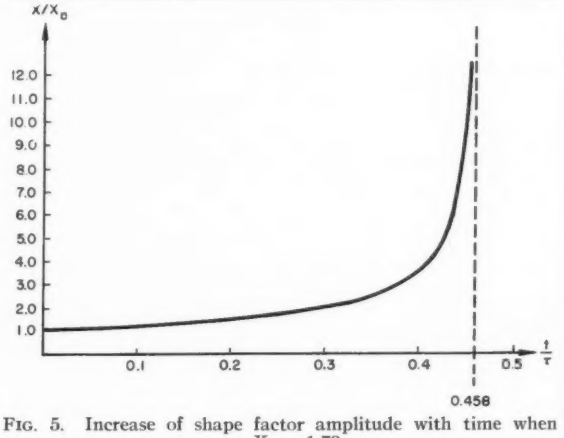

FIG. 5. Increase of shape factor amplitude with time when $X_0 = 1.73$.

former is the ratio of the maximum initial deviation from circularity to the radius of gyration of the shell wall, while the latter is the ratio of the initial maximum deviation from straightness to the radius of gyration of the column.

Eq. (31a) is quite general and shows the dependence of the critical time on initial shape factor amplitude. Fig. 6 has been prepared from Eq. (31a) for a ring with radius ratio $\bar{R}/\rho$ of 346. Thus, the scale of the abscissa may be converted from α_0 to X_0 by multiplying by 346. The logarithmic behavior may be easily observed, and it can be seen that values of critical times are relatively insensitive to minor fluctuations in the initial shape factor amplitude about some prescribed value. This characteristic may be demonstrated further by differentiating Eq. (31a) to obtain the ratio of the variation from the theoretically exact critical time to the critical time as a function of the desired initial shape factor amplitude and small uncontrollable deviations from this value:

$$\left|\frac{\Delta t_{cr}}{t_{cr}}\right| = \frac{9}{X_0^3[1 + (9/2X_0^2)] \log [1 + (9/2X_0^2)]} \Delta X_0 \tag{32}$$

where Δt_{cr} and ΔX_0 are the deviations from t_{cr} and X_0, respectively. Eq. (32) is accurate only when both $|\Delta t_{cr}/t_{cr}|$ and $\Delta X_0/X_0$ are small compared to one. It shows that the percentage variation in collapse time is proportional to the uncertainty in the initial shape-factor amplitude (as one would expect). The proportionality factor, however, is strongly dependent on X_0 as Fig. 7 shows. Values of $|\Delta t_{cr}/t_{cr}|$ versus X_0 have been plotted for ΔX_0 values of 0.1 and 0.2. The scales of Fig. 7 have been so chosen that $|\Delta t_{cr}/t_{cr}|$ and $\Delta X_0/X_0$ will not exceed 0.2 and thus invalidate the use of Eq. (32).

Fig. 7 shows that uncertainties in the desired value of initial shape factor have little effect on the critical time of the tube if the initial amplitudes themselves are sufficiently large. For example, an uncertainty of 0.1 in X_0 when $X_0 = 1.73$ produces only a 7 per cent change in critical time. In actual practice, this deviation would be all but masked by variations in mechanical and physical material properties, which are usually 10 per cent or more. When the X_0 of 1.73 refers to a tube with a radius ratio of 346 and an α_0 of 0.005, a ΔX_0 of 0.1 corresponds to a $\Delta\alpha_0$ of 0.00029. If the tube radius is 1 in., $\Delta\alpha_0$ corresponds to a radial tolerance of about 0.3 mil or less.* Such a tolerance is not difficult to achieve. However, if a smaller X_0 is chosen for the same tube, α_0 and hence $\Delta\alpha_0$ will be reduced, and the correspondingly smaller tolerance may be almost impossible to achieve. At the same time, the variation in critical time will increase. Consequently, information on very slight deviations from circularity must be quite exact if predictions on tube collapse times are to be reasonably accurate. Less precise information on initial shape factor amplitudes is needed when these amplitudes are larger, because the tube critical time is less sensitive for the larger initial amplitudes.

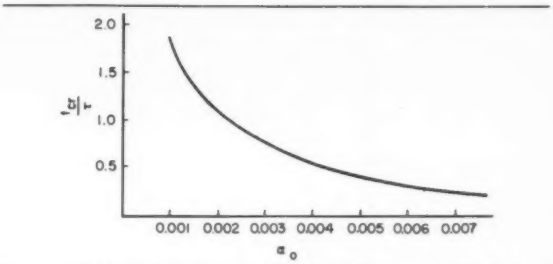

FIG. 6. Critical time versus initial shape factor amplitude for a shell with a radius ratio $\bar{R}/\rho$ of 346.

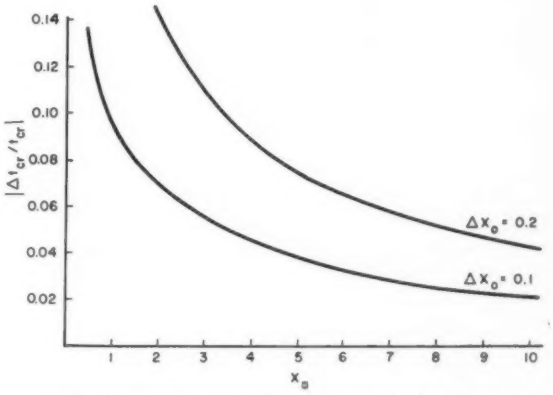

FIG. 7. Variation in critical time versus initial shape factor amplitude for two values of uncontrollable deviations in amplitude ΔX_0.

References

[1] Sundström, E., *Creep Buckling of Cylindrical Shells*, Transactions of the Royal Institute of Technology, No. 115, Stockholm, Sweden, 1957.

[2] Woods, F. S., and Bailey, F. H., *Elementary Calculus*, p. 193; Ginn and Company, New York, 1929.

[3] Patel, S. A., Kempner, J., Erickson, B., and Mobassary, A. H., *Correlation of Creep-Buckling Tests with Theory*, NACA RM 56C20, May, 1956.

[4] Odqvist, F. K. G., *Recent Advances in Theories of Creep of Engineering Materials*, Applied Mechanics Reviews, Vol. 7, No. 12, pp. 517–519, 1954.

[5] Hoff, N. J., *Buckling and Stability*, The Forty-First Wilbur Wright Memorial Lecture, J. R.Ae.S., January, 1954.

* If the external pressure p is sufficiently close to the instantaneous collapse pressure of the tube p_c, the original values of α and $\Delta\alpha$ (α_{00} and $\Delta\alpha_{00}$) must be much less than 0.005 and 0.00029 because of the amplification factor in the expression $\alpha_0 = [1 - (p/p_c)]^{-1}\alpha_{00}$ which becomes very large. The discussion above then applies to original radial tolerances only when p/p_c is small.

Readers' Forum

BRIEF REPORTS of investigations in the aerospace sciences and discussions of papers published in the JOURNAL are presented in this special department. Entries must be restricted to a maximum of 1,300 words or the equivalent of one JOURNAL page including formulas and illustrations. Publication is completed as soon as possible after receipt of the material. The Editorial Committee does not hold itself responsible for the opinions expressed by the correspondents.

Contents

On the Flow Past a Sphere at Hypersonic Speed With a Magnetic Field ..... N. C. FREEMAN 670

Author's Reply ..... NELSON H. KEMP 672

On the Local Elastic Stability of Honeycomb Face Plate Subjected to Uniaxial Compression ..... RAYMOND C. WEIKEL AND ALBERT S. KOBAYASHI 672

On the Concepts of Moving Electric and Magnetic Fields in Magnetohydrodynamics ..... J. E. MCCUNE AND W. R. SEARS 674

Stress Functions for Plates of Convex Polygonal Shape ..... HANS A. BALMER 675

A High-Temperature, Steady-Flow, Supersonic Tunnel ..... ROBERT A. GROSS 676

The Compressible Laminar Boundary Layer With Arbitrary Pressure Gradient and Wall Temperature Distribution ..... JAMES C. WILLIAMS, III 677

Stability Criteria for the Airframe Dynamics of a Liquid-Propellant Rocket ..... JOSEF S. PISTINER 678

A Note on the Blasius Equation With Three-Point Boundary Conditions ..... WILLIAM SQUIRE 678

A Remark Concerning the Vibration of a Delta Wing in Supersonic Flight ..... MILOMIR M. STANIŠIĆ 679

On the Stable Shape of a Slender Ablating Graphite Body ..... GEORGE W. SUTTON 681

Heat Transfer and Recovery Factor in a Laminar Boundary Layer With Arbitrary Pressure Gradient and Wall Temperature Distribution ..... BERNARD LE FUR 682

An Alternative Formulation of the Problem of Flutter in Real Fluids. WEN-HWA CHU AND H. NORMAN ABRAMSON 683

Shock Waves and Dissipation in a Resonance Tube ..... ASCHER H. SHAPIRO 684

On a Generalized Porous-Wall "Couette-Type" Flow ..... G. M. LILLEY 685

The Modified Goodman Diagram and Random Vibration ..... H. C. SCHJELDERUP 686

Calculation by the Integral Method of the Effect of Fluid Injection Upon an Isothermal Boundary Layer ..... MILTON M. KLEIN 686

Comments on "On Slip-Flow Heat Transfer to a Flat Plate" ..... DONALD E. NESTLER 687

On the Flow Past a Sphere at Hypersonic Speed With a Magnetic Field*

N. C. Freeman

Research Associate, Gas Dynamics Laboratory, Princeton University, Princeton, N.J.

March 24, 1959

THE CONSTANT DENSITY SOLUTION to the hypersonic inviscid flow past a sphere obtained by Lighthill[4] has been extended to the case of a sphere with a radial magnetic field in a conducting fluid by Kemp.[2] The solution obtained by Kemp uses the assumption that the magnetic Reynolds Number is small and, hence, the magnetic field induced by the flow is not considered. Since the flow is assumed to have constant density in the region behind the bow shock wave, the problem reduces to consideration of the effect of a ponderomotive force produced by the interaction of the magnetic field with the moving conducting fluid on the flow behind the bow shock wave.

The author became interested in this problem in making an attempt to extend the Newtonian theory of hypersonic flow, reviewed by Hayes and Probstein,[1] to the magnetic field problem. Unfortunately, the result obtained did not reduce to that of Kemp[2] in the region of the stagnation point. The author, therefore, in trying to explain this anomaly, found it necessary to examine Kemp's solution in some detail. In doing this, it was found that result as given by Kemp is incorrect due to assumptions of analyticity of the functions concerned. Kemp chooses to obtain the solution for large density ratio across the shock wave using a simple Taylor expansion to span the region between the shock and body. That this approach is beset with dangers can be seen directly from the equations concerned. The type of difficulty encountered is that discussed by Lighthill[3] where the first

* This research was sponsored by the USAF under Contract AF 49(638)-465 monitored by the AFOSR of the ARDC.

Contributors Please Note

Readers' Forum items must be confined to the equivalent of one page in the *Journal*. Contributions that exceed this limit will be returned to the authors for condensation and rewrite. To avoid inconvenience and delay, please adhere to the following specifications:

(1) Five, double-spaced, typewritten, manuscript pages (8 1/2 by 11 in.), including wide margins, formulas, and headings, equal one printed page.

(2) For every illustration, deduct at least one-half or as much as one manuscript page, depending on the size of the illustration.

approximation in some expansion procedure vanishes, causing a singular behavior in the higher-order terms. However, Lighthill outlines a scheme for making such approximations uniformly valid. It is the author's intention to present such a theory.

In a nondimensional form, the equations of the flow in the region behind the shock wave are

$$u(\partial u/\partial r) + (v/r)(\partial u/\partial \theta) - (v^2/r) + k(\partial p/\partial r) = 0 \quad (1)$$

$$u(\partial v/\partial r) + (v/r)(\partial v/\partial \theta) + (uv/r) + (k/r)(\partial p/\partial \theta) = -kvS_b \quad (2)$$

where the lengths are nondimensionalized with respect to the shock wave, c (assumed spherical) and velocities and pressure with respect to the free-stream conditions. The constant S_b denotes $c\sigma B_b^2/u_\infty \rho_\infty$ where B_b is the magnetic field at the body surface, which is assumed for our purpose to be constant throughout the layer. k is the ratio of the density in front of the shock wave to that behind, which is assumed constant throughout. These equations are, therefore, independent of the energy equations, and the continuity equation is satisfied by a stream function defined by

$$ur^2 \sin O = -(\partial\psi/\partial O), \quad vr \sin O = \partial\psi/\partial r \quad (3)$$

Eqs. (1) and (2) then reduce to

$$2\Psi(d/dr)\{[(d^2\Psi/dr^2) - (\Psi/r^2)](1/r^2)\} = kS_b(d/dr)[(1/r)(d\Psi/dr)] \quad (4)$$

where $\psi = \Psi(r)\sin^2\theta$ and we have assumed that θ is small, such that $\cos\theta \sim 1$. The boundary conditions on this equation then are

$$\Psi = (1/2)c^2k, \quad (d\Psi/dr) = c, \quad \text{and} \quad (d^2\Psi/dr^2) = 1 - 2k + kS_b \text{ on } r = c \quad (5)$$

A change of variables in the equation such that $\Psi = c^2k\phi$ and $ky = 1 - (r/c)$ gives

$$2\phi(d/dy)\left([1/(1 - yk)^2]\{(d^3\phi/dy^2) - [k^2\phi/(1 - ky)^2]\}\right) = -kS_b(d/dy)[(d\phi/dy)/(1 - ky)] \quad (6)$$

with $\phi = 1/2$, $\phi' = -1$ and $\phi'' = 1 - 2k + kS_b$ on $y = 0$.

Kemp attempts to obtain a solution of this equation by using a simple power series. Putting

$$\phi = (1/2) - y + (1/2)y^2(1 - 2k + kS_b) + Ay^3 + \ldots \quad (7)$$

in Eq. (6), we obtain $A = -1/3k - 1/6kS_b$. Now, at the body surface $\psi = 0$ or $\phi = 0$. This occurs when

$$\left.\begin{aligned}(1/2)(1 - y)^2 &= k[(4/3) - (1/3)S_b] \\ \text{or,} \qquad y &= 1 - \sqrt{8/3k[1 - (1/4)S_b]}\end{aligned}\right\} \quad (8)$$

Thus, the stand-off distance is modified to this order in k by the magnetic field. Such an expansion leads to a first-order modification to the pressure on the body surface by the magnetic field.

However, the above procedure will be seen to be suspect if the form of Eq. (6) is noted. For, to a first approximation $\phi = 1/2(1 - y)^2$ by Eq. (7) and, hence, any expansion of Eq. (6) starting with this as the first approximation must fail near $y = 1$ where this approximation vanishes. The resulting approximate form of Eq. (6) giving the higher-order term in ϕ will have its highest derivation multiplied by a factor which vanishes at $y = 1$. This may be clearly seen if we try to expand ϕ in the following manner

$$\phi = \phi_0(y) + k\phi_1(y) + \ldots \quad (9)$$

Substituting in Eq. (6), we obtain

$$\left.\begin{aligned}&\phi_0''' = 0 \\ &2\phi_0\{\phi_1''' + 2\phi_0''\} = -S_b\phi_0'', \text{ etc.}\end{aligned}\right\} \quad (10)$$

Now, we have, therefore,

$$\phi = (1/2)(1 - y)^2 + k[S_b(y^2 - y) - S_b(1 - y) \times \log(1 - y) - (1/3)y^3 - y^2] + 0\{k^2 \log(1 - y)\} \quad (11)$$

If we assume that an expansion of the form (11) converges, we may proceed as before and find that $\phi = 0$ where

$$y = 1 - \sqrt{(8/3)k} \quad (12)$$

This means that to this order the magnetic field does not affect the standoff distance. However, before we can decide that this is indeed the case, it would be necessary to find a more suitable form for the expansion of ϕ which will be uniformly valid near $y = 1$ for k small.

To do this, we follow the method outlined by Lighthill.[3] We introduce a new variable, z, and expand ϕ in the form

$$\phi = \phi_0(z) + k\phi_1(z) + \ldots \quad (13)$$

where

$$y = z + ky_1(z) + \ldots \quad (14)$$

The functions $y_1, \ldots$ are to be determined. Thus, from Eq. (6)

$$\phi_0''' = 0$$

$$\phi_1''' - 2\phi_0''y_1'' - y_1'''\phi_0' + 2\phi_0'' = -S_b\phi_0''/2\phi_0 \quad (15)$$

The boundary conditions become $\phi_0 = 1/2$, $\phi_0' = -1$ and $\phi_0'' = 1$ on $z = 0$; and $\phi_1 = 0$, $\phi_1' = y_1'\phi_0'$, $\phi_1'' = -2 + S_b + 2\phi_0''y_1' + y_1''\phi_0'$ on $z = 1$.

Thus

$$\phi_0 = (1/2)(1 - z)^2$$

and

$$\phi_1''' - 3y_1'' + y_1'''(1 - z) + 2 = -S_b/(1 - z)^2 \quad (16)$$

with

$$\phi_1 = 0, \quad \phi_1' = -y_1' \quad \text{and} \quad \phi_1'' = 2y_1' - y_1'' - 2 + S_b$$

In determining the next approximation to ϕ (i.e., ϕ_1), we are left with one more degree of freedom by being able to choose y_1. We, therefore, choose y_1 to satisfy

$$y_1'''(1 - z) - 3y_1'' = -S_b(1 - z)^2$$

or

$$y_1 = -S_b \log(1 - z) \quad (17)$$

Hence, $\phi_1''' = -2$ giving

$$\phi_1 = -(z^3/3) - z^2 + S_b(z^2 - z) \quad (18)$$

Thus

$$\phi = (1/2)(1 - z)^2 + k[S_b(z^2 - z) - (z^3/3) - z^2] + 0(k^2) \quad (19)$$

which does not have the singular behavior of Eq. (12) as a function of Z. Now $\phi = 0$ when

$$z = 1 - \sqrt{(8/3)k} + 0(k) \quad (20)$$

By Eq. (18)

$$y = 1 - kS_b \log(1 - z) + 0(k^2/[1 - z])$$

and, therefore,

$$y = 1 - \sqrt{(8/3)k} + 0(k \log k) \quad (21)$$

thus giving the stand-off distance to be independent of the magnetic field to this order as was shown previously in Eq. (12).

It is now possible to deduce the magnitudes of the other variables in the resulting expansion. For example, Eq. (2) requires

$$p - p_{stag} = -(1/2k)(\Psi_r^2/r^2)\sin^2\theta + o(1) = -(4/3)\sin^2\theta + o(1)$$

using Eqs. (14), (19), and (20).

This result is in direct contradiction to that of Kemp,[2] which asserts that the pressure is affected by the magnetic field to the order given above.

This result is also obtained from the Newtonian theory of hypersonic flow when a magnetic field and conducting fluid are introduced. Such a theory does not, however, require the assumption of constant density and is not limited to the region near the stagnation point.

References

[1] Hayes, W. D., and Probstein, R. F., *Hypersonic Flow Theory;* Academic Press, Inc., New York, 1959.

[2] Kemp, N. H., *On Hypersonic Stagnation Point Flow With a Magnetic Field,* Readers' Forum, Journal of the Aeronautical Sciences, Vol. 25, No. 6, pp. 405–407, June, 1958.

[3] Lighthill, M. J., *A Technique for Rendering Approximate Solutions for*

Physical Problems Uniformly Valid, Phil. Mag., 7th Series, Vol. 40, No. 311, pp. 1179–1201, December, 1949.

[4] Lighthill, M. J., *Dynamics of a Dissociating Gas, Part I—Equilibrium Flow*, J. Fluid Mech., Vol. 2, Part 1, pp. 1–32, January, 1957.

---

*Author's Reply**

Nelson H. Kemp
Avco Research Laboratory, Everett, Mass.
April 20, 1959

IN THE ABOVE NOTE, N. C. Freeman shows that the analytical solution presented in reference 1 for the spherical stagnation-point flow of an inviscid electrically conducting fluid in the presence of a magnetic field is not correct. He shows that the magnetic field has no effect on the detachment distance and pressure gradient to lowest order in the density ratio, $k = \rho_\infty/\rho$, contrary to the result presented in reference 1. The author agrees that the expansion procedure used in reference 1 is not correct, and so the results given there are wrong.

In order to find correctly the effect of the magnetic field, numerical solutions of the vorticity equation were obtained. The relevant equation and boundary conditions, in the notation of reference 1, are

$$2\Psi(d/dr)\left\{(1/r^2)\left[(2\Psi/r^2) - \Psi''\right]\right\} = -kSC^2(d/dr)(\Psi'/r) \quad (1)$$

$$\Psi(r_b) = 0 \quad (2)$$

$$\Psi'(1) = 1, \quad \Psi(1) = k/2 \quad (3)$$

$$\Psi''(1) = SC^2 + (1 - 2k + 2k^2)/k \quad (4)$$

Here, the first boundary condition expresses the vanishing of the stream function at the (nondimensional) body location r_b; Eqs. (3) require that the velocity components at the shock be given by the Rankine-Hugoniot relations; Eq. (4) relates the vorticity at the shock to the value found by using the Rankine-Hugoniot equations in the equation of motion along the back of the shock. The parameter SC^2 is given by

$$SC^2 = \sigma(B_b^*)^2 r_s^* r_b^4/\rho_\infty U_\infty \equiv S_b r_b^3 \quad (5)$$

where r_s^* is the shock radius, $r_s^* r_b$ the body radius, and B_b^* the magnetic field at the body (which is normal to the body).

The four boundary conditions are necessary for the third-order equation because the body radius r_b is also to be found.

Numerical solutions of the system (1)–(4) have been obtained on an IBM 650 digital computer for $k = 0.1$, $SC^2 = 0.1, 0.5, 1, 4, 10$. The results for detachment distance δ and velocity and pressure gradient are plotted in Fig. 1 from the equations

$$\delta/r_b = (1 - r_b)/r_b \quad (6)$$

$$(\partial v_\theta/\partial\theta)_{st} = \Psi_b'/r_b \quad (7)$$

$$[(\partial p^*/\rho_\infty U_\infty^2)/2 \sin\theta\, \partial\theta)]_{st} = -(1/2)(\Psi_b'/r_b) \times [1 + (kS_b)/(\Psi_b'/r_b)] \quad (8)$$

The subscript 0 denotes zero magnetic field.

The main feature of interest in Fig. 1 is the fact that the pressure gradient is very nearly constant as the magnetic field increases. The assumption that it was exactly constant was used without proof by Neuringer and McIlroy[2, 3] in their study of a viscous, electrically conducting fluid at a two-dimensional stagnation point with a magnetic field. The present calculations show that, at least for the three-dimensional case, this is a good approximation to rather large values of S_b, a result which is quite different from the conclusion the present author drew from the incorrect results of reference 1.

In order to estimate heat transfer and viscous shear stress at a three-dimensional stagnation point, an incompressible boundary-layer calculation has been performed[4] including the magnetic force in the momentum equation. The results in Fig. 1 were used for the inviscid flow. The heat transfer and viscous shear stress were compared with those of references 2 and 3 which are two-dimensional and assume constant pressure gradient. It was found that the ratio of heat-transfer rate with a magnetic field to that without a field was about one per cent smaller for the three-dimensional case than for the two-dimensional one. In the case of viscous shear stress, the three-dimensional ratio was as much as five per cent lower than the two-dimensional ratio at $S_b = 5$. (Notice that in addition to the change in viscous shear stress due to the magnetic field, there will also be a force on the coil producing the field.) It is hoped to publish these boundary-layer calculations shortly.

It should be pointed out that the correct solutions in this note do not change the general conclusion of reference 1 that substantial reductions in heat transfer at a stagnation point with the present field geometry can only be obtained by producing large values of S_b, and this can only be done with bodies large compared to one meter, or fields well over 10,000 gauss, or conductivities well over 100 mho/m.

* This work was supported by the USAF through the Air Force Office of Scientific Research of the Air Research and Development Command under Contract AF 49(638)-61.

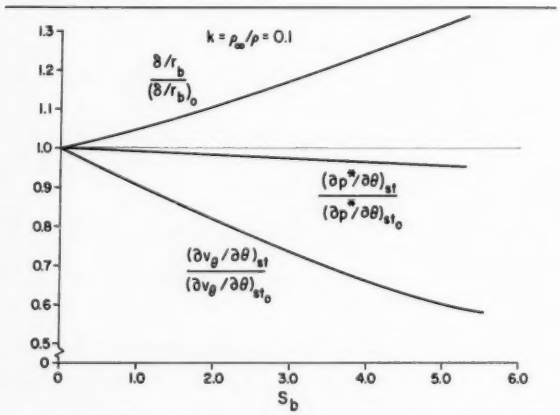

FIG. 1. Effect of magnetic field on shock detachment distance, stagnation-point pressure gradient, and stagnation-point velocity gradient. $S_b = \sigma(B_b^*)^2 r_b^*/\rho_\infty U_\infty$.

REFERENCES

[1] Kemp, N. H., *On Hypersonic Stagnation-Point Flow With a Magnetic Field*, Readers' Forum, Journal of the Aeronautical Sciences, Vol. 25, No. 6, pp. 405–407, June, 1958.

[2] Neuringer, J. L., and McIlroy, W., *Incompressible Two-Dimensional Stagnation-Point Flow of an Electrically Conducting Viscous Fluid in the Presence of a Magnetic Field*, Journal of the Aeronautical Sciences, Vol. 25, No. 3, pp. 194–198, March, 1958.

[3] Neuringer, J. L., and McIlroy, W., *Hydromagnetic Effects on Stagnation-Point Heat Transfer*, Readers' Forum, Journal of the Aeronautical Sciences, Vol. 25, No. 5, pp. 332–334, May, 1958.

[4] Kemp, N. H., *A Further Note on Hypersonic Stagnation-Point Flow with a Magnetic Field*, Research Report, No. 53, Avco Research Laboratory, Everett, Mass.

On the Local Elastic Stability of Honeycomb Face Plate Subjected to Uniaxial Compression

Raymond C. Weikel and Albert S. Kobayashi
Research Specialist, Boeing Airplane Company, Seattle, Wash., and Assistant Professor of Mechanical Engineering, University of Washington, Seattle, Wash., Respectively
March 27, 1959

INTRODUCTION

RECENT THEORETICAL INVESTIGATION on the elastic stability of honeycomb structures has been mostly concerned with the overall stability of the structural elements. Little reference is available on the theoretical investigation of local buckling phe-

nomena which are known as "intracell buckling" and "wrinkling" of the honeycomb structures.

"Intracell buckling" is the buckling of the honeycomb face plate within each individual honeycomb cell. Although the honeycomb structure will retain part of its load carrying capacity after intracell buckling has occurred, the buckled face plate may have undesirable influence on the aerodynamic properties of the structure, and, thus, it is important to know the load at which this intracell buckling does occur.

"Wrinkling" is the buckling of the honeycomb face plate over a row of several honeycomb cells. It appears as a sharp trough on the face plate and it is accompanied either by the crushing of the honeycomb core or the separation of the core and face plate under this sharp trough. This trough is perpendicular to the applied load and is also known to discontinuously form across the face plate. When wrinkling occurs, for all practical purposes, the honeycomb structure has lost its load carrying capacity. It is the purpose of this note to estimate the critical load at which intracell buckling and/or wrinkling occur by considering the elastic stability of the face plate within a honeycomb cell where the face plate is simply supported at its four edges by an elastic core.

Method of Approach

The following assumptions were made to simplify the analysis:

(a) A honeycomb face plate loaded under uniaxial compression alone is considered. The honeycomb cells are oriented such that this load is parallel to the diagonal of the cell.

(b) The honeycomb cell is square in shape.

(c) The thickness of the honeycomb core is infinite in comparison with the cell size.

(d) Face-plate deflection for intracell buckling is obtained by assuming that the face plate is simply supported along its four edges at the cell.

(e) Face-plate deflection for wrinkling is obtained by assuming that the face plate is simply supported along two ridges of the wrinkling trough. This trough is perpendicular to the applied load, and the two edges of the trough pass through two diagonally opposite corners of the cell.

(f) Deflection due to wrinkling deforms the core elastically, and will cause springback force to act on the entire face plate.

Assumption (d) is based on the experimental evidences available at Boeing, and also reference 1. Assumption (e) is also based on the experimental evidences available at Boeing. Assumption (f) enables one to consider the face plate as being supported by an elastic core which is continuous and, thus, reduces this portion of the problem to a plate on an elastic foundation. However, this assumption fails to consider the stability of the honeycomb core itself.

Within these assumptions, the face-plate deflections were approximated by only one or two terms of the double trigonometric series. Face-plate deflection due to intracell buckling is approximated by

$$w_i = A_{11} \sin(\pi x/a) \sin(\pi y/a) + A_{22} \sin(2\pi x/a) \sin(2\pi y/a) \quad (1)$$

Face-plate deflection due to wrinkling is

$$w_w = A_w \cos[\pi(x - y)/2a] \quad (2)$$

Here, A_{11}, A_{22}, and A_w are the unknown amplitudes of the series, a is the length of the side of the square, D is the flexural rigidity of the face plate, ν is the Poisson's ratio of the face plate, and k is the apparent core stiffness. The xy coordinate system employed here and the orientation of the applied load, N, is shown in the upper corner of Fig. 2.

The strain energy due to bending of the face plate is

$$V_B = (D/2) \int_0^a \int_0^a \Big(\{ [\partial^2(w_i + w_w)/\partial x^2] + [\partial^2(w_i + w_w)/\partial y^2] \}^2 - 2(1 - \nu) \{ [\partial^2(w_i + w_w)/\partial x^2] \times [\partial^2(w_i + w_w)/\partial y^2] - [\partial^2(w_i + w_w)/\partial x \partial y]^2 \} \Big) dxdy \quad (3)$$

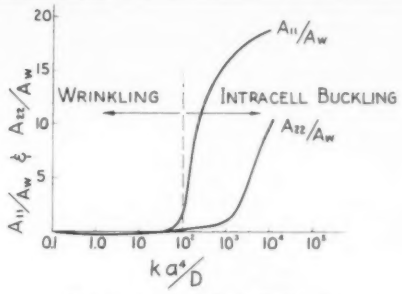

FIG. 1. Face plate deflections.

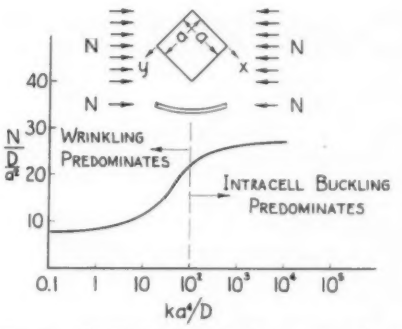

FIG. 2. Elastic buckling load vs. core spring constant for honeycomb cells. N-load in face plate, lb./in.; k = apparent core stiffness, lb./in.^{2}/in. deflection; D = face-plate stiffness, lb./in.; a = cell size, in.

The energy due to deflection of the core is

$$V_D = (1/2) \int_0^a \int_0^a k\, w_w^2\, dxdy \quad (4)$$

Finally, the work done by the external force is

$$T = (1/2)(N/\sqrt{2}) \int_0^a \int_0^a \{ [\partial(w_i + w_w)/\partial x]^2 + [\partial(w_i + w_w)/\partial y]^2 - 2[\partial(w_i + w_w)/\partial x] \times [\partial(w_i + w_w)/\partial y] \}\, dxdy \quad (5)$$

Since

$$\delta(V_B + V_D + T) = 0$$

it is now possible to determine A_{11}, A_{22}, and A_w which minimizes the applied load N by the conventional variational method which will not be elaborated here.

Results

The computed results are shown in graphical forms. Fig. 1 shows the relation between the amplitude ratios of intracell buckling to wrinkling, A_{11}/A_w and A_{22}/A_w, vs. apparent core-stiffness coefficient, ka^4/D. It can be seen that for a given face plate and cell size of a honeycomb core, the predominant mode of buckling failure will be wrinkling for a relatively weak core. With the increase in the apparent core stiffness, k, intracell buckling becomes the predominant mode of buckling failure. The approximate division between the two modes of buckling failure is $ka^4/D = 100$ from Fig. 1.

Fig. 2 shows the relations between the critical-load coefficient and the apparent core-stiffness coefficient. Here again, the approximate division between the two modes of buckling failure is shown. This figure shows that, for a given face plate and cell size, it is fruitless to increase the apparent core stiffness, k, beyond a certain point since the critical-load coefficient, Na^2/D, will not exceed a value of about 27. Actually, in order to increase the apparent core stiffness, k, for a given cell size and a given core

material, one can only increase the gage of the core material. This will result in an increase of weight which is directly proportional to the increase in k. With this consideration of weight, the optimum apparent core-stiffness coefficient will be about $Ka^4/D = 100$, and the corresponding critical load coefficient is about $Na^2/D = 22$.

REFERENCE

[1] Norris, C. B., and Kommer, W. J., *Short-Column Compressive Strength of Sandwich Constructions as Affected by the Size of the Cells of Honeycomb-Core Materials*, Forest Products Laboratory Report No. 1817, Madison, Wis., August, 1950.

On the Concepts of Moving Electric and Magnetic Fields in Magnetohydrodynamics

J. E. McCune and W. R. Sears
Instructor and Director, Respectively, Graduate School of Aeronautical Engineering, Cornell University, Ithaca, N. Y.
March 31, 1959

RECENTLY THERE HAVE APPEARED in the literature[1, 2, 3] certain statements regarding "moving magnetic fields," which, if not altogether erroneous, are at least misleading if applied without further consideration to problems of magnetohydrodynamic interest. Thus, for example, both Rossow[1] and Ong and Nicholls[3] discuss motion in a conducting fluid of an infinite flat plate in the presence of a uniform transverse magnetic field and distinguish two cases: (1) the source of the magnetic field "fixed relative to the plate" and (2) the source of the magnetic field "fixed relative to the fluid" far from the plate. Similarly, Bleviss,[2] in his discussion of magnetohydrodynamic Couette flow, makes brief reference to his assumption that the magnetic field is "attached to the stationary wall." Both he and Rossow also refer to the induced electromotive force, $\boldsymbol{q} \times \boldsymbol{B}$, (where $\boldsymbol{q}$ is the fluid velocity and $\boldsymbol{B}$ the magnetic field strength) as "arising from the motion of the conducting fluid relative to the magnetic field."

Statements of this kind imply, among other things, that it would be possible (with electric fields of practical strength and neglecting terms of order q^2/c^2) to detect the motion of a uniform magnetic field. Also, interpreted literally, they suggest that one should be able to ascertain by physical measurement whether the magnetic lines from a rotating magnet actually rotate with the magnet or not.

Yet, Panofsky and Phillips[4] state unequivocally in their discussion of the motion of conductors in uniform magnetic fields that "whether the source of $\boldsymbol{B}$ is stationary or is in motion is entirely irrelevant," and Alfvén[5] takes some pains to illustrate that the voltage induced by a unipolar inductor is the same regardless of whether one assumes the magnetic lines to rotate with the magnet or to stay fixed in space.

These facts follow from the equations of relativity as they apply to electric and magnetic fields. If in a given coordinate system—say, one "at rest"—the electric and magnetic fields have strengths $\boldsymbol{E}$ and $\boldsymbol{B}$, respectively, then in a second system moving at velocity $\boldsymbol{v}$, with respect to the first, an observer will measure (in electromagnetic units)

$$\boldsymbol{E}'_{\perp} = (\boldsymbol{E}_{\perp} + \boldsymbol{v} \times \boldsymbol{B})/\sqrt{1 - (v^2/c^2)}; \quad E_{\parallel}{}' = E_{\parallel} \tag{1}$$

and

$$\boldsymbol{B}'_{\perp} = (\boldsymbol{B}_{\perp} - \boldsymbol{v} \times \boldsymbol{E}/c^2)/\sqrt{1 - (v^2/c^2)}; \quad B_{\parallel}{}' = B_{\parallel} \tag{2}$$

where $\boldsymbol{E}'$ and $\boldsymbol{B}'$ are, respectively, the effective electric and magnetic field strengths in the moving system and the subscripts $\perp$ and $\parallel$ denote the components of these vectors perpendicular and parallel, respectively, to the velocity vector $\boldsymbol{v}$.

If we assume, as is nearly always the case in magnetohydrodynamic problems, that $\boldsymbol{E}$ and $\boldsymbol{v} \times \boldsymbol{B}$ are of the same order, and if we agree to neglect terms of order v^2/c^2, Eqs. (1) and (2) become those conventionally used in magnetohydrodynamics:

$$\boldsymbol{E}' = \boldsymbol{E} + \boldsymbol{v} \times \boldsymbol{B} \tag{3}$$

and

$$\boldsymbol{B}' = \boldsymbol{B} \tag{4}$$

Thus, as Alfvén[5] points out, "to speak of an electric field without defining exactly the coordinate system to which it refers is meaningless," and we see from Eq. (4), on the other hand, that the motion of a uniform *magnetic* field is indeed irrelevant.

(To be sure, the concept of a "moving magnetic field" has long been useful in electrical engineering, where it refers to a field that is nonuniform and is steady when viewed in a certain moving coordinate system. It is natural to say that such a field is stationary in the last-mentioned coordinate system and, therefore, "moving" with respect to other frames, but this practice is actually unrelated to the question under discussion, which has to do with uniform fields. The "motion" of this kind of field is detected, through its nonuniformities, by means of Faraday's experiment—i.e., a voltage is induced in a stationary coil as the flux through the coil changes with time.)

In magnetohydrodynamics, therefore, when we speak of the induced electromotive force $\boldsymbol{q} \times \boldsymbol{B}$, we must keep clearly in mind that this effective field does not arise from the motion of the conductor "relative to the magnetic field," but, rather it arises from the motion (at velocity $\boldsymbol{q}$) of the conducting fluid particle relative to the system in which the observer measures the electric field $\boldsymbol{E}$. Essentially, one must remember that not only the lines of force cut by the particle but also those cut by the voltmeter closing the loop between the observer and the particle must be taken into account. These concepts are very clearly set forth in Table 9-1 of reference 4.

That these points are important and not mere semantics can be made clear by pointing out from Eqs. (3) and (4) that in the Couette-flow problem treated by Bleviss the answer would necessarily be the *same* whether one assumes the magnetic field to be "attached" (1) to the stationary wall or (2) to the moving wall, or, indeed, whether it is considered to be in motion with respect to both walls. Yet, if one believed that the induced electromotive force really arose because of relative motion between the fluid and the magnetic field, one would be forced to write the induced e.m.f. experienced by a moving particle (when $\boldsymbol{E}$ is referred to the system fixed in the stationary wall) as $\boldsymbol{q} \times \boldsymbol{B}$ in the first case and $(\boldsymbol{q} - U\boldsymbol{i}) \times \boldsymbol{B}$ in the second, thus obtaining completely different solutions. This would provide a direct means of detecting the motion of the uniform magnetic field, in violation of the principles described above.

It is interesting to note, on the other hand, that these two different solutions for Couette flow can be realized in the following way. Instead of their being associated with different states of motion of the magnetic field, they can, in fact, be considered to correspond to different boundary conditions on the applied electric field. For example, Bleviss clearly states that he chooses $\boldsymbol{E} = 0$ in the system fixed in the stationary wall. An alternative choice would have been to choose the applied electric field to be zero measured in a system fixed in the moving wall. In that case, the applied electric field in the stationary-wall system would have been $E = -UB_0$ and the effective electric field experienced by a moving particle would have been $\boldsymbol{E} + \boldsymbol{q} \times \boldsymbol{B} = (\boldsymbol{q} - U\boldsymbol{i}) \times \boldsymbol{B}$. Thus, the application of an electric field of appropriate strength provides a physical means of setting up solutions that could have been erroneously associated with motion of the magnetic field. Of course, in any case only the $\boldsymbol{q} \times \boldsymbol{B}$ term is the "induced electromotive force" in the stationary-wall system.

These results illustrate a possible interpretation of the results of Rossow[1] and Ong and Nicholls.[3] The separate cases treated by these authors, which they distinguish according to the state of motion of the magnetic field, can be more correctly thought of as corresponding to different values of the applied electric field. For example, Rossow's second solution (magnetic field "fixed relative to fluid") corresponds to choosing the applied electric

field $\boldsymbol{E}$ to be zero in the space-fixed (or fluid-fixed) system. However, his first solution, within the linearizations that he made, must be interpreted as requiring the application of an electric field of strength $-u_\infty B_0$ in the fluid-fixed system. This situation does not seem to be a realistic approximation to a plate moving through the atmosphere. On the other hand, since the applied electric field for this case is zero in the *plate-fixed system*, the arrangement could be set up in a wind tunnel or shock tube.

It would be somewhat more difficult to imagine setting up a physical case corresponding to the solution denoted by Ong and Nicholls as that for which the magnetic field is fixed in their oscillating plate. For that case, one is led to the necessity of applying an electric field (in the far-fluid-fixed system) that varies sinusoidally with time, or otherwise assuring that the applied voltage in the system of the oscillating plate is zero. It seems questionable whether this is a particularly meaningful arrangement.

By interpreting the different cases treated in references 1 and 3 in the way that we have indicated, it can be shown that the (linearized) results obtained correspond (with the possible exception of the case just discussed) to interesting and useful magnetohydrodynamic problems. Nevertheless, these papers point up the importance of keeping clearly in mind the correct transformations applying to the various field quantities. It is not likely that future treatments, if based on erroneous electrodynamic concepts, can all be shown so readily to correspond to problems of real interest.

References

[1] Rossow, V. J., *On Flow of Electrically Conducting Fluids over a Flat Plate in the Presence of a Transverse Magnetic Field*, NACA TN 3971, May, 1957.

[2] Bleviss, Z. O., *Magnetogasdynamics of Hypersonic Couette Flow*, Journal of the Aero/Space Sciences, Vol. 25, No. 10, pp. 601–615, October, 1958.

[3] Ong, R. S., and Nicholls, J. A., *The Flow of a HydroMagnetic Fluid Near an Oscillating Flat Plate*, Readers' Forum, Journal of the Aero/Space Sciences, Vol. 26, No. 5, pp. 313–314, May, 1959.

[4] Panofsky, W. K. H., and Phillips, M., *Classical Electricity and Magnetism*, pp. 148–151; Addison-Wesley, Cambridge, Mass., 1955.

[5] Alfvén, H., *Cosmical Electrodynamics*, pp. 6–9; Oxford at the Clarendon Press, 1950.

Stress Functions for Plates of Convex Polygonal Shape*

Hans A. Balmer

Research Staff Member, Aeroelastic and Structures Research Laboratory, Massachusetts Institute of Technology, Cambridge, Mass.

April 1, 1959

In determining the in-plane stress distribution of arbitrary shaped plates, variational methods utilizing functions which must satisfy force boundary conditions are frequently used.

For a rectangular plate, the standard expression for the Airy stress function[1]

$$\phi = (x^2 - a^2)^2 (y^2 - b^2)^2 P(x, y) \tag{1}$$

fulfills the stress-free boundary conditions

$$\left.\begin{aligned} N_x &= \partial^2\phi/\partial y^2 = 0,\ N_{xy} = -(\partial^3\phi/\partial x \partial y) = 0 \text{ at } x = \pm a \\ N_y &= \partial^2\phi/\partial x^2 = 0,\ N_{xy} = -(\partial^3\phi/\partial x \partial y) = 0 \text{ at } y = \pm b \end{aligned}\right\} \tag{2}$$

where $P(x, y)$ is an arbitrary polynomial in x and y and N_x, N_y, and N_{xy} are stress resultants.

When Eq. (1) is written in the form

$$\phi = (x + a)^2 (x - a)^2 (y + b)^2 (y - b)^2 P(x, y) \tag{3}$$

it is seen that the expressions in parentheses of Eq. (3) represent the left-hand sides of the edge equations

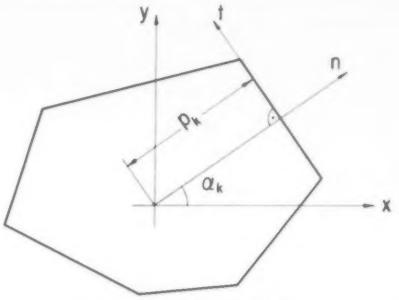

FIG. 1. Arbitrary polygon.

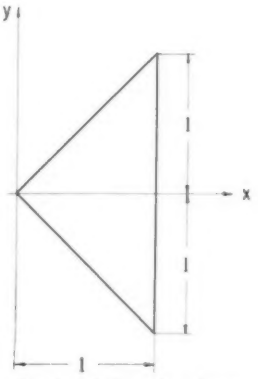

FIG. 2. Delta wing shape.

$$x + a = 0,\quad x - a = 0,\quad y + b = 0,\quad y - b = 0 \tag{4}$$

Analogous equations for the edges of an N-edge polygon (Fig. 1) can be expressed in the normal forms

$$x \cos \alpha_k + y \sin \alpha_k - p_k = 0 \quad (k = 1, 2, \ldots, N) \tag{5}$$

and an analogous stress function can be assumed in the form

$$\phi = P(x, y) \prod_{k=1}^{N} (x \cos \alpha_k + y \sin \alpha_k - p_k)^2 \tag{6}$$

In order to show that at any edge k, the expression (6) satisfies the stress-free boundary conditions

$$N_n = \partial^2\phi/\partial t^2 = 0,\quad N_{nt} = -(\partial^2\phi/\partial n \partial t) = 0 \tag{7}$$

it is written in the following form

$$\phi = (x \cos \alpha_k + y \sin \alpha_k - p_k)^2 Q(x, y) \tag{8}$$

where $Q(x, y)$ includes $P(x, y)$ and the remaining factors.

The second derivatives of ϕ in the directions n and t are

$$\left.\begin{aligned} \phi_{nn} &= \phi_{xx} \cos^2 \alpha_k + \phi_{yy} \sin^2 \alpha_k + 2\phi_{xy} \sin \alpha_k \cos \alpha_k \\ \phi_{tt} &= \phi_{yy} \cos^2 \alpha_k + \phi_{xx} \sin^2 \alpha_k - 2\phi_{xy} \sin \alpha_k \cos \alpha_k \\ \phi_{nt} &= \phi_{xy}(\cos^2 \alpha_k - \sin^2 \alpha_k) + (\phi_{yy} - \phi_{xx}) \sin \alpha_k \cos \alpha_k \end{aligned}\right\} \tag{9}$$

The values of ϕ_{xx}, ϕ_{yy}, and ϕ_{xy} obtained by differentiating Eq. (8) become

$$\left.\begin{aligned} \phi_{xx} &= 2Q \cos^2 \alpha_k + 4Q_x g_k \cos \alpha_k + Q_{xx} g_k^2 \\ \phi_{yy} &= 2Q \sin^2 \alpha_k + 4Q_y g_k \sin \alpha_k + Q_{yy} g_k^2 \\ \phi_{xy} &= 2Q \sin \alpha_k \cos \alpha_k + 2Q_x g_k \sin \alpha_k + \\ &\qquad 2Q_y g_k \cos \alpha_k + Q_{xy} g_k^2 \end{aligned}\right\} \tag{10}$$

where $$g_k = x \cos \alpha_k + y \sin \alpha_k - p_k$$

At the edge k, $g_k = 0$ and Eq. (10) reduce to

$$\phi_{xx} = 2Q \cos^2 \alpha_k,\quad \phi_{yy} = 2Q \sin^2 \alpha_k,\quad \phi_{xy} = 2Q \sin \alpha_k \cos \alpha_k \tag{11}$$

Substituting Eq. (11) into Eq. (9) gives

* This work was done in the course of research sponsored by the Aircraft Laboratory, Wright Air Development Center, USAF, under Contract No. AF33(616)-5504.

$$\left.\begin{aligned}\phi_{nn} &= 2Q\,(\cos^4\alpha_k + \sin^4\alpha_k + 2\sin^2\alpha_k\cos^2\alpha_k)\\ &= 2Q(\sin^2\alpha_k + \cos^2\alpha_k)^2 = 2Q\\ \phi_{tt} &= 2Q(\sin^2\alpha_k\cos^2\alpha_k + \cos^2\alpha_k\sin^2\alpha_k - \\ &\qquad 2\sin^2\alpha_k\cos^2\alpha_k) = 0\\ \phi_{nt} &= 2Q[\sin\alpha_k\cos\alpha_k(\cos^2\alpha_k - \sin^2\alpha_k) + \\ &\qquad (\sin^2\alpha_k - \cos^2\alpha_k)\sin\alpha_k\cos\alpha_k] = 0\end{aligned}\right\} \quad (12)$$

thus showing that the expression (6) fulfills the stress-free boundary conditions.

This approach is restricted to plates bounded by a convex polygon in order to obtain a physically reasonable solution. Instead of the normal form (5), any other convenient form $A_k x + B_k y + C_k = 0$ of the edge equation may be used.

An application of the above to airplane problems occurs in the determination of the in-plane thermal stress distribution in delta and tapered wings.

As an example, a stress function for the delta wing shape in Fig. 2 is given below.

The edge equations are

$$x + y = 0, \quad x - y = 0, \quad x - 1 = 0 \quad (13)$$

and the stress function becomes

$$\left.\begin{aligned}\phi &= (x+y)^2(x-y)^2(x-1)^2P(x,y)\\ &= (x^2-y^2)^2(x-1)^2P(x,y)\end{aligned}\right\} \quad (14)$$

For a cantilever delta wing (the delta of Fig. 2 clamped at $y = 0$), the stress function becomes

$$\phi = (x-y)^2(x-1)^2\,P(x,y) \quad (15)$$

Use of the variational principle then takes care of the displacement boundary conditions on the $y = 0$ edge, in an average way.

Reference

[1] Timoshenko, S., *Theory of Elasticity*, 1st Ed., p. 153; McGraw-Hill Book Company, Inc., New York, 1934.

A High-Temperature, Steady-Flow, Supersonic Tunnel†

Robert A. Gross*
Chief Research Engineer, Fairchild Engine Division, Fairchild Engine and Airplane Corp., Deer Park, N.Y.
April 10, 1959

Introduction

STARTING in October, 1956, we designed and built a Mach 3, steady flow tunnel to permit experimental exploration of chemical energy release in supersonic flow. This tunnel was put in operation in late 1957 and has now accumulated approximately 500 hours of test time. Some unusual characteristics of this tunnel, such as its ability to run steadily at an inlet stagnation temperature of approximately 3,500°F., are presented here.

† This work was supported by the USAF Office of Scientific Research under Contract No. AF49(638)-15.

* Now, National Science Foundation Senior Post-Doctoral Fellow. Physics Department, University of California, Berkeley, Calif.

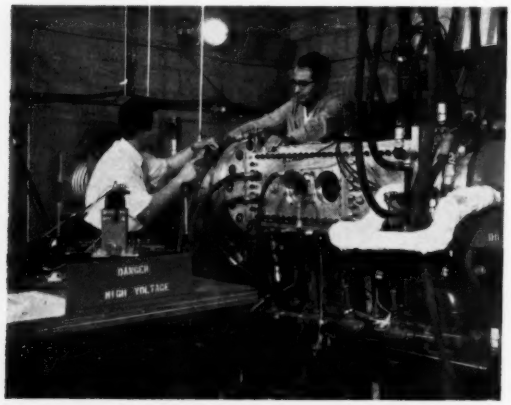

FIG. 1. Mach 3, High-Temperature, Steady-Flow Tunnel.

TABLE 1

Inlet total temperature (°F.)	500	1,000	1,500*	2,000*	2,500*	3,000*
Throat metal temperature (°F.)	94	163	168	170	180	186
Tunnel heat removal (B.t.u./sec.)	2.5	3.9	6.2	11.0	18.5	27.2

* Data obtained when the air preheater gave a temperature of 1,030°F. and the additional temperature rise resulted from hydrogen combustion in the plenum chamber.

The tunnel is of fixed rectangular geometry, and the test-section flow area is approximately 3 × 6 in. The exit diffuser consists of a variable-area second throat joining a spray cooler and an exhaust silencer which leads to the atmosphere. The tunnel-inlet stagnation pressure varies from ambient to approximately 125 psia and the design-point mass flow is about 5 lb./sec. The tunnel is shown in Fig. 1.

The air, supplied by a 10:1-pressure-ratio compressor plant, is fed to a heat exchanger designed for 1,200°F. but which, in fact, has been used to 1,590°F. This hot, compressed air is then ducted via an insulated strainless-steel pipe to the plenum chamber, tunnel, and exhaust system. The tunnel is constructed of aluminum and is completely water-cooled. Original design details are given in reference 1.

Experience

Early experience with the tunnel indicated that an original tunnel heat-transfer design was conservative. This came about largely because of the boundary-layer behavior upstream of the throat. The transition section from the round plenum chamber to the rectangular tunnel consists of a smoothly contoured, water-cooled, aluminum casting. The hot-air boundary layer is cooled upstream of the throat, and a thin, relatively cool, laminar-air boundary layer does, indeed, effectively help to protect the throat and downstream tunnel walls. This pleasant performance leads us to higher temperature capability.

We installed a hydrogen injection system in the plenum chamber about 3 ft. upstream of the throat. By burning this hydrogen, we were able to easily increase the gas temperature and thereby achieve operation above 1,500°F.

Combustion in the plenum chamber is arranged to permit a relatively cool (1,200°F.) layer of air to remain along the walls. Thus, we have succeeded in running the supersonic tunnel steadily with an inlet stagnation temperature about 3,000°F. Typical operating conditions are summarized in Table 1.

Testing time depends upon the size of the fuel supply. We presently can test for about an hour at 2,000°F. The throat temperature was measured by means of a thermocouple imbedded in the aluminum skin about 1/16 in. from the gas surface. The throat temperature is quite sensitive to the cooling-water flow rate.[1] The values given in the above table are typical average conditions at the throat. The tunnel heat removal was determined by measuring the cooling-water flow rate and temperature rise. The inlet cooling water was normally at about 51°F.

Theoretically, a temperature of about 4,800°F. can be achieved by burning hydrogen in 1,200°F., 125 psia, air. For certain tests, we have added oxygen to the plenum to make up for the depletion of that molecule resulting from combustion.

We have succeeded in obtaining remarkably good schlieren photographs through 6-in. diameter, 1-in. thick quartz windows during high-temperature operation. The optical shape of the windows changes as the temperature rises, but we have learned how to correct for this easily by simple adjustments of a normal "zee"-type schlieren system.

We experienced one throat failure at 3,000°F. operation. The failure is believed to have resulted from a partial blockage of the water cooling passage. The damage was localized to the throat area by the resulting water leak, and the throat has been subsequently repaired. The inlet total temperature can be varied easily and quickly by adjusting the fuel rate to the hydrogen superheater. The present manual control easily permits a temperature rate of change of the order of 1,000°F. per sec. This may afford an interesting high-temperature structural testing technique.

REFERENCE

[1] Gross, Robert A., *Design Report: Supersonic Combustion Tunnel*, AFOSR-TN-57-677, ASTIA No. 136-667, October, 1957.

The Compressible Laminar Boundary Layer With Arbitrary Pressure Gradient and Wall Temperature Distribution*

James C. Williams, III

Research Engineer, Engineering Center, University of Southern California, Los Angeles, Calif.

April 15, 1959

IN A FAIRLY RECENT and very complete paper, Cohen and Reshotko[1] solved the equations of motion for the compressible laminar boundary layer with heat transfer and pressure gradient. In this analysis, however, the pressure gradients allowed were only those which could be treated by the method of similar solutions and, also to meet conditions of similarity, the wall temperature was assumed constant. It is possible, as will be shown here, to remove the restriction of similar solutions and thereby obtain solutions to the compressible laminar boundary layer with arbitrary pressure gradient and wall temperature distribution.

The equations of continuity, momentum, and energy for a steady, thin, compressible laminar boundary layer are well known and will not be reproduced here. By making the assumptions of: (1) constant specific heat, (2) Prandtl Number of unity, and (3) a viscosity-temperature relationship $\mu = \mu_0 \lambda T/T_0$, and by employing the Stewartson type of transformation of reference 1, the compressible laminar boundary-layer equations can be transformed into the set

$$(\partial U/\partial X) + (\partial V/\partial Y) = 0 \tag{1}$$

$$U(\partial U/\partial X) + V(\partial U/\partial Y) = U_E(dU_E/dX)(1 + S) + \nu_0(\partial^2 U/\partial Y^2) \tag{2}$$

$$U(\partial S/\partial X) + V(\partial S/\partial Y) = \nu_0(\partial^2 S/\partial Y^2) \tag{3}$$

The notation here is identical with that of reference 1. The transformed coordinates are related to the physical coordinates by the transformation relation, and the transformed and physical velocity components are related through the stream function, ψ, which is common to both systems. Thus,

$$\left.\begin{aligned} dX &= \lambda(a_e/a_0)(\rho e/\rho_0)dx, \quad dY = (\rho/\rho_0)(a_e/a_0)dy \\ U &= (\partial\psi/\partial X) = (a_0/a_e)u, \quad V = \partial\psi/\partial Y \end{aligned}\right\} \tag{4}$$

Any solution of the transformed set of Eqs. (1)–(3) is a solution of a physical boundary-layer problem and is related to the physical problem through Eqs. (4).

Now, instead of attempting to solve Eqs. (1)–(3) by the method of similar solutions as did Cohen and Reshotko, a series solution type of analysis, which is a slight modification of the well-known Blasius series of incompressible boundary-layer theory, is used. Thus, the velocity at the edge of the boundary layer (in the transformed system) is written as a power series in X,

$$U_e = a_1X + a_2X^2 + a_3X^3 + a_4X^4 + \dots \tag{5}$$

where the a_n are constants determined from the potential flow and the transformation equations. Following the conventional Blasius-series procedure, the distance from the wall is made dimensionless by introducing $\eta = Y\sqrt{a_1/\nu_0}$, and the stream function is also written as a power series in X with coefficients $f_n(n = 1, 2, 3, \text{etc.})$ which are functions of the dimensionless normal coordinate. Thus,

$$\psi = \sqrt{\nu_0/a_1}\{a_1Xf_1 + a_2X^2f_2 + a_3X^3f_3 + a_4X^4f_4 + \dots\} \tag{6}$$

Finally, the enthalpy function S is written as a power series in X with coefficients $S_n(n = 1, 2, 3, 4, \text{etc.})$ which are also functions of the dimensionless normal coordinate.

$$S = S_0 + S_1X + S_2X^2 + S_3X^3 + S_4X^4 + \dots \tag{7}$$

Now, if the velocities and their derivatives [obtained from the stream function, Eq. (6)], the external stream velocity, Eq. (5), and the temperature (enthalpy) function, Eq. (7), and its derivatives are introduced into the transformed momentum and energy equations, and coefficients of like powers of X are equated, a number of sets of simultaneous ordinary differential equations are obtained for the functions f_n and S_n. The *first two* equations obtained from the momentum equation are:

$$f_1'^2 - f_1f_1'' = (1 + S_0) + f_1''' \tag{8a}$$

$$3f_1'f_2' - (2f_2f_1'' + f_1f_2'') = [3(1 + S_0) + (a_1/a_2)S_1] + f_2''' \tag{8b}$$

and the first two equations obtained from the energy equation are:

$$f_1S_0' + S_0'' = 0 \tag{9a}$$

$$a_1f_1'S_1 - 2a_2f_2S_0' - a_1f_1S_1' = a_1S_1'' \tag{9b}$$

where primes denote differentiation with respect to η.

Eqs. (8a) and (9a) can be solved simultaneously to yield f_1 and S_0, Eqs. (8b) and (9b) yield f_2 and S_1, and so forth. It should be noted that only the first set [Eqs. (8a), (9a)] is nonlinear. (In fact, this set is identical with the equations solved by Cohen and Reshotko if their pressure-gradient parameter, β, is taken as unity.) The other sets of equations are linear in the undetermined variables f_n and S_{n-1} when the preceding functions (f_1 through f_{n-1} and S_0 through S_{n-2}) have been determined.

The boundary conditions on the transformed boundary-layer Eqs. (1)–(3) are:

$$U(X, 0) = V(X, 0) = 0$$

$$S(X, 0) = S_w(X)$$

$$\lim_{Y \to \infty} S = 0 \qquad \lim_{y \to \infty} U = U_e(X)$$

The corresponding boundary conditions on the functions f_n are:

$$f_n(0) = f_n'(0) = 0; \quad \lim_{\eta \to \infty} f' = 1$$

If the wall temperature is a given function of X, then the enthalpy function at the wall may be written

$$S_w(X) = S_{0_w} + XS_{1_w} + X^2S_{2_w} + X^3S_{3_w} + \dots$$

where S_{n_w} are constants determined by the prescribed wall temperature distribution. In light of this, the boundary conditions on the functions S_n are

$$S_n(0) = S_{n_w}, \quad \lim_{\eta \to \infty} S_n = 0$$

The method which has been described here yields a set of simultaneous ordinary differential equations [Eqs. (8) and (9)] which, when solved with the appropriate boundary conditions, yields the functions f_n and S_n which completely describe the boundary layer on a body with arbitrary pressure distribution and arbitrary wall temperature distribution. Unfortunately, the added generality obtained in this method is somewhat offset by the complexity of the resulting equations. With modern high-speed computing devices available, this complexity should, however, offer little difficulty.

* This research was supported in whole by the USAF under Contract AF 18(603)-95 monitored by the Air Force Office of Scientific Research of the Air Research and Development Command.

REFERENCES

[1] Cohen, Clarence B., and Reshotko, Eli, *Similar Solutions for the Compressible Laminar Boundary Layer with Heat Transfer and Pressure Gradient*, NACA Rep. 1293, 1956.

[2] Schlichting, Hermann, *Boundary Layer Theory;* McGraw-Hill Book Co., Inc., New York, 1955.

[3] Williams, James C., III, *On the Laminar Boundary Layer with Arbitrary Pressure Gradient and Wall Temperature Distributions*, AFOSR TN 58-583, AD-162 103, USCEC Rept. 40-204, July 31, 1958.

Stability Criteria for the Airframe Dynamics of a Liquid-Propellant Rocket

Josef S. Pistiner
Design Engineer, Systems Analysis Section Staff, The Martin Company, Denver, Colo.

April 20, 1959

IT CAN BE SHOWN[1] that the pitch (or yaw) rigid-body dynamics of a gimbaled-engine rocket containing two sloshing masses may be represented, for assumed zero fluid damping, by an open-loop transfer function (in Laplace-transform notation) of the form

$$\theta(s)/\delta(s) = KN(s)/s^2D(s) \tag{1}$$

where θ = pitch (or yaw) vehicle attitude, δ = engine deflection,

$$N(s) = s^4 + a_1s^2 + a_0 \tag{2}$$

$$D(s) = s^4 + b_1s^2 + b_0 \tag{3}$$

K = gain constant, and a_0, a_1, b_0, and b_1 are all real and positive coefficients. Furthermore, it can be shown on a root-locus plot that for rockets with flight-control systems which sense angular rate and displacement, the airframe-autopilot loop may be stabilized if $N(s)/D(s)$ possesses a zero-pole-zero-pole configuration along the imaginary axis in the s-plane.

$N(s)$ and $D(s)$ may be written in the following form:

$$N(s) = (s^2 - s_1^2)(s^2 - s_2^2) \tag{4}$$

$$D(s) = (s^2 - s_2^2)(s^2 - s_4^2) \tag{5}$$

Then the stability condition defining the required alternation of the zeros and poles is expressed by:

$$0 < |s_1| < |s_2| < |s_3| < |s_4| < \infty \tag{6}$$

By use of Eqs. (2) and (3), condition (6) may be redefined by three separate inequalities (omitting the trivial conditions of $|s_1| > 0$ and $s_4 < \infty$). These three stability conditions are:

$$\text{(a)}\quad b_1 - \sqrt{b_1^2 - 4b_0} > a_1 - \sqrt{a_1^2 - 4a_0} \tag{7}$$

$$\text{(b)}\quad a_1 - \sqrt{a_1^2 - 4a_0} > b_1 - \sqrt{b_1^2 - 4b_0} \tag{8}$$

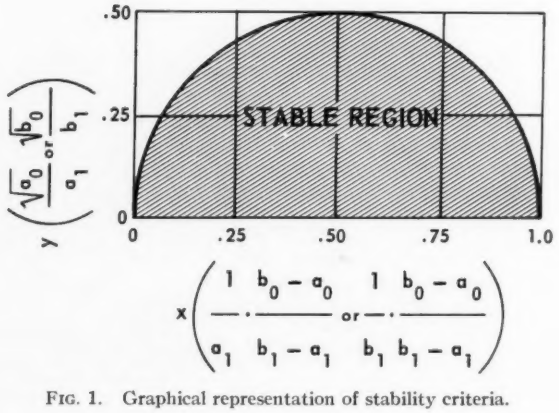

FIG. 1. Graphical representation of stability criteria.

$$\text{(c)}\quad b_1 + \sqrt{b_1^2 - 4b_0} > a_1 + \sqrt{a_1^2 - 4a_0} \tag{9}$$

By manipulation of inequalities (7) through (9), the following necessary and sufficient conditions for proper alternation of zeros and poles are obtained:

$$b_0 > a_0 \tag{10}$$

$$b_1 > a_1 \tag{11}$$

$$(b_0 - a_0)^2 < (b_0a_1 - a_0b_1)(b_1 - a_1) \tag{12}$$

Inequality (12) implies also that

$$b_0a_1 - a_0b_1 > 0 \tag{13}$$

It should be noted, however, that inequality (13) is a necessary but not a sufficient condition. Inequality (12) may be rewritten as:

$$[(b_0 - a_0)/(b_1 - a_1)] < a_1 - [(b_1 - a_1)/(b_0 - a_0)]a_0 \tag{12a}$$

If we let $$(b_0 - a_0)/(b_1 - a_1) = z \tag{14}$$

then, for stability, $$z^2 < a_1z - a_0 \tag{15}$$

and the stability boundary is

$$z^2 - a_1z + a_0 = 0 \tag{16}$$

Setting $$x = z/a_1 = (1/a_1)[(b_0 - a_0)/(b_1 - a_1)] \tag{17}$$

and $$y = \sqrt{a_0}/a_1 \tag{18}$$

we obtain $$(x - 0.5)^2 + y^2 = (0.5)^2 \tag{19}$$

This is the equation of a circle in the x-y plane with origin at ($x = 0.5$, $y = 0$) and radius of 0.5. The region for stability, therefore, is the area within the semicircle in that quadrant of the x-y plane where x and y are both positive (Fig. 1).

Since condition (12) may be rewritten also in the form

$$[(b_0 - a_0)/(b_1 - a_1)] < b_1 - [(b_1 - a_1)/(b_0 - a_0)]b_0 \tag{12b}$$

the same semicircle will define the stability region if we alternately

let $$x = x' = (1/b_1)[(b_1 - a_0)/(b_1 - a_1)] \tag{20}$$

and $$y = y' = \sqrt{b_0}/b_1 \tag{21}$$

REFERENCE

[1] Heist, E. K., *Equations of Motion of a Missile with Sloshing*, Rep. No. GM-TM-146, Guided Missile Research Division, The Ramo-Wooldridge Corporation, February 8, 1956.

A Note on the Blasius Equation With Three-Point Boundary Conditions

William Squire
Bell Aircraft Corporation, Buffalo, N.Y.

April 20, 1959

RECENTLY, Napolitano[1] has shown that a number of mixing problems involve the Blasius equation subject to conditions at three points ($\pm\infty$, 0). Analytical approximation by a perturbation technique and numerical solutions on a high-speed computer were reported. In this note, a numerical technique for evaluating integrals over an infinite range, which the author has shown[2] to be applicable to ordinary boundary-layer problems, will be applied.

We consider $$f''' + 2ff'' = 0 \tag{1}$$

subject to $$f'(+\infty) = 1 \tag{2a}$$

$$f'(-\infty) = 1 - \lambda, \quad 0 \leq \lambda \leq 1 \tag{2b}$$

$$f(0) = 0 \tag{2c}$$

Let $f'(0)$ and $f''(0)$, which are required to start the numerical integration from $\eta = 0$, be denoted by α and β, respectively. A formal integration of Eq. (1) gives

$$f''(\eta) = \beta e^{-2\int_0^\eta f d\eta} \tag{3}$$

By integrating Eq. (3) from $-\infty$ to $+\infty$, the relation

$$f'(+\infty) - f'(-\infty) = \lambda = \beta \int_{-\infty}^{+\infty} e^{-2\int_0^\eta f d\eta} d\eta \tag{4}$$

is obtained, while integration from 0 to $+\infty$ gives

$$1 - \alpha = \beta \int_0^\infty e^{-2\int f d\eta} d\eta \tag{5}$$

The integral in Eq. (5) can be brought into the form for Gauss-Laguerre quadrature by introducing the new variable

$$x = 2\int_0^\eta f d\eta \tag{6}$$

Because of the difference in the conditions at $\eta = 0$, the integral must be written as

$$1 - \alpha = \beta \int_0^\infty x^{-(1/2)} e^{-x} \{x^{1/2}/2f(x)\} dx \tag{7}$$

since it is $x^{1/2}/f$ which approaches a finite value, $^1/_2\alpha^{-1/2}$. The weights and abscissas for the quadrature are readily determined.[3] For the first-order case, we have

$$a_1 = 1/2, \quad H_1 = \sqrt{\pi}$$

and if we use only the leading term, we obtain

$$\beta = (1/2)(1 - \alpha)\sqrt{\alpha/\pi} \tag{8}$$

The integral in Eq. (4) which goes from $-\infty$ to $+\infty$ cannot be evaluated by Gauss-Laguerre quadrature but can be handled by the related Gauss-Hermite method.[3] This formula states

$$\int_{-\infty}^{+\infty} e^{-t^2} g(t) dt = \Sigma H_j g(aj) \tag{9}$$

The weights and abscissas are determined by relations analogous to those for Gauss-Laguerre quadrature but involving Hermite polynomials. The first-order case is

$$a_1 = 0, \quad H_1 = \sqrt{\pi}$$

The values of the 2(1) 20 order are given by Salzer[4] and Kopal.[3] The quadrature is exact when $g(t)$ is a polynomial of degree $2n - 1$ or less.

Introducing the new variable

$$t = \sqrt{2\int_0^\eta f d\eta} \tag{10}$$

transforms Eq. (4) into

$$\lambda = \beta \int_{-\infty}^{+\infty} e^{-t^2} [t/f(t)] dt \tag{11}$$

If we use only the leading term in the power series $t/f(t) = \alpha^{-1/2}$ and in conjunction with the first-order quadrature formula Eq. (11) gives

$$\lambda = \beta\sqrt{\pi/\alpha} \tag{12}$$

From Eq. (12) and Eq. (18) it is found that

$$\alpha = 1 - \lambda/2 \tag{13a}$$

$$\beta = \lambda\sqrt{[1 - \lambda/2]/\pi} \tag{13b}$$

While Eq. (13a) corresponds to the first approximation in Napolitano's perturbation procedure, Eq. (13b) compares favorably with the third approximation, as seen in Table 1 in which the exact values are those obtained numerically by Napolitano.

TABLE 1

λ	α Eq. (13a)	α Exact	β Eq. (13b)	β Exact
0.2678	0.8661	0.8698	0.1406	0.1406
0.4796	0.7602	0.7739	0.2359	0.2360
0.5541	0.7229	0.7421	0.2658	0.2660
0.6915	0.6543	0.6870	0.3156	0.3158

Unfortunately, the calculation of higher-order approximations by the present method does not give simple analytical expressions but is a numerical process.

REFERENCES

[1] Napolitano, L. G., *The Blasius Equation with Three-Point Boundary Condition*, Quart. Appl. Math., Vol. 16, No. 4, pp. 397–408, January, 1959.

[2] Squire, W., *Application of Generalized Gauss-Laguerre Quadrature to Boundary-Layer Problems*, Readers' Forum, Journal of the Aero/Space Sciences, Vol. 26, No. 8, pp. 540, 541, August, 1959.

[3] Kopal, Z., *Numerical Analysis*, Chapt. 7; John Wiley and Sons, New York, 1955.

[4] Salzer, H. E., Zucker, R., and Capuano, R., *Table of the Zeros and Weight Factors of the First Twenty Hermite Polynomials*, J. Res., Vol. 48, No. 2, pp. 111–116, February, 1952.

A Remark Concerning the Vibration of a Delta Wing in Supersonic Flight

Milomir M. Stanišić

Associate Professor of Engineering Sciences, Purdue University, Lafayette, Ind.

April 20, 1959

INTRODUCTION

THIS PAPER is concerned with the formulation of an integral equation, resulting as a consequence of the boundary conditions on a delta wing by the supersonic motion in three-dimensional nonsteady flow. The method of velocity potential has been used in order to formulate this equation, which solution leads to the determination of a source function. The integral equation obtained is not solved in this paper because of the enormous difficulties imposed by its domain of integration and its unsymmetric kernel. However, the object of this paper is to show that the method of velocity potential is inconvenient for the solution of such an important problem. The Prandtl method, known as "acceleration-potential method," is much more suitable. Furthermore, this paper shows that much more remains to be learned in the theory of singular integral equations.

FORMULATION OF THE PROBLEM

The Euler equation, neglecting the body force, can be written as

$$\boldsymbol{b} + (1/\rho)\text{grad } p = 0 \tag{1}$$

where $\boldsymbol{b}$ is acceleration vector, p characterizes the pressure field, so that $p = f(\rho)$, with ρ as density. However,

$$(1/\rho) \text{ grad } p = \text{grad } P(p) \tag{2}$$

letting

$$\boldsymbol{b} = \text{grad } \chi \tag{3}$$

Then, Eqs. (1) and (2) lead to

$$\chi + P(p) = \text{constant} \tag{4}$$

where $\chi = \chi(x, y, z, t)$ represents the acceleration potential. Therefore, for linearized motion in the x-direction, we have

$$b_x = \partial\chi/\partial x = (\partial u/\partial t) + U(\partial u/\partial x) \tag{5}$$

where U is velocity of the wing and

$$u = \partial\varphi/\partial x \tag{6}$$

with $\varphi = \varphi(x, y, z, t)$ as a velocity potential function. Hence, Eqs. (5) and (6) lead to

$$\partial\chi/\partial x = (\partial/\partial x)[(\partial\varphi/\partial x) + U(\partial\varphi/\partial x)] \tag{7}$$

Using the transformation

$$x = \xi + U\tau; \quad y = \eta; \quad z = \zeta; \quad t = \tau \tag{8}$$

one has $\partial/\partial x = (\partial/\partial\xi)(\partial\xi/\partial x) + (\partial/\partial\tau)(\partial\tau/\partial x)$

and $\partial/\partial t = (\partial/\partial\xi)(\partial\xi/\partial t) + (\partial/\partial\tau)(\partial\tau/\partial t)$ (9)

Moreover,

$$\partial\xi/\partial x = 1; \quad \partial\tau/\partial x = 0; \quad \partial\xi/\partial t = -U; \quad \partial t/\partial\tau = 1 \tag{10}$$

Therefore, Eqs. (7)–(10) lead to

$$\chi(\xi + U\tau, \eta, \zeta, \tau) = [\partial\varphi(\xi + U\tau, \eta, \zeta, \tau)]/\partial\tau \tag{11}$$

Hence, $$\varphi(\xi + U\tau, \eta, \zeta, \tau) = \int_{-\infty}^{\tau} \chi(\xi + U\theta, \eta, \zeta, \theta)d\theta \tag{12}$$

Note that the acceleration potential $\chi(x, y, z, t)$ for nonsteady three-dimensional flow is a given function[1] of the form

$$\chi(x, y, z, t) = -(e^{-i\omega t}/\pi)(\partial/\partial x)\iint_{(D)} A(x_1, y_1, 0) \times K(x, y, z; x_1, y_1, 0)\, dx_1 dy_1 \tag{13}$$

where ω is the frequency of the flow, $A(x_1, y_1, 0)$ is the source function for three-dimensional nonsteady flow, D is the domain of integration, obtained by the intersection of the aftercone with the wing surface, (see Fig. 1), and $K(x, y, z; x_1, y_1, 0)$ is a singular kernel resulting from the solution of the basic wave equation for three-dimensional nonsteady flow given by Eq. (1).

$$K(x, y, z; x_1, y_1, 0) = \frac{z\Lambda}{\sqrt{(y - y_1)^2 + z^2}} \int_0^{\cosh^{-1}[(x-x_1)/\beta\sqrt{(y-y_1)^2+z^2}]} \sinh\theta \sin\left[\Lambda\beta\sqrt{(y - y_1)^2 + z^2}\sinh\theta\right] d\theta + \frac{(x - x_1)z\cos\left\{\Lambda\sqrt{(x - x_1)^2 - \beta^2[(y - y_1)^2 + z^2]}\right\}}{[(y - y_1)^2 + z^2]\sqrt{(x - x_1)^2 - \beta^2[(y - y_1)^2 + z^2]}} \tag{14}$$

where Λ is an eigenvalue and β is the Mach coefficient. For $\Lambda = 0$, Eq. (14) is reduced exactly to the equation for steady flow.[2] Eqs. (13) and (12) lead to

$$\varphi(\xi + U\tau, \eta, \zeta, \tau) = -(1/\pi)\int_{-\infty}^{\tau} (\partial/\partial\xi)\left\{\iint_{(D)} A(x_1, y_1, 0)K(\xi + U\theta, \eta, \xi; x_1, y_1, 0)dx_1dy_1\right\} \cdot e^{-i\omega\theta}\, d\theta \tag{15}$$

Let $$\xi + U\theta = \mu \tag{16}$$

Then, Eqs. (15) and (16) lead to

$$\varphi(\xi + U\tau, \eta, \zeta, \tau) = -(1/\pi U)(\partial/\partial\xi)\int_{-\infty}^{\xi+U\tau}\left(\iint_{(D)} A(x_1, y_1, 0)K(\mu, \eta, \zeta, x_1, y_1)dx_1dy_1\right)e^{-i\omega[(\mu-\xi)/U]}d\mu \tag{17}$$

Therefore, in spite of Eq. (8),

$$\varphi(x, y, z, t) = -(1/\pi U)(\partial/\partial x)\left\{e^{(i\omega/U)(x-Ut)}\int_{-\infty}^{x}\iint_{(D)} A(x_1, y_1 0)K(\mu, y, z; x_1, y_1, 0)e^{-(i\omega\mu/U)}dx_1dy_1d\mu\right\} \tag{18}$$

Eq. (18) shows the relation between velocity and acceleration potential for three-dimensional nonsteady motion. Denote the surface of the wing for any time as

$$z = g(x, y)e^{-i\omega t} \tag{19}$$

where $g(x, y)$ is prescribed function, regular everywhere in the region under consideration; then, the velocity of the wing is

$$\Omega = \Omega(0, 0, -i\omega g(x, y)e^{-i\omega t}) \tag{20}$$

However, the velocity of the field of flow is

$$\boldsymbol{C} = \boldsymbol{C}(U + u, v, w) \tag{21}$$

Then, the normal component of the velocity of the wing must be equal to the normal component of the velocity of the flow—i.e.,

$$\Omega \cdot \boldsymbol{n} = \boldsymbol{C} \cdot \boldsymbol{n} \tag{22}$$

where $\boldsymbol{n}$ is normal to the surface given by

$$\boldsymbol{n} = \boldsymbol{n}\{g_x(x, y)e^{-i\omega t}, g_y(x, y)e^{-i\omega t}, -1\} \tag{23}$$

where subscripts x and y denote derivatives with respect to x and y, respectively. Eqs. (20)–(23) lead to

$$w = e^{-i\omega t}[Ug_x(x, y) - i\omega g(x, y)] \tag{24}$$

However, $$w = \lim_{z\to 0} \partial\varphi/\partial z \tag{25}$$

Hence, Eqs. (18), (24), and (25) lead to

$$Ug_x(x, y) - i\omega g(x, y) = -(1/\pi U)(\partial/\partial x) \times \left\{e^{(i\omega x/U)}\int_{-\infty}^{x}\lim_{z\to 0}(\partial/\partial z)\left(\iint_{(D)} A(x_1, y_1, 0) \times K(\mu, y, z; x_1, y_1, 0)dx_1dy_1\right)\cdot e^{(i\omega\mu/U)}\, d\mu\right\} \tag{26}$$

This is an integral equation which has to be solved with respect to $A(x_1, y_1, 0)$. The equation is of a very complicated nature and does not belong to any type of integral equations treated in the literature of today. The exact solution of this integral equation seems hopeless. Even an approximate solution is extremely hard to find. Note that the integration has to be performed in the Hadamard sense. Hence, the velocity potential leads to a very complicated integral equation, and therefore this method is not convenient for formulation of such a problem. However, the method of acceleration potential is more convenient and, as such, has been used by the author in his work.[3]

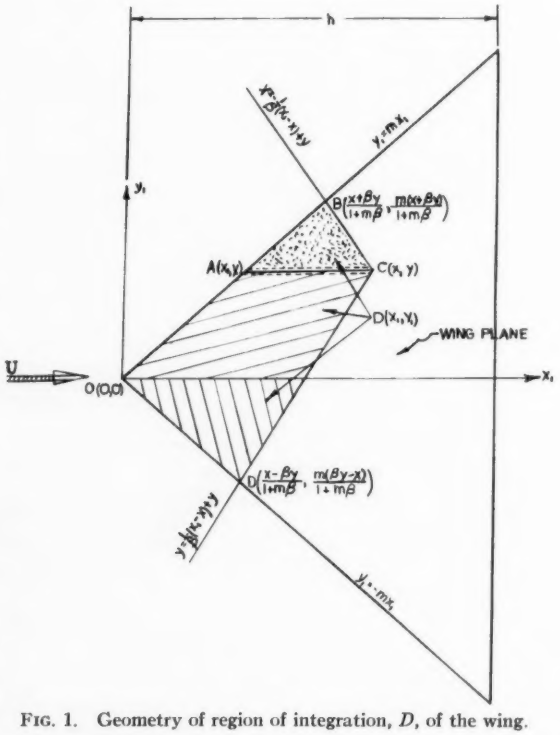

FIG. 1. Geometry of region of integration, D, of the wing.

References

[1] Stanišić, M. M., *On the Oscillation of a Delta Wing in Supersonic Flow*, Doctoral thesis, submitted to Department of Mathematics, Illinois Institute of Technology; Vol. 7, p. 11, December, 1958.

[2] Heaslet, A. M., Lomax, H., and Jones, A. L., *Volterra's Solution of the Wave Equation as Applied to the Three-dimensional Supersonic Airfoil Problems*, NACA TN 1412, September, 1947.

[3] Stanišić, M. M., *On the Solution of an Integral Equation Appearing in Delta-wing theory*, to be published in ZAMM.

On the Stable Shape of a Slender Ablating Graphite Body*

George W. Sutton

Consulting Research Engineer, General Electric Company, Philadelphia, Pa.

April 28, 1959

Symbols

C = mass concentration
D = diffusion coefficient
m = mass flow
p = pressure
S_c = Schmidt Number
R = gas constant
t = time
T = temperature
u = axial velocity
v = radial velocity
V = ablation rate of tip
x = axial coordinate
y = radial coordinate
ρ = density
μ = viscosity

Subscripts

o = oxygen
c = carbon
e = edge of gaseous boundary layer
w = wall
∞ = free stream

Introduction

It has been demonstrated that a slender graphite rod, when placed in the flow of an air-plasma tunnel, ablates into a slender ogive whose shape then remains fixed during further ablation.[1]

In this note, the terminal shape is calculated under the assumption that the graphite burns to form CO at the surface. Under these conditions, stoichiometry requires that

$$m_c = \rho_c(dy_w/dt) = 0.75m_0 = 0.75\rho_0 v_0 \tag{1}$$

For this assumption, calculations of the terminal shape have been made.

Equations

Continuity

$$(\partial/\partial x)(\rho\, uy) + (\partial/\partial y)(\rho\, vy) = 0 \tag{2}$$

Momentum

$$\rho u(\partial u/\partial x) + \rho v(\partial u/\partial y) = \rho_e u_e(du_e/dx) + y^{-1}(\partial/\partial y)[\mu y(\partial u/\partial y)] \tag{3}$$

Diffusion

$$\rho u(\partial C_0/\partial x) + \rho v(\partial C_0/\partial y) = y^{-1}(\partial/\partial y)[y\rho D(\partial C_0/\partial y)] \tag{4}$$

where C_0 is the mass density fraction of O plus O_2.[2]

* This work was supported by the USAF, Ballistic Missile Division, under Contract No. AF 04(647)-269. The author wishes to thank Dr. H. G. Lew and Dr. Irving Korobkin for their stimulating discussions and helpful suggestions, and Ruth Lyons for programing the integration.

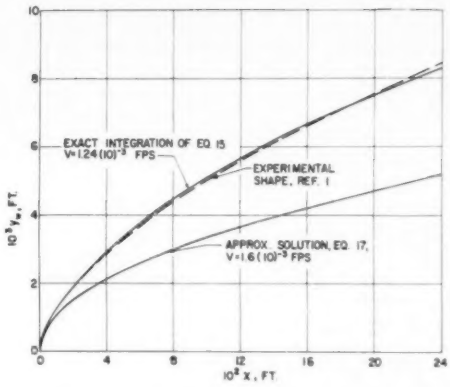

FIG. 1. Experimental and calculated shape of slender ablating graphite rod.

To reduce the above equations to ordinary equations, Pai's transform for slender bodies of revolution[3] is modified as follows:

$$\eta = [\rho_e u_e/(2\xi)^{1/2}]\int_0^y (\rho/\rho_e)y dy \tag{5}$$

$$\xi = \int_0^x \rho_w \mu_w\, u_e\, y_w^2\, dx \tag{6}$$

$$\rho uy = \partial\psi/\partial y,\ \rho vy = -\partial\psi/\partial x \tag{7}$$

$$\psi = (2\xi)^{1/2} f(\eta) \tag{8}$$

Using the above transforms, Eqs. (3) and (4) become

Momentum

$$[(\rho\mu y^2/\rho_w\mu_w y_w^2)f'']' + ff'' + \beta(\rho_e/\rho - f'^2) = 0 \tag{9}$$

Diffusion

$$[(\rho\mu y^2/\rho_w\mu_w y_w^2)S_c^{-1}C_0']' + fC_0' = 0 \tag{10}$$

For the configuration of reference 1, the change in u_e is less than 1 per cent along the body, hence, u_e is taken as u_∞, and β is then zero. If the Schmidt Number for diffusion of the oxygen is unity, then, by comparison of Eqs. (9) and (10), it follows that:

$$C_0 = (C_{0e} - C_{0w})f'(\eta) + C_{0w} \tag{11}$$

where C_{0w}, the concentration of oxygen at the wall, is approximately zero for perfect combustion.

With the assumption that $(\rho\mu y^2/\rho_w\mu_w y_w^2)$ is unity, Eq. (9) reduces to the Blasius equation for a flat plate. With the use of the transforms and Eq. (11) corrected by a factor $S_c^{1/3}$, Eq. (1) becomes

$$f_w = 0.75 S_{cw}^{-2/3} C_{0e} f''_w \tag{12}$$

which indicates that the concentration profiles are similar. With S_{cw} taken as 0.735,[4] and $C_{0e} = 0.231$, tables of Emmons and Leigh[5] give $f_w = -0.090$.

Finally, use is made of the ideal-gas law and the following slender-body relationship:[6]

$$p_w = p_\infty + \rho_\infty u_\infty^2 \ln\left\{[2/(dy_w/dx)](M_\infty^2 - 1)^{-1/2}\right\}(dy_w/dx)^2 \tag{13}$$

Now, if the shape does not change with time, then a Galilean transformation may be used—that is,

$$dy_w/dt = V(dy_w/dx) \tag{14}$$

so that Eq. (1) finally becomes:

$$\frac{dy_w}{dx} = \frac{-(f_w/\rho_c V)(\mu_w u_\infty p_\infty/2R_w T_w)^{1/2} y[1 + G(dy_w/dx)^2]}{\left\{\int_0^x y^2[1 + G(dy_w/dx)^2]dx\right\}^{1/2}} \tag{15}$$

where $G = (\rho_\infty u_\infty^2/p_\infty)\ln\left\{[2/(dy_w/dx)](M_\infty^2 - 1)^{-(1/2)}\right\}$ (16)

Eq. (15) describes the terminal shape of a slender ablating graphite rod.

Solutions

For the conditions which existed during the experiment, G is less than 0.1, hence, as a first approximation, G may be neglected. Then, Eq. (15) may be integrated directly to obtain:

$$y_w = -2(f_w/\rho_e V)(\mu_w u_\infty p_\infty / R_w T_w)^{1/2} x^{1/2} \tag{17}$$

Note that the shape depends on V, which is not yet determined. For the experimentally determined value of $1.6(10)^{-3}$ ft. per sec., the shape predicted by Eq. (17) is shown in Fig. 1, where it may be seen that the agreement is only fair, since the experimental shape is closer to $y \sim x^{0.6}$. A more important objection to Eq. (17) is that it does not indicate a method for obtaining V.

If it is assumed that continuum theory applies at the nose, and that the nose is slightly blunted, then Eqs. (2)–(4), when integrated at an axially symmetric stagnation point, indicate that for the experimentally determined value of V, the nose radius of curvature is the same as the molecular mean free path in the undisturbed flow. Hence, it may be possible that the rate at which the tip recedes may be predicted by free molecule theory. The calculated free molecule graphite combustion is $V = 2.92(10)^{-3}$ ft. per sec., which agrees with the observed value within a factor of two. Hence, it appears that there is a region of shock-boundary-layer interaction at the tip, and that Eq. (15) cannot be used near the tip.

In order to obtain more realistic results, Eq. (15) was integrated numerically on an IBM 704, starting from a point 5 mm. from the tip, using the experimentally determined value of dy_w/dx and y_w at this point. The best fit with the experimental curve was obtained with a value of $V = 1.21(10)^{-3}$ ft. per sec., which is 26 per cent less than the observed value. In addition, the calculated shape correlates as $y \sim x^{0.65}$, which is in better agreement with the observed shape. This curve is also shown in Fig. 1.

References

[1] Christensen, D., and Buhler, R. D., *On the Stable Shape of an Ablating Graphite Body*, Readers' Forum, Journal of the Aero/Space Sciences, Vol. 26, No. 1, p. 54, January, 1959.

[2] Dennison, R., and Dooley, D., *Combustion in the Laminar Boundary Layer of Chemically Active Sublimators*, Aeronutronic Systems Publication, U-110, September 23, 1957.

[3] Pai, S. I., *On the Boundary-Layer Equations of a Very Slender Body of Revolution*, Readers' Forum, Journal of the Aeronautical Sciences, Vol. 23, No. 8, pp. 795–796, August, 1956.

[4] Baulknight, C. W., *Transport Properties for Engineering Calculations*, General Electric Company, MSVD, Aerophysics Research Memorandum No. 19, November 3, 1958.

[5] Emmons, H. W., and Leigh, D., *Tabulation of the Blasius Function with Blowing and Suction*, Harvard University, Combustion Aerodynamics Laboratory Interim TR 9, Army Ordnance Department, Contract DA-19-020-ORD-1029, November, 1954.

[6] Shapiro, A. H., *Compressible Fluid Flow*, Vol. 2, p. 671; Ronald Press, New York, 1954.

Heat Transfer and Recovery Factor in a Laminar Boundary Layer With Arbitrary Pressure Gradient and Wall Temperature Distribution

Bernard Le Fur
Engineer, Nord Aviation, Châtillon-sous-Bagneux, France

April 28, 1959

Symbols

Subscripts

- δ = outer edge of boundary layer
- w = wall conditions
- r = insulated wall

LIGHTHILL[1] HAS INTRODUCED a method to determine the heat transfer at the wall when the pressure gradient and the wall temperature are arbitrary, but does not take into account the friction heating. It will be proved in this note that it is possible to treat the case where this heating is not negligible and to calculate the temperature recovery factor.

If the stream velocity u_δ and the difference between the wall temperature T_w and the stream temperature T_δ are small, then it can be assumed that the viscosity μ, the density ρ, the heat conductivity k, and the specific heat at constant pressure C_p are constant throughout the fluid.

Using as independent variables the abscissa x and the stream function ψ, the differential eqautions of conservation of momentum and energy take the form given to them by von Mises:

$$(\partial Z/\partial x) - \rho\mu u(\partial^2 Z/\partial\psi^2) \tag{1}$$

$$(\partial\Theta/\partial x) - (\rho\mu/Pr)(\partial/\partial\psi)[u(\partial\Theta/\partial\psi)] = -(\rho\mu/2C_p)(\partial u/\partial\psi)(\partial Z/\partial\psi) \tag{2}$$

with $Z(x, \psi) = u_\delta^2 - u^2$ and $\Theta(x, \psi) = T - T_\delta$.

The following boundary conditions must be satisfied:

$$\lim_{x\to 0} Z(x, \psi) = 0; \quad \lim_{\psi\to 0} Z(x, \psi) = u_\delta^2; \quad \lim_{\psi\to\infty} Z(x, \psi) = 0 \tag{3}$$

$$\lim_{x\to 0} \Theta(x, \psi) = 0; \quad \lim_{\psi\to 0} \Theta(x, \psi) = T_w - T_\delta; \quad \lim_{\psi\to\infty} \Theta(x, \psi) = 0 \tag{4}$$

An iterative solution of the system of Eqs. (1) and (2) can be carried out.

Let us take the departure step:

$$u_0 = (2\tau_w/\rho\mu)^{1/2}\psi^{1/2} \tag{5}$$

where the shear stress τ_w at the wall will be determined by the integration of the approximated momentum Eq. (6) hereafter.

The first approximation Z_1 and Θ_1 will be obtained as a solution of the system:

$$(\partial Z_1/\partial x) - \rho\mu u_0(\partial^2 Z_1/\partial\psi^2) = 0 \tag{6}$$

$$(\partial\Theta_1/\partial x) - (\rho\mu/Pr)(\partial/\partial\psi)[u_0(\partial\Theta_1/\partial\psi)] = -(\rho\mu/2c_p)(\partial u_0/\partial\psi)(\partial Z_1/\partial\psi) \tag{7}$$

using the boundary conditions (3) and (4).

Eqs. (6) and (7) have been solved by Lighthill in the case where the right-hand term of Eq. (7) is negligible; the variable t was introduced:

$$t = \int_0^x (2\rho\mu\tau_w)^{1/2} dx \tag{8}$$

and the Laplace transformation with respect to t was used.

The shear stress τ_w becomes a solution of the integral equation:

$$\int_0^x \left(\int_{x'}^x \sqrt{\tau_w(z)}\,dz\right)^{-1/3} [\tau_w(x')]^{3/2} dx' = [(\rho\mu)^{2/3}\Gamma(1/3)/2.3^{1/3}] u_\delta^2(x) \tag{9}$$

Eq. (7) can now be integrated with a right-hand term, using the method of variation of constants.

The heat flux at the wall:

$$q_w = -k(\partial T/\partial y)_w = -(2\rho\mu\tau_w)^{1/2}(c_p/Pr) \lim_{\psi\to 0} \psi^{1/2}(\partial\Theta/\partial\psi)$$

is obtained as a Stieltjes integral:

$$q_w = [3^{1/3}/\Gamma(1/3)] c_p(\rho\mu)^{1/3} Pr^{-2/3} \tau_w^{1/2} \int_0^x \left(\int_{x'}^x \sqrt{\tau_w(z)}\,dz\right)^{-1/3} d[T_w(x') - T_r(x')] \tag{10}$$

where τ_w is the solution of the integral Eq. (9). T_r is the recovery temperature:

$$T_r = T_\delta + r(Pr) u_\delta^2/2c_p$$

The recovery factor r is a function of Pr, either of the form:

$$r(Pr) = Pr^{2/3} {}_2F_1(1/3, 2/3; 4/3; 1 - Pr) \tag{11}$$

where the hypergeometric series converges for $0 < Pr < 2$; or of the form:

TABLE 1
Values of $Nu_x \cdot Re_x^{-1/2}$ for $Pr = 1$

m	E. Eckert	Present paper	Lighthill
−0.0654	0.284	0.265	0.262
0	0.332	0.332	0.339
1/9	0.378	0.395	0.405
1/3	0.440	0.478	0.491
1	0.570	0.643	0.661
4	0.939	1.091	1.121

$$r(Pr) = Pr^{1/3}{}_2F_1[1/3, 2/3; 4/3; (Pr - 1)/Pr] \quad (12)$$

where the hypergeometric series converges for $1/2 < Pr < \infty$.

Thus, in the first approximation, the recovery factor is independent of the pressure gradient.

The values of the recovery factor for some values of the Prandtl Number are given in reference 2. When $Pr \to 0$, the expression (11) reduces to:

$$[\Gamma^2(1/3)/2\pi\sqrt{3}]Pr^{2/3} = 1.7668Pr^{2/3} \quad (13)$$

When $Pr \to \infty$, the expression (12) reduces to:

$$[\Gamma^2(1/3)/2\pi\sqrt{3}]Pr^{1/3} = 1.7668Pr^{1/3} \quad (14)$$

THE HEAT-TRANSFER COEFFICIENT ON WEDGES

When $u_\delta = cx^m$ and the wall temperature T_w is uniform, the effective temperature T_{eff} for which $q_w = 0$ on a given point, is:

$$T_{eff} = T_\delta + \Big(1 + (r - 1)\Gamma(2/3) \times \{\Gamma[(11m + 3)/(3m + 3)]/\Gamma[(10m + 2)/(3m + 3)]\}\Big)(u_\delta^2/2c_p) \quad (15)$$

Then the local Nusselt number is:

$$Nu_x = q_w x/k(T_w - T_{eff}) \quad (16)$$

We have:

$$Nu_x \cdot Re_x^{-1/2} = Pr^{1/3}\{3^{7/8}(m + 1)^{1/2}/2^{3/2}\pi^{1/4}[\Gamma(1/3)]^{1/2}\} \times \{\Gamma[(11m + 3)/(3m + 3)]/\Gamma[(9m + 1)/(3m + 3)]\}^{1/4} \quad (17)$$

When $Pr = 1$, T_{eff} equals the stagnation temperature T_s, and we have with the method of reference 1:

$$Nu_x \cdot Re_x^{-1/2} = \{3^{3/2}(m + 1)^{1/2}[f''(0)]^{1/2}\}/[2^{5/6}\Gamma(1/3)] \quad (18)$$

where the function $f''(0)$ has been calculated by Hartree[3] for certain values of m.

The values of $Nu_x \cdot Re_x^{-1/2}$ for some values of m are shown on Table 1 and compared with the exact values calculated by E. Eckert[4] and those calculated by the formula (18).

Thus, in the case of wedges, the method presented in this note yields a closed form expression (17) for $Nu_x \cdot Re_x^{-1/2}$, which departs further from the exact values as m increases, but is always closer than Lighthill's expression (18).

CONCLUSION

Although approximate values of τ_w, as given by the integral Eq. (9) are used in formula (10), the latter yields better results than the Lighthill's method, which, on the other hand, is only justified for large Prandtl Numbers. The recovery-factor expression given in this paper is—as far as the author knows—the first closed form theoretically justified for any value of Prandtl Number.

REFERENCES

[1] Lighthill, M. J., *Contributions to the theory of heat transfer through a laminar boundary layer*, Proc. Royal Soc. (London), Ser. A, Vol. 202, No. 1070, pp. 359–377, August, 1950.

[2] Le Fur, B., *Facteur thermique pariétal et densité de flux de chaleur á la paroi dans une couche limite laminaire á propriétés physiques constantes avec gradient de pression*, Comptes Rendus de l'Académie des Sciences, Vol. 247, No. 25, pp. 2287–2290, 1958.

[3] Hartree, D. R., *On an equation occurring in Falkner and Skan's approximate treatment of the equations of the boundary layer*, Proc. Cambridge Philos. Soc., Vol. 33, Part 2, pp. 223–239, 1937.

[4] Eckert, E., *Die Berechnung des Wärmeüberganges in der laminaren Grenzschicht umströmter Körper*, VDI-Forschungsheft, No. 416, 1942.

An Alternative Formulation of the Problem of Flutter in Real Fluids*

Wen-Hwa Chu and H. Norman Abramson
Research Engineer and Manager, Respectively, Engineering Analysis Section, Southwest Research Institute, San Antonio, Tex.

May 1, 1959

IT IS WELL KNOWN, in steady flow, that the actual lift curve slope is somewhat less than that predicted by inviscid flow theory, even at small angles of attack. As the stall angle is approached, the lift curve slope continually decreases and thus deviates even more from the theoretical value. Pinkerton[1] employed the measured circulation to determine the pressure distribution and found that the resulting prediction of the moment is considerably improved over that given by the classical theory. This amounts to replacing the conventional Kutta-Joukowski condition with the condition that the total lift should agree with the measured value, and this, in turn, completely determines the flow pattern. Practically, this is accomplished by giving a fictitious camber to the profile. Since potential flow theory is valid outside of the boundary layer, once the boundary-layer thickness is known, the potential flow may be corrected for the displacement thickness and the viscous wake by appropriate source distributions. The boundary layer cannot be evaluated, of course, until the potential flow is known and the circulation is applied. A criterion to determine the circulation, by generalizing the Kutta-Joukowski condition, was proposed by Preston[2] and Spence[3] by assuming that the pressure at the trailing edge shall have the same value when determined from the potential-flow values above and below the airfoil. This procedure gives qualitative information concerning viscous effects in steady flow.[4]

Turning now to unsteady flow, it is noted that numerous complications arise.[4] For example, if the separation does not occur forward of the trailing edge, it would seem that the Preston-Spence criterion might apply; but if separation does occur forward of the trailing edge, then the criterion to determine the value of the instantaneous circulation definitely requires some modification. To overcome such difficulties, various semiempirical methods have been proposed.[4–7] These various methods are discussed by Sears[4] and Van de Vooren.[5] One of the most promising of these is that of Rott and George[7] who propose to relax the Kutta-Joukowski condition in the case of unsteady flow and to employ in its place a functional relationship between leading-edge and trailing-edge *pressure* singularities. By assuming this functional relationship to be a linear one, they have actually made a crude unsteady boundary-layer approximation based on the idea that the mean instantaneous pressure gradient depends on the difference between the leading and trailing-edge singularities, which, in turn, determines the magnitude of the trailing edge singularity. The range of applicability of any such linear relationship naturally has to be determined from experimental data. On the other hand, in any combined torsional and flexural oscillation of a lifting surface, the leading and trailing-edge singularities consist of two parts, corresponding to the two prescribed motions, and since these two motions do not produce similar boundary layers, a single factor of proportionality seems insufficient to describe the actual flow condition. Indeed, only single-degree-of-freedom flutter is discussed.

Since the trailing edge singularity is a measure of the boundary-layer thickness at the trailing edge, or, alternatively, is a measure of the shift in location of the rear stagnation point, a straightforward but general approach suggests itself—that is, to treat the problem in the *velocity* field rather than in the pressure field. Thus, we consider the well-known integral equation for the circulation of the bound vortex sheet which can be studied in terms

* The results presented in this note were obtained during the course of research carried out under the BuShips Fundamental Hydromechanics Research Program administered by the David Taylor Model Basin.

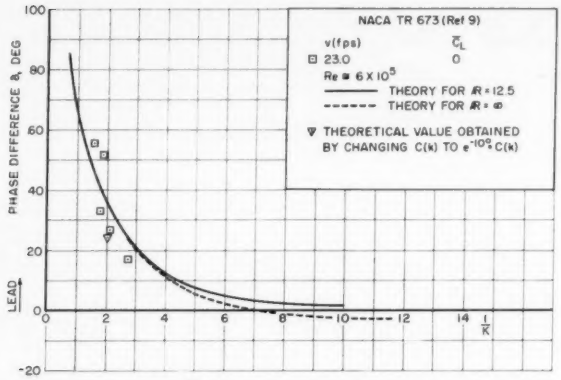

FIG. 1. The phase difference δ between lift and a sine oscillation against wave length parameter $1/k$.

of the simple Joukowski transformation or by Glauert's expansion method.[9]

Let $-2A_0$ and $2A_t$ be the tangential velocities at the leading edge and trailing edge, respectively, in the circle plane, and by deleting these singular parts the remaining part of the bound vortex distribution can be expanded into a Fourier sine series. Thus, one obtains an expression, equivalent to the Glauert-Birnbaum formula,[7] of the form

$$\gamma(x) = 2U\left\{A_0[(1 + \cos\theta)/\sin\theta] - A_t[(1 - \cos\theta)/\sin\theta] + \sum_{n=1}^{\infty} A_n \sin(n\theta)\right\} \quad (1)$$

The first and second terms represent the singularities at the leading edge and trailing edge, respectively. A_0, A_t, and A_n are constant coefficients. It is noted that for a general unsteady motion the bound vortex distribution $\gamma(x)$ can be expressed in an identical form with time dependent coefficients. Only the first few coefficients, up to A_3, are necessary to determine the lift and moment. For flapping/pitching oscillations, the Glauert method then leads to

$$\bar{L} = \pi\rho U^2 b[-ikv_0 - 2(v_1 + 2A_t)C(k)] \quad (2)$$

$$\bar{M} = \bar{L}\,ab + \pi\rho U^2 b^2[(v_1 + 2A_t) - v_0 + (ik/4)(v_1 - v_0) - C(k)(v_1 + 2A_t)] \quad (3)$$

where $C(k)$ is the Theodorsen circulation function, and v_0 and v_1 are the nondimensional complex amplitudes of the normal velocities at the $1/2$ − chord and $3/4$ − chord points, respectively. We note that in the *steady-state* case positive A_t implies a smaller lift coefficient, as required.

Within the scope of linearized theory, it is very general to assume that, for harmonic motions,

$$2A_t = \beta_h(ho/b) + \beta_\alpha\alpha_0 \quad (4)$$

where β_h and β_α are, in general, complex, and depend on the various physical parameters. Physically, α and $\dot{h}$ seem to have the same effect on the boundary-layer flow, and, hence, one may instead assume

$$2A_t = \lambda_2(v_0 - v_1) - \lambda_1 v_1 = \lambda_2 v_0 - (\lambda_1 + \lambda_2)v_1 \quad (5a)$$

$$= -\lambda_1[ik(ho/b) - \alpha_0] + ik\{(1/2)\lambda_2 - \lambda_1[a - (1/2)]\}\alpha_0 \quad (5b)$$

where λ_1 and λ_2 are undetermined parameters which are again, in general, complex quantities dependent on the physical characteristics of the system. These results can be used directly for writing the final modified forms of the flutter coefficients.[10]

While the classical theory has been eminently successful in flutter prediction in many practically important cases, there remain a substantial number of instances where this success has been limited. For example, the phase difference between the lift and the motion for a harmonically oscillating airfoil is known to be a controlling factor in the stability of the motion, but when comparisons of the phase are made between theory and experiment certain discrepancies have been noted.[11] Such discrepancies, though not always significant, depend on the reduced frequency and the mean angle of incidence, and possibly are also affected by the Reynolds Number, the Mach Number, and, to some extent, by the geometrical parameters.

In the preceding analysis, consider the special case $\lambda_2 = 0$, $1 - \lambda_1 = \eta e^{i\phi}$. The expressions for lift and circulation then reduce to those of the classical theory, except that the circulation function $C(k)$ is multiplied by the complex factor $\eta e^{i\phi}$. In the moment equation, there are other slight modifications which, however, may be neglected for purposes of this discussion. To see what this might mean in a practical case, Fig. 1 shows that even when the mean lift coefficient is zero, there is a possible lag of some 5° to 10° in the measured phase at $1/k = 2$, from the value given by classical theory. The theoretical value obtained by choosing $\eta e^{i\phi} = 1e^{-10°}$ is seen to offer some improved agreement with the experimental values. Some possibility of improved agreement between theory and experiment for flutter in high density fluids, by this type of approach, has been discussed elsewhere.[12]

At higher mean angles of incidence, the phase shows an even greater discrepancy between classical theory and experiment.[11] Consequently, the present semiempirical theory may prove to be a useful tool for flutter prediction in those cases where phase differences are likely to be governing factors. In any event, extensive experimental data will probably be required to evaluate the parameters λ_1 and λ_2.

REFERENCES

[1] Pinkerton, R. M., *Calculated and Measured Pressure Distributions Over the Midspan Section of the NACA 4412 Airfoil*, NACA Rep. 563, 1936.

[2] Preston, J. H., *The Calculation of Lift Taking Account of the Boundary Layer*, ARC R & M 2725, 1949.

[3] Spence, D. A., *Prediction of the Characteristics of Two-Dimensional Airfoils*, Journal of the Aeronautical Sciences, Vol. 21, No. 9, pp. 577-587, 620 September, 1954.

[4] Sears, W. R., *Some Recent Developments in Airfoil Theory*, Journal of the Aeronautical Sciences, Vol. 23, No. 5, pp. 490–499, May, 1956.

[5] Jones, W. P., *Airfoil Oscillations at High Mean Incidence*, ARC R&M No. 2654, 1953.

[6] George, M. B. T., *A Theoretical Approach to the Problem of Stall Flutter*, Thesis; Cornell University, Ithaca, N.Y., 1953.

[7] Rott, N., and George, M. B. T., *An Approach to the Flutter Problem in Real Fluids*, Institute of Aeronautical Sciences, Preprint No. 509, 1955.

[8] Van de Vooren, A. I., *Advances in Applied Mechanics*, Vol. 5, "Unsteady Airfoil Theory", pp. 35–89; Academic Press, New York, 1958.

[9] Glauert, H., *The Elements of Aerofoil and Airscrew Theory*; Cambridge University Press, 1926.

[10] Chu, W. H., and Abramson, H. N., *An Alternative Formulation of the Problem of Flutter in Real Fluids*, Tech. Rept. No. 2, Contract Nonr 2470(00), Southwest Research Institute, August, 1958.

[11] Silverstein, A., and Joyner, U. T., *Experimental Verification of the Theory of Oscillating Airfoils*, NACA Rep. 673, 1939.

[12] Abramson, H. N., and Chu, W. H., *A Discussion of the Flutter of Submerged Hydrofoils*, Tech. Rept. No. 1, Contract Nonr 2470(00), Southwest Research Institute, August, 1958 (to appear in J. Ship Res.)

Shock Waves and Dissipation in a Resonance Tube

Ascher H. Shapiro
Professor of Mechanical Engineering, Massachusetts Institute of Technology, Cambridge, Mass.

May 4, 1959

IN A RECENT NOTE,[1] Hall and Berry exhibited shadowgraphs showing the existence of shock waves in resonance tubes, and they queried as to the precise nature of the heating effect first reported in systematic experiments by Sprenger.[2]

About a year ago, in a S.B. thesis at M.I.T. by Howick and Hughes,[3] experiments were made with a stainless steel resonance tube, 14.11 in. long, with an internal diameter of 0.415 in., and a

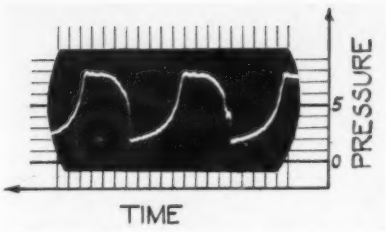

FIG. 1. Pressure-time oscillogram at closed end of resonance tube. Each unit of vertical scale represents one atmosphere; each unit of horizontal scale represents $3.12(10)^{-4}$ sec.

wall thickness of 0.042 in., fed by a convergent nozzle having an exit diameter of 0.415 in. The nozzle was supplied with air at 6 atm. and 70°F. Maximum resonance and tube heating occurred when the axial distance between nozzle and open end was about four tube diameters. Besides measurements of the temperature distribution along the length of the tube, pressure-time histories were measured at the closed end with a quartz-crystal transducer having a natural frequency of 48,000 cps. Fig. 1 shows a typical oscillograph trace, observed with a spacing-to-diameter ratio of 3.6, and corresponding to a time-mean metal temperature measured at the closed end of about 700°F. The vertical pressure jump indicates the existence of shock waves with, in this case, an overall pressure ratio of about 2.0 for the combination of the incident and reflected shocks. These pressure measurements confirm as well as quantify the visual observations of shock waves of Hall and Berry. It may be noticed too that the peak pressure measured is 8 atm., and the time-mean pressure is about 5 atm., as compared with the nozzle supply pressure of 6 atm. The frequency in Fig. 1 is about 365 cps, which corresponds roughly to quarter-wavelength acoustic resonance.

The quantitative pressure measurements also shed some light on the mechanism of heating. Because of the viscous dissipation in the shock wave, there tends to be a net temperature rise at each position in the tube for each period of oscillation. This temperature rise is counterbalanced by heat loss from the tube as the latter heats up. If the shock wave were the only source of dissipation, the product of the frequency with the total amount of energy dissipated in the tube per cycle must, at steady-state conditions, be equal to the rate of heat loss from the tube to the external surroundings. With the data available, we could make only rough estimates of these, but in every case the two energy rates were within a factor of two of each other. Until more refined tests are made, which are now being planned, we can only conclude that while there may be other sources of dissipation—as, for instance, in the oscillating boundary layers on the tube walls—the dissipation in the shock-wave system is surely one of the major mechanisms of heating.

A rough estimate from the data shows that the rate of energy dissipation in the tube is only about 0.2 per cent of the power corresponding to the isentropic enthalpy drop available from the air supply.

The explanation given above suggests that the equilibrium temperature would be higher if the external heat loss were reduced. With the original tube, uninsulated, the maximum time-mean metal temperature achieved at the closed end was about 850°F. When the tube was insulated, this rose to about 1,500°F, although the heat-transfer calculations made *a posteriori* suggest that only a modest fraction of the original heat loss may have been eliminated. Important questions for future investigation are (a) how high a temperature can be achieved if all external heat loss is eliminated, and (b) can the dissipation be made a substantially larger fraction of the energy supply in the jet. The practical implications of these questions are that the resonance tube might possibly be developed into a simple source of very high temperature gas.

REFERENCES

[1] Hall, I. M., and Berry, C. J., *On the Heating Effect in a Resonance Tube*, Readers' Forum, Journal of the Aeronautical Sciences, Vol. 26, No. 4, p. 253, April, 1959.

[2] Sprenger, H., *Thermal Effects in Resonance Tubes*, Mitteilungen aus dem Institut für Aerodynamik, No. 21, pp. 18–34, Zurich, 1954.

[3] Howick, P. E., and Hughes, R. D., *Pressure and Temperature Effects in Resonance Tubes*, S.B. thesis, Department of Mechanical Engineering, M.I.T., June, 1958.

On a Generalized Porous-Wall "Couette-Type" Flow

G. M. Lilley
College of Aeronautics, Department of Aerodynamics, Cranfield, England
May 8, 1959

IN A RECENT PAPER,[1] the problem of a "Couette-type" flow in which the fixed wall is porous has been considered. The results quoted in the above reference can be obtained rigorously by the method stated below in which a different interpretation to one of the parameters is made.

Let us consider the case of a flat plate moving at the constant speed U at a fixed distance from a stationary plate. Let both plates be porous, and assume that uniformly distributed suction or blowing is applied to the fixed surface.

If the velocity components (u, v) are functions of y only, then the equations of motion and continuity for the flow of an incompressible fluid are, respectively:

$$v(du/dy) = -(1/\rho)(\partial p/\partial x) + \nu(d^2u/dy^2) \quad (1)$$

$$v(dv/dy) = -(1/\rho)(\partial p/\partial y) + \nu(d^2v/dy^2) \quad (2)$$

$$(dv/dy) = 0 \quad (3)$$

with the boundary conditions

$$y = 0 \quad u = 0 \quad v = \text{constant} = b$$
$$y = a \quad u = U$$

Eq. (3) shows that v = constant everywhere (implying a porous moving plate) and from Eq. (2), since $(\partial p/\partial y) = 0$, $p = p(x)$ only. In Eq. (1), $(\partial p/\partial x)$ must be constant, for the remaining terms are independent of x.

If $\bar{u} = u/U$; $\bar{v} = b/U$ = constant; $\bar{x} = x/a$; $\bar{y} = y/a$; $Re = Ua/\nu$ and $c = -(Re/\rho U^2)(dp/d\bar{x})$, Eq. (1) can be written

$$(d\bar{u}^2/d\bar{y}^2) - \bar{v}Re(d\bar{u}/d\bar{y}) + c = 0 \quad (4)$$

with the boundary conditions

$$\bar{y} = 0 \quad \bar{u} = 0; \quad \bar{y} = 1 \quad \bar{u} = 1$$

Although Eq. (4) above is similar to Eq. (5) of reference 1, it must be noted that now

$$c = -(Re/\rho U^2)(dp/d\bar{x})$$

and not as given in reference 1.

The term c thus refers to the "Couette-type" problem with a superimposed axial pressure gradient. The solution of Eq. (4) satisfying the above boundary conditions is

$$\bar{u} = \{[(c/\bar{v}Re) - 1]/[1 - e^{\bar{v}Re}]\}(e^{\bar{v}Re\bar{y}} - e^{\bar{v}Re}) + (c/\bar{v}Re) \times [\bar{y} - 1] + 1 \quad (5)$$

as given in reference 1.

Separation at the fixed wall is obtained when $(d\bar{u}/d\bar{y})_{\bar{y}=0} = 0$ which from Eq. (5) is equivalent to

$$c = (\bar{v}Re)^2/[1 + \bar{v}Re - e^{\bar{v}Re}] \quad (6)$$

When $(\bar{v}Re) \ll 1$, Eq. (6) reduces to

$$c = -2 + (2/3)(\bar{v}Re) + 0(\bar{v}Re)^2 \quad (6a)$$

Thus, separation occurs when the applied positive pressure gradient

$$(dp/d\bar{x})/(1/2)\rho U^2 = (4/Re)[1 - (\bar{v}Re/3) + 0(\bar{v}Re)^2] \quad (6b)$$

Hence, a smaller adverse pressure gradient will provoke separation when blowing ($\bar{v}$ positive) than for suction ($\bar{v}$ negative).

When the pressure gradient is zero ($c = 0$), the shear stress at the stationary wall

$$(\tau_w/\rho U^2) = (d\bar{u}/dy)/Re = \bar{v}/(e^{\bar{v}Re} - 1) \quad (7)$$

$$= (1/Re)\,[1 - (\bar{v}Re)/2 + 0(\bar{v}Re)^2] \quad (7a)$$

for $\bar{v}Re \ll 1$. Thus, the skin friction is reduced by blowing and increased by suction at the stationary wall. Separation does not strictly occur in the case of zero pressure gradient except in the limit as $(\bar{v}Re)$ tends to infinity with $\bar{v}$ positive (blowing).

REFERENCE

[1] Cramer, K. R., *A Generalized Porous-Wall "Couette-type" Flow*, Readers' Forum, Journal of the Aero/Space Sciences, Vol. 26, No. 2, pp. 121–122, February, 1959.

The Modified Goodman Diagram and Random Vibration

H. C. Schjelderup

National Engineering Science Co., Pasadena, Calif.

May 13, 1959

SYMBOLS

N_0	= the SN curve for mean stress zero
N_{SM}	= the SN curve for mean stress S_M
N_R	= the random SN curve
ΔS	= amplitude of sinusoidal stress fluctuation with nonzero mean, psi
ΔS_0	= amplitude of sinusoidal stress fluctuation with zero mean, psi
S_M	= mean stress, psi
S_U	= ultimate stress, psi
$\bar{S}$	= peak-stress amplitude, random vibration
$\bar{S}$	= root-mean-stress amplitude, random vibration, non-zero mean
$\bar{S}_0$	= root-mean-stress amplitude, random vibration, zero mean
$\sigma = S/\bar{S}$	= a dimensionless stress ratio
$P(\sigma)$	= the probability-density distribution of peak-stress amplitudes
n	= an exponent

MOST DISCUSSIONS of the problem of fatigue damage associated to random vibration[1, 2] have been about vibration with mean stress zero. Although this assumption was made, the methods presented are not restricted to this condition. However, accumulation of fatigue data covering all possible combinations of amplitude distributions and mean stress would be prohibitive. For this reason, a method of extrapolating known fatigue data would be of interest.

A method of extrapolation which has been applied to the simple cyclic fatigue problem is to use the modified Goodman or Gerber diagrams. Analytically, these diagrams may be expressed by Eq. (1).

$$\Delta S/S_U = (\Delta S_0/S_U)[1 - (S_M/S_U)^n] \quad (1)$$

which is the equation of a line of constant fatigue life. The exponent n takes values of unity and two for the Goodman and Gerber diagram, respectively.

Eq. (1) may be reformed, as shown in Eq. (2)

$$\Delta S_0 = \Delta S/1 - (S_M/S_U)^n \quad (2)$$

In this form, ΔS_0 may be interpreted as the fluctuating stress at zero mean stress giving equivalent life to a fluctuating stress ΔS at mean stress S_M. Or, if $N_0(\Delta S_0)$ is the S-N curve for zero mean stress, $N_0[\Delta S/1 - (S_M/S_0)^n]$ is the S-N curve $N_{SM}(\Delta S)$ for mean stress S_M.

In order to apply the above to the random vibration problem, first make the following assumptions:

(a) The probability-density distribution of peak-stress amplitudes $P(\sigma)$ will not alter with change in mean stress.

(b) Miner's linear cumulative damage will satisfactorily provide a tool for computing changes in life with variations of mean stress.

Then a family of Random Fatigue Curves could be computed from Eq. (3)

$$1/N_R(\bar{S}) = \int_0^\infty [P(\sigma)d\sigma/N_{SM}(\sigma)] \quad (3)$$

Or, substituting $N_0\{\sigma/[1 - (S_M/S_U)^n]\}$ for $N_{SM}(\sigma)$, Eq. (3) may be rewritten

$$1/N_R(\bar{S}) = \int_0^\infty \left(P(\sigma)d\sigma/N_0\{\sigma/[1 - (S_M/S_U)^n]\}\right) \quad (4)$$

Since Eq. (4) is now expressed in terms of the fundamental S-N curve $N_0(\Delta S_0)$, the effects of change in mean stress can be simply interpreted as a change in the effective root-mean-stress $\bar{S}$ by the factor $1 - (S_M/S_U)^n$.

Thus, changes in the random fatigue curve $N_R(\bar{S})$ caused by nonzero mean stress S_M may also be approximated by Goodman-type diagrams of the form of Eq. (5).

$$\bar{S}/S_U = (\bar{S}_0/S_U)[1 - (S_M/S_U)^n] \quad (5)$$

The implication of the above result is that one might expect similar trends in fatigue phenomena for random vibration as has been experienced in the more simple sinusoidal tests. However, the restrictions imposed by the preceding assumptions limits this observation to the long-life, low-stress fatigue regime.

REFERENCES

[1] Miles, John W., *On Structural Fatigue Under Random Loading*, Journal of the Aeronautical Sciences, Vol. 21, No. 11, pp. 753–762, November, 1954.

[2] Head, A. K., and Hooke, F. N., *Random Noise Fatigue Testing*, International Conference on the Fatigue of Metals, Session 3, Paper 9, London, September, 1956.

Calculation by the Integral Method of the Effect of Fluid Injection Upon an Isothermal Boundary Layer*[5]

Milton M. Klein

Physicist, General Electric Company, Aerosciences Laboratory, Missile and Space Vehicle Department, Philadelphia, Pa.

May 11, 1959

NUMERICAL SOLUTIONS have recently been obtained for the problem of fluid injection into an isothermal boundary layer by Smith,[1] and Eckert and Schneider.[2] We have investigated the applicability of the integral method as a labor-saving tool in fluid-injection problems, but without the restrictive assumption of constant fluid properties.[3] Fourth-degree polynomials were used along with the usual boundary conditions. We have assumed for purpose of comparison,[2] that the air velocity relative

* Work performed under the auspices of the USAF Ballistic Missiles Division, Contract No. AF 04(645)24.

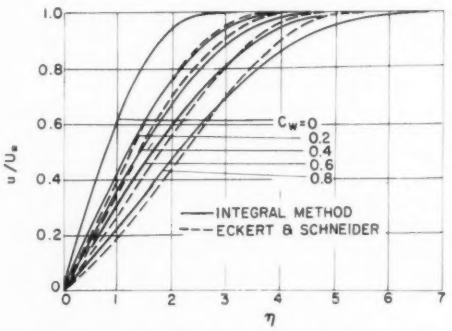

FIG. 1. Effect of injection of hydrogen upon velocity profiles for several values of C_w.

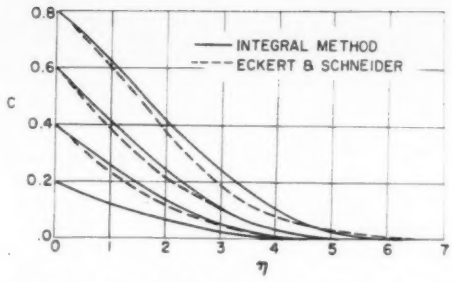

FIG. 2. Effect of injection of hydrogen upon concentration profiles for several values of C_w.

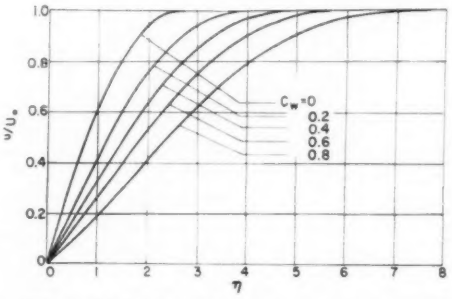

FIG. 3. Effect of injection of helium upon velocity profiles for several values of C_w.

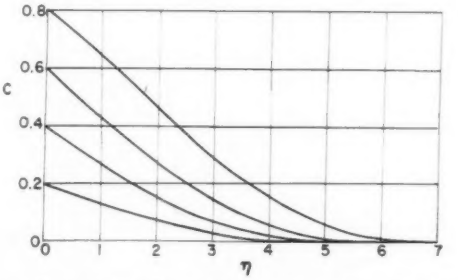

FIG. 4. Effect of injection of helium upon concentration profiles for several values of C_w.

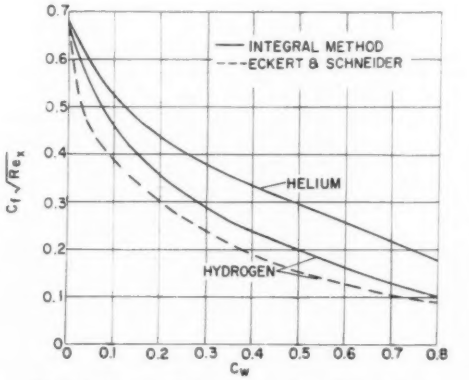

FIG. 5. Skin-friction coefficient c_f for injection of hydrogen or helium.

to the wall is zero. Calculations were made for hydrogen and helium as the injected gases. The fluid properties were obtained from the work of Carlson and Schneider;[4] for the case of hydrogen, these properties are the same as those of reference 2.[5]

The velocity and concentration profiles are given in Figs. 1 and 2 for hydrogen, and in Figs. 3 and 4 for helium, for several wall concentrations C_w; for comparison, the corresponding results of reference 2 for hydrogen are given in Figs. 1 and 2. In general, the results obtained here are in good agreement with those of reference 2 except at the higher wall concentrations. The local skin-friction coefficient c_f for hydrogen and helium obtained herein and the corresponding results of reference 2 for hydrogen are given in Fig. 5 as a function of C_w. The values of c_f by the integral method are about 20 per cent higher than those of reference 2, an agreement somewhat less than that corresponding to the velocity profiles. The lesser accuracy for the derivatives of the velocity than for the velocity is generally to be expected with the integral method.

REFERENCES

[1] Smith, John W., *Effect of Diffusion Fields on the Laminar Boundary Layer*, Journal of the Aeronautical Sciences, Vol. 21, No. 3, pp. 154–162, 178, March, 1954.

[2] Eckert, E. R. G., and Schneider, P. J., *Effect of Diffusion in an Isothermal Boundary Layer*, Readers' Forum, Journal of the Aeronautical Sciences, Vol. 23, No. 4, pp. 384–387, April, 1956.

[3] Spalding, D. B., *Mass transfer in laminar flow*, Proc. Royal Soc. (London) Ser. A, Vol. 221, No. 1144, pp. 78–99, January 7, 1954.

[4] Carlson, W. O., and Schneider, P. J., *Transport Properties for Binary Gas Mixtures*, University of Minnesota, Heat Transfer Laboratory, Tech. Rep. No. 7, January, 1956.

[5] Klein, Milton M., *Calculation by the Integral Method of the Effect of Fluid Injection Upon an Isothermal Boundary Layer*, RM 13, No. R58SD225, Technical Information Series, General Electric Co., Missile and Space Vehicle Department, April, 1958.

Comments on "On Slip-Flow Heat Transfer to a Flat Plate"

Donald E. Nestler

General Electric Company, Aerophysics Engineering, Missile and Space Vehicle Department, Philadelphia, Pa.

May 13, 1959

SYMBOLS

Subscripts

e = at edge of boundary layer
0 = continuum-flow value
w = at wall

OMAN AND SCHEUING'S NOTE[1] presented a solution for the slip-flow heat-transfer rate to a flat plate. They plotted q/q_0 vs. Knudsen Number Kn for $Pr = 0.72$, $\gamma = 1.4$, $\sigma = \alpha = 0.9$, and several values of the wall-temperature parameter n. For values of Kn less than 0.5, the ratio q/q_0 was relatively insensitive to the parameter n. For $n = 0$, the authors obtained $q/q_0 = 0.82$ for $Kn = 0.1$. This is a significant reduction in heat transfer due to slip, in contrast with Maslen's statement[2] that there is zero first-order effect of slip on heat transfer.

A partial cause of this discrepancy appears to be the assumption of the authors that the boundary-layer thickness δ is unaffected by the slip velocity at the wall. Donaldson[3] has obtained the effect of slip on the boundary-layer thickness for the incompressible case by use of the von Kármán momentum-integral method and an assumed quadratic velocity profile. His results can be written:

$$\delta/\delta_0 = 1/5.48Kn[f_2(k)]^{0.5} \quad (1)$$

in which $k = 1/Kn$ and

$$f_2(k) = (k^2/10) - (8/15) + (16/15)[1/(2+k)] - (1/15)[k^3/(2+k)] + (8/15)\log_e[(2+k)/2] \quad (2)$$

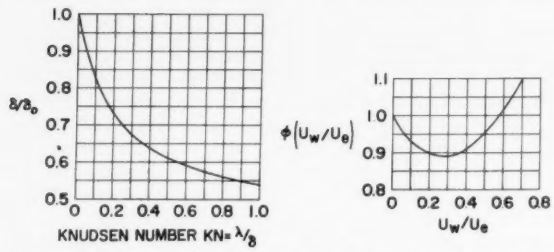

FIG. 1 (*left*). Effect of slip flow on boundary-layer thickness. FIG. 2 (*right*). Reynolds-analogy function for slip flow (Eq. 7).

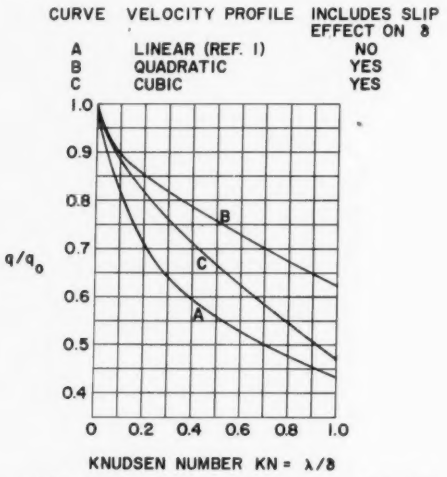

FIG. 3. Effect of slip flow on heat transfer to a flat plate. $n = 0$, $\sigma = \alpha = 0.9$, $Pr = 0.72$, $(T_w/T_e) = 1$, $\gamma = 1.4$.

Eq. (1) is shown plotted in Fig. 1. It is seen that the effect of slip on boundary-layer thickness is by no means negligible.

Since Oman and Scheuing's numerical results were based on a linear velocity profile, it would not be consistent to adjust them for the change in δ based on a quadratic profile. However, general relations were obtained in reference 1 which are independent of the velocity-profile assumption. For $n = 0$, Eq. (13) of reference 1 yields:

$$q/q_0 = (\partial U/\partial y)_w/[(\partial U/\partial y)_w]_0 \times \left(2\sqrt{Pr}(U_w/U_e) + \{[(1 - U_w/U_e)^2 - A_1(U_w/U_e)^2] \div [1 - A_2(U_w/U_e)]\}\right) \quad (3)$$

in which $A_1 = [8\gamma/(\gamma + 1)\sqrt{Pr}][(1 - \alpha)/\alpha][\sigma/(2 - \sigma)]$ (4)

and $A_2 = 1 - [2\gamma/(\gamma + 1)][\sigma/(2 - \sigma)][(2 - \alpha)/\alpha][1/Pr)$ (5)

By definition of the skin-friction coefficient c_f,

$$(\partial U/\partial y)_w/[(\partial U/\partial y)_w]_0 = \tau_w/(\tau_w)_0 = c_f/(c_f)_0 \quad (6)$$

Combining Eq. (3) and (6):

$$q/q_0 = c_f/(c_f)_0\phi(U_w/U_e) \quad (7)$$

in which

$$\phi(U_w/U_e) = 2\sqrt{Pr}(U_w/U_e) + \{[(1 - U_w/U_e)^2 - A_1(U_w/U_e)^2]/[1 - A_2(U_w/U_e)]\} \quad (8)$$

The function $\phi(U_w/U_e)$ is a measure of how well the Reynolds analogy holds in slip flow. It is plotted in Fig. 2 for $\sigma = 0.9$, $Pr = 0.72$, and $\gamma = 1.4$. The slip-velocity ratio U_w/U_e can be shown to be related to Kn by

$$U_w/U_e = \{m[(2 - \sigma)/\sigma]Kn\}/\{1 + m[(2 - \sigma)/\sigma]Kn\} \quad (9)$$

in which m is the order of the assumed velocity profile ($m = 1$, linear; $m = 2$, quadratic; etc.). Eq. (9) has been verified for $m = 1$, 2, and 3. Finally, the values of c_f/c_{f0} are available from the solutions of Donaldson[3] and Laurmann,[4] respectively, which include the effect of slip on δ. Their results can be written:

Quadratic velocity profile (Donaldson): $c_f/(c_f)_0 = 5.5[f_2(k)]^{0.5}/(2 + k)$ (10)

Cubic velocity profile (Laurmann): $c_f/(c_f)_0 = 7.48[f_3(k)]^{0.5}/(3 + k)$ (11)

in which $f_2(k)$ is given in Eq. (2), and

$$f_3(k) = (1/7)\{(k^2/8) + (3/4)[k(k - 5)/(k + 3)] + (15/4)\log_e[1 + (k/3)]\} \quad (12)$$

Using Eqs. (7)–(11), the curves of q/q_0 of Fig. 3 were computed for $\sigma = \alpha = 0.9$, $Pr = 0.72$, and $\gamma = 1.4$. The values of Oman aud Scheuing are shown for comparison. The cubic profile values are not necessarily more exact than the quadratic profile values, since an increase in the order of the velocity-profile polynomial does not necessarily produce improved accuracy—e.g., Schlichting,[5] p. 205.

CONCLUSIONS

The investigations reported herein, which are part of reference 6, have yielded the following conclusions:

(1) The effect of slip on boundary-layer thickness is not negligible. Inclusion of this effect gives a smaller reduction in heat transfer due to slip than was obtained in reference 1.

(2) The Reynolds analogy holds reasonably well in the slip-flow regime, as indicated by Eq. (7) and Fig. 2. Thus, a reasonable assumption for engineering purposes is

$$q/q_0 = c_f/(c_f)_0$$

(3) The validity of the theoretical method based on continuum boundary-layer equations with slip conditions at the wall awaits experimental verification. The values of Fig. 3 must therefore be regarded as first approximations.

REFERENCES

[1] Oman, R. A., and Scheuing, R. A., *On Slip-Flow Heat Transfer to a Flat Plate*, Readers' Forum, Journal of the Aero/Space Sciences, Vol. 26, No. 2, pp. 126–127, February, 1959.

[2] Maslen, S. H., *On Heat Transfer in Slip Flow*, Readers' Forum, Journal of the Aeronautical Sciences, Vol. 25, No. 6, pp. 400–401, June, 1958.

[3] Donaldson, C. du P., *An Approximate Method for Estimating the Incompressible Laminar Boundary-Layer Characteristics on a Flat Plate in Slipping Flow*, NACA RM L9CO2, May, 1949.

[4] Laurmann, J. A., *The Momentum Integral Method Applied to the Compressible Boundary Layer with a Slip Boundary Condition*, University of California, Technical Report HE-150-160, August 20, 1958.

[5] Schlichting, H., *Boundary Layer Theory*, McGraw-Hill Book Co., New York, 1955.

[6] Nestler, D. E., *Survey of Theoretical and Experimental Determinations of Skin Friction in Compressible Boundary Layers: Part 5. The Effect of Slip Flow*, TIS R59SD343, General Electric Co., Missile and Space Vehicle Dept., Philadelphia, Pa.

REQUIREMENTS *for* CONTRIBUTIONS
to the publications of the
INSTITUTE *of the* AERONAUTICAL SCIENCES

The Institute of the Aeronautical Sciences invites both members and nonmembers from any country to submit papers for publication in the JOURNAL OF THE AERO/SPACE SCIENCES and AERO/SPACE ENGINEERING. The Institute, following the practice of other societies, does not pay for contributions.

The following directions for the preparation of papers, if followed by authors, will save correspondence, avoid the return of papers for changes, minimize the work of preparation for the printer, and save the expense due to the charges made for "author's corrections."

MANUSCRIPTS: The original typewritten copy of the paper is desired. **To expedite review, an additional copy of both the manuscript and figures should be submitted.** The manuscript must be double or triple spaced on one side of white paper sheets, consecutively numbered. There should be wide margins to allow for the marking of directions to the printer. Correcting, changing, or adding to papers after they are in type is costly. It is, therefore, imperative that papers submitted be in final form. Typographical errors may be corrected on proofs, but if authors wish to add material, they may do so at their own expense. In mailing, drawings may be rolled, but manuscripts should be sent flat. Send by first-class mail (register if you wish for your own protection) to the Editorial Office, Institute of the Aeronautical Sciences, 2 East 64th Street, New York 21, N.Y. All manuscripts will be examined by the Editorial Committee and by the Editor. Authors will be advised as promptly as possible whether the paper is acceptable for publication.

TITLES: The title of the paper should be brief. The name and initials of the author should be written as he prefers. The use of the full name of an author is advocated because of the frequent duplication of initials and surnames which sometimes makes it difficult to establish the identity of the author. This is particularly important for large annual indexing and abstracting services. All titles and degrees or honors are omitted. The name of the organization with which the author is associated should be placed after his name on a separate line. The date on which the paper is received will be inserted by the Editor. The author's title or position should be indicated in a footnote.

SUMMARIES OR ABSTRACTS: An abstract to be printed at the beginning should accompany each article. It should be adequate as an *index* and as a *summary*. It should contain a statement of major conclusions reached, since summaries in many cases constitute the only source of information used in compiling scientific reference indexes. Abstracts printed in other journals, especially foreign, in most cases consist of summaries from printed papers. The summary should explain as adequately as possible the major conclusions to a nonspecialist in the subject and should contain from 100 to 300 words, depending on the length of the paper.

SUBHEADINGS: Subheadings should be inserted by the author at frequent intervals. The work of editorial preparation will be simplified by the author's provision of many subheadings.

MATTER USUALLY DELETED: Photographs or illustrations of little technical interest and not showing advances in general practice. Too detailed tabular matter (general results of such tables may be included in the text). Lengthy descriptions of materials or processes or of preliminary experiments of theories that preceded final results; salient features only are of interest.

REFERENCES: References should be numbered consecutively and grouped together at the end of the manuscript, with only the corresponding number being mentioned in the text. The arrangement should be as follows. For books: [1]Durand, W. F., *Aerodynamic Theory*, 1st Ed., Vol. 1, p. 23; Julius Springer, Berlin, 1934. For magazines: [1]England, C. R., Crawford, A. B., and Mumford, W. W., *Some Results of a Study of Ultra-Short-Wave Transmission Phenomenon*, Proc. IRE, Vol. 20, No. 12, pp. 481–482, March, 1933. Please give author, title, edition, volume, number, page, publisher, and place and date of publication as indicated. Omission of one required fact causes much extra editorial work and possible inaccuracies.

ILLUSTRATIONS: Illustrations should accompany manuscripts, and each should always be referred to in the text by number. Drawings or graphs should not be larger than 12 × 16 inches, and must be made with jet black India ink on white paper or tracing cloth, the latter being preferred. *Do not use typewriter for lettering.* The smallest lettering on 8 × 10 inch figures should be no less than $^1/_4$ inch high. Cross-section paper (white with black lines) may be used, but it should not have more than 4 lines per inch. If finer ruled paper is used, the major division lines should be drawn in with black ink, omitting the finer divisions. In the case of finely ruled paper, only blue-lined paper can be accepted. *Tracing paper and blueprints* are not acceptable. Lettering and all markings must be large enough to be readable after reduction to single-column width ($3^5/_{16}$ in.). Mail rolled or flat; never fold. Drawings that cannot be reproduced (including pencil drawings) will be returned to the author for redrawing, thus delaying publication of the paper. Photographs should be distinct and show clear black and white contrasts. They must be on glossy white paper. Avoid round or oval photographs.

CAPTIONS AND LEGENDS: Legends or captions must accompany each drawing or photograph submitted. If written on the drawing or photograph, they should be placed below and well outside the part to be reproduced. Each table should have a caption such as Table 1, Table 2, Table 3, etc. Captions should be complete in themselves so as to make the data intelligible to the reader without reference to the text. A duplicate list of captions for figures should be included as the last page of the manuscript. Use "Fig. 1" (not Figure 1), "Figs. 3 and 4," etc., in both the text and the numbering of illustrations. In the text, "Eq. (1)" or "Eqs. (1) and (2)" is used, not "Equation (1)." In captions, legends, and in table headings, write all words in full; do not abbreviate, except for "Fig." and "Eq."

MATHEMATICAL WORK: Formulas may be typewritten or carefully written in pen and ink, the writing to be large enough so that it can be marked for the printer. Considerable space for marking should be allowed above and below all equations. All complicated equations should be repeated on separate sheets with plenty of space left for marking. The solidus should be used for simple fractions appearing within the text. Make all expressions clear to the typesetter. Greek letters used in formulas should be clearly designated by name in the margin of the manuscript. The difference between capital and lower-case letters should be clearly distinguished and care taken to avoid confusion between zero (0) and the letter (o), between the numeral (one), and the letter (ell) and the prime (′), between alpha and a, kappa and k, u and mu, v and nu, n and eta. All subscripts and exponents should be clearly distinguished. Avoid complicated exponents and subscripts. Dots and bars over letters or mathematical expressions should also be avoided. When it is necessary to repeat a complicated expression, it should be represented by some convenient symbol.

SYMBOLS AND ABBREVIATIONS: The symbols recommended in the American Standard Association "Letter Symbols for Aeronautical Sciences," ASA Y10.7—1954, should be used wherever practicable. All symbols should be clearly written and carefully checked. Standard abbreviations should be used, and it should be noted that most abbreviations are lower case, such as m.p.h., b.m.e.p., i.h.p., b.hp., hp., etc.

CORPORATE MEMBERS

OF THE

INSTITUTE OF THE AERONAUTICAL SCIENCES

AC SPARK PLUG DIVISION, GENERAL MOTORS CORPORATION

ACADEMY OF AERONAUTICS

ADAMS RITE MANUFACTURING COMPANY

AEROJET-GENERAL CORPORATION

AEROLAB DEVELOPMENT COMPANY

AERONCA MANUFACTURING CORPORATION

AERONUTRONIC SYSTEMS, INC.

AEROQUIP CORPORATION

AGAWAM AIRCRAFT PRODUCTS, INC

ALLIED RESEARCH ASSOCIATES, INC.

ALLISON DIVISION, GENERAL MOTORS CORPORATION

ALUMINUM COMPANY OF AMERICA

AMERICAN AIRLINES, INC.

AMERICAN BOSCH ARMA CORPORATION

AMERICAN STEEL & WIRE DIVISION, UNITED STATES STEEL CORPORATION

AMOCO CHEMICALS CORPORATION

AMPHENOL-BORG ELECTRONICS CORPORATION

ANDERSON, GREENWOOD & CO.

ARDE ASSOCIATES

ASSOCIATED AVIATION UNDERWRITERS

AVCO RESEARCH LABORATORY

AVIEN, INC.

AVRO AIRCRAFT LIMITED

BAKER STEEL & TUBE COMPANY

BEECH AIRCRAFT CORPORATION

BELL AIRCRAFT CORPORATION

BENDIX AVIATION CORPORATION

BOEING AIRPLANE COMPANY

BOOZ, ALLEN & HAMILTON

THE BRISTOL AEROPLANE COMPANY (U.S.A.) INC.

BULOVA RESEARCH AND DEVELOPMENT LABORATORIES, INC.

CANADAIR, LTD.

THE CESSNA AIRCRAFT COMPANY

CHANCE VOUGHT AIRCRAFT, INCORPORATED

THE CHASE MANHATTAN BANK

CHICAGO AERIAL INDUSTRIES, INC.

THE CLEVELAND PNEUMATIC INDUSTRIES, INC.

CONSOLIDATED CONTROLS CORPORATION

CONTINENTAL MOTORS CORPORATION

CORNELL AERONAUTICAL LABORATORY, INC.

CURTISS-WRIGHT CORPORATION

DANIEL, MANN, JOHNSON, & MENDENHALL

THE DECKER CORPORATION

DEL MAR ENGINEERING LABORATORIES

DELCO-REMY DIVISION, GENERAL MOTORS CORPORATION

DOAK AIRCRAFT COMPANY, INC.

DOUGLAS AIRCRAFT COMPANY, INC.

DZUS FASTENER COMPANY, INC.

EASTERN AIR LINES, INC.

EATON MANUFACTURING COMPANY

EDO CORPORATION

ELASTIC STOP NUT CORPORATION OF AMERICA

ELECTROL INCORPORATED

ENGINEERING SUPERVISION COMPANY

ESSO STANDARD OIL COMPANY

FAIRCHILD CAMERA AND INSTRUMENT CORPORATION

FAIRCHILD ENGINE AND AIRPLANE CORPORATION

THE FIRESTONE TIRE & RUBBER COMPANY

THE GARRETT CORPORATION

GENERAL APPLIED SCIENCE LABORATORIES, INC.

GENERAL DYNAMICS CORPORATION

GENERAL ELECTRIC COMPANY

GENERAL PRECISION EQUIPMENT CORPORATION

G. M. GIANNINI & CO., INC.

GIANNINI PLASMADYNE CORPORATION

THE B. F. GOODRICH COMPANY

GOODYEAR AIRCRAFT CORPORATION

GRUMMAN AIRCRAFT ENGINEERING CORPORATION

HYDRO-AIRE, INC.

INSURANCE COMPANY OF NORTH AMERICA COMPANIES

INTERNATIONAL BUSINESS MACHINES CORPORATION

THE INTERNATIONAL NICKEL COMPANY, INC.

ITT LABORATORIES, DIVISION OF INTERNATIONAL TELEPHONE AND TELEGRAPH CORPORATION

JANITROL AIRCRAFT DIVISION, SURFACE COMBUSTION CORPORATION

JOHNS-MANVILLE SALES CORPORATION

EARLE M. JORGENSEN CO.

WALTER KIDDE & COMPANY, INC.

KOLLSMAN INSTRUMENT CORPORATION

LAVELLE AIRCRAFT CORPORATION

LEAR, INCORPORATED

C. W. LEMMERMAN, INC.

LIBRASCOPE, INCORPORATED

THE LIQUIDOMETER CORPORATION

LOCKHEED AIRCRAFT CORPORATION

LOEWY-HYDROPRESS DIVISION OF BALDWIN-LIMA-HAMILTON CORPORATION

LONGINES-WITTNAUER WATCH COMPANY, INC.

THE MARQUARDT CORPORATION

THE MARTIN COMPANY

MARTIN STEEL PRODUCTS CORPORATION

McDONNELL AIRCRAFT CORPORATION

MELETRON CORPORATION

MID-CONTINENT MANUFACTURING, INC.

MINNEAPOLIS-HONEYWELL REGULATOR COMPANY

NATIONAL CREDIT OFFICE, INC.

NORTH AMERICAN AVIATION, INC.

NORTHROP CORPORATION

NUCLEAR DEVELOPMENT CORPORATION OF AME

PAN AMERICAN WORLD AIRWAYS, INC.

THE RALPH M. PARSONS COMPANY

PESCO PRODUCTS DIVISION, BORG-WARNER CORP TION

PHILLIPS PETROLEUM COMPANY

PIASECKI AIRCRAFT CORPORATION

RADIO CORPORATION OF AMERICA DEFENSE ELECTRONIC PRODUCTS

REPUBLIC AVIATION CORPORATION

ROHR AIRCRAFT CORPORATION

PAUL ROSENBERG ASSOCIATES

RYAN AERONAUTICAL COMPANY

SANDBERG-SERRELL CORPORATION

SHAFER BEARING DIVISION, CHAIN BELT COM

SHELL OIL COMPANY

SIMMONDS AEROCESSORIES, INC.

SOCONY MOBIL OIL COMPANY, INC.

SOLAR AIRCRAFT COMPANY

SOUTHWEST PRODUCTS CO.

SPACE TECHNOLOGY LABORATORIES, INC.

R. DIXON SPEAS ASSOCIATES

SPERRY GYROSCOPE COMPANY DIVISION OF SP RAND CORPORATION

STANDARD OIL COMPANY OF CALIFORNIA

STANDARD OIL COMPANY (INDIANA)

STANDARD-THOMSON CORPORATION CLIFFORD MANUFACTURING DIVISION

STANLEY AVIATION CORPORATION

THIOKOL CHEMICAL CORPORATION

THOMPSON RAMO WOOLDRIDGE INC.

TRANS WORLD AIRLINES, INC.

TURBO PRODUCTS, INC.

UNION CARBIDE CORPORATION

UNITED AIR LINES, INC.

UNITED AIRCRAFT CORPORATION

UNITED STATES AVIATION UNDERWRITERS, I

VARD, INC.

VERTOL AIRCRAFT CORPORATION

VITRO CORPORATION OF AMERICA

WESTERN GEAR CORPORATION

WESTINGHOUSE ELECTRIC CORPORATION

WESTON INSTRUMENTS DIVISION OF DAYST INC.

WYMAN-GORDON COMPANY

YOUNG RADIATOR COMPANY